Universität Augsburg
Lehrstuhl für
Experimentalphysik I

Universität Augsburg
Chair for
Experimental Physics I

Acousto-Electrically Driven Charge Carrier Dynamics in Metal Halide Perovskites: From Fundamental Studies to Sensor Applications

Dissertation

zur Erlangung des akademischen Grades
Dr. rer. nat.

eingereicht an der
Mathematisch-Naturwissenschaftlich-Technischen Fakultät
der Universität Augsburg

von

Lisa Janker

Januar 2020

Deutsche Forschungsgemeinschaft
German Research Foundation

First referee: Prof. Dr. Hubert J. Krenner
Second referee: Prof. Dr. Alexander S. Urban
Date of oral exam: 07.07.2020

Abstract

In recent research on solar cells that can surpass with the efficient conventional modules on the basis of silicon, ever more new materials are synthesized and tested. One class of these materials which is highly promising for the application in solar cells is in perovskite structure. After a few years of research it was already shown to reach efficiencies as high as commercial cells. This crystal structure can be formed with various different material combinations. This thesis focuses on the group of metal halide perovskites as they have very promising optoelectronic properties. Beside variations in the composition, structures with lower dimensionality have also gained more interest. Their very flexible and easy fabrication process paired with their very interesting and exceptionally good electronic properties makes them exciting objects to study. The high absorption and photoluminescence quantum yield in the perovskite nanostructures opens up a whole field of possible studies to conduct. This thesis deals with electrical characterizations and manipulations of the charge carrier dynamics in nanowires of metal halide perovskites.

In order to investigate the mechanisms that happen during transport of electrons and holes in such small systems, the contact-free detection method of acousto-optoelectric spectroscopy via surface acoustic wave application is chosen. This method is especially helpful in the examination of these small structures because it lacks the necessity of precisely defining metal contacts on the sample. Instead, the electric field accompanying the mechanical wave is exploited to act upon the charge carriers in a quasi-static approach as the field is adapted to the velocity of the sound wave which is much slower than the speed of light in the medium. In this way the electrons and holes react to the wave and can follow its movement and thus, be transported. In $CsPbI_3$ perovskite nanowires the effect on excitons, bound electron hole pairs, is observed. Time-resolved measurements show that both charge carriers have similar mobilities and that both are moved. The effect of the surface acoustic wave on an exciton can be described by two phenomena: a dissociation and a polarization of the quasi-particle. This is validated in this thesis by the application of a phenomenological model that mimics exactly those two processes. A subsequent numerical calculation of the drift and diffusion equations applied to the system reveals more insights into the dynamics that happen during the application of the surface acoustic wave and confirms that the mobilities of electrons and holes are indeed equal and can be quantified to around 3 $\frac{\mathrm{cm}^2}{\mathrm{Vs}}$. Low temperature studies confirm the findings and provide a deeper understanding of the system. A final repetition of the time-resolved experiment on the perovskite structure $CsPbBr_3$ corroborates the great influence of the exciton binding energy on the strength of the observed phenomena.

Additionally, the easily bandgap-tunable nanowires are perfect sensing materials via the effect of photoconductivity. In a tapered transducer design, the spatially resolved detection of light absorption via the nanostructures is realized. Through the photo-induced charge carrier creation in material deposited in the travelling path, the transmission of a surface acoustic wave can be altered by the reciprocal impact of charge carriers and electric field. This is exploited in the construction of a wavelength and position resolved detector. In the measurements, the recorded absorption edge of several materials nicely reproduces optical absorption measurements and matches the energy of the photoluminescence of the nanowires. The addition of a perpendicular

pair of surface acoustic wave transmitter and receiver enables a full two dimensional position detection.

The switch from a simple delay line to a resonator-based design shows that the surface acoustic wave can even be used as a mass load detector with high sensitivity through the shifts in resonance frequency induced by the mass. Through the stiffness changes, this works even for rather light material and small amounts. Furthermore, this design is also capable of sensing the conductivity of deposited material analogously to the aforementioned system. As a proof of principle, the absorption edge of one exemplary material is presented for this chip as well, which coincides nicely with the previous investigations.

Zusammenfassung

In der aktuellen Forschung zu Solarzellen, die mit den effizienten Modulen aus industriellem Silizium mithalten können, werden immer mehr neue Materialien hergestellt und getestet. Eine sehr vielversprechende Klasse von solchen Materialien für den Einsatz in Solarzellen ist die der Perowskitstrukturen. Nach nur wenigen Jahren der Forschung konnten diese bereits die gleiche Effizienz erreichen wie kommerzielle Solarzellen. Die besondere Kristallstruktur kann mit vielfältigen Materialkombinationen erreicht werden. Diese Arbeit fokussiert sich dabei auf die Gruppe der Metall-Halogen-Perowskite. Neben den Variationen in der Zusammensetzung des Materials haben auch niederdimensionale Strukturen an Interesse gewonnen. Ihre Flexibiltät und einfache Herstellung gepaart mit ihren sehr interessanten und außergewöhnlich guten elektrischen Eigenschaften, machen sie zu einem spannenden Forschungsobjekt. Die hohe Absorptionsrate und die hohe Quantenausbeute in der Photolumineszenz eröffnen ein ganz neues Feld möglicher Studien. Diese Arbeit beschäftigt sich mit der elektronischen Charakterisierung und der Manipulation der Ladungsträger in Nanodrähten aus Metall-Halogen-Perowskit.

Um die Mechanismen während des Ladungsträgertransportes in so kleinen Systemen untersuchen zu können, wurde die Methode der akusto-optoelektrischen Spektroskopie mithilfe von Oberflächenwellen gewählt. Diese Messmethode ist besonders dann hilfreich, wenn ultrakleine Strukturen untersucht werden sollen, da keine Metallkontakte hochpräzise auf der Probe aufgebracht werden müssen. Stattdessen wird das elektrische Feld, welches die mechanische Wellen auf einem piezoelektrischen Substrat begleitet, ausgenutzt, um die Ladungsträger zu beeinflussen. Dies geschieht quasi-statisch, da die Feldgeschwindigkeit an die Schallgeschwindigkeit der akustischen Welle angepasst ist und sich nicht mit der Lichtgeschwindigkeit im Substrat ausbreitet. Dadurch haben die Elektronen und Löcher genug Zeit auf das Feld zu reagieren und können der Bewegung der Welle folgen, wodurch ein Transport stattfindet. In den $CsPbI_3$-Nanodrähten wird der Effekt der Wellen auf Exzitonen, gebundene Elektron-Loch-Paare, beobachtet. In zeitaufgelösten Messungen zeigt sich, dass beide Ladungsträger die gleiche Mobilität haben und beide von der Welle gleichermaßen bewegt werden. Der Effekt der Oberflächenwelle auf die Exzitonen kann durch zwei Phänomene beschrieben werden: die Aufspaltung und die Polarisation des Quasi-Teilchens. Das wird in der Arbeit durch die Anwendung eines phänomenologischen Models bestätigt, welches genau diese beiden Effekte modelliert. Eine numerische Simulation der Drift- und Diffusionsgleichungen, angewendet auf das zu untersuchende System, bringt tiefere Einblicke in die Dynamik der Ladungsträger innerhalb der Nanostruktur und bestätigt, dass die Mobilitäten von Elektronen und Löchern gleich sind und kann zudem deren Wert auf rund 3 $\frac{\mathrm{cm}^2}{\mathrm{Vs}}$ quantifizieren. Messungen bei tiefen Temperaturen untermauern die Ergebnisse und liefern ein tieferes Verständnis des Systems. Eine Wiederholung der zeitaufgelösten Messung an $CsPbBr_3$-Nanodrähten bestätigt den großen Einfluss der Bindungsenergie der Exzitonen auf die Stärke des beobachteten Effekts.

Neben der Untersuchung der Nanodrähte selbst, können diese durch ihre einfach anzupassende Bandlücke über ihre Photoleitfähigkeit auch als Sensormaterial dienen. In einem speziellen, konischen Design der Schallwandler kann eine ortsaufgelöste Detektion realisiert werden. Durch die photoinduzierte Ladungsträgerbildung in dem im Schallpfad deponierten Material

kann die Übertragung einer akustischen Oberflächenwelle durch die wechselseitige Wirkung von Ladungsträgern und elektrischem Feld verändert werden. Dies wird bei der Konstruktion eines wellenlängen- und positionsaufgelösten Detektors genutzt. Während der Messungen bildet die aufgenommene Absorptionskante mehrerer Materialien optische Absorptionsmessungen gut nach und passt zur Photolumineszenz der Nanodrähte. Das Hinzufügen eines senkrechten Paares von akustischem Oberflächenwellen-Sender und -Empfänger ermöglicht eine vollständige zweidimensionale Positionserfassung.

Der Wechsel von einer einfachen Verzögerungsstrecke zu einem resonatorbasierten Design zeigt, dass die SAW auch als Massendetektor mit hoher Empfindlichkeit eingesetzt werden kann, wobei die Masse Verschiebungen in der Resonanzfrequenz induziert. Durch die Steifigkeitsänderungen funktioniert dies auch bei eher leichtem Material und kleinen Mengen. Darüber hinaus ist diese Anordnung auch in der Lage, zusätzlich die Leitfähigkeit des abgeschiedenen Materials analog zum vorgenannten System zu detektieren. Als Proof-of-principle wird auch für diesen Chip die Absorptionskante eines exemplarischen Materials vorgestellt, die gut mit den bisherigen Studien übereinstimmt.

Contents

Chapter 1

Motivation

There is little doubt that in the modern world the need for alternative energy sources is increasing more than ever. It comes to mind easily that the most plentiful and readily accessible energy source is solar power. Photovoltaic technology offers the most effective way to transform the energy that is provided by the sun into usable electric power [Lei15]. The underlying electrical properties of charge carriers in the used semiconductors are a key factor in the determination of their efficiency in solar modules as well as in the evaluation of their usability in other electronic devices. The drive towards ever smaller components with ever higher performance raises the urge for a reduced dimensionality in the materials used for designing the devices. In the race for increased efficiencies in solar cells, the crystal class of metal halide perovskites has emerged and started a very promising journey. Back in 2009, Kojima *et al.* [Koj09] reported the first-ever application of perovskites for solar cells. From there on, the efficiency of modules based on this crystal class rose in an unprecedented manner until today, where *Oxford PV* reaches values as high as 28 % [She18]. Especially the category of metal halide perovskites are among the most appealing research hotspots for photovoltaic materials in recent years. They have desirable optical, electronic and optoelectronic properties, such as excellent absorption values, long diffusion lengths, long lifetimes of charge carriers and an easily tunable direct bandgap, alongside a relatively high thermal stability [Xia19; Str13; Ber18; Bre17]. One key obstacle still to overcome is their stability under ambient conditions, which is one main reason why they have not yet fully entered the commercial market. The main challenges are factors such as UV light, moisture, oxygen and surface defects [Luo17]. Despite these challenges, tandem cells that combine perovskite with silicon are already available [Oxf19].

It was found that especially the low processing temperature of the perovskites makes them ideal candidates for tandem cells [Bus17; Han18] with expected power conversion efficiencies (defined as the ratio between incident solar power and useful output electric power) up to 35-40% [Ahm17]. The scientific community has also put much effort in the development of improvements, for example through composition engineering or through coatings to increase the robustness of the light-absorbing layers [Zha18b; Abd18]. These include mixed-ion hybrid perovskites, low-dimensional perovskites and all-inorganic perovskites [Zha18b].

One major advantage of the perovskite materials is the vast number of different, mostly solution-based and cost effective fabrication methods of the crystals. Originally, two processes were published: the ligand-assisted reprecipitation method, published by Zhang *et al.* [Zha15], and the hot-injection method by Protesescu *et al.* [Pro15]. Shortly afterwards, many other groups followed and developed a large variety of other synthesis methods that produce high-quality perovskite nanocrystals, including ultrasonication [Hua17; Ton16], emulsion-based [Hua15] and solvothermal-based methods [Che17a], synthesis of ink-based nanocrystals [Akk16], and microwave heating-assisted methods [Li18]. As a result, the purity of the crystals was very soon highly controllable, producing nanostructures with low trap-state density.

In addition to the massive efforts around perovskites in photovoltaic, which started the hype about the material, there is also a lot of research performed in the field of other electric devices. Due to its high photoluminescence quantum yield the perovskite material is highly suitable for all sorts of light emitting devices, including light emitting diodes and lasers [Cho18; Mi19; Eat16; Fu16; Zha18a; Tan14; Sut14; Xin14; Zhu15; Yak15; Cha18; Xin15]. In recent years, perovskites were demonstrated to have great potential in such devices as their electroluminescence efficiency reaches values comparable to those of organic and quantum dot light emitting diodes. Progress was achieved in bulk and nanostructured perovskites [Kim16]. Some of these suffer from materials and operation instabilities that have yet to be overcome before the devices are fully functional and efficient [Boy19]. But the very high photoluminescence quantum yields for various different perovskite materials range around 90-100% which justifies the effort that is put into stabilizing the devices [Li19].

Though it proved to be challenging, even continuous wave lasing was achieved with perovskite nanostructures, overcoming the Auger recombination losses and the high intrinsic thermal damage [Mi19]. This proves that the usage of perovskites as gain medium can be a key of future technology alongside the already established silicon. Even optoelectronic devices could be already realised with perovskite material, for example, already around 2000 Mitzi *et al.* fabricated perovskite thin film transistors [Mit01; Sap16]. With their very precise and easy bandgap tuneability through the material composition via halide exchange or through the control of the nanocrystal's size, ranging from the near ultraviolet to the near infrared, metal halide perovskites are even thought to be usable in full color displays of screen technology [Sut16].

Besides, with the help of nanostructures electronic devices can be drastically shrunk in size and be a key in the ever increasing drive towards very small, high-performance electronic components. This is why low dimensional perovskites have gained more and more attention and are under examination in many ongoing research projects. For all these devices a key figure of merit is the behaviour of electrons and holes in the structure. It determines all the important properties for device performance and operation range. In addition to the carrier diffusion length and lifetime, the mobilities of both, electrons and holes, were found to be of major importance to understand the behaviour of electronic and optoelectronic devices and to optimize their performance. For bulk crystals, most of the properties are today well known, but for nanostructures a precise determination can be difficult due to the necessary very high fabrication precision of contacts applied to them and the high effort of receiving statistically significant amounts of data. Moreover, most methods for determining the mobilities of electrons and holes can allow for only one sort of charge carriers or a summed value over both [Her17]. In Chapter 5 of this thesis, we will present a contact-free method for the examination of nanostructures where the mobilities of both charge carriers can be determined separately to a large precision and, moreover, circumvent the complicated process of subtracting out the electronic properties of metal contacts. It is based on the observation of charge carrier dynamics enabled by the long lifetimes in metal halide perovskite nanowires. This knowledge can help to understand the advanced behaviour of the nanostructures in electronic devices and is key to new improvements.

* * *

As mentioned before, the perovskite crystals can be affected by many factors and the environment is a non-trivial component in the operation of any metal halide perovskite device [Ahm19]. But instead of trying to reduce the influence of the surroundings and making the

devices more stable, they can also be converted into an advantage and be used in sensor applications. Under controlled conditions, changes in the structure and composition through phase transition, hydration and dehydration, gas ad- and desorption or ion intercalation and decalation, can be reversed. This offers great potential for perovskite sensing applications in many different fields of life [Zhu18]. In fact, recently they were used to probe temperature [Dai16; Swa15; Pal16; Tom17; Xu19], humidity [Man16b; Gra15; Ren17; Xu16], gases [Bao15; Zha14; Che17b; Hua16], metal ions [Liu18; Aam16a] and solvents [Aam16b]. In these applications, the crystal undergoes either structural or compositional changes and can alter its optical properties such as emission energy or electrical properties such as resistance. Fortunately, many of these processes are fully reversible, providing an optimal characteristic for a reusable sensing material. Additionally, the crystals are processed in solution and can be used in nanostructures and thin films, opening up the possibilities of very thin and flexible sensors that can be integrated in almost every imaginable object.

The material can even be used as a photodetector [Dou14; Don15; Xia14], reversing the processes of light emission and instead sensing the creation of charge carriers in the semiconductor [Sto13]. It has already become reality that researchers have designed artificial retinas with microcavity perovskite photoreceptors [Tsa19] and with the right bio-inspired materials ecofriendly, low cost, high performance perovskite photodetectors could be realized [Gao19]. Having efficient, small photodetectors together with very highly efficient photon emitters, this perovskite-based technology can be the low-cost future of optical communication [Bao18].

The second main part of this thesis, chapters 6 and 7, focuses on the potential of the perovskite nanostructures to be excellent and highly sensitive photodetectors. We combine this feature with the high sensitivity of surface acoustic waves (SAWs) travelling on a substrate material and sensing any changes in their environment. The technique of surface acoustic waves is well understood and established in the area of telecommunication. Today, surface acoustic wave filters are used widely in mobile devices to define precise frequency bands, thanks to their high performance, reproducibility and small size [Rup93]. This means that the integration into the commercial silicon-based technology is already optimized and introducing new applications is no technical challenge. Devices that rely on the surface acoustic wave technology are thus fully integrable into established standard devices and need no additional technique to be commercially utilized. The principle of SAW-based conductivity measurements was known before [Wix89]. Here, we apply this technique and create a device with a two dimensional detection array that is highly flexible and reusable. Furthermore, the implementation of the metal halide perovskite material with a surface acoustic wave resonator in chapter 7 shows a drastically increased sensitivity to the viscous mass loading of the device while still being capable of sensing the comparatively small changes in conductivity due to the exposure to light.

* * *

In the following, this thesis will report on the reciprocal influence of metal halide perovskites and surface acoustic waves. Chapter 2 and 3 describe the fundamentals of the two elementary parts, the perovskite nanostructures with their properties and synthesis and the theory and practical implementation of surface acoustic waves in devices. The experimental setups as key requirements of the performed examinations are presented in chapter 4 together with some fundamental measurement techniques. The subsequent three chapters concentrate on the presentation of the obtained results: Chapter 5 explains in detail the observed charge carrier dynamics in the nanowires, including a comparison with a developed phenomenological model

and the determination of the mobilities of electrons and holes through numerical calculations of the drift and diffusion equations. Furthermore, additional studies on the influences of temperature and charge carrier density are shown. The inverse effect, namely the influence of mobile charge carriers in metal halide perovskites on the transmission of surface acoustic waves is covered in chapter 6, where a two dimensional absorption tomography device and its application is demonstrated. Chapter 7 extends this research by the introduction of a surface acoustic wave resonator. This allows a very sensitive detection of viscous load while maintaining the sensitivity on photo-induced conduction. Finally, chapter 8 concludes the thesis with a summary of the main findings and provides and outlook on possible future extensions of this work.

Chapter 2

Fundamentals of Perovskite Nanowires

Although the first perovskite material was already discovered in 1839 [Ros39], it began to attract broad interest only in recent years. After a few research groups found this crystal structure to be well suited for the fabrication of solar cells, the international community started to intensely work in that field. Within only three to four years they reached efficiencies already close to the range of commercial silicon cells [Nat19]. Due to the high absorption in some of the materials it is possible to use thin films as active material which enables the production of flexible solar cells for smart clothes or other bendable applications. Moreover, the fabrication of these materials can be very simple in a solution-based process that is easily scalable. All this sped up the research for new material combinations and their characterisation as well as their implementation into first cells. This success in the field of photovoltaics makes the metal halide perovskites also interesting for other optoelectronic applications. Already, light emitting diodes and lasers fabricated from these materials have been reported [Tan14; Xin14; Zhu15; Des14]. The first studies on metal halide perovskites focused on bulk-like crystals or films. However, it was found that colloidal semiconductor nanocrystals exhibit enhanced optical properties as well as unique advantages such as very high photoluminescence (PL) quantum yields and a wide tuneability [Dab97]. Recently researchers managed to process the new materials into arrangements of lower dimensionality, such as 1D nanowires, 2D platelets, 3D nanocubes or 3D supercrystals which all affect the inner electronic structure and cover a wide range of surface to volume ratios [Sch14a; Sic15; Ton17; Zha16]. The first report of inorganic metal trihalide perovskites with the formula $CsPbX_3$ was only presented in 1893 by H. L. Wells [Wel93], more than half a century after the initial discovery of the perovskite structure. Interestingly, many of the perovskite structures exhibit piezoelectric behaviour [Uch15]. The substrate material $LiNbO_3$ used in this thesis is also a perovskite with a non-cubic ordering that enables its piezoelectricity.

The focus in this work lies on nanowires of the materials $CsPbX_3$ and thus the following section will introduce this material with its structure and its basic parameters (section 2.1). Subsequently, the fabrication process will be sketched briefly in section 2.2. The chapter will be completed by an overview over the basic photon dynamics inside high and low dimensional semiconductors in section 2.3.

2.1 Structure and Basic Properties

The structure called perovskite was originally discovered in a calcium titanium oxide $CaTiO_3$ which is known as perovskite and was eponymous for the structure [Ros39]. Every material combination with ABX_3 stoichiometry (A and B being metal cations of very different sizes and X being an anion that bonds to both) having a type of crystal structure that relates to $CaTiO_3$

is now called a perovskite. The large A cation is surrounded by cubically arranged smaller B cations which form the centre of an octahedral arrangement of the X anions [Joh05]. This is the cubic form, which is the idealized, undistorted version with the highest crystal symmetry with a $Pm\bar{3}m$ space group [How98; Gla75]. However, the symmetry of the structure can be cubic, orthorhombic, tetragonal or trigonal depending on the composition, pressure and temperature [Jac81; Lin12; Whi16; Bre19; Vog93]. Even the original perovskite mineral is slightly distorted. A sketch of the cubic crystal ordering with its different atoms is shown in figure 2.1, highlighting the components in different colour and size. Here the A cations are in position $(\pm\frac{1}{2},\pm\frac{1}{2},\pm\frac{1}{2})$, the B cations in the centre $(0,0,0)$ and the X anions surround them at $(\pm\frac{1}{2},\pm\frac{1}{2},0)$, $(0,\pm\frac{1}{2},\pm\frac{1}{2})$ and $(\pm\frac{1}{2},0,\pm\frac{1}{2})$. In many material combinations the cubic form is not stable at room

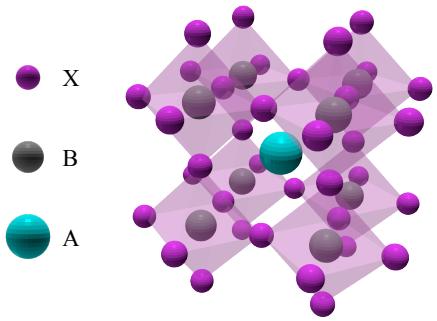

Figure 2.1: The crystal structure of perovskite consists of three atoms. The large cation (A, cyan) builds up the centre of the unit cell. The smaller cation (B, grey) is ordered around it at the corners of a cube. And the X (violet) represents the anion which is ordered around B in an octagonal shape. This results in a chemical formula of ABX_3.

temperature and a phase transition in the perovskites reorders into a lower-symmetry structure through octahedral rotations [Gla75; How98; Joh05]. These transitions strongly influence the electronic structure and consequently alter the optical and electronic properties [Mat04; Hir71; Man16a]. In the case of $CsPbX_3$ with X being chlorine, bromine or iodine, the cubic structure is conserved in nanostructures even up to room temperature. $LiNbO_3$ in contrast, builds up a trigonal form and is therefore capable of exhibiting piezoelectricity due to the broken symmetry. The structural ordering of the perovskite can be predicted through a semi-empirical geometry factor, the Goldschmidt tolerance factor [Gol26; Joh05], which gives an estimate about the formability of a metal halide perovskite. It can be calculated via the ionic radii of the atoms in consideration.

$$t = \frac{r_A + r_X}{\sqrt{2}(r_B + r_X)} \tag{2.1}$$

In the ideal, cubic form $t = 1$. But if the A ion is smaller or B is larger than in the ideal case, t becomes smaller than 1. In this case, the octahedra will tilt to fill the space and finally build up an orthorhombic structure. On the other hand, if A is large or B is small, t becomes larger than 1 and the ordering results in hexagonal variants of the perovskite structure [Joh05]. Since this is only an estimate based on the assumption of truly ionic compounds and depends on the values taken for the radii, the tolerance factor is only a rough estimate. But together with the octahedral factor $\mu = {}^{r_B}/_{r_X}$ [Li08] that determines the octahedral stability, the most probable form of the material can be predicted more accurately.

The cubic shape is preserved in $CsPbX_3$ when forming nanowires (NWs) such that they are actual cuboid blocks with a nice quadratic cross section. The TEM picture of figure 2.2 shows

the forming of nicely aligned bundles of several NWs sticking together. The single wires have cross sections of around 10 nm × 10 nm and lengths between 0.5 µm and 1 µm. The bundles they form range from 4.5 µm to 6 µm in length and from 1 µm to 1.5 µm in width and contain an average number of around 150 nanowires.

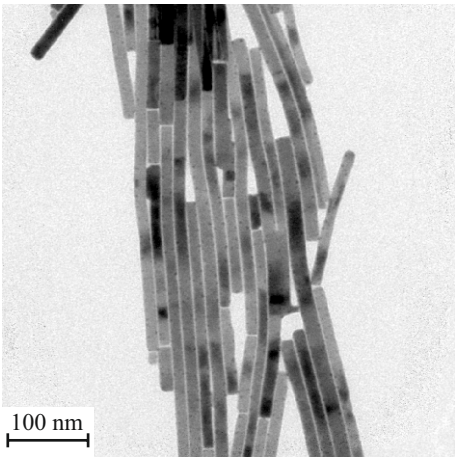

Figure 2.2: TEM image of part of a nanowire bundle of $CsPbI_3$ forming cuboid blocks that nicely align, pointing all in approximately the same direction. The picture is kindly provided by Yu Tong from the Photonics and Optoelectronics Group of the LMU, who prepared the perovskite structures.

The size of nanocrystals can be tuned to form platelets, cubes or nanowires by controlling the power and time of ultrasonication of the solution [Ton17]. Through a halide ion exchange mechanism the original $CsPbBr_3$ nanowires can be tuned in their emission through the whole visible spectrum by introducing chloride (shifting the emission towards blue) or iodide (shifting towards red). By controlling of the inserted amount, the composition can be varied from pure bromide over mixed halide compositions to fully iodide- or chloride-based nanowires. This process has the huge advantage that the structure itself stays the same as only the anions are exchanged one by one during the process. This simplifies a comparison between the different compositions in their energetic and electronic properties where structural changes can make a difference.

The ability to efficiently emit light arises from the semiconducting nature of the metal halide perovskites which even form direct bandgap semiconductors for the examined material combinations. In a free atom, the electrons normally occupy discrete energy levels and can only be excited if the additionally introduced energy matches the gap between two levels. However, in a periodically arranged lattice with the atoms close enough together the wave functions of those energy levels overlap and form common energetic bands. The electronic structure near the band edge is strongly dependent on the choice of material and the size of the atoms which determine the lattice constants and the overlap of the orbitals [Bor08]. The orbitals forming the conduction and valence bands are the Pb 6s and Pb 6p as well as the I 5s and the I 5p orbitals for $CsPbI_3$. This results in continuous energy bands inside the crystal where the charge carriers are free to have any energy within the range of the band. Hence, it is not necessary to match exactly the bandgap to excite an electron into the conduction band but it is sufficient to deposit energy larger than the bandgap. The global minimum of the conduction band (CB) matches the spatial position of the maximum in the valence band (VB) near the R point. Thus, a recombination of an electron from the conduction band with a hole from the valence band can occur without the

intake of a phonon just by following the energy conservation through the emission of a photon with the energy of the bandgap.

The bandgaps of the compositions under examination range from 2.4 eV for $CsPbBr_3$ to 1.8 eV for $CsPbI_3$, measured via PL emission. $CsPbCl_3$ perovskite nanostructures have a too high bandgap of around 3 eV [Ton16] to be examined with the available excitation lasers during this work. Therefore the studies were restricted to compositions of bromide and iodide. The nanowires follow the trend of metal halide perovskites where the bandgap changes with the halide according to $E_g(\mathrm{Cl}) > E_g(\mathrm{Br}) > E_g(\mathrm{I})$ [Hua13; Dir18].

Both bands, CB and VB, can be approximated as parabolas at the R point which, in huge contrast to conventional semiconductors, have approximately the same curvature. This points towards comparable effective masses of electrons and holes in these structures. With the dispersion relation, the effective masses m^* can be calculated from the energy E of the band structure according to formula 2.3. It results from the comparison of $F = m^* \cdot a$ with the calculation of the force from the derivative of carrier movement with the group velocity v_g (equation 2.2).

$$v_g = \frac{\partial \omega}{\partial k} = \frac{1}{\hbar}\frac{\partial E(k)}{\partial k} \tag{2.2}$$

$$E = E_0 \frac{\hbar^2 k^2}{2m^*} \tag{2.3}$$

Hereby denotes ω the angular frequency and k the wavenumber which are related by the Planck constant $\hbar$. The similar masses of the two charge carriers in the $CsPbX_3$ (e. g. $m_e^* = 0.13m_e$ and $m_h^* = 0.11m_e$ for $CsPbI_3$ [Pro15]) and similar perovskites lead to comparable conductivities of both species and the assumption of comparable mobilities as will be discussed in the simulations of chapter 5.3.

Furthermore, these perovskite structures are an interesting field of study for their comparably long PL lifetimes of several tens of nanoseconds enable a significant impact on charge carriers before their recombination. This opens up the possibility of charge transport and modulation of the inner dynamics of the nanowires. Due to their high excitonic binding energy in the range of 25 meV in comparison to conventional semiconductor nanowires it is even possible to dynamically modulate the exciton without separating it. The strong PL emission at room temperature is another major advantage as the integration time during time-resolved measurements can be reduced, boosting stability.

2.2 Solution-Based Synthesis

These low dimensional semiconductors have been studied for a long time and for various different materials because they are of huge importance for possible advanced applications. Importantly, they can also be used to gain deep insight into fundamental physics [But93; Aha16; Nov04]. Conventional low dimensional semiconductors are fabricated using epitaxy like molecular beam epitaxy or chemical vapour deposition in a bottom-up approach or by using electron-beam or photo-lithography in a top-down fabrication. But a third form started to rise to attention about 40 years ago: the solution-based synthesis of colloidal semiconductor quantum structures turned into a standard method as a supplement to the solid state approaches. It is especially easy and cost-efficient in comparison with the traditional methods, making it an ideal

candidate for industrial growth. Moreover, the easy exchange of single parts of the structure to tune the bandgap and the possibility of controlling the size with layer precision makes them an ideal candidate for light detecting and emitting applications. Nowadays, even heterostructures with core-shell arrangements and radial variations of the electronic structure similar to those fabricated by epitaxy have been realized [Mas16; Smi10]. While in the beginning only 0D quantum dots were studied, today it is possible to produce 1D nanowires, 2D nanoplatelets, 3D nanocubes, and recently also supercrystals, all from colloidal nanomaterials.

The easy one-step solution-based fabrication process of the perovskite nanowires was developed by the Photonics and Optoelectronics Group at the LMU in Munich, who prepared all the perovskite structures examined in this work. The following section is based on the two papers of the group describing the principle and the specific growth of nanowires [Ton16; Ton17]. The source materials are the precursor salts $CsCO_3$ and $PbBr_2$ and organic capping ligands (oleylamine and oleic acid). These are mixed in a nonpolar solvent (mineral oil or octadecene) under ambient atmospheric conditions. The mixing is performed by a direct tip sonication which induces the formation of caesium-olceate complexes which are soluble in nonpolar solvents. The complexes react with $PbBr_2$ in the presence of the organic ligands to form colloidal crystals of perovskites. The big advantage in this method is the direct production of the nanocrystals from the precursors without an intermediate step while preserving the scalability. It is called single-step because all precursor powders and ligands are loaded in the organic solvent at the same time. A centrifugation process after the forming of the nanostructures can remove the non-reacted precursors and excess ligands from the solution.

With this process, colloidal nanocrystals can be obtained and the formation of larger structures can be induced. The control of the exact structure that is produced, such as nanocrystals, nanoplatelets or nanowires, is performed by the sonication time and the ratio between the two precursors. A longer treatment and a higher Cs content both result in a lengthening of the structures. To achieve a high density of nanowires in the solution they are washed in the solvent hexane for several times to get rid of non-reacted precursors and parts of the smaller structures. In order to purify the solution further an extra centrifugation step is performed to separate the small portion of nanocubes that formed during the nanowire growth. The basic synthesis is conducted with bromide containing material and to get $CsPbI_3$ nanowires an additional halide ion exchange process has to be executed. The ion exchange is performed by adding the precursor powder with the desired halide, e. g. PbI_2, to the already existing nanowire dispersion. The exchange can also be implemented in such a way that only a part of the ions is substituted revealing mixed halide perovskites with bandgaps in between the values of the pure single halide ones. This is controlled by the amount of added precursors which is varied by one order of magnitude.

For the work performed in this thesis we exploited that the nanowires already grow in solution, which simplifies the transfer process from the growth medium to the piezoelectric substrate needed for the SAW-based electric analysis. The nanowires are drop cast from the liquid onto the substrate. To this end, a pipette is used to grab a very small amount of solution which is then dropped at the desired position on the sample. The density of the NWs in the dispersion and the size of the droplet are crucial for the success of the measurements and have to be controlled precisely. In order to study small bundles of nanowires, the solution is diluted further to ensure a low density of structures on the substrate. The aligned bundles form automatically due to surface adhesion forces between the single nanowires which are highest on the long sides of the structures. The low density also leads to the droplet spreading out over a larger area, further reducing the density of NW bundles on the substrate. The solution for photoconductivity

measurements, on the other hand, needs to be of high density and concentrated at a small area on the substrate to induce conductivity in a large number of structures and reach significant alteration on the probing SAW. The drop density and size are especially crucial here, as a too high semiconducting load can suppress the wave completely, but too few nanowires will not have a large enough effect to be distinguished from the electrical noise.

Despite the nanowires made from metal halide perovskites having a significantly reduced PL quantum yield of 11 % in comparison to nanocubes (92 %) [Ton17], they are still highly emissive at room temperature in contrast to conventional semiconductor nanowires from GaAs. In addition, their absorption is relatively high which makes them an ideal candidate for improved efficiency solar cells as their surface to volume ratio is much higher than for thin films or even bulk material.

2.3 Charge Carrier and Photon Dynamics

The typical applications of the newly invented materials include not only solar cells but also all other sorts of optoelectronic devices like lasers and light emitting diodes [Tan14; Xin14; Zhu15; Des14]. For these devices the interaction between free or bound charge carriers with photons plays an important role. In order to understand this interplay, the following section will introduce the basic carrier and photon dynamics in semiconductors in general and in the perovskite structures in particular.

There are two possible types of semiconductors characterized by the transition of an electron from the conduction to the valence band: direct and indirect bandgap semiconductors. In the indirect case, the electron in addition to the energy transfer needs also a momentum transfer through a phonon. As for most applications a direct semiconductor is of advantage and the perovskites examined during this work are of this type, the following explanation will be restricted to that case.

When a semiconducting material is deviated from its equilibrium state e. g. through a laser pulse, it forms a new quasi-equilibrium where the electrons and holes occupy excited states. The two fundamental light-matter interactions that cause the transitions between equilibrium and excited states are introduced in figure 2.3. These are the central parts of the photoluminescence spectroscopy, a fundamental method to examine charge carriers and their evolution in semiconductor material. Through a photon with above-bandgap energy an electron from the valence band can be excited to the conduction band. The carrier increases its energy by the amount of the photon's through absorption and gains access to higher level states. After excitation to the CB the electron relaxes down to the lowest unoccupied state respecting its fermionic nature. The excess energy is transformed into thermal phonons as lattice vibrations. This process happens on a time scale below 100 ps in semiconductors [Leh79; She17] and is thus much faster then the radiative recombination times which lie in the range of ns for the examined perovskites.

If two charge carriers of opposite sign are at the same position in the real and k-space of the crystal, i. e. if their expanding wave functions overlap, the electron recombines back with the hole with a radiative lifetime τ_r. The emitted photon has a wavelength that corresponds to the energy of the bandgap to transport the excess energy of the charge carriers away. In practice the emission energy broadens due to thermal variations of the carrier energies. The emitted photon can be separated from reflected laser photons through a spectrometer or filters as it is always lower in energy in non-resonant measurements. For the $CsPbI_3$ perovskites the lifetime

amounts to between $\tau_r = 1.8\,\text{ns}$ and $\tau_r = 17\,\text{ns}$ in a triple exponential decay, which justifies the assumption of a quasi-equilibrium.

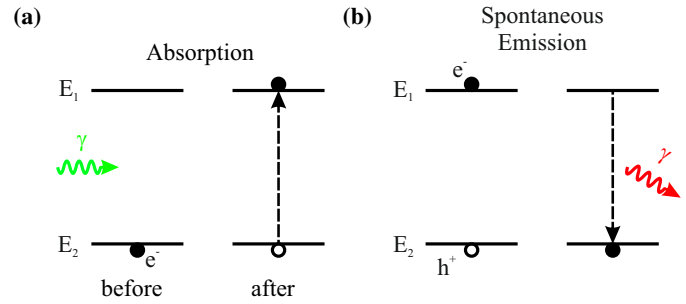

Figure 2.3: Fundamental photonic transitions inside a direct bandgap semiconductor. (**a**) An above-bandgap incident photon which transfers its energy to an electron in the valence band and excites it to a free state in the conduction band leaving back a hole in the valence band. (**b**) In the reverse process, the electron in the excited state drops back to its corresponding hole in the valence band under emission of a photon that carries away the energy difference between the two states. This process has a certain average lifetime after which the electron leaves the excited state.

The excited electron can remain bound to its corresponding hole to form a so called exciton. The two charge carriers are then still attracted to each other via the coulomb interaction and build up a two particle system which cannot move independently through the crystal. The photon energy of a decaying exciton is lowered by the amount of its binding energy and it is called a neutral quasi-particle that is in first approximation not influenced by any electric field. Hence, at low temperatures the formation of excitons is enhanced as it can lower the energy of the two participating particles.

There are two basic types of excitons in solids which differ mainly by the distance between the particles or, in other words, by the strength of the Coulomb interaction

$$F(r) = \frac{q_1 \cdot q_2}{4\pi\varepsilon_0 r^2}, \tag{2.4}$$

with q_i the charge of the two particles and r their distance. Frenkel excitons [Fre31] form tightly bound structures and are found in materials with small dielectric constants like organic molecules or alkali halide crystals. The strong interaction results in a small Bohr radius and electrons that are localized very close to the atom which holds the corresponding hole. The second type of excitons, hydrogen-like Wannier-Mott excitons [Wan37], form rather loose bonds where the electron is still partly free to move across the crystal in a certain range. These excitons are found in many semiconducting materials whose dielectric constants are generally large. The Bohr radius of this type is typically larger than the lattice spacing and favours a delocalization of the electron around its hole. These excitons can be largely polarized due to their partly free nature. In the semiconducting metal halide perovskites Wannier-Mott excitons can be found but free carriers also exist in the material [Sab16; Til16]. With the introduction of a high electric field the ratio between the two can be distorted whilst ripping the excitons apart.

The binding energy and radius are of major importance for the probability of and the force needed for their dissociation and separation. The Wannier-Mott excitons can be treated as hydrogen-like and the radius and energy can be calculated analogously within the effective mass approximation [Yu10]. For the $CsPbI_3$ nanowires the two properties are $E_{bind} = 25\,\text{meV}$ and $r_{exciton} = 12\,\text{nm}$ [Dir18; Pro15]. The latter is the predominant reason why it is not possible

to separate the exciton perpendicular to the nanowire axis if no inter-wire transport of charge carriers is possible as the cross section is only 10 nm wide. This exciton is a polar, but to the outside charge neutral quasi-particle. It is as a whole not affected by an external electric field, but the two parts of it, the electron and the hole, can each separately be influenced by an outer field. Under low fields the two charge carriers are separated to a maximum of their binding radius as then the attractive force keeps them from moving further apart. In an increased electric field, it is possible to destroy the exciton and completely separate the two parts. The then free electron and hole can follow the conduction and valence bands which are altered by the external electric field.

Through Fermi's Golden Rule one can describe the absorption and stimulated emission in a time-dependent perturbation theory with a periodic perturbation V [Mer85; Mer98]:

$$\Gamma_{i\to f} = \frac{2\pi}{\hbar} |\langle f|V|i\rangle|^2 \delta(E_f - E_i \pm \hbar\omega) \tag{2.5}$$

The equation 2.5 states that the transition rate $\Gamma_{i\to f}$ from an initial state $|i\rangle$ to the final state $\langle f|$ depends on the matrix element $\langle f|V|i\rangle$ of the perturbation and the difference of the final and initial state's energy E_f and E_i. The overlap of the wavefunctions also enters the calculation through the matrix element. To calculate the rate for the spontaneous emission, an integration over all possible final states has to be made to account for the randomness of this state. The basic result is then a constant decay rate of an excited state. Hence, the number X of elements being in the excited state is described in an exponential function with decay time τ and the initial number X_0.

$$X(t) = X_0 \cdot e^{-\frac{t}{\tau}} \tag{2.6}$$

In bulk semiconductors the charge carriers are free to move around once excited. In low dimensional materials there is a confinement in one or more directions such that the electron and hole are restricted to stay inside the potential well, once they were captured. If the dimension m of this containment is small, one talks about quantum confinement which dramatically modifies the electronic behaviour by converting the continuous energy band into discrete levels with distinct energies, depending on the effective mass m^*, the Planck constant $\hbar$ and the particle's wave vectors k_i [Gru06]:

$$E_n = \frac{\hbar^2}{2m^*} \sum_1^m k_i^2 \tag{2.7}$$

k_i can take value of $\pm\pi n_i/L_i$, where n_i is an integer and L_i the width of the confinement in that dimension. The density of states (DOS) for electrons and holes in the different low-dimensional semiconductors also shows major changes as to where the charge carriers can be located. The functions for 3D, 2D and 1D are depicted in figure 2.4. The DOS describes the available states that can be occupied in the different energy levels and hence, defines what energy the electrons and holes can have. For the electrons to occupy the states in the conduction band they have to be excited to gain the energy needed for the negotiation of the energy gap.

The Coulomb interaction is also influenced by the dimensionality of the semiconductor which thus changes the properties of excitons in the material. Their impact on the absorption of the material can be described by the Elliot equation [Ell57]. This model assumes single particles whose binding is expressed through an envelope function. This theory can be used to extract the exciton binding energy for Wannier-Mott excitons. The reduced dimensionality is taken into account and changes the theoretical absorption according to the Elliott formula.

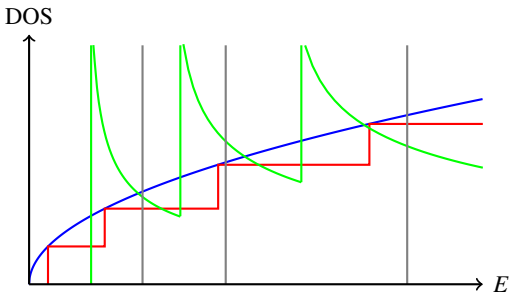

Figure 2.4: DOS for 3D bulk and lower dimensional semiconductors as a function of the energy E. The functions are sketched for electrons in 3D (blue), 2D (red), 1D (green) and 0D (grey) structures according to [Pra04].

The high optical absorption together with a large diffusion length is thought to be the main reason for the high performance of perovskites in solar cells. The efficient transformation of light into a large number of charge carriers produces a possible high current of particles that can be extracted [Mal13; Wol14]. The low trap-state density results in an efficient transport through the device and an enhance extraction rate [Shi15; Str13]. This is the reason why a study of the electronic and photoconductive properties of this material is of high interest in order to explain those good values in more detail.

The diffusion length L_D is a crucial parameter for especially solar cells but also all other devices that rely on the transport of carriers. It is defined as the average distance a charge carrier diffuses in the material before recombination occurs. It is thus dependent on the lifetime τ of the charge carriers.

$$L_D = \sqrt{D\tau} \tag{2.8}$$

where D is the diffusion constant, related to the material specific carrier mobility μ_q, the charge q and the temperature T via the the Boltzmann constant k_B through the Einstein relation [Gru06]

$$D = \frac{\mu_q k_B T}{q} \tag{2.9}$$

The diffusion constant is also an important parameter in the diffusion equation which describes the diffusive motion in a material. It correlates the temporal change of the charge carriers with the spatial change and the decay, here for the electrons (indicated by the use of n) [Gru06].

$$\frac{\partial n(x,t)}{\partial t} = D_n \frac{\partial^2 n(x,t)}{\partial x^2} - G(t,x,n) \tag{2.10}$$

The $G(t,x,n)$ represents all generation and loss mechanisms of the particle, e. g. laser excitation, PL emission or exciton generation where the free charge carrier is then lost.

In the presence of an electric field this equation has to be extended to include the drift mechanism. The field $\mathscr{E}$ induces a motion of charged particles along the field lines and is assumed to be constant for the following equation.

$$\frac{\partial n(x,t)}{\partial t} = D_n \frac{\partial^2 n(x,t)}{\partial x^2} + \mu_n \mathscr{E}_x \frac{\partial n(x,t)}{\partial x} - G(t,x,n) \tag{2.11}$$

The motivation and further discussion of this equation is postponed to section 3.5.5 after the

introduction of the electric field by the SAW. For the moment it shows the importance of the mobilities of electrons and holes and their massive influence on the electrical dynamics inside the nanostructure.

Chapter 3

Surface Acoustic Waves

Today, we use many electronic devices on a daily basis often without knowing much about their interior. This results in the concept of SAWs being widely used but seldom their existence is even known by the users. While their existence was already discovered in 1885 [Ray85], only in 1965 [Whi65] were they first exploited for applications. Due to the invention of the interdigital transducer (IDT) it became possible to efficiently excite and detect SAWs on a piezoelectric surface. This opened up the way to the main applications of today, e. g. the radio module in mobile phones. SAWs are periodic displacements of the surface material of a solid that propagate only at the surface and mainly as a linear wave front. IDTs are used to define the wavelengths that can pass through the structure. The sound velocity in the material then defines the frequency of the periodic movement. In order to filter the right band used for telecommunication and data transport the incoming signal is sent through such a surface acoustic filter operating at precisely selectable frequencies ranging from about 10 MHz up to a few GHz. SAW-based devices have some excellent features compared to competing technologies [Cam89]. They can be designed to provide very complex signal processing functions in only one single pair of IDTs. Even in mass production SAW devices remain reproducible while still being analogue electronic that can be easily implemented in digital circuits. And for modern device development it is very important that they can be implemented in small, light modules and can be tuned efficiently to gigahertz frequencies through higher harmonics. All this has raised the interest in SAWs throughout the years and helped to develop them also as a measurement tool. Being easy to integrate into standard semiconductor fabrication mechanisms, SAWs on piezoelectric materials provide a versatile tool to apply variable stress, strain and electric fields to nanostructures and thus probe and manipulate their behaviour contact-free under various different conditions.

This chapter first gives an introduction into the basic physics of surface acoustic waves and the important parameters in section 3.1. Afterwards, section 3.2 focuses on the fabrication of SAW chips onto a piezoelectric $LiNbO_3$ substrate by different lithography methods. Then excitation and detection of SAWs with so called IDTs and what limits their quality and the power of the signal coupled into the material is discussed in section 3.3 before the characterization methods of the quality and characteristics of the SAW chip are described in section 3.4. Finally the influence of the surface acoustic wave on the band structure and charge carriers in semiconductor materials are discussed in section 3.5.

3.1 Theory

A surface acoustic wave is a sound wave characterized by its low penetration depth of approximately one wavelength into the substrate due to an exponentially decaying displacement

amplitude in that direction. That implies that the wave is localized at and travels parallel to the surface. The most important types of waves are Rayleigh waves, named after Lord Rayleigh who discovered them in 1885 [Ray85], and shear waves. The Rayleigh wave consists of a transversal and a longitudinal wave component with an elliptical movement of the particles in the sagittal plane, which is the plain that is stretched by the propagation direction and the surface normal. In contrast, the shear wave deflects the material in-plane but perpendicular to the propagation direction. Rayleigh waves have long been used for non-destructive testing based on their property of being reflected by cracks in the crystal. The research that lead to the theoretical description of those waves is based on the examination of earthquakes and thus, the surface acoustic waves that act on the small scales of chip samples are sometimes called *nano-earthquakes*.

In order to understand the propagation of these waves on the surface of materials, it is essential to study the elasticity. At first, non-piezoelectric, isotropic materials are described before the piezoelectric effect is introduced. The latter is important to be considered as in most cases it is used to excite the SAW.

The elasticity of a material, describing the reaction on a partial displacement from equilibrium can be split up into a stress tensor **T** expressing the resulting forces and a strain tensor **S** characterizing the displacements. The following theoretical considerations are based on chapter 2 of [Mor07]. The deflection of a point can consist of a translation, a deformation and a rotation of the lattice distances in the crystal. The diagonal elements of the tensor represent the strain along the coordinate axis, while the off-diagonal elements describe the shear strain. It can be expressed as gradients in the three spatial directions. The displacement from the equilibrium is denoted as $\vec{u}(x_1,x_2,x_3) = (u_1,u_2,u_3)$, resulting in a new position of $\vec{x}+\vec{u}$ for the point.

$$S_{ij}(x_1,x_2,x_3) = \frac{1}{2}\left(\frac{\partial u_i}{\partial x_j} + \frac{\partial u_j}{\partial x_i}\right) \tag{3.1}$$

In this definition a displacement or rotation of the whole crystal does not result in an internal strain. Due to symmetry reasons the second rank strain tensor follows $S_{ij} = S_{ji}$ and reduces to only six independent components.

In most practical contexts, many materials behave elastically, meaning that after being deformed by an external force, they return to their original state upon the release of the force. This is a result of the forces induced in the material by the deformation as every infinitesimally small volume element transfers force to its neighbouring elements in the corresponding direction. These internal forces are represented in their strength and their area of application by the stress tensor **T** as schematically depicted in figure 3.1. In addition, a generalization of Hooke's law can be applied, which states that the stress is proportional to the strain for small values of stress. The linear dependence is characterized by the stiffness **c**, a tensor of rank 4.

$$T_{ij} = \sum_k \sum_m c_{ijkm} S_{km} \tag{3.2}$$

To simplify the appearance of the equation, Einstein's summation convention can be used and is applied in the following, in which the summation sign for an index is omitted, if the index appears twice in a product term. Thus, in the equation above, both summation signs can be dropped.

As the stress T_{ij} is the force acting on an area, it can also be described by Newton's law

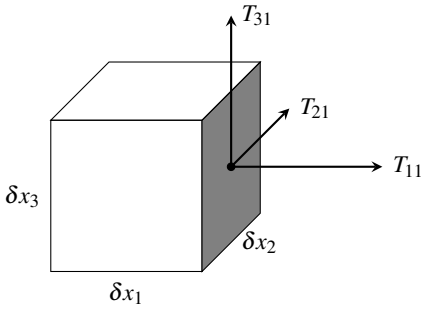

Figure 3.1: Forces on the centre of one side of an infinitesimal volume element δV. The T_{ij} describe the force acting on an area and its direction. Figure adapted from [Kin14].

$F = m \cdot a$. A rearrangement and the introduction of the density $\rho = {}^{m}/_{(dx \cdot A)}$ result in $\rho \ddot{u} = \frac{\partial}{\partial x} \frac{F}{A}$ with the mass m, the acceleration a and the area A. With these, the equation of motion can be derived:

$$\rho \frac{\partial^2 u_j}{\partial t^2} = \frac{\partial T_{ij}}{\partial x_i} \tag{3.3}$$

The inclusion of piezoelectricity adds more complexity to the above equations. Nevertheless, it is important to be considered as piezoelectricity is often used to excite the SAW on a solid material. The basic principle is a coupling of elastic strain and stress in a crystal to electric fields and displacements. It can only be found in anisotropic media which do not have a centre of symmetry in their crystal structure. In order to excite a SAW, the piezoelectric effect hast to be of measurable strength and can not be neglected in the theoretical analysis. The following considerations are applied to insulating material, such as $LiNbO_3$, which is used in this thesis as substrate material.

In a homogeneous piezoelectric insulator, the correlation of stress and strain components is complemented by a dependence on the electric field $\mathscr{E}$. An external electric field can induce mechanical displacements via the inverse piezoelectric effect. Analogously, a mechanical displacement in the material can lead to electric displacement **D** which, in turn, induces an electric field given by $D_i = \varepsilon_{ij} \cdot \mathscr{E}_j$ with ε being the permittivity. If all components are small, a linear relationship can be assumed and the equations can be written as follows [Mor07].

$$T_{ij} = c_{ijkm} S_{km} - e_{kij} \mathscr{E}_k \tag{3.4}$$

$$D_i = e_{ijk} S_{jk} + \varepsilon_{ij} \mathscr{E}_j \tag{3.5}$$

The piezoelectric tensor e_{kij} relates the elasticity to the electric fields and has the symmetry of $e_{kij} = e_{kji}$ as a consequence of the symmetry in T_{ij}. The first index is related to the electric field, while the other two indices relate to the mechanical changes. One can picture the stress tensor **T** in equation 3.4 as a spring constant that is stiffened by the electric field. Equation 3.5 describes the introduction of an additional polarization through the mechanical displacement **S**.

The equation of motion, equation 3.3, is also valid in piezoelectric materials. In addition to the three spatial displacement directions from $\vec{u}$, the electric potential Φ has to be considered. In the quasi-static approximation where the temporal changes of the elastic disturbances are much slower then electromagnetic field changes, the electric field can be expressed as gradient of the potential. The first Maxwell equation under the premise of no charge sources being present due to the assumed insulating nature of the material provides the fourth relation between the four

quantities u_i and Φ.

$$\mathscr{E}_i = -\frac{\partial \Phi}{\partial x_i} \tag{3.6}$$

$$\frac{\partial D_i}{\partial x_i} = 0 \tag{3.7}$$

A combination of the equation of motion (equation 3.3) with equation 3.4, the definition of the strain tensor **S** (equation 3.1) and the electric field as gradient of the potential (equation 3.6) results in the first three equations to determine the four unknown parameters. The last equation can be obtained through the equations 3.5 and 3.7 and the definitions of **S** and $\mathscr{E}$, equations 3.1 and 3.6, respectively.

$$\begin{aligned} \rho \frac{\partial^2 u_j}{\partial t^2} &= c_{ijkm} \frac{\partial^2 u_k}{\partial x_i \partial x_m} + e_{kij} \frac{\partial^2 \Phi}{\partial x_i \partial x_k} \\ \varepsilon_{ij} \frac{\partial^2 \Phi}{\partial x_i \partial x_j} &= e_{ijk} \frac{\partial^2 u_j}{\partial x_i \partial x_k} \end{aligned} \tag{3.8}$$

These coupled differential equations are in general not solvable by analytic methods, but have to be calculated in numerical procedures [Cam68; Mor07]. In anisotropic materials plane wave solutions of the form $u_i = u_i^{(0)} \cdot \exp\left(i(\vec{k}\vec{x} - \omega t)\right)$ and Φ analogously, generally give four solutions when plugged into the above differential equation system. One is an essentially electrostatic solution which is of low interest. The other three results correspond to non-dispersive acoustic waves travelling in the material. They can be divided into one quasi-longitudinal and two quasi-shear wave which means that their displacement vector $\vec{u}^{(0)}$ is essentially parallel or perpendicular to $\vec{k}$, respectively [Mor07].

In a simplified version a plane wave with propagation direction along x_1 is chosen as ansatz for the coupled differential equation system [Sch14b]. Thus, all displacements u_i and the electric potential only depend on x_1 and t:

$$u_i = u_i^{(0)} \cdot e^{i(kx_1 - \omega t)} \tag{3.9}$$

$$\Phi = \Phi^{(0)} \cdot e^{i(kx_1 - \omega t)} \tag{3.10}$$

As this wave spatially only depends on x_1 the derivatives in the two other directions disappear $\left(\frac{\partial}{\partial x_2} = \frac{\partial}{\partial x_3} = 0\right)$ and the equation system 3.8 simplifies to

$$\begin{aligned} \rho \frac{\partial^2 u_j}{\partial t^2} &= c_{1jk1} \frac{\partial^2 u_k}{\partial x_1^2} + e_{11j} \frac{\partial^2 \Phi}{\partial x_1^2} \\ \frac{\partial^2 \Phi}{\partial x_1^2} &= \frac{e_{1j1}}{\varepsilon_{11}} \frac{\partial^2 u_j}{\partial x_1^2} \end{aligned} \tag{3.11}$$

Substituting one into the other removes the dependence on Φ and shows that the piezoelectricity essentially changes the sound velocity as for non-piezoelectric materials $e = 0$.

$$\rho \frac{\partial^2 u_j}{\partial t^2} = \underbrace{\left(c_{1jk1} + \frac{e_{11j} e_{1k1}}{\varepsilon_{11}}\right)}_{c'_{1jk1}} \frac{\partial^2 u_k}{\partial x_1^2} \tag{3.12}$$

The definition of the effective piezoelectric coupling constant c'_{1jk1} can also be used to define the coupling constant K^2, which denotes how efficiently the electric excitation wave can be coupled into a piezoelectric wave.

$$c'_{1jk1} = c_{1jk1}\left(1 + \frac{e_{11j}e_{1k1}}{\varepsilon_{11}c_{1jk1}}\right) = c_{1jk1}(1+K^2) \tag{3.13}$$

From equation 3.12 the phase velocity of the wave packet can be extracted as $v = \sqrt{c'_{1jk1}/\rho}$. How much the velocity is altered depends on the permittivity and the relevant component of the piezoelectric tensor and is expressed in K^2. Thus, it can vary as a function of the propagation direction in the crystal. The relations between the piezoelectric components of different crystal classes and some values for selected materials are presented in [Roy00].

To determine the coupling constant K^2, one can make use of the velocities with and without piezoelectric effect in the material. The influence of the piezoelectric effect can be avoided in experiments by metallizing the surface and so enabling a charge transfers that compensates for the polarization that would occur in the crystal. With both velocities known, K^2 can then be estimated via

$$v_{free} = \sqrt{\frac{c'}{\rho}} = \sqrt{\frac{c(1+K^2)}{\rho}} \approx v_{short} \cdot \left(1 + \frac{1}{2}K^2\right) \tag{3.14}$$

$$\frac{K^2}{2} \approx \frac{v_{free} - v_{short}}{v_{short}} \tag{3.15}$$

As discussed in [Kov90] the difference between both velocities strongly depends on the angle that the propagation direction includes with the major direction (e. g. X in case of Y-cut $LiNbO_3$). Their angle-dependent studies of free and shorted SAW velocities perfectly reproduce that for 0° the difference is the greatest. But they also show that for a propagation perpendicular to the X direction, the coupling is very week. To reach equally good coupling of the signal into the SAW for two perpendicular directions, it is only possible with reduced coupling efficiency and in a geometry such that both build up an angle of 45° with the X direction.

So far, the crystal under consideration for the calculations had an infinite extension. For the mathematical description of a surface wave, boundary conditions have to be fulfilled. There can be no forces on the surface $x_3 = 0$, meaning that the stress components have to vanish.

$$T_{31} = T_{32} = T_{33} = 0 \mid_{x_3=0} \tag{3.16}$$

Furthermore, Laplace's equation demands continuity at the surface: the dielectric displacement D_3 and the potential Φ at the border $x_3 = 0$ have to be equal in both media. At last, for the wave to be a surface wave the displacements have to decay towards the lower end of the crystal $u_i = 0 \mid_{x_3=-\infty}$ and electric potential has to vanish at infinity in both half-spaces $\Phi = 0 \mid_{x_3=\pm\infty}$ [Sch14b].

A general solution for the four components can not be derived analytically, but is performed via numerical simulations. In many materials one possible solution is the piezoelectric Rayleigh wave. Its displacement is restricted to the sagittal plane and has an associated electric field [Mor07]. This is the wave that is typically used when working with $LiNbO_3$ where it dominates over the shear and bulk waves. Its penetration depth is about one wavelength. Due to the anisotropy the sound velocity of the wave differs largely depending on the crystal cut and

the propagation direction. The two most prominent cuts of $LiNbO_3$ are the Y-cut with major propagation direction along the Z axis and the 128°Y-cut where the Y plane for cutting was tilted by 128° around the X axis with major propagation along the X axis. For each cut these are the directions with the highest coupling constant enabling strong acoustic waves.

The crystal structure of the lithium niobate is similar to the one of the examined nanowires. But in contrast to the nanostructures, the $LiNbO_3$ orders in a trigonal unit cell of crystal class $3m$ [Hsu97]. This anisotropic structure is a key requirement for the piezoelectric nature of the material. Moreover, a negligible electric conductivity is needed and a deformation of the unit cell has to lead to a polarization and the creation of a macroscopic dipole within the crystal [Mül09]. The different directions in $LiNbO_3$ exhibit diverse polarizabilities and thus, piezoelectric strengths. As seen above, the direction of travel plays a major role in the coupling efficiency and the amount of power that can be converted into the mechanical wave and it influences the velocity of the wave through the direction-dependent permittivity, stiffness and piezoelectricity. In table 3.1, relevant parameters of the two often-used $LiNbO_3$ crystal cuts are presented for two perpendicular propagation directions.

	Y-cut $LiNbO_3$		128°Y-cut $LiNbO_3$	
propagation direction	X	Z	X	128°YZ
sound velocity (m/s)	3720	3488	3980	3650
permittivity ε (ε_0)	44.5	27.5	56	8.1
coupling constant K^2	0.015	0.048	0.056	0.02

Table 3.1: Summary of the most relevant parameters of two $LiNbO_3$ crystal cuts and two perpendicular propagation directions on the surfaces, respectively. [Mat77; Ash85; Dat86; Roy00; Kin14]

While there are plenty of ways in nature to excite a SAW, most of them are rather unspecific in their direction. The most prominent example of surface waves are water waves. These propagate as a circular wave around the excitation spot. The reason why Rayleigh discovered the wave named after him was because he found strange elliptic movements in certain waves in earthquakes [Ray85]. In contrast to nature, with today's high precision fabrication methods it is possible to perfectly address one defined propagation direction on the crystal. For this thesis, a well established electric excitation approach was used based on the evaporation of small stripes of electrodes, called fingers. They are ordered to form so called interdigital transducers (IDTs) where two sets of electrodes are arranged in a comb shape interlock as shown in figure 3.2(a). This method was first introduced by White and Voltmer in 1965 [Whi65]. When a high frequency alternating voltage as indicated in figure 3.2(b) is applied to the structure, the piezoelectric crystal underneath starts to vibrate as the electric fields are converted into mechanical displacements. If the frequency meets the dispersion relation, equation 3.17, the movements happen in resonance and constructive interference of the waves results in a travelling wave propagating in both directions from the IDT.

$$\lambda_{SAW} = 4 \cdot p = \frac{v_{SAW}}{f_{HF}} \tag{3.17}$$

with the wavelength, velocity and frequency of the SAW λ_{SAW}, v_{SAW} and f_{HF} as well as the pitch of the electrodes p.

It is also possible to excite higher harmonics of the resonance frequency, but in the design shown in figure 3.2(a) only odd numbered harmonics can be observed as the even harmonics

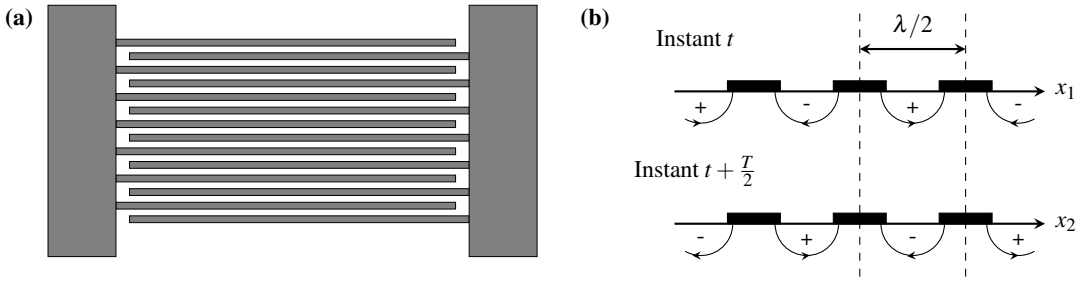

Figure 3.2: (**a**) Schematic of an IDT structure design with a single finger arrangement. (**b**) The high frequency voltage applied across the electrodes produces stress at the surface. Schematic adapted from [Roy00].

cancel out due to the symmetric arrangement of the fingers. Panel (b) sketches the potential distribution upon the application of a high frequency voltage for the creation of a SAW at two points in time separated by $T_{SAW}/2$. The transition from a single finger to a split-2 IDT allows the more efficient generation of higher odd harmonic frequencies. In this design, pairs of two electrodes per side alternate which results in a wavelength-to-pitch relation of $\lambda = 8 \cdot p$. Special designs to be able to also used even harmonic frequencies, such as split-52 arrangements with an asymmetric ordering and neutral, floating electrodes integrated, are presented elsewhere [Sch15]. The aperture of the SAW is defined by the width of overlap between the fingers of the two connections and defines the lateral expansion of the travelling wave. The nominal metallization ratio is set to 50% in this work meaning that the width of the finger structures equals their distance. The metallization ratio is crucial for the efficiency of higher harmonic excitation [Smi75].

The 3 dB bandwidth of the wave output linearly depends on the inverse of the number of finger pairs while the temporal width is linearly proportional to the number of pairs. This function in practice can be read out by a second IDT which then acts as a receiver but also adds its own characteristic function on the signal. Moreover, this second transducer also acts as a reflector for the incoming wave. Every single finger has a small reflectivity which interferes constructively or destructively depending on the incident wave. If the incoming wavelength equals the periodicity of the electrodes, the reflection will be the highest. Around the centre frequency f_0, the reflections from the metal strips add up in phase. Similar to Distributed Bragg Reflectors in the optical regime, there exists a frequency band of reflection whose width depends on the number of fingers in the reflector. The reflection coefficient of an array of N fingers, each with reflectivity r is given by [Dat86]. For the metal electrodes considered here, this reflectivity of each finger is purely imaginary.

$$|R| \approx \tanh(N \cdot |r|) \tag{3.18}$$

For large numbers of N, R can be regarded as 1, indicating a reflectivity of almost 100 %. The bandwidth of the reflector under this assumption can be calculated as

$$\frac{B}{f_0} = \frac{2|r|}{\pi}\sqrt{1+\left(\frac{\pi}{N|r|}\right)^2} \tag{3.19}$$

$$\approx \frac{2|r|}{\pi}, \text{ if } N|r| \gg \pi \tag{3.20}$$

according to [Dat86]. The bandwidth B is here defined as the separation between the two

frequencies with zero reflection symmetrically around the centre frequency. Intuitively, one would expect that the bandwidth scales with the length of the reflector, but, provided it is long enough to have $R \approx 1$, the wave is already almost completely reflected by the first n fingers with $n \approx 1/|r|$. If the number of stripes is small, the bandwidth becomes dependent on it, but independent of $|r|$. The reflectivity of each finger arises from two components, an electrical term and a mechanical term: $r \approx r_E + r_M$. In a simplification the two terms can be assumed to be independent from each others origin. This can be done as the perturbation arising from it is small. The electric component depends on the piezoelectric coupling constant K^2 and the metallization ratio while the mechanical part changes with the thickness h of the electrodes. Mathematical descriptions of those terms are given in [Dat86] and [Mor07].

$$r_E = \pm\frac{1}{4}\cdot i\pi K^2\left[\mp\cos\frac{\pi a}{p}+\frac{P_{1/2}(\pm\cos\frac{\pi a}{p})}{P_{-1/2}(\pm\cos\frac{\pi a}{p})}\right] \tag{3.21}$$

$$r_M = iR_M\frac{h}{2p}\sin\frac{\pi a}{p}\text{ , with} \tag{3.22}$$

$$R_M = -\frac{\pi K^2}{C_s}\left[\left(\frac{u_1}{\Phi}\right)^2(\alpha_1+\rho v_{\text{free}}^2)+\left(\frac{u_2}{\Phi}\right)^2(\alpha_2+\rho v_{\text{free}}^2)+\left(\frac{u_3}{\Phi}\right)^2\rho v_{\text{free}}^2\right]$$

Here, a and p denote the width and pitch of the electrode fingers and $P_\nu(x)$ is the Legendre function. The upper and lower signs refer to open- and short-circuit electrodes. In the calculations of the mechanical component, C_s is the equivalent dielectric constant, u_i the surface displacements on a free surface with directions as before (x_1 the propagation direction and x_3 the surface normal) and Φ the corresponding electric potential. As before the free surface velocity v_{free} is used here and the density ρ. Also, the material-dependent parameter of the stiffness plays a major role. With the Lamé constants λ_L and μ_L in an isotropic medium, the effective stiffness coefficients α_1 and α_2 are expressed as:

$$\alpha_1 = \mu_L \tag{3.23}$$

$$\alpha_2 = \frac{4\mu_L(\lambda_L+\mu_L)}{\lambda_L+2\mu_L} \tag{3.24}$$

In the case of anisotropic materials, the calculation is a lot more complicated and not discussed here. For 128°Y-cut $LiNbO_3$, for example, $\alpha_1 = 7.7\cdot 10^{10}\,\frac{\text{N}}{\text{m}^2}$ and $\alpha_2 = 18.6\cdot 10^{10}\,\frac{\text{N}}{\text{m}^2}$. Similar considerations can be made for the wave velocity which is perturbed by the metal electrodes due to electrical and mechanical loading $v_{\text{eff}} = v_{\text{free}} + \Delta v_E + \Delta v_M$. However, the changes are not very significant [Mor07].

Another important parameter of a reflector is the effective centre of reflection. The incoming wave decays exponentially into the array of fingers and depends on the reflectivity of each electrode strip. In practice, a position can be defined as to be the effective reflector. Its distance L_p in units of the SAW wavelength λ from the leading edge of the structure is determined by an analysis of the phase of the reflected wave and its slope at the centre frequency [Dat86].

$$\frac{L_p}{\lambda} = \frac{f_0}{4\pi}\left|\frac{d\theta}{df}\right| \approx \frac{1}{4|r|} \tag{3.25}$$

The penetration depth into the reflector is actually slightly frequency-dependent, but is assumed

to be constant here for simplicity. The effective centre of reflection is especially relevant in the construction of resonators for the determination of their effective length. To construct resonators, a similar design to IDTs is used, except that the finger-like electrodes are either all connected or all left floating. To insert a wave into the resonator an IDT is placed between the two reflectors. The wavelength that can exist in the resonator can be calculated taking the distance between the effective centres of reflection into account.

$$n \cdot \frac{\lambda}{2} = L_1 + L_2 \pm \frac{\lambda}{4} \tag{3.26}$$

The L_i are defined here as the distances from the effective centre of reflection of each reflector to the middle of the exciting IDT. The extra $\lambda/4$ arises from the phase shift of $\pi/2$ at the reflectors. Considering that reflection already occurs at the first strip, the absolute distance between the two reflectors also has to match the condition for resonance:

$$m \cdot \frac{\lambda}{2} = d \pm \frac{\lambda}{4} \tag{3.27}$$

with the distance between the two reflectors d taken from the middle of the first strip of each. Both equations together imply that the effective centre of reflection has to be rounded to a centre of a strip to have physically useful results in the calculations. For the mode spacing of the resonator, the effective length should be used which is $L_{\text{eff}} = L_1 + L_2 = d + 2 \cdot L_p$. Solving equation 3.27 for λ, the mode spacing is:

$$\frac{\Delta f_m}{f_1} = \frac{f_2 - f_1}{f_1} = \frac{\frac{c}{\lambda_2} - \frac{c}{\lambda_1}}{\frac{c}{\lambda_1}} = \frac{1}{m + \frac{1}{2}} = \frac{\lambda_1}{2L_{\text{eff}}} \tag{3.28}$$

With the approximation from equation 3.25, this can be written as $\Delta f_m / f_1 \approx 1/\left(d/p + 1/|r|\right)$. If the distance d between the reflectors is small compared to their pitch p, the relative mode spacing is approximately equal to $|r|$. Since for high numbers of strips and small distances d, the bandwidth is only about 0.6 times the mode spacing, the resonators can usually be designed to have only one active resonance mode, even for an effective cavity length L_{eff} of many wavelengths [Mor07]. For larger values of d there will be larger numbers of resonances present in the system.

A measure for the quality of a resonance mode in the reflector is defined by the Q-factor.

$$Q = \frac{f}{\Delta f} \tag{3.29}$$

Δf denotes here the full width half maximum (FWHM) of the resonance dip of frequency f. The quality is dependent on the reflectivity of the mirror and the losses in the system. The more energy is confined in the resonance mode, the higher the Q-factor will be. In order to track changes in the resonator, the Q-factor can be adduced besides tracking the resonance frequency.

3.2 Fabrication of the Chip

To apply a SAW onto a nanostructure it has to be efficiently excited on a substrate. As the nanowires examined in this work are in solution and can be placed on any material, the substrate can be chosen to best fit the requirements for the highest coupling of energy into the electro-

mechanical wave. Thus, $LiNbO_3$ was selected as its piezoelectric coupling coefficient is highest among the standard materials used for surface acoustic waves [Roy00; Dat86]. The IDT structure already explained in the previous section is fabricated by optical or electron beam lithography. The whole fabrication process is sketched in figure 3.3 and the parameters that were used are summarized in the table in appendix 8.2. For optical lithography the positive AZ-MIR resist is spin coated on the substrate and baked on a hot plate. Using a chromium mask the pattern is transferred with UV light into the resist before a developer solution removes the structurally changed material and leaves open the bare substrate at the exposed areas.

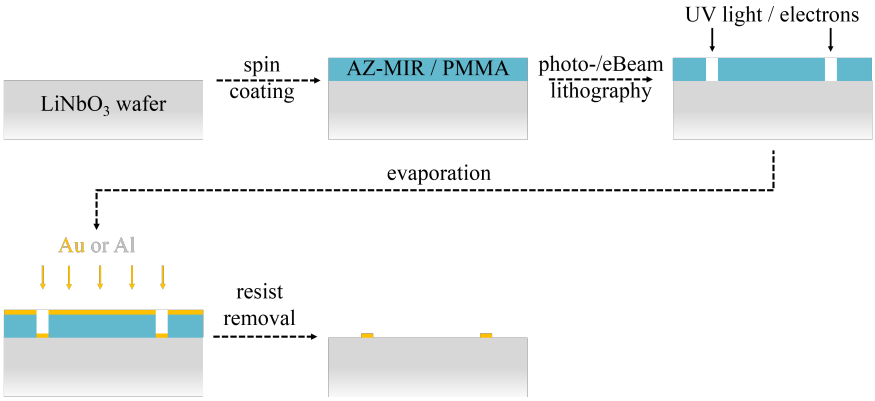

Figure 3.3: Sketch of the fabrication process of a SAW chip using photo- or electron-beam lithography. The $LiNbO_3$ substrate is spin coated with a resist and illuminated with UV light through a mask or with an electron beam to structurally change the resist at defined areas which is then removed with a developer solution. After a short cleaning metal is evaporated on the chip to fabricate the IDTs. In the last step, the remaining resist is removed to leave only the exposed areas as metal structure on the substrate.

If the pattern design needs to be flexible to be adapted from chip to chip or if the structures to be defined are smaller than a few µm then the photo-lithography is not appropriate any more and it is better to take advantage of the electron beam lithography. This is a serial writing technique in which a focused beam of electrons scans the chip. At the areas that should not be exposed a shutter blanks the beam and the resist is left unchanged. Small movements of the beam are performed via electric fields inside the optics of the machine. The maximum distance of these movements is defined by so called write fields and can be adjusted to ones needs. For larger movements the stage drives to a new position in such a way that the edge of the new write field matches the one of the old field. In order to write structures larger than the write field, a precise alignment has to be executed in advance. Due to small imperfections in this alignment shifts at the other side of the chip can not be excluded. Therefore it is highly recommended to place all fingers of an IDT in the same write field to avoid errors in the periodicity of the structure. The bonding pads are then defined in new, shifted write fields to prevent a write field edge directly crossing the pad. In order to avoid charging effects on the chip a specially prepared $LiNbO_3$, so called black $LiNbO_3$, has to be used. The untreated $LiNbO_3$ is a strong isolator which easily accumulates local charges which might deflect the electron beam during lithography and thus would blur or even totally misalign the transferred structures. Black $LiNbO_3$ is produced by a chemical reduction using nitrogen and hydrogen at temperature of several hundred degree Celsius. This treatment increases the conductivity by a factor of 10^5 and also enlarges the absorptivity in the visible spectrum, thus changing the appearance of the material from transparent to black. Alternatively, it is possible to add a top layer of Electra 92,

a conductive protective coating, if the transparency or the high isolating nature should be kept. Both methods can also be combined to further reduce the resistance of black $LiNbO_3$ and get a higher stability in the alignment procedure.

As resist either a single layer of ZEP or a double layer of PMMA was spin coated onto the substrate where the lower layer has a higher sensitivity to light. This is a commonly used trick to produce an undercut in the resist and thus simplify the final lift-off.

After a short cleaning in a plasma cleaner the chips are inserted in an evaporation chamber to evaporate 5 to 10 nm of titanium as adhesion agent before adding 50 to 70 nm of either Gold or Aluminium for the metal fingers and contacts. For higher intended frequencies of the SAW Aluminium should be used as its mass loading and therefore the mechanical attenuation of the wave is lower. It is also preferred when the chip has to be rebonded several times as the sticking of Al to the adhesion agent is higher than for Au leaving the contact pad intact when removing the bond. After evaporation the rest of the resist was removed in a lift-off process in Acetone or PG-Remover. To apply the electrical signals for the measurements, the pads of the IDTs have to be connected to chip holders that can easily be integrated in optoelectrical setups. Therefore they are bonded with a standard bonding machine onto the chip carrier shown in figure 3.4(a). The holder can then be used in the different setups to connect the electronics to the chip and apply and detect the SAW.

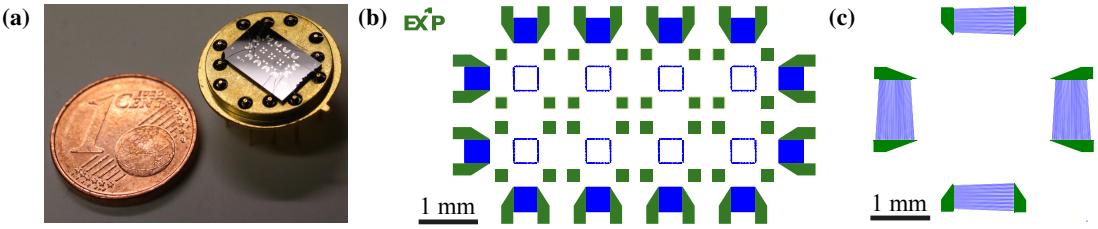

Figure 3.4: (**a**) Sample chip on a carrier with IDTs bonded to the pins. The carrier is such that it fits into the socket of the cryostat which leads the electrical connections via high frequency wires outside to the connectors. (**b**) Example of a SAW chip design with six IDT pairs in two perpendicular directions on a single chip. It is designed such that the delay lines cover most of the chip and the markers (green squares) and the coordinate systems in between enable an easy recognition of examined structures. (**c**) Alternative chip design with TIDT packed closely together to effectively cover most of the interior space with a given aperture.

In this work, three major chip designs were used. In the two that are presented in figure 3.4(b) and (c) each pair of IDTs forms a delay line with exchangeable transmitting and receiving transducers. The name results from the delay of the signal compared to its propagation in air. The first design (figure 3.4(b)) was developed such that the six delay lines cover most of the space on the substrate and that everywhere in between the IDTs two SAWs from perpendicular directions can be applied. The interdigital transducers are designed to have one basic frequency they are optimized for. Due to the periodic arrangement of the fingers, however, the odd harmonics can also be resonantly excited. The layout of the delay lines is adapted to the rectangular geometry of the substrate, hence, two SAW paths are aligned to be parallel to the long edge and four to be perpendicular. The area between them is filled with coordinate systems to help recognize the examined nanostructures and to indicate the travelling path of the SAW and thus make sure that the nanostructure to study is located in vicinity to the propagating wave.

The second design (figure 3.4(c)) is based on tapered interdigital transducers (TIDTs) that are arranged in one or two squares rather closely packed to minimize the area in between that is not affected by the SAW. The tapering results in a frequency variation along the aperture and

thus enables a spacial resolution of the measurement simply by applying different frequencies. This principle will be discuss in detail in section 6.1 where it is exploited for a 2D tomography of the sample. These chips do not have a coordinate system because the area in between the IDTs is much smaller and they were used for investigations on huge ensembles of nanowires instead of single ones or small bundles of nanostructures.

In chapter 7 the third chip design is applied which is a SAW-based resonator. In contrast to the delay line, there exists only one IDT which is placed between two reflectors. The exact design and its characteristics are shown in section 7.1.

3.3 Measurement Techniques for SAW

A surface acoustic wave can be generated and detected on chip with the application of an alternating electric field on the IDT. This section will introduce the basic instruments that are required to excite a wave on a piezoelectric substrate and shows how to detect it. Subsection 3.3.1 will briefly explain the use of a signal generator and oscilloscope to send SAWs through the chip. Afterwards, subsection 3.3.2 discusses loss mechanisms that result in insertion losses of the electrical power into the SAW. In the last part of the section, the insertion losses are used to estimate the amplitude (subsection 3.3.3).

3.3.1 Generation and Detection

The generation of a SAW on a piezoelectric substrate can be reached by applying a sinusoidal alternating voltage whose frequency is matched to the resonance of the IDT. An example setup is depicted in figure 3.5 which consists of a signal generator, a delay line on a chip and an oscilloscope. The signal generator can very precisely apply an high frequency voltage and, if needed, the signal can also be enhanced by an RF amplifier. For this work, two types of generators were used: *SME03* (Rohde and Schwarz) and *SG382* (Stanford Research Systems). Those can also be used to modulate the signal such that only small wave packets of a few µs travel through the sample instead of a continuous excitation. This helps prevent the chip

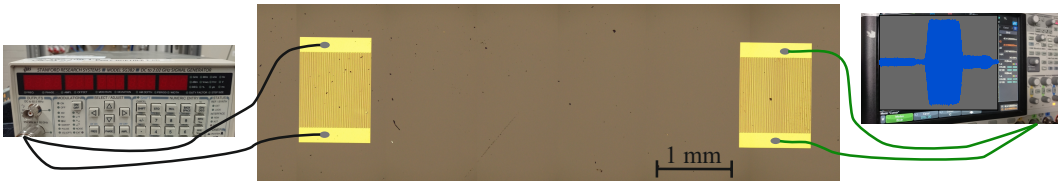

Figure 3.5: A signal generator (left) applies a sinusoidal wave packet to the left IDT where it generates a mechanical wave. This wave travels trough the substrate, interacts with the nanostructure on its way and finally reaches the right IDT where it is collected and transformed back into an electric signal and recorded by an oscilloscope (right).

from heating up too much and also reduces the interference with reflected waves that bounce back and forth between the IDTs. This way it is even possible to separate the direct electrical crossing from one IDT to the other from the actual wave in a time-resolved detection as it appears instantaneously without the delay of a reduced velocity through the substrate. The wave that is efficiently coupled into the substrate crosses the chip and is recorded on the other side at the IDT and transformed back into an electric signal which is then recorded by a WaveRunner 620 Zi oscilloscope (*LeCroy*) and displayed on the screen. As a reference the signal generator

sends out a rectangular shaped function which is high whenever the output of a wave is on and zero at all other times.

An example of a SAW wave packet is shown in figure 3.6 measured by the oscilloscope which records all the electric signals that are in any way transported to the receiving IDT. This includes the electrical crosstalk which appears immediately after the wave signal is sent out by the signal generator. It does not pass through the substrate but is the electric field that travelled through the air from one end of the chip to the other. Like this the signal can spread with the speed of light such that the time it needs to overcame the distance is much smaller than the resolution of the instrument. The actual SAW is the second and the largest wave packet that can be seen in figure 3.6. It is delayed compared to the input signal because the mechanical wave travels only at the speed of sound in $LiNbO_3$. Thus the delay can be used to estimate this reduced speed just by precisely measuring the distance between the IDTs. Another important feature in the graph is the finite rise and fall time of the SAW pulse compared to, for example, the electrical crosstalk. The mechanical wave needs time to built up when the alternating voltage is applied and will oscillate for a short amount of time even after the excitation is already turned off. This is a result of the spatial distribution of the fingers in the IDTs. The first oscillation of the packet was only induced by the furthermost finger pair while the second oscillation is already amplified by a second pair. An impulse that is created at the end of the IDT passes along its way all of the fingers and is amplified by them. An analogous effect happens at the end of the SAW pulse where the last wave oscillation meets all the fingers but does not get an amplification as the voltage is already turned off. Mathematically, this is a convolution of the sinusoidal SAW pulse with the rectangular shape of the excitation at the IDT which results in a linear increase and decrease after the sender IDT and becomes quadratic after the receiver where the convolution is performed a second time with the rectangular signal. The length of the rise and fall times are thus dependent on the number of fingers and is reduced for shorter IDTs.

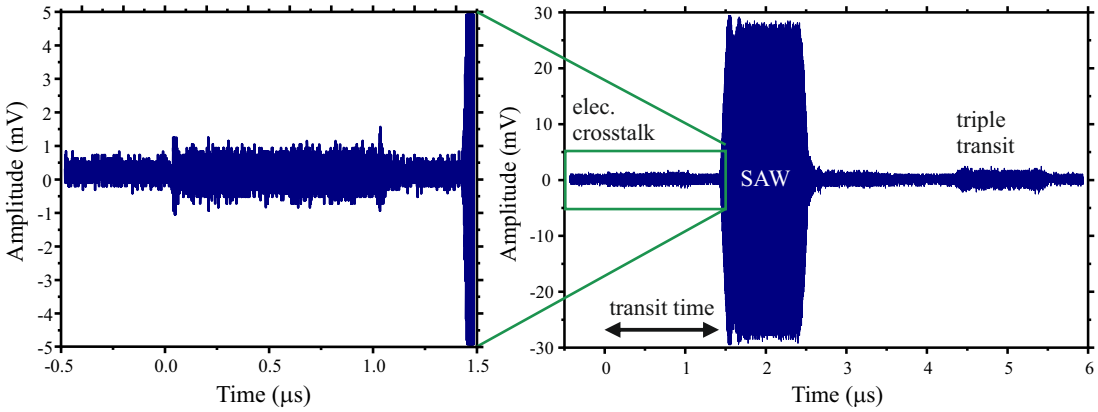

Figure 3.6: Example of a wave packet recorded by an oscilloscope after passing a delay line. The first appearing signal is electric crosstalk, indicated by the green box and enhanced in the left graph. The actual wave packet is delayed by a transit time of around 1425 ns due to the reduced velocity in $LiNbO_3$ compared to air. The triple transit signal passed the delay line three times and thus appears after three times the transit time.

The third signal showing up on the oscilloscope is the so called triple transit. If the receiving IDT is closely matched, a significant fraction of the power can be reflected, travel back to the transmitter where it is reflected again. Therefore the wave traverses the delay line three times before being collected and thus appears exactly at thrice the delay of the original SAW pulse.

Its magnitude depends on the matching conditions of both IDTs with a maximum of 12 dB below the original signal for perfect conjugate matching [Dat86]. Furthermore the design has a significant influence as, for example, the split-2 electrode arrangement already suppresses part of the unwanted reflection as it has negligible internal reflections [Mor07]. Additionally, if the triple transit interferes with the original signal, the length of the wave packet is too long for the travel distance. Thus, the distance between the two IDTs should be increased or the temporal width of the signal decreased in order to separate the two wave packets in the detection.

The time difference either between the onset point of the electric crosstalk or the triple transit and the main wave can be used to calculate the velocity of the SAW as they are all measured by the same two IDTs. This is important because then the delays produced by the electric cables that provide the connection between the instruments and the chip can be neglected as they are the same for all signals. The data shown above is now used to calculate the sound velocity of $LiNbO_3$ in the Z direction of the Y-cut. First, the time differences have to be determined as accurately as possible. The beginning of the crosstalk can be identified clearly to $t_{ct,0} = (37 \pm 2)\,\text{ns}$ and its width is known to be 1000 ns which is the length of the applied electric signal. The identification of the starting time of the SAW pulse is slightly more difficult because of the convolution with the two IDTs. One can either simply guess the middle of the wave packet or if the signal is broad enough to exhibit a flat part in between the rise and the fall, as in this case, it is possible the estimate the middle of the wave packet by only taking into account the flat part. This is possible because the convolution is symmetric and inhibits the same changes at the beginning and at the end of the wave packet. The estimated middle of the wave packet is then $t_{SAW} = (1971 \pm 6)\,\text{ns}$ and the width of the flat part is extracted to be $\Delta t_{SAW} = 903\,\text{ns}$. The width of the overall wave packet is bigger than the applied signal exactly by the amount of the rise time (or fall time). So at the end of the input signal the end of the flat part of the wave packet leaves the sender. Afterwards it declines in amplitude according to the convolution. The time this same point of the wave reaches the receiver is determined by the starting of the decrease in amplitude in the recorded data. With this knowledge, the travelling time of the SAW and together with the nominal distance of the IDTs of $d = 4804.6\mu\text{m}$ the velocity can be calculated:

$$t_{\text{travel}} = t_{SAW} + \frac{1}{2}\Delta t_{SAW} - (t_{ct,0} + \Delta t_{ct}) = (1385.5 \pm 8.0)\,\text{ns} \tag{3.30}$$

$$v_{SAW} = \frac{d}{t_{\text{travel}}} = (3468 \pm 20)\,\frac{\text{m}}{\text{s}} \tag{3.31}$$

The result is quite close to the literature value of 3488 $\frac{\text{m}}{\text{s}}$ [Ash85]. The small discrepancy arises from the uncertainty of the estimate of the centre of the SAW signal. In this case it was especially hard to determine because of the overshoot in the beginning. The uncertainty arising from the distance of the IDTs is small as electron beam lithography is a very accurate fabrication technique.

3.3.2 Influences on the Generation Efficiency of a SAW

The amount of power transferred from an electric signal applied to an IDT into the mechanical wave is dependent on a lot of factors. The first choices to make are the material, its crystal cut and the direction of propagation. If one is not limited to a certain substrate, a good choice for a high coupling efficiency into a surface mode is $LiNbO_3$ for its high, but direction-dependent piezoelectric coupling constant K^2. Because the piezoelectric constant is a tensor, it depends

on the exact travel direction of the wave which includes the cut. In order to find the best direction for one specific cut, the free and shorted sound velocities have to be considered whose difference essentially defines the efficiency of coupling. For the shorted measurement a thin metal film is deposited on the substrate to suppress the piezoelectric effect on the surface and reduce the wave to its mechanical part. K^2 is linearly dependent on the relative difference of those two velocities (c. f. equation 3.15 and [Dat86]):

$$K^2 \approx 2 \cdot \frac{v_{\text{free}} - v_{\text{short}}}{v_{\text{free}}} \tag{3.32}$$

The angle dependence of the two velocities arises from the underlying anisotropic crystal structure which is a prerequisite for the piezoelectricity in the first place. It is also the reason for beam steering to appear which limits efficient wave propagation to the directions with extrema in the velocity. In anisotropic media the power flow is not necessarily perpendicular to the phase fronts. It makes an angle with the perpendicular direction which is given by $\alpha = \frac{1}{v} \mathrm{d}v/\mathrm{d}\theta$ [Dat86]. In a simplified view one can say that the velocity on the left side is different from that on the right of the wave and that guides the wave towards the slower direction. At the extrema of the angle-dependent velocity, the beam steering is zero so that the wave takes the straight path. For $LiNbO_3$ in a Y-cut the only suitable directions are $0°$, $\pm\ 25°$, and $\pm\ 90°$ [Dat86]. For the right crystal cut, one also has to take into account the efficient generation of surface waves compared to bulk waves and the type of wave that is desired. For Rayleigh waves in $LiNbO_3$, for example, the Y-cut or the $128°$Y-cut are ideal candidates. If temperature stability is of importance, quartz crystals are widely used, since their first order temperature coefficient of the velocity is zero around room temperature. As a result, the temperature stability of the operating frequency is very good [Dat86].

A more technical factor influencing the efficiency of the coupling is meeting the exact resonance frequency as all others will experience destructive interference of the reflected waves at the different fingers and create heat instead of a travelling wave. Especially the electrical crosstalk decreases with the efficiency of the coupling. The better the insertion of power into the wave is, the lower is the electrical crosstalk. This can be used as one measure of quality for the fabricated chip, though the relative transmitted power is a more direct and significant one. Another technically relevant parameter is the mechanical loading of the IDT. The weight of the metal deposited to define the finger structure puts load onto the substrate exactly at the generation point of the SAW. This influences the stiffness of the piezoelectric, reducing the mechanical amplitude of the in-coupled wave. This effect also appears when heavy load is placed on top of the delay line in the propagation path. The weight then blocks the free path and reduces the power transmitted through the chip (c. f. section 3.5.2).

Another major influence, but complicated to optimize, is the impedance matching to the circuit around the IDT. The relation between the reflection r and the impedance of the system Z_0 as well as the impedance of the load Z is given by

$$r = \frac{Z - Z_0}{Z + Z_0} = \frac{a_{refl}}{a_{in}} \equiv S_{11}. \tag{3.33}$$

Thus, if the load impedance is not matched to the system impedance, this means if $Z \ll Z_0$ or $Z \gg Z_0$, then $|r| \to 1$ which means that most of the signal is reflected instead of passed to the wave. In commercial high frequency products the impedance of the system is usually matched to $50\,\Omega$. As the studies performed in this work were not strongly dependent on maximized power

throughput, the theoretical and practical impedance matching with capacitors and inductors will not be discussed here. Further information can be found, for example, in [Dat86; Roy00].

3.3.3 Evaluation of the SAW Amplitude

The overall loss during the generation of a SAW is given by the insertion loss (IL),

$$\mathrm{IL} = \frac{P_{\mathrm{in}} - P_{SAW}}{P_{\mathrm{in}}} \tag{3.34}$$

with the inserted power P_{in} and the power transformed into a wave P_{SAW}. This is different for each sample but influences the power of the signal applied to the nanostructure under examination. Thus it is important to roughly estimate the insertion loss when comparing studies of different chips or even only different IDT designs. In this section, an example calculation of the losses of an IDT is performed. At first, the transmission amplitude of the SAW as a function of applied power is measured. The wave is excited by a signal generator and recorded with an oscilloscope. It's transmitted output power is compared in figure 3.7 to the applied power from the signal generator for exactly the same settings. Both result in a linear increase with a constant offset between them in a double logarithmic scale (note the unit dBm).

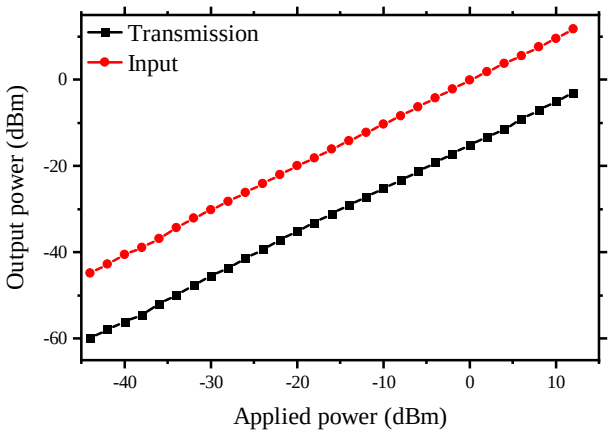

Figure 3.7: Output of the signal generator and the reduced transmitted power through the delay line 1 on SAW chip LJ40 as a function of the nominal applied power. The difference between the two is the summed insertion loss of both IDTs.

From this graph with data from delay line 1 on chip LJ40 the insertion loss is determined as the difference between the two signals. Here $\mathrm{IL} = (15.0 \pm 0.5)\,\mathrm{dB}$ which is the sum of the influences of both IDTs. Assuming both IDTs to have the same efficiency results in a per IDT loss of 7.5 dB. This assumption will be compared later in subsection 3.4.1 with a calculation of the amount of power reflected from both IDTs. For an applied power of $1\,\mathrm{mW} = 0\,\mathrm{dBm}$ the power transformed into a wave at this specific input IDT is then 178 µW.

For an estimation of the mechanical amplitude of the SAW, Datta [Dat86] used a transmission line model to relate the acoustic power to the electric potential:

$$P_{SAW} = \frac{1}{2}\frac{A}{\lambda} y_0 \left|\Phi\right|^2 \tag{3.35}$$

Here, A denotes the aperture of the IDT and Φ the electric potential. The characteristic admittance y_0, a material-dependent constant that describes the acoustic conductivity, is known to be $y_0 = 0.21\,\mathrm{mS}$ [Dat86] for $LiNbO_3$. With this, the electric potential of the sample analysed here is $\Phi = 0.5\,\mathrm{V}$ (with $A = 400\,\mu\mathrm{m}$ and $\lambda = 10.7\,\mu\mathrm{m}$). With the maximum output power of 32 dBm of the electrical amplifier set up behind the signal generator, the maximum potential of the wave without any losses considered, could be $\Phi = 20\,\mathrm{V}$.

3.4 Characterization of the Chip

Before the chip is used for measurements it is important to characterize it fully to know its exact resonance frequency and the quality of the output. One part is the determination of the insertion loss as presented in the section above. But besides that, some general characterizations are needed.

In the first part of this section, the vector network analyser (VNA) is introduced which is used for the high frequency characterization of the chip and can also be used to estimate the insertion loss of the IDTs. In the second part, typical transmission and reflection measurements are presented for different types of IDTs and the phase evolution of the signal is introduced.

3.4.1 The Vector Network Analyser

The characteristic frequency dependence of a SAW chip is an important feature of a sample. The vector network analyser (VNA) is a very specialized instrument compared to the oscilloscope, thus its way of functioning will be briefly discussed in this section. It has typically two ports where high-frequency cables can be connected. In a full characterization it determines four parameters: S_{11}, S_{22}, S_{21} and S_{12}, the reflection for each port and the transmission in both directions. They are defined by the inserted, reflected and transmitted signal amplitudes as $S_{11} = {a_{\mathrm{refl}}}/{a_{\mathrm{in}}}$ and $S_{21} = {a_{\mathrm{trans}}}/{a_{\mathrm{in}}}$ and S_{22} as well as S_{12} analogously. For a measurement the instrument sends out small pulses of defined frequencies and records how much of it is reflected back as well as how much is being transmitted to the other port. This data is then plotted as a function of frequency and saved together with the phase shift the signal exhibits during its path. The amplitude is commonly referred to in dB with respect to the inserted signal. Thus, S_{11} and S_{21} are defined using the input, reflected and transmitted amplitudes a_i as:

$$S_{11} = 20 \cdot \log_{10}\left(\frac{a_{\mathrm{refl}}}{a_{\mathrm{in}}}\right) \quad [\mathrm{dB}] \tag{3.36}$$

$$S_{21} = 20 \cdot \log_{10}\left(\frac{a_{\mathrm{trans}}}{a_{\mathrm{in}}}\right) \quad [\mathrm{dB}] \tag{3.37}$$

As S_{11} is a measure for the amount of reflected signal, an efficient IDT results in a deep dip showing very little reflection at the resonance frequency. S_{21} in contrast, shows a peak where the coupling into and out of the wave is good (compare figure 3.8 for sample data). The insertion loss is the amount of power that is not transmitted nor reflected. But as the reflection of power at the resonance frequency is very low, the IL can be set equal to the amount that is not transmitted. Therefore, the insertion loss of the whole system consisting of two IDTs is just the negative of the transmission in the calculations (in decibel notation) for their sum has to

equal 0 dB to be equal to the input power.

$$\mathrm{IL}_{\mathrm{VNA,trans}} = -20 \cdot \log_{10}(|S_{21}|) \tag{3.38}$$

Of course, the cables and the sample box or the cryostat also have internal reflections and losses. These are all summed up and contribute to the overall measured data. In order to ensure that those do not influence the measurement, reference calibrations can be performed with chip holders that are all the same but without the piezoelectric sample. In this way, one can exclude any resonances and back reflections from the setup and really measure only the effect of the bonding wires and the chip itself. It is also possible to perform time-resolved measurements and see the temporal characteristics of the chip's response. The actual measurement is still performed as a frequency sweep but with an inverse Fourier transform it is possible to calculate the temporal dependence of the signal. This can be used to gate the VNA and thus prevent unwanted reflected waves from being measured and is a fast, alternative method to the reference calibrations if the instrument is able to perform gating and can help increase the signal to noise ratio for low signal amplitudes. The time delays in the reflection measurement allow for a spatial analysis of the signal path which is capable of distinguishing precisely between effects of the cables, the box and the sample. For transmission measurements it is even possible like in the oscilloscope recordings of figure 3.6 to nicely discriminate between the first signal and the triple transit.

The frequency-dependent measurements of the VNA can also be used to determine the insertion loss and have the advantage of being able to distinguish between the two IDTs of a delay line as it is possible to perform the calculations on the basis of the reflection measurements. This is particularly important when one of the two IDTs of a delay line is not fully functioning or significantly lower in performance. Then one can not assume equality in insertion loss and thus a investigation of the transmission data which only results in the sum of both losses is not of great use.

In order to determine the insertion loss of a single IDT, some considerations have to be taken into account. A wave that is sent out by the VNA can either be reflected somewhere or be transmitted to the other port, if we assume a lossless system. Then $|S_{11}|^2 + |S_{21}|^2 = 1$ with the *S* parameters in units of the input signal. But this is not true for real SAW devices as standard IDTs transmit waves in both directions which implies a loss of 3 dB for the signal coupled in. Moreover there are losses in the form of heat and other dissipation in the piezoelectric substrate due to wave attenuation. But for a brief estimate in a system where it is not possible to use the transmission data, the assumption can be useful. For a slight improvement one could include the 3 dB decrease due to the bidirectionality. The final formula is received by inserting $|S_{11}|^2 + |S_{21}|^2 = 1$ into equation 3.38. The insertion loss for a single transducer can thus be calculated from only the reflection data via equation (3.39) or using the transmission data with equation (3.40) which is half of equation 3.38 assuming equal contributions of both IDTs.

$$\mathrm{IL}_{\mathrm{VNA,\,refl}} = -20 \cdot \tfrac{1}{2} \cdot \log_{10}\left(1 - |S_{11}|^2\right) + 3\,\mathrm{dB} = 3.3\,\mathrm{dB} \tag{3.39}$$

$$\mathrm{IL}_{\mathrm{VNA,\,trans}} = -20 \cdot \tfrac{1}{2} \cdot \log_{10}(|S_{21}|) = \frac{1}{2}(15.5 \pm 0.5)\,\mathrm{dB} \tag{3.40}$$

A comparison with the value calculated in subsection 3.3.3 of $\mathrm{IL}_{\mathrm{VNA,\,trans}} = (7.50 \pm 0.25)\,\mathrm{dB}$ (c.f. equation 3.40) for the same delay line 1 on the same chip LJ40 reveals the limits of using only the reflection and gives an estimate of around 4 dB of extra losses. But it also shows that

using the transmission for a calculation of the losses, the two methods nicely coincide.

With a maximum input energy of 32 dBm the insertion loss calculation reveals a maximum power input in the wave of 24.5 dBm which is equal to 282 mW of electrical power transformed into the acoustic wave.

3.4.2 Transmission and Reflection Characteristics

With the VNA introduced in the previous section the main characteristics of a SAW device can be studied. The reflection and transmission data in amplitude and phase give information about the resonance and higher harmonic frequencies as well as the quality and quantity of the insertion. In addition, the inverse Fourier transform can provide insight in the temporal evolution of the signal such as reflections at the chip edges or back reflections of IDTs. Figure 3.8(a) displays an example study with a VNA on delay line 1 on the chip LJ40 consisting of reflection (black) and transmission (red) data as a function of the applied frequency. These studies are typical recordings for the characterization of high frequency dependent electrical circuits.

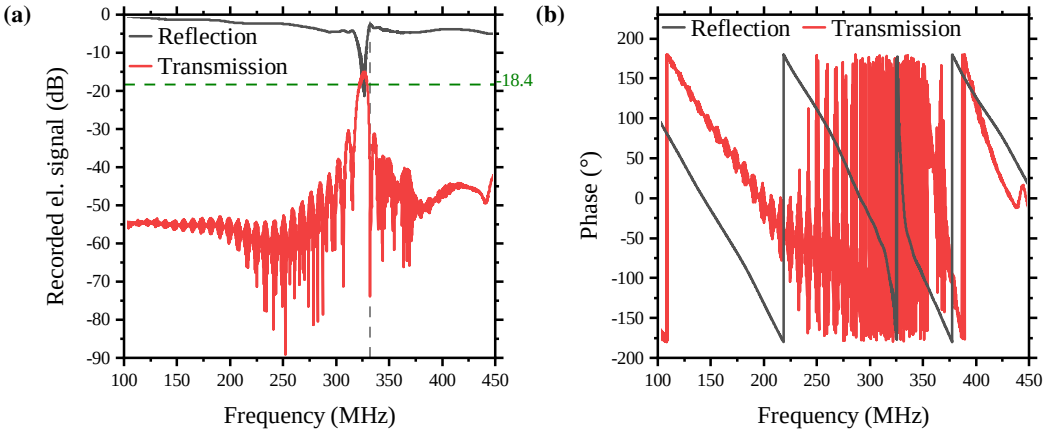

Figure 3.8: (**a**) Reflection and transmission measurement with a VNA of delay line 1 on sample LJ40. The resonance frequency results in a dip for the reflection (black line) at 324 MHz. The transmission (red line) shows a peak at the same frequency and ripples to the left and right of the main peak. The green horizontal dashed line indicates the 3 dB cut-off and the grey vertical dashed line shows the nominal frequency of the IDT. (**b**) The phase of the signal detected by the VNA also shows a distinct feature in the reflection measurement at the resonance frequency. The phase of the transmission reproduces the Fraunhofer pattern from the amplitude in panel (a).

In this example, the reflection of the signal far away from the resonance is almost flat and above -5 dB while the resonance dip reaches down to around -20 dB. The actual resonance frequency lies at 324 MHz, slightly below the designed value of 332 MHz (indicated by the dashed vertical line). This shift occurs as a result of small imperfections and shifts during the fabrication process and the non-perfect distribution of the mass loading. But the exact resonance also depends on the temperature as the sound velocity in the substrate does so [Sch93; Mor05]. Even the defined wavelength changes due to contractions and expansions with temperature, but this is only on the order of 0.5 % for a temperature change of 300 K [Pig07] and is negligible in comparison to the change in the sound velocity. The width of the transmission band around the resonance frequency is defined by the number of fingers which is in turn inversely proportional to the temporal spread of the wave packet (c. f. subsection 3.3.1).

The red curve in figure 3.8(a) displays the frequency-dependent transmission through the SAW chip with an input signal of $P_{rf} = -3\,\mathrm{dBm}$. The main peak corresponds exactly to the black resonance dip of the reflection curve proving that the not reflected power actually is transformed into a wave that travels along the surface and can be detected by the second IDT. The fact that it does not reach the 0 dB line was exploited in subsection 3.4.1 to determine the insertion losses. The full width half maximum of this sample is 7 MHz, from 322 MHz to 329 MHz, with 38 finger quadruplets in a split-2 design (c. f. section 3.1). The cut-off is shown in the figure by the green horizontal dashed line which shows the 3 dB line below the maximum of the transmission which is equivalent to a halving of the signal power. Only the region above this cut-off is used in the investigations to ensure a good energy transfer into the wave packet and enough power to manipulate the nanostructures. The background of the transmission signal is between $-45\,\mathrm{dB}$ and $-55\,\mathrm{dB}$ or in other words about five orders of magnitude lower then the incoming power. Thus the IDT is an operative bandpass with a 7 MHz small band around its resonance frequency and efficient suppression of all other frequencies.

Moreover, an asymmetric pattern of ripples can be seen. On the left side of the main peak a repeating pattern of interferences appears while on the right side only the first side peak is visible. In theory these Fraunhofer patterns [Bas95] can be calculated with the discrete source model which assumes a delta pulse like charge spike at the centre of each finger. Thus the impulse response of a transducer is the sum of Dirac functions for each finger. The frequency response which is studied in the experiment can be calculated in this model to be

$$H(f) = A_0 N_s \frac{\sin X}{X}, \qquad \text{with} \qquad X = N_s \frac{\pi}{2} \frac{f - f_0}{f_0}. \tag{3.41}$$

Here, A_0 denotes the amplitude and N_s the number of delta pulse sources. f_0 is the resonance frequency under consideration. This predicts that the response of the IDT shows a $\mathrm{sinc}(f)$ like behaviour which explains the oscillations around the resonance frequency.

The phase evolution of the same reflection measurement depicted in figure 3.8(b) shows a linear dependence of the phase from the frequency arising simply from the change in wavelength and thus the number of periods fitting in the distance between the instrument and the reflection at the IDT. At the resonance though, the phase changes much faster due to a change in the impedance close to the resonance. This feature appears exactly at the same frequency as the dip in the amplitude of reflected signal, further confirming the efficient coupling of electric power to the mechanical wave. The phase of the transmitted signal in the region around the resonance undergoes several fast phase changes that overlap perfectly in frequency with the modulations in the amplitude of the transmitted signal, substantiating that actual small side resonances with energy transfer through the chip occur.

The transmission and reflection characteristics as a function of frequency differ significantly when TIDTs are investigated. The change of the width and pitch of the electrodes along the aperture is illustrated in figure 3.9(a) and results in a frequency variation along the IDT. The principle will be discussed in detail in chapter 6, but the sketch already gives a brief idea of the layout. The main characteristic, needed for the understanding of the data presented here, is its wide band of frequencies which is reproduced in the transmission and reflection data in figure 3.9(b) recorded with an input signal of $P_{rf} = -3\,\mathrm{dBm}$. Instead of one single resonance frequency, the TIDT shows a whole band. Despite the reflection being rather high even in resonance a clear transmission band stands out from the background noise. As the energy sent in can only be reflected, transmitted or lost, this means that for this delay line the losses are

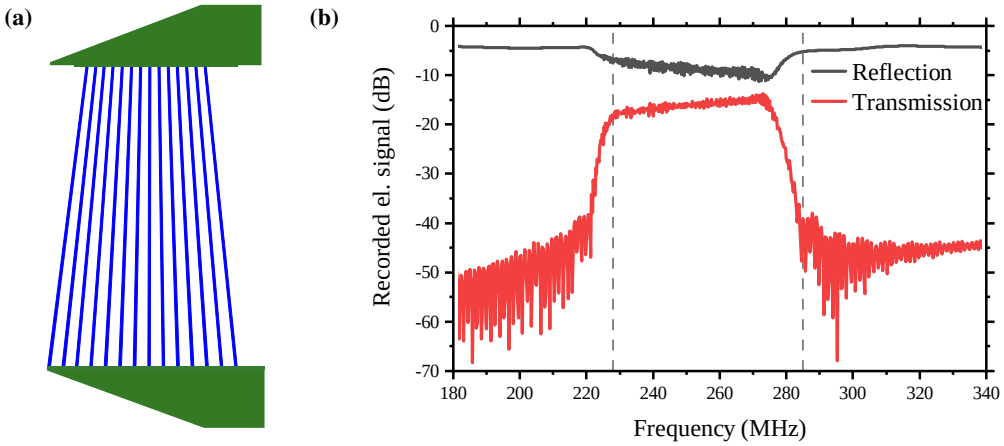

Figure 3.9: (**a**) Schematic of a TIDT. The width and pitch of the electrodes and thus the generated frequency change along the aperture. It can be seen here that the electrodes are not perpendicular to the pads, but fan out towards one side. (**b**) Reflection and transmission data from an VNA study of delay line Z on chip LJ70 with TIDTs (IDT Z 1 and IDT Z 2). The actual frequency band is slightly shifted from the nominal one indicated by the dashed lines.

lower compared to the one analysed in figure 3.8.

The boundary frequencies are again slightly shifted to lower values compared to the designed band indicated by the dashed vertical lines. This is probably an effect of the fabrication process and does not play a big role in the experiments the chip is used for. The nominal and actual frequencies of the chips used in this work are summarized in table 3.2 showing good agreements between the designed wavelengths and the real resonances of the fabricated chips.

IDT	nominal frequency (MHz)	actual frequency (MHz)
LJ40 IDT 6	332	326
LJ40 IDT 12	332	326
LJ40 IDT 1	354	352
LJ40 IDT 7	354	352 and 433
LJ70 IDT Z 1	228 – 285	223 – 281
LJ70 IDT Z 2	228 – 285	223 – 280
LJ70 IDT X 1	294 – 343	294 – 343
LJ70 IDT X 2	294 – 343	294 – 343
LJ82 both IDTs	300	290

Table 3.2: Summary of the nominal and the actual resonance frequencies at room temperature for the delay lines used for the studies presented in this work.

The only larger discrepancy appears for IDT 7 on chip LJ40. It shows only a very small resonance around the defined wavelength of 354 MHz but instead a very good resonance at 433 MHz.

3.5 Effect on Semiconductors

The effect of a SAW on a semiconductor consists of three main parts which will be explained in this section. First of all, the heat dissipation into the crystal is to be mentioned. Moreover, the piezoelectric substrate transports the mechanical wave with an accompanying electric field along the propagation path. All three effects will first be discussed separately before their combined effect is analysed. For nanowires, the much smaller effect of the mechanical deformation plays only a minor role and thus the focus of this section lies on the influences of the electric field as this is the basis for the following investigations.

3.5.1 Heating

Every mechanical movement induces some friction and so does the surface acoustic wave on its way along the substrate surface. The displacement of the atoms in the crystal produces heat which is a loss of energy of the wave. This loss increases with frequency and is dependent on the material [Mat77]. For $LiNbO_3$ the attenuation at 1 GHz is about 2.6 $\frac{\mathrm{dB}}{\mathrm{cm}}$. For studies at low temperature, the deposited heat can actually be measured as a significant increase of several K and results in a drop of the heating power used to stabilize the temperature. For high acoustic powers in a modulation of the SAW with a duty cycle of only 2 %, i. e. with the SAW being turned on only 2 % of the time, the heating power can be reduced by up to 25 mW. This energy deposition, when not compensated for, results in a red shift of the emission spectrum of semiconductors arising from the temperature dependence of the bandgap following the formula

$$E_g(T) = E_g(0\,\mathrm{K}) - \frac{\alpha T^2}{T+\beta}, \tag{3.42}$$

with α and β being material constants. Most of the heat generated in the substrate is in the acoustic path, thus heating up the nanostructures under examination on top of the substrate while the cooling of the sample is mostly realized at the bottom. If heat plays a major role for an experiment, the SAW modulation frequency and the width of the window function can be reduced further. This will increase the measurement time as it raises integration time, but can significantly reduce the heat intake as the SAW pulses are kept short and the time between them long enough for the nanostructures and the substrate to cool down again.

3.5.2 Mechanical Wave

The main part which defines the surface acoustic wave is the mechanical wave. This part, also present in earthquakes, has a huge destructive potential and also generates most of the heat along the way. Usually the displacements in the lab are rather small and in the range of pm up to a few nm depending on the applied power and the substrate in use. Nevertheless, they can have a huge impact on nanostructures via the deformation potential. As the atoms follow the elliptic movement into which the wave guides them, their lattice constant is changed and builds up stress and strain. This pressure is directly correlated with the SAW's mechanical amplitude and potential. This could in principle also be used to determine the acoustic power via a determination of the energy shift due to the deformation potential, but it is then necessary to suppress the effect of the electric field on the band structure as it is in most cases far bigger. Alternatively, one needs to be able to distinguish between the two types of band edge modulation that can occur. The mechanical potential induces a type I band edge modulation, that is a

shift of conduction and valence band in different directions away from and towards each other depending on the spatial position (c. f. figure 3.10(a)). Thus a sinusoidal deformation would result in a spatial dependence of the bandgap being small where there is large mechanical pressure and being large where the atoms are torn apart [Sha14; Bal19]. In contrast, a type II modulation shifts both bands in parallel as depicted in figure 3.10(b). This effect is induced on the semiconductors by an electric field and will be discussed in the next subsection.

But the mechanical wave also plays an important role in the transportation of the energy. A heavy load put onto the substrate in the acoustic path or onto the IDT will result in a significant decrease of the power transported through or coupled into the chip (c. f. section 7.2).

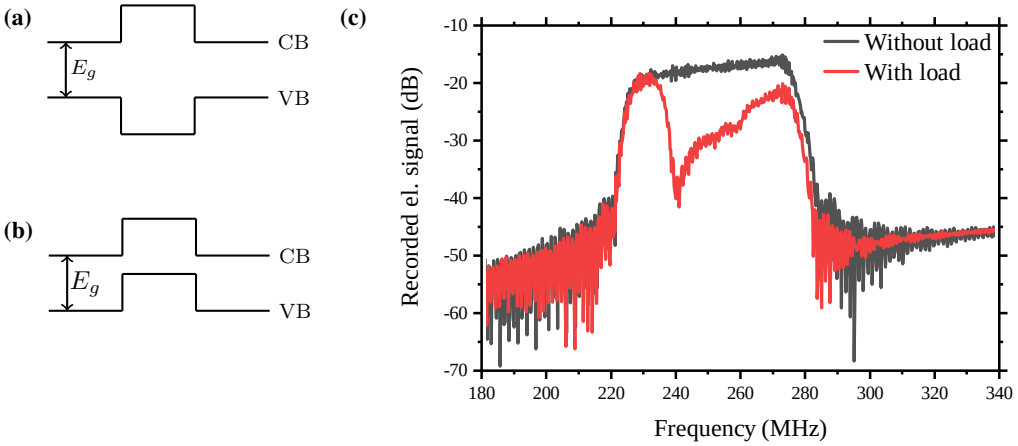

Figure 3.10: (**a**) Sketch of a type I band modulation of conduction band (CB) and valance band (VB) in a material with bandgap E_g. (**b**) Type II band modulation of the same material. (**c**) Transmission band of a TIDT delay line without (black) and with (red) a viscous load placed in the acoustic path resulting in a significant drop of the signal exactly at the area of the load, even showing the load distribution inside the drop.

The so called *mass loading* is caused by the translation of layer mass by the mechanical part of the SAW. Furthermore, elastic and viscoelastic effects occur especially when fluid material is generating the perturbations. In the case of very thin or rigid material being deposited on the delay line, which moves fully synchronously with the SAW's mechanical deflections, no dissipation of the wave's energy takes place. It only increases the kinetic energy density and hence reduces the wave velocity. The results can be summarized in the following equation [Bal97].

$$\begin{aligned} \frac{\Delta v}{v_0} &= -c_m f \rho_s \\ c_m &= \frac{v_0}{4}\left(\frac{v_{x0}^2}{fP_{SAW}} + \frac{v_{y0}^2}{fP_{SAW}} + \frac{v_{z0}^2}{fP_{SAW}}\right) \end{aligned} \tag{3.43}$$

Here, f denotes the SAW frequency and ρ_s the density of the substrate. The material-dependent constant c_m that is introduced here includes the particle velocities at the surface v_{x0}, v_{y0}, v_{z0} and the wave's power P_{SAW} and velocity v_0. The expression in parentheses can be seen as constant despite its dependency on f because due to the greater confinement of the wave's energy near the surface when increasing the frequency, the surface particle velocity increases proportional to $\sqrt{fP_{SAW}}$. The change in velocity can be measured by recording the time delay or the phase of

a propagating SAW and compare it to a non-disturbed signal. The phase can easily be analysed and calculated back to the change in velocity which then gives a measure for the amount of load that influences the wave (see also section 6.1).

As long as the mass layer is assumed to be lossless, no attenuation will occur. This can not be assumed for the materials that are under examination in this thesis as the perovskite NW mixture is not fully rigid, but the NWs come in a viscous fluid despite the solvent which evaporates fully under the drying process. The jelly like substance, resulting from excess ligand material during the growth process, can not be washed away fully and thus contributes to an attenuation of the SAW.

Figure 3.10(c) shows such a reduction of the transmission function. The transmitted signal through the delay line relative to the input signal of $P_{rf} = -3\,\mathrm{dBm}$ is analysed by a VNA in the relevant frequency range of the IDT for the loaded (black line) and the unloaded (red line) chip. The reduction in the transmitted signal evoked by placing a big drop of semiconductor nanowires diluted in a carrier solution on the acoustic path can be seen. A TIDT is used, so the IDT has a band of frequencies distributed along the aperture which can be used for spatial discrimination perpendicular to the propagation direction (the mechanism behind this is explained briefly in section 3.1 and in detail in section 6.1). It can be seen that the low-frequency side stays unperturbed, while the middle and right side are reduced by different amounts which correlate with the amount of viscous material at the relevant position. Due to the NWs being in solution the weight distribution is not uniform because during the drying process the wires and the excess ligands cluster and are flushed to the outer borders of the drop. This explains the huge decrease in transmission right in the middle of the IDT: the drop was not distributed equally over the width of the SAW path but placed only on one side. The signal attenuation is an effect of the coupling with the additional viscous mass that will reduce the wave's energy [Bal97]. In the application as a sensor, the SAW signal is always presented with respect to a reference signal to eliminate the influence of the substrate [Pas17]. Furthermore, the load sensitivity of the mechanical wave is fully reversible, meaning that a removal of the substance suppressing the SAW will result in a full restoration of the transmission characteristic.

3.5.3 Electric Field

Beside the mechanical wave, the signal is accompanied by an electric field due to the piezoelectric effect in most of the substrates used for SAW devices. The material used in this work is a strong piezoelectric giving rise to a non negligible electric wave that travels with the speed of sound as it can be seen as quasi-static field produced by the displacement of the atoms in the crystal. It is not an electric field that travels by itself but is coupled to the potential gradient from the mechanical motion. The electric field has a huge influence on free carriers and can even ionize excitons and separate the single carriers from each other, preventing their recombination. But the electric field also induces a type II band edge modulation of conduction and valance band (c. f. figure 3.10(b)) and the sinusoidal electric field results in a spatial, sinusoidal shift of both bands in parallel [Kin11; Roc97] (c. f. the schematics of the bandstructures in figure 3.11). In contrast, a type I modulation (c. f. subsection 3.5.2 and figure 3.10(a)) always shifts the conduction and valance band in opposite directions. The electrons and holes then follow the bands towards their minimum or maximum which are separated in space by half an acoustic wavelength for type II modulation. For the experiments performed in this work, the mechanical wave plays only a minor role and the electric field is the major tool used for the studies.

The schematic in figure 3.11 illustrates the behaviour for type II band edge modulation: at

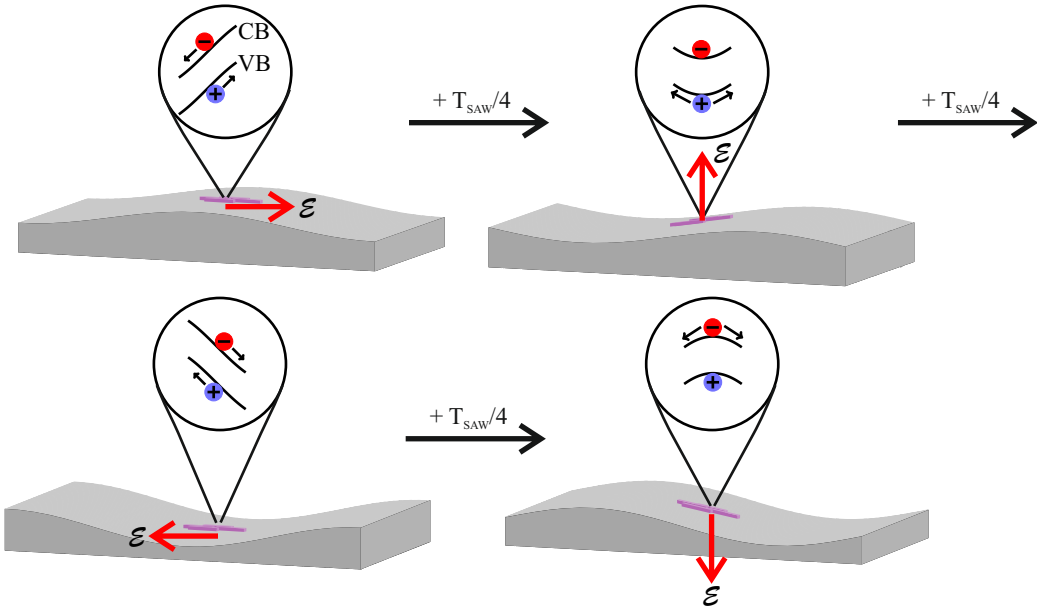

Figure 3.11: Dynamics of the spatial type II band edge modulation imprinted by the electric field of the SAW separating the electrons and holes into different positions and thus suppressing their recombination. The graph was adapted from [Jan19].

the maximal mechanical displacement of the atoms the electric field points towards the inside of the substrate resulting in a maximum of the energy of conduction and valance band. The opposite happens at the minimum of the displacement. At positions where the particles remain in place, the electric field is aligned parallel or anti-parallel to the propagation direction of the SAW and induces a steep slope in the energy bands. The changing of the electric field direction with the phase of the mechanical wave is a result of the induction of three different electric fields in the three directions whose amplitude changes with the potential landscape formed by the phase of the SAW.

The travelling acoustic wave induces a constantly changing electric field along its path where the extrema follow the movement of the mechanical wave. Free electrons in the influence of the field will stay at the minimum of the conduction band even if that moves along the substrate and will follow the path until they hit a barrier or a metallized region with high conductivity that eliminates the electric field. Similarly the holes follow the maximum of the valence band which, in this case, is spatially separated from the minimum in the conduction band. This “surfing” of the charge carriers can be exploited for their transportation. It was shown that optically excited electrons and holes on one end of a sample can be transported over several µm across the chip to be detected at the other end [Roc97; Als01; Als02; Cec04]. The detection is realized with a thin metal film that short-circuits the SAW and enables the recombination of the two carriers.

In low-dimensional semiconductors the electric field of the SAW can induce a tunnelling between several quantum structures as it acts similar to a constant field that tilts the bands and as a consequence reduces the width of the tunnelling barrier which in turn increases the probability of the charge to escape the confinement [See04]. The probability is highest if the low-dimensional semiconductor is aligned in the propagation direction of the SAW because the electric field is the strongest in that direction. But for low confinement it is also possible in all other directions.

Similar to the mechanical wave, the electric field can also be manipulated by a material placed in the propagation path. This time the relevant parameter that disturbs the transmission is the conductivity. A highly conductive material such as a metal completely suppresses the electric field in the metallized area. But as the mechanical movement stays unaffected the field builds up again after the treated area. Despite the recovery of the field, the suppression does not go unnoticed by the SAW. In the conductive area, electrons are moved to compensate for the electric field. This leads to an induced current with ohmic losses proportional to $\sigma\mathscr{E}^2$ in the case for a material that does have a finite conductivity. This energy is drawn from the SAW and results in a measurable attenuation of the transmitted energy.

3.5.4 Attenuation and Velocity Change

Most of the time, all three effects discussed above happen simultaneously on the substrate and can not be regarded as independent mechanisms. Material deposited on the SAW delay line has an effect on both the electrical and the mechanical part of the wave. While the attenuation of the SAW is intuitively mostly caused by losing energy through the electric field, the sound velocity of the substrate is altered by piezoelectric stiffening and thus influences the travel time through the delay line. The relative changes in velocity and the attenuation are defined as functions of the conductivity for the case of a homogeneous piezoelectric conductor [Wix89].

$$\frac{\Delta v}{v_0} = \frac{K_{eff}^2}{2}\frac{1}{1+(\omega_c/\omega)^2} \tag{3.44}$$

$$\Gamma = \frac{\omega}{v_0}\frac{K_{eff}^2}{2}\frac{(\omega_c/\omega)}{1+(\omega_c/\omega)^2} \tag{3.45}$$

Here, v_0 and ω are the ultrasonic velocity and frequency, respectively. K_{eff}^2 is denoting the piezoelectric coupling coefficient. $\omega_c = \sigma/(\varepsilon_1+\varepsilon_2)$ is the conductivity relaxation frequency with ε_i the dielectric constants of the piezoelectric substrate and the half-space above it, and σ the conductivity in the layer above the piezoelectric. This relaxation frequency is the inverse of the time the electronic system needs to relax from an external perturbation into its equilibrium state. If the SAW frequency is much lower than this, the carriers will be able to follow the alternating field and screen it. If ω is comparable or larger than ω_c the screening becomes incomplete and the electric field can penetrate the material. With increasing σ, ω_c also becomes larger, raising the value for possible non screened frequencies. The maximum attenuation is reached for $\omega = \omega_c$.

In the work presented here, the thickness d of the material under examination is very small, much thinner than the wavelength of typical SAW devices $d \ll \lambda$. Therefore, the model of a thin film is employed to approach further the real circumstances. If the conduction layer is so thin, the electric screening can only occur at the surface. Further down in the substrate material the electric field still persists. The equations above can still be used for this case, but the relaxation frequency has to be adapted to the fact that the conductivity is restricted to a very thin layer. ω_c now becomes dependent on the wave vector of the SAW $k = 2\pi/\lambda$ [Bie72; Adl71; Rid88]. The restriction of the current to the small sheet results in an increase of the effective resistance by a factor of $1/kd$ [Adl71]. Hence, the relaxation frequency is now $\omega_c = \sigma_\square k/\varepsilon_1+\varepsilon_2$ with the sheet conductivity $\sigma_\square = \sigma d$. With $\sigma_M = v_0(\varepsilon_1+\varepsilon_2)$, the relative velocity change and

the attenuation become

$$\frac{\Delta v}{v_0} = \frac{K_{eff}^2}{2} \frac{1}{1+(\sigma_\square/\sigma_M)^2} \tag{3.46}$$

$$\Gamma = k\frac{K_{eff}^2}{2} \frac{(\sigma_\square/\sigma_M)}{1+(\sigma_\square/\sigma_M)^2} \tag{3.47}$$

for $\omega \ll \omega_c$ and $d \ll \lambda$ [Wix89]. In this regime $\sigma_\square$ can be regarded as frequency independent. Figure 3.12 illustrates the relationships of the equations (3.46) and (3.47), i. e. the relative change in sound velocity and the attenuation of the SAW as a function of the conductivity and thickness of the thin layer. The characteristic conductivity σ_M is a material constant and for $LiNbO_3$ it can be calculated to $\sigma_M \approx 1.6 \cdot 10^{-6} \frac{1}{\Omega}$ with an estimate of the effective dielectric constant after Simon [Sim96].

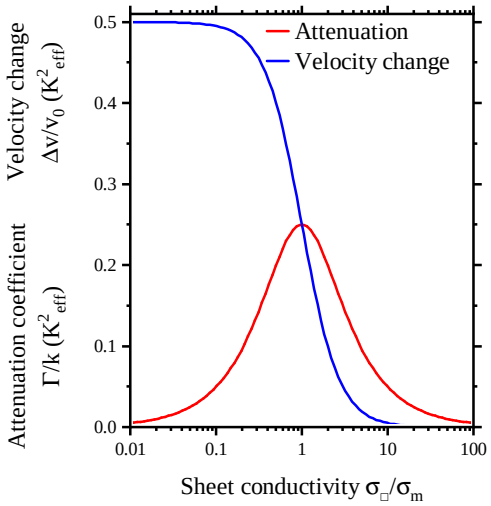

Figure 3.12: Relative velocity v/v_0 and attenuation Γ per unit wave vector k in units of K_{eff}^2 as a function of the conductivity $\sigma_\square$ in units of σ_M of a thin film placed on top of the piezoelectric substrate.

For $\sigma_\square \gg \sigma_M$, i. e. when a metallic film is deposited onto the piezoelectric substrate, the velocity change is negligible as the piezoelectric stiffening is low. The highest change occurs for $\sigma_\square \ll \sigma_M$ where the deposited material behaves like an insulator. In between, the change in velocity follows a rather step-like function around $\sigma_\square = \sigma_M$. The attenuation peaks at $\sigma_\square = \sigma_M$ where the number of charge carriers following the acoustic wave is the highest. For $\sigma_\square \ll \sigma_M$ it is proportional to the conductivity while for $\sigma_\square \gg \sigma_M$ the proportionality goes with $1/\sigma_\square$. This is consistent with the intuitive picture that an insulator would result in no attenuation but a large velocity change due to piezoelectric stiffening, while a perfect conductor with no losses would have no effect at all.

3.5.5 Mathematical Description of Drift and Diffusion

Beside the influence of semiconductors on the transmission of the SAW and the modulation of the bandstructure through the electric field, the acoustic wave also has an influence on the transport of the charge carriers inside a semiconductor. If electron and hole are free to move in

the propagation direction of the wave, drift currents can set in for large enough field strengths. For this transport in the electric field, the mobility, which is proportional to the inverse of the effective mass, is of importance as it defines the drift velocity at a given electric field for electrons and holes $\vec{v}_{e,h} = \mp\mu_{e,h} \cdot \vec{\mathscr{E}}_{SAW}$. If this velocity is significantly lower than the speed of the SAW, the particles can not follow the field and will not be affected. But if the velocity becomes comparable to the sound velocity in the medium, the charge carriers are transported by the electric field. Due to the possibly different mobilities of electrons and holes, they have to be considered separately. Moreover, in areas with inhomogeneous densities of particle types, diffusion sets in which is also dependent on the mobility as well as the effective mass of the particles: Particles with lower mass or higher mobility distribute faster along equal energy levels. In the following paragraph a derivation of the drift and diffusion equations based on [Gar04], [Sze07] and [Thu05] is presented.

If there are free particles generated in a semiconductor which are not equally distributed there will be a particle flow $\vec{j}_{diff}$ to compensate for the imbalance. This is called the diffusion, defined as product of a material- and particle-dependent diffusion constant D and the spatially dependent particle density $\rho(\vec{x})$ in the Poisson equation shortened by the use of the Nabla operator $\nabla = \left(\frac{\partial}{\partial x_1}, \frac{\partial}{\partial x_2}, \frac{\partial}{\partial x_3}\right)$.

$$\vec{j}_{diff} = -D\nabla\rho \tag{3.48}$$

For charged particles there is an extra current $\vec{j}_{drift}$ resulting from the electric field $\vec{\mathscr{E}}$.

$$\vec{j}_{drift} = \rho \cdot \vec{v}_{drift} = \mu_i \cdot \rho \cdot \vec{\mathscr{E}} \tag{3.49}$$

If there is no net increase or decrease of particles, the continuity equation holds and the temporal change of the overall particle current has to equal the spatial change for each charge carrier species on its own.

$$\begin{aligned} \frac{\partial n}{\partial t} &= D_n\nabla^2 n + \mu_n\nabla(n \cdot \vec{\mathscr{E}}) \\ \frac{\partial p}{\partial t} &= D_p\nabla^2 p - \mu_p\nabla(p \cdot \vec{\mathscr{E}}) \end{aligned} \tag{3.50}$$

These two equations describe the distribution of charge carriers n and p under the influence of an electric field. The diffusion constants can be calculated from the Einstein relation $D_{n,p} = \mu_{n,p} \cdot k_B \cdot T/e$ with the Boltzmann constant k_B and the elementary charge e [Sel84]. In order to describe real experiments, the generation and annihilation rates have to be included additionally. In the model the initial creation of electrons and holes is solely determined by the excitation pulse of a laser. The recombination of the two charge carriers first results in a bound state, the exciton, which then decays with a certain probability, sending out a photon or dissociates back into an electron and a hole. The exciton is a neutral quasi-particle that can in good approximation be assumed to be unaffected by the electric field and thus undergoes only the diffusion process. As it is polarizable, it could be influenced by an inhomogeneous electric field, but this second-order effect is neglected in this study here.

Via the drift and diffusion equations coupled with the Poisson equation of electrons, holes and excitons, the SAW-induced movement can now be calculated. For simplicity, it is assumed that the particles can only move in the xy-plane parallel to the surface which is the case for carriers in a thin film deposited on top of the substrate. Moreover, the excitation of electrons and holes will be taken as uniform along the y-direction which is in the plane, but perpendicular to the propagation direction of the SAW. These assumptions are fairly realistic for the quasi one-

dimensional nanostructures examined in this work and reduce the problem to a one-dimensional calculation which helps lower the complexity of a computational implementation.

$$\begin{aligned}
\frac{\partial n}{\partial t} &= D_n \frac{\partial^2 n}{\partial x^2} + \mu_n \frac{\partial (\mathscr{E}_x \cdot n)}{\partial x} + G - R + T \\
\frac{\partial p}{\partial t} &= D_p \frac{\partial^2 p}{\partial x^2} - \mu_p \frac{\partial (\mathscr{E}_x \cdot p)}{\partial x} + G - R + T \\
\frac{\partial X}{\partial t} &= D_X \frac{\partial^2 X}{\partial x^2} + R - \frac{X}{\tau_X} - T
\end{aligned} \tag{3.51}$$

n, p and X are the numbers of electrons, holes and excitons, respectively. $\mathscr{E}_x$ denotes the electric field in x-direction, and G the generation rate of free charge carriers produced by the laser. The recombination rate can be approximated for low concentrations of charge carriers with $R = c_X \cdot n \cdot p$ [Sin03] describing the generation of excitons with c_X being the probability of an exciton creation. The inverse process is denoted by T, the ionization rate of excitons via tunnelling, and breaks down to almost zero for low temperatures in the absence of an electric field. Another way of losing excitons is by radiative decay with decay constant τ_X and the creation of a photon γ. If the decay is multi-exponential, there exist several decay terms in the equation. With an applied electric field the process can not be neglected as the field pushes the two carriers into opposite directions and thus promotes their spatial separation.

There are two contributions to the electric field $\mathscr{E} = \mathscr{E}_{SAW} + \mathscr{E}_{ind}$: the external part, which is generated by the SAW, and an induced part that arises from the displacement of electrons and holes. For $\mathscr{E}_{SAW}$ only the longitudinal part of the SAW's piezoelectric field is considered for the one dimensional calculation and is expressed as

$$\mathscr{E}_{SAW}(x,t) = \mathscr{E}_0 \sin(kx - \omega t + \varphi) = -\nabla \phi_{SAW} \tag{3.52}$$

where $\mathscr{E}_0$ is the amplitude of the oscillating field, and k and ω are the wave vector and the frequency, respectively. The second contribution to the electric field is the field induced by the separation of electrons and holes, calculated via the Poisson equation:

$$\frac{\partial \mathscr{E}_{ind}}{\partial x} = \frac{e(p-n)}{\varepsilon} \tag{3.53}$$

with the elementary electric charge e and the dielectric constant ε.

For the transport of charged particles, the resulting electric field has to overcome a threshold which depends on the drift velocity $v_i = \mu_i \cdot \mathscr{E}$ ($i = n,p$ for electrons and holes, respectively). If this is comparable to the speed of the surface acoustic wave, the charge carriers can be transported.

$$\mathscr{E}_{crit,i} = \frac{v_{SAW}}{\mu_i} \tag{3.54}$$

For absolute fields being higher than the critical value, the charged particles are transported. This happens at the phase during the cycle which exceeds the critical value at first. This means that for a field that reaches exactly the critical field, there exist two points during one period of the sinusoidal wave where the critical field value is reached. The two points differ in their sign and thus, in the direction they point to, meaning that only at one of them the force on the

electron points towards the propagation direction of the SAW. At increased acoustic power, the critical value of the electric field is lower than the extrema and there exist four possible points with the critical field strength. Analogous to before, only two of them have to be considered as at the other two, the force points in the opposite direction. Of the two transport points, only one is stable where slightly delayed electrons are accelerated more, while electrons slightly ahead experience less force. At the other point it is vice versa and hence, unstable. Analogous considerations can be applied to the transport of holes. The transportation points of both charge carriers are shifted from the extremum of the field at $\mathscr{E} = \mathscr{E}_{crit}$ towards the zero crossing when the field strength is increased. As the onset of transportation depends on the mobility of the charge carrier, it can be different for electrons and holes. But at high enough fields, when both charge carriers are significantly mobile, their transportation happens with a phase shift of around 180°, suppressing an efficient recombination.

The mathematical description of the charge carrier dynamics presented in this section is the basis of the simulation used in section 5.3 to calculate the mobility of examined semiconductors. The numerical solution to the coupled differential equations (3.51) is performed with the finite element method in an explicit way.

The practical implementation of these calculations was performed by F. Schülein in his PhD thesis [Sch14b] and were modified for the purposes of the new perovskite materials in focus here.

Chapter 4

Experimental Methods

For the SAW investigation on nanowires, two different setups were used. Either the behaviour of excitons and free carriers in the nanostructure is recorded as a reaction to the surface acoustic wave (section 4.1) or the change of the SAW transmission due to the presence of excited carriers in nanostructures in the propagation path is probed (section 4.2).

For both, standard optical characterization setups were used and combined with electrical circuits for the application and detection of the SAW. For the first kind of studies a μ-PL setup was combined with the electronic extension. This chapter describes the basic layout including the electric excitation of a SAW which influences the nanostructure that was in turn excited by a laser. The signal emitted by the investigated structure is then collected and its wavelength- and time-resolved behaviour are analysed. Despite the exact positioning of the laser to target the relevant nanostructure with an accuracy below 1 µm, the correct timing of all components plays a major role and constitutes a challenge. The temporal alignment of SAW, laser and possibly detector has to be well adjusted to enable the established method of phase-resolved correlations [Völ11]. This setup also opens up the opportunity for either time-integrated but energy-resolved detection or time-resolved detection at a fixed energy. Both methods give different insights into the properties and dynamics of the investigated system. Further varying the temperature from room temperature to lower temperatures can in both cases reveal the effects of additional thermal energy deposited in the system. In the spectral analysis, the temperature has an influence on the central emission wavelength, as well as on the broadening of the luminescence. In time-resolved studies one can observe that the temperature changes the lifetime as the excess energy of the particles is largely determined by the kinetic energy.

The second type of studies is also based on μ-photoluminescence (μ-PL), but has significantly different requirements on the setup and is missing the detection of the luminescence. Now, the synchronization is not important any more as the time scales considered are on a larger scale and thus phase integrated investigations can be performed. The major condition is a flexibility in the wavelength of the laser over a broad range of around 540 nm to 750 nm without a gap to be able to probe the absorption edge of the material. Furthermore, the detection of the SAW becomes relevant for probing the influence of conductive material on the transmission of the acoustic wave, requiring a second IDT forming a delay line together with the first one and instruments detecting the received signal.

4.1 μ-Photoluminescence Measurements

The well established μ-PL setup is widely used for optical characterization of small structures. It is commonly used to probe the electronic structures and influences of various kinds of

semiconductors across a range of temperatures. lifetime studies can be conducted as well as photonic correlations and recombination processes. The basic design is very flexible regarding the combination of lasers, optical filters and detection methods. The combination with the SAW enables the contact-free probing of the influence of strain and electric fields or can be used as a manipulator to tune nanostructures, e. g. to energetically align them with other components of a device. On the other hand, the field of the SAW can be applied as a tool to examine the electronic properties of a material such as the mobility of both charge carriers or the directionality of their transport.

The integration of electrical components into the standard μ-PL setup is limited by the introduction of radio frequency capable cables into the vacuum chamber of the cryostat. All other aspects of the design are fairly standard and will be explained in detail in subsection 4.1.1. The already mentioned synchronization process is the focus of subsection 4.1.2 which also deals with the phase locking and the resulting possibility of phase-resolved measurements. Detailed information about the temporal dynamics are obtained with time-correlated studies, described in subsection 4.1.3. The recorded dynamics are aligned with respect to the laser pulse and are imprinted by the SAW and thus are very sensitive on the correct synchronization and phase locking.

4.1.1 Basic Experimental Setup

The standard μ-PL setup with all its components is illustrated in figure 4.1 and can be divided into several different parts which are indicated by the dashed boxes. The excitation with an above-bandgap laser (a) creates electron-hole pairs inside the nanowires, explained in section 2.3. A helium flow cryostat (b) gives the opportunity to place the sample in a vacuum and cool it down to 4.2 K. The light emitted by the radiative recombination process in the nanostructure can be recorded and spectrally analysed with a spectrometer (d). The PL recordings give insight into the wavelength and intensity of the probed light. The temporal evolution can be recorded with a single photon avalanche diode (SPAD). In addition, to probe the influence of the SAW, the high frequency instruments are connected to the cryostat. In the following, the optical setup to excite, manipulate and detect the light emitted from the nanowires and the technical integration of the SAW are explained.

The excitation (a) includes the above-bandgap, fibre-coupled laser (7) LDH-D-TA-530 or free space laser LDH-P-C-405 from *PicoQuant* which provide short 532 nm or 405 nm pulses with a width below 120 ps at a variable repetition frequency from 10 Hz up to 80 MHz. It can be triggered externally by a controller which will be relevant for the next section to synchronize all instruments. The beam path is illustrated in green to separate it from the detected light, indicated in red. The fibre-coupled laser (7) is collimated by a coupler (8) to fit into the free space designed optical setup and is guided with mirrors (9) towards the sample. A power wheel (10) with a variable neutral density filter provides up to two orders of magnitude stepless attenuation on the laser power. This method is superior to an adjustment of the diode current because a change in the electronic power could influence the pulse's shape and duration [Pico]. The light is then split by a 50:50 beam splitter (11) towards a power meter (12) to record the actual power even during a measurement and towards the microscope on top of the cryostat.

Figure 4.1 (b) schematically illustrates the interior of the microscope. With an additional beam splitter (13) that separates the incoming from the outgoing light, the exciting laser beam is reflected to pass a 50$\times$ objective that focuses it onto the sample (1). The resulting spot size is (1.6 ± 0.2) µm determined by reflection measurements on metal-coated areas on the sample.

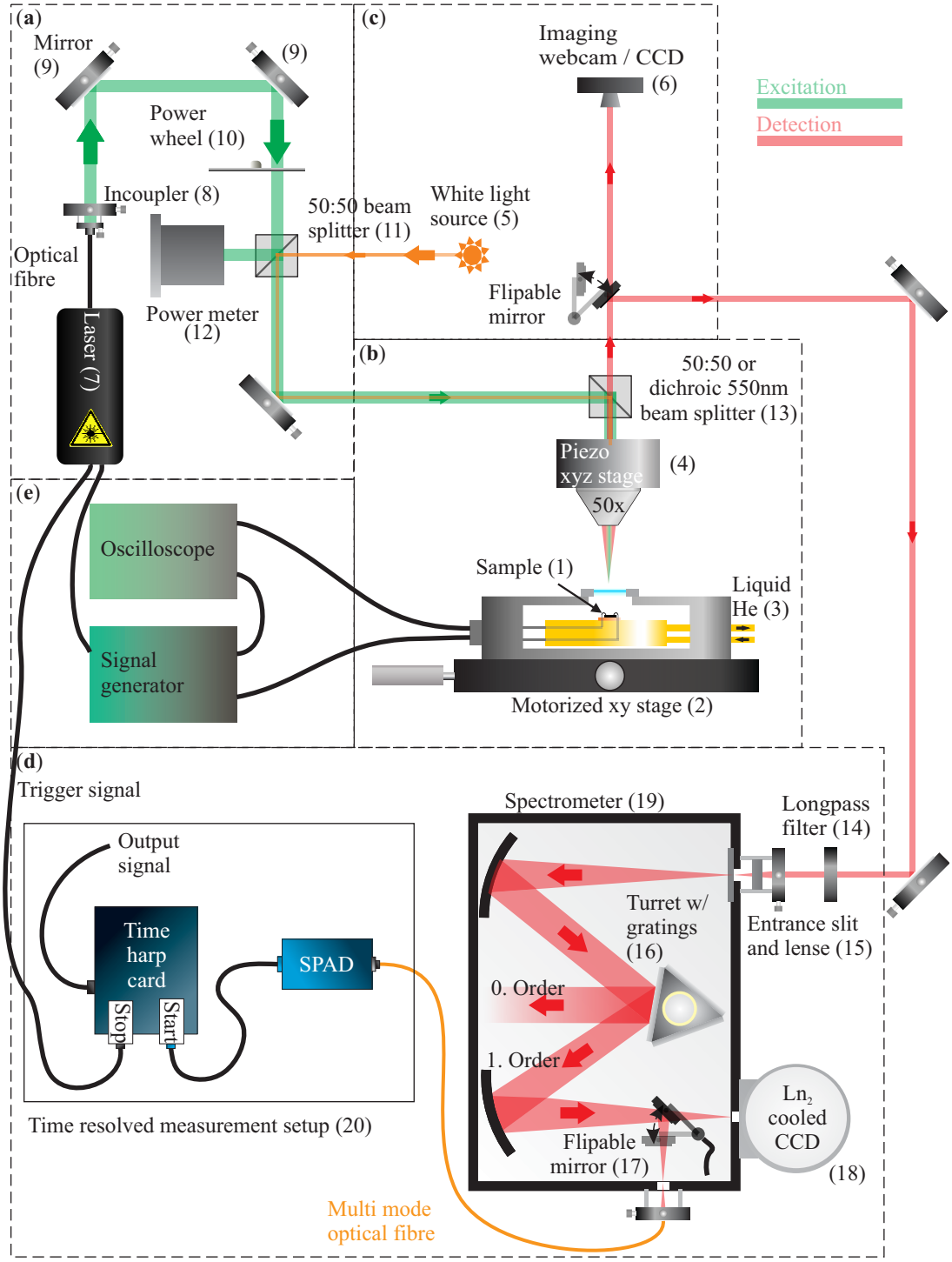

Figure 4.1: Components of the basic setup for μ-photoluminescence measurements combined with the electrical instrumentation for the SAW. (**a**) Optical excitation of the nanostructures with a diode laser. (**b**) Alignment and focus of the excitation and detection on the chip in a liquid helium cryostat. (**c**) A white light LED and a webcam or a CCD are used to image the sample and to guide the alignment. (**d**) Detection of the emission signal from the nanostructures with spatial, temporal and energy resolution. (**e**) Generation and detection of the high frequency SAW signal.

A liquid helium flow cryostat (3) provides the ability of investigations in vacuum and at low temperatures down to 4.2 K but is also capable of handling experiments at room temperature and slightly above with an integrated heater of 50 W. The cryostat is equipped with a motorized stage (2) for coarse movement of the sample. The fine tuning of the laser and detection position as well as the focus is done by open loop piezoelectric motors (4) of the series TRITOR 102 from *PiezoJena*. The beam splitter at the top of the microscope (13) can be varied between a normal 50:50 and a dichroic one with a cut-off wavelength of 550 nm. The latter can be used to increase both the laser power deposited on the chip and the amount of light that is detected. The dichroic beam splitter has a reflective coating that increases the reflectivity for wavelengths above 550 nm. So these wavelengths are reflected to almost 100 % while all other are transmitted. The downside of using this beam splitter instead of a simple 50:50 one is the more complicated alignment as the backscattered laser light coming from the sample is again reflected at the beam splitter and not transmitted to the imaging optics. But this effect in turn can be exploited to filter out the laser of the photo-detection and replace the extra longpass filter (14) before the spectrometer.

The imaging (c) of the sample used for aligning the laser spot to the correct position consists of a white light LED (5) and a webcam or a charge-coupled device (CCD) (6). For increased signal a flippable mirror changes between collecting the signal in the imaging optics and guiding it towards the more elaborate detection instruments. The actual analysis of the collected light is performed by the instruments in (d). A 520 nm longpass filter (14) in the detection path blocks the laser light and hinders it from damaging the liquid nitrogen cooled Si CCD (18). The remaining beam is focused at the entrance slit (15) of a SpectraPro 2500i spectrometer (19) from *Acton Research* with a focal length of 0.5 m. In the inside, different gratings (16) can be used to spectrally split the light with different resolutions and efficiencies. For the studies presented in this thesis gratings with 1200 lines/mm and a blazing wavelength of 500 nm or 750 nm were used. A flippable mirror (17) can be inserted into the beam path inside the spectrometer to direct a small spectral region of the light into a multi mode fibre connected to a SPAD (20). Every time a photon hits the detector, a pulse is sent to the time harp card which correlates its arrival time with a trigger signal from the laser controller and calculates the time delay for exactly this photon. A collection of these time stamps for many photons demonstrates the temporal decay of the photoluminescence in form of a histogram. An example will be shown and explained in subsection 4.1.3.

So far, the setup is fairly standard and used in many scientific experiments for the analysis of luminescence in various different materials. The singularity of the setup used here consists of the integration of the SAW components. The cryostat has additional high-frequency electric cables that lead from the sample holder to the outside for connecting the instruments. The cables are additionally connected to the cold finger to reduce heat intake from the surroundings. The signal generator is used for applying an electric signal in form of a sinusoidal wave to the IDTs on the chip. The SAW can be detected with an oscilloscope which uses a trigger from the signal generator as time base. The trigger is also fed to a delay generator that controls the emission of the laser in order to be able to temporarily shift the laser emission in relation to the SAW signal. If both are modulated with a rectangular function, the delay generator can be used to align the time windows of both signals to match at the excitation of the nanostructure.

A sample time-integrated PL spectrum recorded with the liquid nitrogen cooled Si CCD behind the spectrometer is shown in figure 4.2. The grating transforms the energy distribution of the light into a spatial distribution which is detected by the Si CCD which has a resolution of 2048×512 pixels. Through a calibration, the pixels in the x direction are assigned to a specific

wavelength depending on the tilting angle of the grating. The spectrum shown here is taken from a GaAs nanowire without any SAW applied. This nanowire's data will be used throughout the chapter to explain the experimental details and the specifics of the recorded data. The in-depth interpretation of the data is left out here and can be found in [Son20] as it is not in focus of this thesis.

The spectrum exhibits three distinct peaks arising from different bandgaps in the electronic structure inside the nanowire. The heterostructure is nicely reflected in the μ-PL data. The broad core in the middle of the hexagonal wire follows the bulk-like emission at 820 nm. It is surrounded by a layer of AlGaAs which forms a barrier to a very thin layer of GaAs capped by another layer of AlGaAs. The thin GaAs in between the two areas with higher bandgap forms a quantum well (QW). Due to inhomogeneous growth the thickness varies along the nanowire and also between the side facets of the hexagonal structure. As the energy of a two dimensional quantum layer, this means with a one dimensional confinement, depends inversely on the square of the thickness, a small change will result in measurable energy shift. The two left peaks in the spectrum show two different side facets with different thicknesses at the same position of one nanowire.

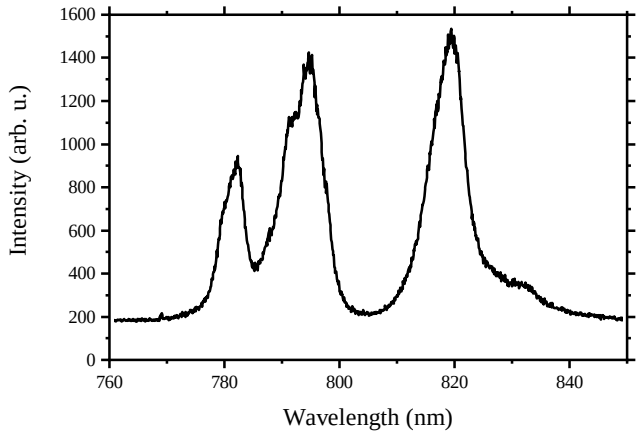

Figure 4.2: Time-integrated PL-spectrum of GaAs nanowires recorded in a standard μ-PL setup showing two peaks of interconnected radial QW structures and one of the inner core. The 200 counts offset are the noise background of the detector and are constant for all measurements.

In this way, the standard μ-PL setup can already give insight into the basic band structure of a material whose charge carrier undergo radiative decay. These investigations can then be performed at different conditions like the temperature or the population density through the laser power or in this thesis, at varying electric field.

4.1.2 Synchronization and Phase-lock

To reduce the heat intake of the SAW and additionally prevent too much interference of reflected beams at IDTs or sample edges, the wave is modulated in time. Only an about 1 µs long pulse is excited every 50 or 100 µs. This significantly lowers the heating of the substrate and with a synchronized timing of the laser excitation it can ensure that only the primary pulse of the SAW is taking part in the recording. But this also complicates the setup: The pulsing of the laser needs to be modulated now as well to prevent background PL-signal from the nanostructure that is not affected by the SAW. Thus, a time window of 800 ns for the laser is introduced and its

synchronization with the SAW pulse has to be conducted. The signal generator producing the electric pulses for the SAW sends out a reference signal at the beginning of every time window during which the output is turned on. This trigger signal is fed through a delay generator which adds a rectangular pulse with the width of the desired laser window and is capable of adding a delay with sub-nanosecond precision. Afterwards, the rectangular pulse is multiplied with a sinusoidal wave and used as external trigger input of the laser controller. It is important to use the delay generator to synchronize the arrival of the laser pulses to exactly the time when the SAW pulse reaches the NW. This variable delay is needed mainly to compensate for the slow acoustic velocity of the Rayleigh wave in the piezoelectric material. The coarse delay can be estimated by the distance of the point of measurement from the IDT which is approximately known due to markers along the delay line. In theory all other delays would have to be considered, too, but the signal travel time in the cables, the trigger delay of the laser controller and temporal uncertainty of the light pulse generation are all on the order of 50 ns which is negligible for a SAW pulse length of 1000 ns. If these delays are of importance, it is easier to perform a time-correlated measurement (c. f. subsection 4.1.3) and adapt the delays according to the result.

To get more insight into the temporal dynamics of a process, a time alignment has to be introduced and all instruments have to be adapted to it. This includes not only the overlapping of the time frames where the SAW or laser are on, but also a synchronization of the frequencies of both. For this purpose, the frequency of the SAW has to be an integer multiple of the laser frequency. Additionally, the lasing frequency has to be divisible by the frequency of the amplitude modulation of SAW and laser. For the SAW with its varying electric field, it is especially important to lock the excitation of the laser to a specific phase of the wave to correlate the recorded behaviour to the applied electric field.

In order to make sure that the time scales of all the different instruments are the same, they are temporally coupled via a clock reference signal of 10 MHz. Through multiplication and division of integers, the instruments generate all their internal frequencies. This implies that every multiple of a frequency $n \cdot f_0$ at the SAW frequency generator is stable in comparison to f_0 at the laser signal generator. The integer n accounts here for the number of SAW periods between two laser pulses. For the experiment shown in figure 4.4, a SAW frequency of $f_{SAW} = 194\,\text{MHz}$ is used together with a laser of $f_{laser} = 19.4\,\text{MHz}$. Thus, the laser pulse hits the sample only at every tenth SAW period. This ensures in slow decaying processes that the excitons and free charge carriers in the nanostructures all recombine back to the ground state before the next laser pulse is applied.

In the phase locked case, the laser pulse has a fixed relation to the phase of the SAW. This relation is sketched in figure 4.3 to illustrate the principle. This fixed phase difference between the two signals, where one arbitrary but fixed position of the SAW cycle is used as a reference, is denoted as relative phase φ. Through a variation of this relative phase in the same experiment, it is possible to probe the behaviour of different SAW phases in a stroboscopic measurement. For every phase φ a time integrated spectrum or a time-resolved histogram is recorded where the laser hits the nanostructure always at exactly the same phase φ_0 of the SAW. For the next recording this phase is changed to $\varphi = \varphi_0 + \delta$ and stays fixed for the complete study. In this way the dynamics induced by the SAW can be probed even in time integrated experiments. Without the coupling of the phases, they would drift away and a measurement would be an average over all relative positions. The aforementioned GaAs nanowires, for example, show an intensity modulation dependent on the electric field at the moment of excitation. This behaviour is illustrated in figure 4.4 which shows the intensity of the PL as a function of the relative phase

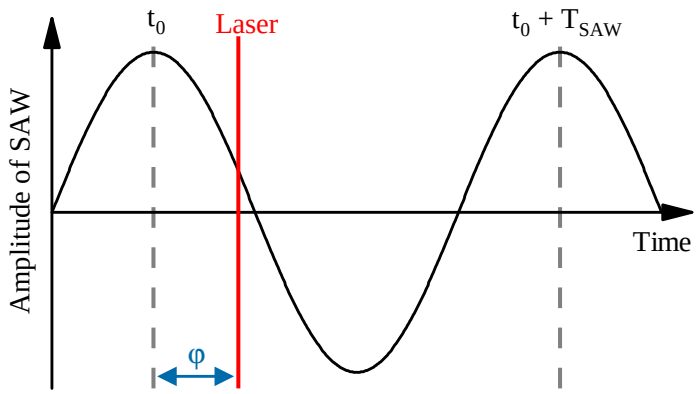

Figure 4.3: Definition of the relative phase φ as difference between an arbitrary but fixed phase of the SAW and the laser excitation point in time. The φ can be varied to probe the effects of different SAW phases at the excitation.

of the sinusoidal function of the SAW at the moment of the laser excitation. The intensity resembles the sinusoidal variation of the electric field of the SAW and reflects the drift of the electrons away from the static holes. Depending on the electric field direction and strength, the overlap of electrons and holes persists for a shorter or longer time and thus the emission intensity from recombination processes varies with the phase of the wave. Without the phase lock, the number of photons from recombinations would be different for each laser pulse and would average for the study to a relatively constant value.

In practice the variation of the relative phase is performed by slightly delaying the trigger for the laser pulse. It is generated by a sinusoidal wave from a signal generator and its phase can easily be tuned which then results in a time shift of the zero-crossing of the electric signal. A phase shift of 360° or 2π is delaying the laser by exactly one period and results due to the periodicity in exactly the same setting as 0°. It is also possible to change the phase of the SAW generator. In principle this is the same, but one has to take into account that this shifts the delay between the two signals in the other direction.

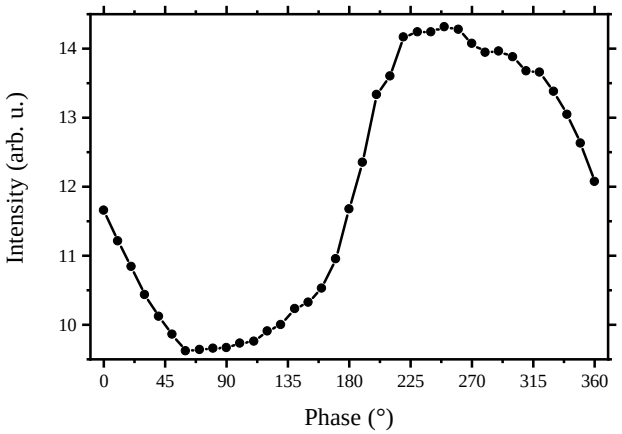

Figure 4.4: Integrated PL intensity for one emission peak in the spectrum of a GaAs nanowire at varying starting phases of the SAW. The time of excitation during a full SAW cycle clearly matters as to how many charge carriers can recombine and decay into a photon.

In a type II band modulation, which is impinged on the semiconductor by the SAW (c. f. subsection 3.5.3), the height of the bandgap itself stays the same over the whole structure, only the absolute values of the bands at different positions are affected. This means that the wavelength of the emitted light from the radiative decay stays the same, but the intensity is changed. As a consequence of the high effective mass of holes in GaAs, these stay unaffected by the field strength of the SAW because their drift velocity at the applied electric fields stays too small to follow the movement of the wave at these high frequencies. Thus, the holes can be assumed to be static and only the electrons with a much lower effective mass are transported in this system which makes it a perfect material to demonstrate the importance of the phase locking between SAW and laser.

The resolution of the phase locking is determined mainly by the size of the laser spot. The locking of the two frequencies works perfectly well thanks to the phase-locked loop and is stable over many hours. The diameter of the laser spot on the sample was determined to be (1.6 ± 0.2) µm for an excitation with the 532 nm fibre-coupled laser. The frequency of the SAW of 200 MHz to 450 MHz results in wavelengths from 8 µm to 20 µm. Thus, in the worst case only five laser pulses placed next to each other fit in the spatial length of a SAW period. The phase resolution of the measurements accounts then to values between 72° and 29°. Under these circumstances it is not reasonable to use frequencies above 1 GHz or equivalent below 3 µm for phase-resolved studies.

In experiments where the exact phase of the SAW should be probed, it is important to have decay times of at least one order of magnitude smaller than the period of the SAW. But for the investigations presented in the following chapters, the temporal resolution of the phase locking in comparison to the decay times does not play a role. It is exploited that the lifetimes of perovskite nanowires are much larger then the period of a SAW and the dynamics of many wave cycles can be imprinted on the decay function of the nanostructure.

The phase locking is also very useful for time-resolved investigations which will be explained in the next subsection. Through this method, the aforementioned temporal dynamics induced by the SAW onto the charge carriers inside nanostructures can be made visible. But the long integration times and thus many cycles needed for time-resolved experiments require a long time stable phase locking.

In order to be able to record these dynamics, the time-resolved recorder, the time harp, also needs to be synchronized to the time windows of the two other instruments. Basically, it is triggered by the same signal as the laser controller. By modifying the cable lengths, small adjustments of several 10 ns of the delay between the experiment and the time-resolved recording can be made. If longer delays are needed, it is more feasible to introduce another delay generator and to adjust the triggering time in fixed steps. This adaptation is especially relevant to shift the starting point of the decay to the beginning of the time frame. Otherwise the reference from the trigger signal could arrive at the time correlation instrument right in the middle of a decay due to different internal delays and cable lengths, thus splitting the display of the decaying function into two parts.

4.1.3 Time-Correlation – Single Photon Counting

The time-correlation describes the temporal evolution of a signal – it correlates the signal to the time. In order to be able to record the precise point in time of the arrival of e. g. a photon, the rate at which particles hit the detector have to be small. This is why it is often called single photon counting. In the case of a PL decay, the emission signal is correlated with the trigger

signal of the pulsed excitation laser. Through multiple repetitions of the same experiment, one can lower the emission rate of the investigated structure to enable single photon counting, but still receive enough counts to observe the temporal evolution of the decay. This then shows the decay dynamics in temporal relation to the excitation. The photons from the sample are spatially separated according to their wavelength by the grating and subsequently coupled into a multimode fibre at the side exit of the spectrometer. The light is then guided to a single photon counter like a SPAD, also referred to as a Geiger-mode avalanche photodiode.

The operating principle of such a device is based on the internal photoelectric effect of one photon hitting a p-n junction in reverse bias mode and the impact ionization of the created electron and hole [Fis18]. The photon generates two charge carriers which are accelerated to high kinetic energies above the ionization energy of the material (here: silicon) through a large potential and liberate further carriers on their way. This process repeats itself until the cloud of particles passes the anode or cathode of the high voltage source. Through this mechanism, the number of carriers is growing exponentially to a large number in a very short time. But the process also defines the output pulse width of the instrument which is stated to be 10 ns for the *Perkin Elmer* Single Photon Counting Module that was used in the experiments. Together with the recharging process, the total dead time, which is the minimal time needed between two events to be able to detect them both as individual counts, sums up to 22 ns. This means that per event at the nanostructure, thus per laser pulse, only one event can be registered. In total the theoretical maximum count rate is 37 Mc/s. A much lower value should be aimed for to maintain a low probability of registering more than one photon per excitation pulse. If the number of photons per cycle were typically grater than one, the SPAD would often register the first photon, but miss the next one. The result would be an underrepresentation of later events and thus a shortening of the apparent decay times. As a rule of thumb only around 1 to 5 % of the excitations should result in a photon at the detector in order to get real single photon statistics [Pico]. In addition, the time correlation module Time Harp from *Pico Quant* can only handle up to 2 Mc/s in average.

The current pulse created by the SPAD can then be detected by the time harp which compares it to the trigger signal it receives from the laser controller. A repetition of this process plotted in a histogram reveals the temporal dynamics of the examined process. The time slot width provided by the instrument can be varied, but the number of bins is fixed to 4096. So a reduction of the width to the minimum of 33 ps limits the time window where events can be registered to 135 ns. For larger binning this time can be increased up to 4.3 µs. The minimal decay time that can be resolved is limited by the instrument response function (IRF) and the width of the laser pulse. Here the instrument's limit is around 350 ps while the laser has a FWHM below 120 ps. If the time scales to examine are in the range of the IRF, a reference function with the laser is recorded and can later be deconvoluted from the recorded signal to get the real temporal dynamics. In this way, lifetimes of the order of $1/10$ of the IRF width can still be resolved [Pico].

The decay of an exciton is a statistical process and follows an exponential curve. In order to record it, the excitation has to be performed with a pulsed laser. The decay constant denotes the inverse of the time after which the signal has dropped to $1/\mathrm{e}$ of its original value. Such studies are displayed in figure 4.5 for two different channels inside a nanowire and for different relative phases of the laser excitation. The first panel shows the unperturbed emission of these two channels revealing their non-monoexponential decaying nature and their correlation. From a certain point in time ($\approx$ at 1.5 ns) one channel's decay rate increases while the other one's decay is slowing down. This indicates a crosstalk of the two channels where one is leaking

charge carriers into the other one and thus slowing down the other's decay process and fastening its own.

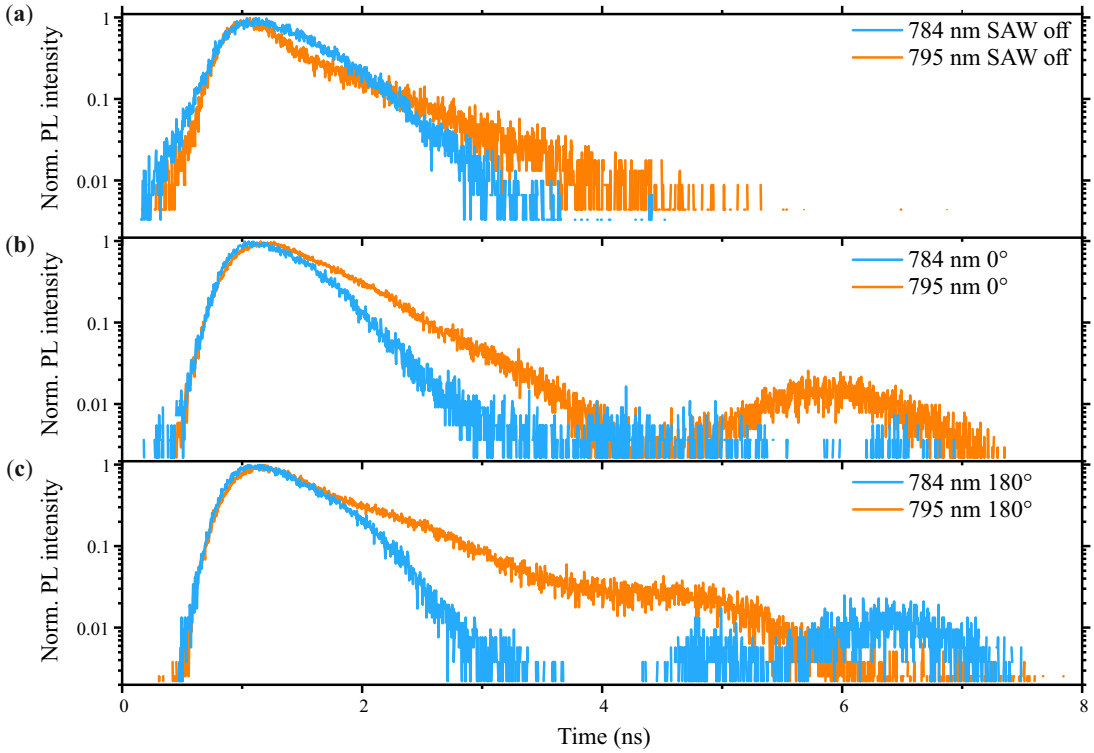

Figure 4.5: Temporal evolution of two decay channels of excitons in QWs of different thickness in a radial heterostructured GaAs nanowire. The plots are presented in a semi-logarithmic scale. (**a**) The unperturbed decay reveals a crosstalk between the two channels. (**b**) and (**c**) show the importance of the synchronization between laser, SAW and time-resolved detector to reveal the changing temporal dynamics depending on the electric field at the point of excitation.

The detection of the photons arising from the recombination of excitons in the nanostructure allows a deep insight in the underlying processes and dynamics of electrons and holes. The data recorded can be used to extract the lifetime of excited carriers and can reveal the existence of more than one decay process. In this case, by comparing the emission of two different emission centres which differ by their energy gap, and thus their wavelength, the change in the decay can be attributed to crosstalk. The biexponential decay of the two QW structures results from a charge carrier transfer from the higher energetic system to the lower one. It is modelled by the sum of two exponential systems with different decay constants. This is a clear indication that the two processes feed from different reservoirs [Pra04]. If this were not the case, one could define an effective decay constant as the reciprocal sum of the single process constants.

The charge transfer can even be triggered and reversed on a sub-nanosecond time scale with the acousto-electric effect. By applying a SAW with $f_{SAW} = 194\,\mathrm{MHz}$ an $P_{SAW} = 18\,\mathrm{dBm}$ on these nanowires transferred on a $LiNbO_3$ subtrate with predefined IDTs, SAW-driven dynamics can be induced. Figure 4.5(b) and (c) demonstrate the influence of the SAW on the temporal evolution of the decays shown in (a). The difference between the two is the relative phase of the SAW at the excitation point of the laser as explained in the previous subsection. Through the gyrating electric field in the sagittal plane photoexcited excitons are dissociated and dynamic

motion is induced. In the system presented in this section, the holes are quasi-static due to their higher effective mass and lower mobility. The SAW-driven dynamics of the electrons lead to their depletion and reinjection into the emission region where the free holes still remain. This change in the overlap of free electrons and holes causes an increased or decreased optical signal with a temporal modulation of the total decay rate. For two spatially overlapping QWs, the dynamic can even drive the charge carrier to the other QW. The corresponding temporal evolutions of the decays are shown in figure 4.5(b) and (c) and exhibit clear anticorrelations. At a phase shift of π the reoccurring emission around 6 to 6.5 ns switches from one to the other. This is a result of the electric field pointing towards the other direction and pumping the electrons either towards the higher energetic system or the lower energetic one. A detailed analysis of this and more data on the radial-heterostructured nanowire can be found in [Son19; Son20].

These anticorrelations are only clearly visible in the time-resolved investigations as their appearance in a time integrated, spectral recording shows only a slight shift in the intensities of both channels. The main intensity still comes from the emission right at the beginning of the decay. In the time integrated study these can not be distinguished from the later occurring events and the oscillation of the emission intensity is only averaged.

4.2 SAW-Based Absorption Detection

The second type of setup that is relevant in this thesis is depicted in figure 4.6 and is used to investigate the effect a conductive layer above the piezoelectric substrate has on the propagating SAW. Instead of detecting the PL of the excited excitons, the reduction in the amplitude of the SAW is recorded when the semiconducting layer is illuminated with laser light. To this end, the transmitted SAW is recorded with and without optical excitation. The attenuation and the phase shift of the wave correlate with the conductivity of the system (see subsection 3.5.4). The principle behind this measurement is a result of the current produced by the electric field operating on the free electrons in the system and the resulting ohmic losses [Wix89]. This effect can be exploited to study the absorption edge of a material as charge carriers are only excited with illumination above the bandgap. A necessary prerequisite of these kinds of recordings is a detection of the transmitted SAW by a second IDT in the travelling path behind the material to probe. Then it is possible to study the attenuation of the SAW and its dependence on excitation wavelength and power as well as the deposited material.

The combination of optical excitation and electrical detection is implemented through a basic setup similar to the one described in subsection 4.1.1. But here, the detection is limited to verifying the excitation wavelength and the emission from the recombination inside the material is neglected. Another new aspect is the excitation source: a supercontinuum laser is used to tune the wavelength over a broad range from visible to near infrared. All the components and their integration are described in subsection 4.2.1 before subsection 4.2.2 emphasizes possibilities of wave generation and detection. The last part then covers the analysis and interpretation of the obtained data.

4.2.1 Basic Experimental Setup

Though the basic instruments and their arrangement resemble the μ-PL setup, the arrangement designed for photoconductivity absorption investigations has a different focus. While the laser

energy in the μ-PL studies normally is not of great importance as long as it is above the bandgap of the material to examine, it is essential for absorption edge investigations to be able to tune the laser over a broad range of wavelengths during one set of recordings. Hence, a *NKT Photonics* SuperK EXTREME supercontinuum laser was used in figure 4.6(a) (4) whose output can be switched between visible and infrared. The principle of supercontinuum light generation relies on short high power pulses from a pumping laser sent through non-linear media in a photonic crystal fibre (5). This implies that the temporal coherence is very low, but the spatial coherence remains high. As the output is not monochromatic, it can not be called an actual laser, but this light source can maintain single mode beam characteristics and excellent spatial coherence while reaching the brightness of a laser. The wavelength range of the SuperK EXTREME is 500 nm to 1800 nm with a total output power of 5 W. This light source perfectly fits the requirements of this setup. It can be filtered coarsely with a free grating and a pinhole resulting in a spatially and energetically broad illumination of the sample or it can be fine tuned with a monochromator (7) and an optical fibre to result in higher wavelength resolution but also lower excitation power. Figure 4.6(b) generically depicts the selection of a wavelength with the monochromator. The light from the supercontinuum source is focused with a lens onto the entrance slit and illuminates a grating (8) that converts the spectral information into a spatial separation. The wavelength that is leaving the monochromator through the exit slit can be chosen by the angle of the grating. It is then sent through a multi mode fibre (9) to lower the divergence of the beam. The light is focused by an 5 $\times$ objective (3) onto the sample (1) which is mounted on a triple stage (figure 4.6(c) (2)). For the illumination of the whole sample with high power, red and blue high power LEDs could also be used. A use of the cryostat or even the vacuum is not necessary here as the investigations are all performed at room temperature and atmospheric pressure. The examined perovskite structures are fully functional under ambient conditions. The main detection is all-electrical and the luminescence and reflection of light from the sample are not recorded. The only measure of interest in the photoconductivity analysis is the change of the SAW. But for a verification of the actual energy and the FWHM of the laser beam a spectrometer, shown in figure 4.6(d) (11), is still integrated in the setup with a flippable mirror (10). This path is especially important if a manually adjustable free grating is used instead of the motorized and calibrated monochromator to ensure a correct alignment to the desired wavelength.

Once the alignment has been done, an automatized script can be run to sweep the frequency of the SAW with the VNA (figure 4.6(e)) and simultaneously detect the reflection and transmission of the electrical signal. With a motorized beam blank (6) the reference recording without the excitation of the nanostructures can be integrated in the script. Alternatively to the VNA, a signal generator in combination with an oscilloscope can be used to record the waveform of the propagating SAW. The differences and advantages of both methods will be discussed in subsection 4.2.2. For the probed material in these studies the signal to noise ratio (SNR) in an electrical measurement is much lower than in the optical analysis. Hence, for a significant effect on the transmission of the SAW one single nanowire or even a bundle of around 150 is not enough to generate sufficient change. This means that in order to probe the absorption of these perovskite structures a huge ensemble of nanostructures is used generating a macroscopic area with high density of material on the substrate. It is visible by bare eye in contrast to single nanowires or small bundles that can only be mapped under scanning electron or optical microscopes. As a consequence, the laser spot also has to be enlarged to cover a broader extent of the deposited material. The exact size is not of importance here and in some experiments is even scaled to illuminate the whole active area between the two IDTs of a delay line. Therefore,

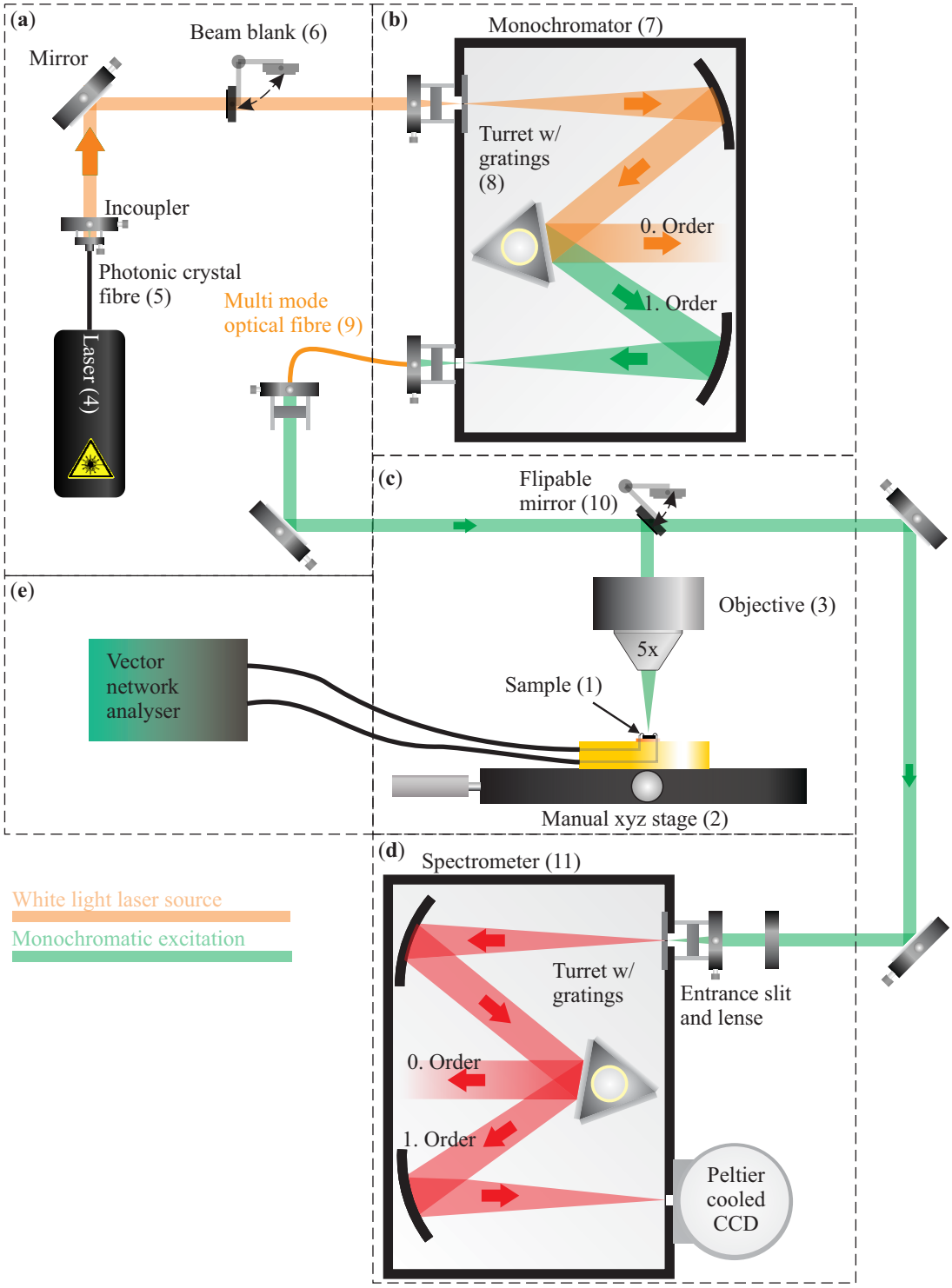

Figure 4.6: Components of the basic setup for photoconductivity-based absorption investigations. The emission from the supercontinuum light source used for excitation (**a**) is filtered by a monochromator (**b**) to tune the wavelength over a broad range of the visible spectrum up to the infrared. Through a 5× objective the monochromatic light is focused on the sample (**c**) . With a flippable mirror the excitation light can be switched between the sample and a spectrometer (**d**) which is used to confirm the wavelength of the filtered light. The SAW is excited and detected with a VNA (**e**).

the laser power has to be significantly higher in comparison to the experimental setup described in subsection 4.1.1 to maintain the same deposited energy per area. But the bigger structures also have a big advantage: An imaging of the sample with the white LED and the webcam is not needed in this setup because the alignment of the laser spot onto the cluster of nanowires can be performed with the bare eye and is not crucial at this point. What is more important is the quality of the IDTs. As mentioned above, the electrical SNR is decisive in this setting and hence a delay line with noisy or low transmission characteristics would not be able to resolve the small effect of attenuation. This requires not only good IDTs that have a high coupling of the radio frequency electrical signal into the surface wave, but also low noise electrical connections between all participating instruments and adapters. In this setting especially the previously mentioned electrical crosstalk plays an important role as it has the same frequency as the SAW but is not affected by any structure on the substrate. The amount of crosstalk disturbing the signal can also be of importance for the choice of the detection method which will be covered in the next subsection.

4.2.2 Surface Acoustic Wave Detection

The two possible excitation and detection methods of the transmitted SAW are based on two different principles. The VNA was already introduced in subsection 3.4.1 and will now be compared to a combination of signal generator and oscilloscope. In both cases a sinusoidal wave packet is sent to one IDT which creates the surface wave. On the other end of the sample another IDT detects the wave and converts it back to an electric signal which is then detected by the instrument.

In one case, a signal generator provides a wave packet of a single frequency with tunable duration and adjustable starting phase. This instrument is also suitable to apply continuous waves, but in this work, the focus lies on wave packets of finite length to reduce the heat intake and the interference with signals reflected at the metal structures or the edge of the sample. A length of several hundreds of nanoseconds can be helpful to stabilize the system.

The transmitted signal is recorded by a *LeCroy* WaveRunner 620 Zi oscilloscope which is triggered by the signal generator every time a wave packet is emitted. Hence, for investigations with this method it is essential to have a second IDT building a delay line together with the sending IDT. The oscilloscope then plots the wave as a function of time and can perform some basic analysis on the fly. Thus, the wave attenuation can be seen in the reduction of the amplitude directly on the screen which is convenient while still implementing adjustments for proof-of-principle tests. Here, the electrical crosstalk can be distinguished from the signal that propagates along the substrate and even from multiple reflected signals like the triple transit (c. f. subsection 3.3.1) as they all occur on different time scales. For huge amounts of data, the oscilloscope is not the preferred instrument as it is slow in saving the data to the internal disk or sending them to an external computer.

A frequency sweep with the signal generator can be performed by applying wave packets of different frequencies sequentially. But for every data point an extra study has to be conducted. This is time consuming and if the raw data and not only processed data like the root mean square or the peak to peak amplitude should be saved it occupies a lot of memory space. It is also possible to let the generator perform a frequency sweep within every wave packet. This would increase the speed and reduce the amount of saved data. The disadvantage of this method is the increased effort for analysing the data. In order to distinguish the attenuation for the different frequencies a Fourier transform has to be applied. This is the principle used

by the VNA which naturally performs the frequency sweep in every wave packet and presents the recorded data in a Fourier transform. The instrument has two channels and tracks the reflection of the emitted signal at each port and the transmission in each direction of the two ports. The reflection measurement is unique to the VNA and can not be realized with signal generator and oscilloscope in a simple way. With the VNA it is possible to evaluate the quality of each single IDT and the transmission through the sample in distinct data sets. Though for the photoconductivity investigation only the transmission in one direction is of relevance. This is a fast and efficient way to compare the evolution of different frequencies in a single series. But it is only possible if the dynamics under study are slow enough so that the fixed length of the pulses of each frequency from the instrument is sufficient to track the changes.

For some versions of VNAs the electrical crosstalk can be reduced to increase the SNR by applying a time gating to the recorded data. The instrument can be set to perform an inverse Fourier transform of the data and display the temporal evolution of the signal. It is then possible to define a time window to be solely evaluated for displaying the frequency-resolved reflection and transmission data. The PicoVNA from *pico Technology* applied here is not capable of this but its advantage is the controllability by computers and hence the integration into scripted measurements. As the samples had a rather low electrical crosstalk when driven at their resonance frequencies, it was also not mandatory.

The VNA is optimised for performing the Fourier transform which results in one data point per frequency, the recording and the saving of the data can be done very fast, reducing the overall measurement time and the load of memory.

Both of the aforedescribed methods can be applied in the setup for SAW attenuation investigations and are implemented in the script-based automation. For the data presented in the following chapters using this setup, the VNA was used if not stated otherwise.

4.2.3 Data Analysis

The analysis of the data slightly depends on the method of data acquisition but the basic principle is the same. In both cases, the investigations with the signal generator or with the VNA, the difference between the signal recorded with the excitation by the strong light source and a reference signal without the excitation is of interest. A subtraction of the two data sets reveals the influence of the photoexcited carriers. It is important to perform the reference on the same sample already with deposited nanostructures and the exact same delay line that will be used for the study since each IDT has a slightly different characteristic and already the deposition of semiconducting load in the path of the SAW will alter the transmission signal. These effects are shown in section 7.2, but are otherwise not subject of the studies and should therefore be eliminated in the final recordings.

The full waveform gathered by the oscilloscope can be analysed either directly using its amplitude or indirectly by applying a Fast Fourier Transform (FFT) and considering the coefficient at the SAW's frequency. Figure 4.7 summarizes this process in showing the individual steps. The wave is applied to the IDT with a signal generator at an rf power of $P_{rf} = -15\,\mathrm{dBm}$ and a frequency of $f_{SAW} = 324\,\mathrm{MHz}$. The recorded data by the oscilloscope and a zoom-in of the sinusoidal signal without (black) and with (red) an LED illuminating the sample are shown in panels (a) and (b), respectively. On this data an FFT is applied and the resulting amplitude is plotted in panel (c). Finally, panel (d) shows the extracted amplitudes of several studies where the sample was fully illuminated by a blue high power LED during the indicated recordings. Before and afterwards, the light source was switched off for several reference

recordings. In the recording of the oscilloscope, shown in figure 4.7(a), the modulation of

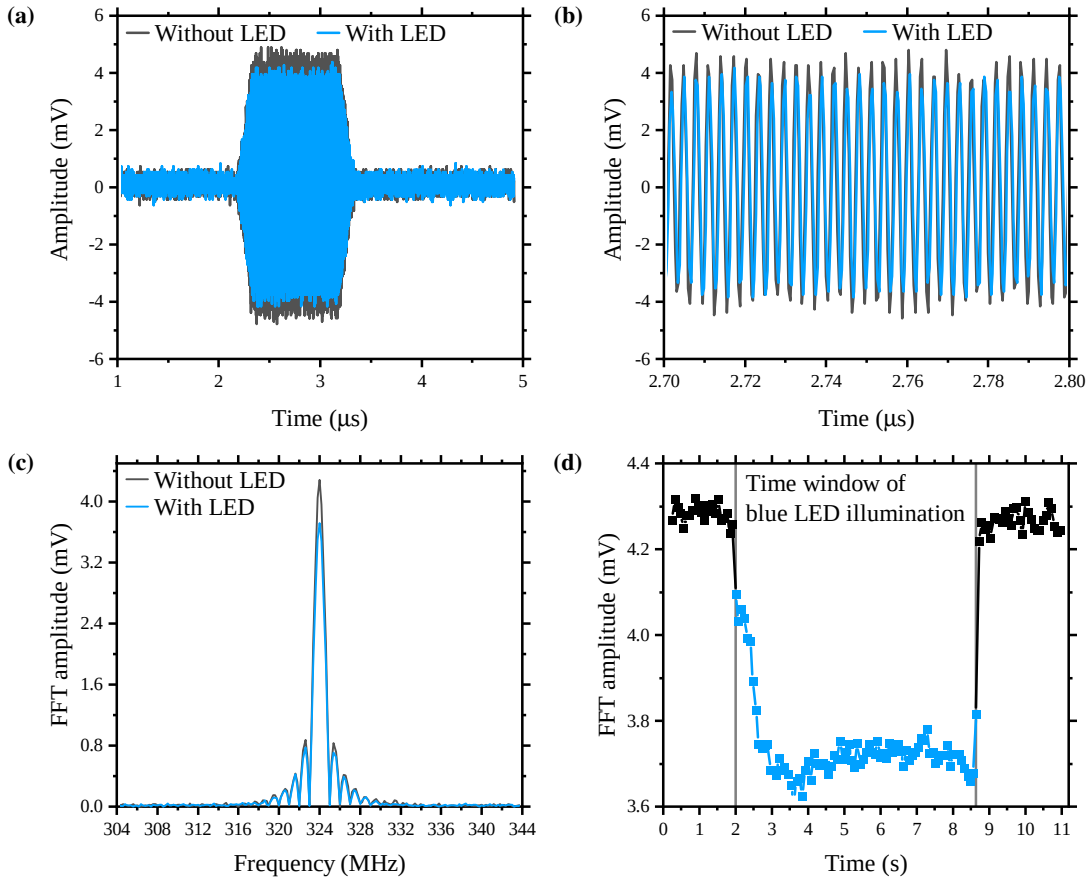

Figure 4.7: (**a**) Oscilloscope recordings of an unperturbed (black) and an attenuated (blue) SAW. The attenuation was created by photoconductivity of deposited material induced by a blue high power LED. (**b**) Zoom-in of the two wave packets presented in (a). (**c**) FFT of both recordings. (**d**) Fourier amplitudes of the SAW frequency of the attenuated wave with reference recordings at the beginning and the end. The recorded waveforms are Fourier transformed and the relevant coefficient is extracted and plotted for each single recording.

the SAW's excitation signal can be seen. A comparison between the non-illuminated (black) study and the study under illumination by a blue high-power LED with 5 W electrical power shows a clear reduction of the SAW's amplitude. The zoom-in presented in panel (b) not only shows more accurately the reduction in amplitude of the transmitted signal but also shows its sinusoidal waveform. This data is recorded multiple times per second during one experiment with the sample being several seconds in the dark before and after the LED is switched on. All the recordings are subsequently analysed with an FFT which is shown exemplary for two measurements in figure 4.7(c), one before the switching on of the LED (black) and the other one during the illumination (red). A summary of all the extracted FFT amplitudes as a function of time is shown in panel (d). The clear reduction of the amplitude during the illumination with the LED proves the photo-induced conductivity of the perovskite material. In principle, this reduced amplitude could already be used for a comparison with other studies of the same chip and either the same or different deposited materials. However, in order to compare different materials and increase the reproducibility, the difference between the attenuated signal and the

reference is extracted and used for comparison with other studies. This is important because even temperature changes or a switch of the connecting cables can lead to an altering of the reference amplitude and would thus also change the recorded attenuation if taken in absolute values instead of relative ones.

A study with the VNA provides already the Fourier transform of the data and can therefore eliminate the first step of the analysis. All the other calculations remain the same and the resulting relative change in the transmission can also be used for comparison with recordings preformed by the oscilloscope.

Chapter 5

Charge Carrier Dynamics in Perovskite Nanowires

The effect of a SAW on semiconductor nanostructures in general [Bha19; Urb13; Gel07; Als01; Roc97; Pus95; Isl69] and on nanowires in particular has already been studied in other materials [Laz18; Laz17; Kin16; Wei14a; Wei14b; Che13; Sch13; Reg13; Her11; Gov00]. This has demonstrated SAW spectroscopy as a versatile tool to study and manipulate these materials. But so far, the mechanism has not yet been applied to the novel class of perovskites. In particular for the application in solar cells however, the optoelectronic characterization is of significant importance to understand the underlying dynamics and properties and to further improve the usage and combination of materials. One of the key figures of merit for an optoelectronic device is the mobility of its charge carriers as this is a major factor for the efficient charge transport. Studies were already conducted on perovskite bulk and thin film materials [Her17], but the emerging field of nanostructures proved to be challenging. The contacting of the small structures with high precision not only evinced to be complicated, but in the case of UV and electron irradiation sensitive materials also destructive. The contact-free acousto-optoelectronic spectroscopy employed through the SAW solves all these restrictions. Furthermore, the metal halide perovskites have perfect preconditions for an extended study regarding their long lifetimes, their exciton binding energy and the comparability of the exciton radius with the cross section of the NW. The dynamic piezoelectric field provided by the prefabricated SAW chip strongly modulates the optical emission of the deposited nanowires. The strong effect on the photogenerated carriers in the $CsPbI_3$ NWs persists over all times and carrier densities. It is even possible to conduct the investigation on a variety of different sample sizes: from single NWs over small bundles to large ensembles. All of these can be analysed using the acousto-optoelectronic spectroscopy. This chapter contains dynamic transport studies of $CsPbX_3$ NW bundles that consist of roughly 100 to 300 NWs on a Y-cut $LiNbO_3$ chip and a detailed analysis of the underlying process. Due to the high exciton binding energy it is possible to study the behaviour of bound and unbound charge carriers at room temperature. The SAW device geometry was designed in a perpendicular arrangement of two IDTs with different frequencies, such that the influence of the SAW propagation direction can be analysed independently.

Section 5.1 presents time integrated and time-resolved studies on the $CsPbI_3$ NWs and visualizes the dynamics of the charge carriers. In section 5.2 this data is then combined with an analytic model based on the phenomenological observations of the effect from the wave on the excitons and free particles. To round up this analysis, section 5.3 concentrates on numerical simulations based on the drift and diffusion equations to calculate the mobility for the dynamics observed in the investigations. Additional studies proving the directionality of the dynamics with the alignment of the propagation direction of the SAW are presented in section 5.4. A temperature study in section 5.5 reveals that the dynamic control of the photoemission persists down to cryogenic temperatures confirming the theory of exciton dynamics. Subsequently, a

variation of the charge carrier density gives insight into the field screening and the low density limit. And finally, a study on $CsPbBr_3$ NWs is presented and the results are correlated with the changed lifetime and exciton binding energy of this material compared to the previous one. The main results of sections 5.1, 5.3 and 5.4 are published in [Jan19].

5.1 Real-Time Transport Dynamics

The influence of a surface acoustic wave on semiconductor nanostructures was already introduced in subsection 4.1.2 using the example of a GaAs heterostructure NW. Though the perovskite crystals largely differ in their electronic structure, such as bandgap, carrier lifetimes or mobilities, the same SAW can be used to analyse and manipulate the behaviour of the charge carriers inside the material. This demonstrates the versatility of this method. Being contact-free, the technique is highly suitable for nanoscale objects and avoids the need to disentangle the influence of metal contacts like Schottky barriers. It is also suitable for single nano-objects, clusters, assemblies or macroscopic thin films. The charge carriers in the system can be induced by laser irradiation and their transport is driven by the propagating electric field of the SAW [Sch13; Rot97]. Here, the electric field and the mechanical wave propagate with the sound velocity, which is much smaller then the speed of light and thus provides a quasi-static, flexible probe. On the other hand, the high frequency of the wave can image the actual dynamics in the system as the local spatial variation of the electric field is high. This induces a motion on electrons and holes in opposing directions which results in a reduced recombination rate of the charge carriers. Both properties together make the SAW a unique analysis tool for probing the behaviour of charge carriers under applied electric fields. In this section the separation of the charge carriers in the nanostructure will be confirmed by time-integrated and time-resolved studies performed on the NW bundle NWB1 of roughly 150 NWs of $CsPbI_3$ on a Y-cut $LiNbO_3$ chip at room temperature. The comparison of variations of excitation phases and powers in both methods gives a deep insight into the real-time transport dynamics [Sch13; Roc97]. A SEM picture of the NW bundle is presented in figure 5.1.

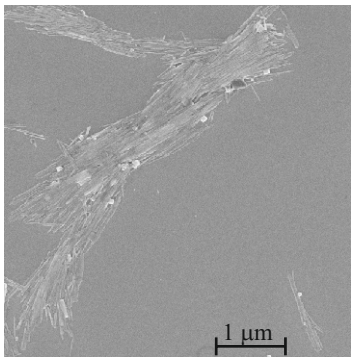

Figure 5.1: SEM picture of NW bundle NWB1 on a $LiNbO_3$ chip.

As a first step, the quenching of the PL emission of the $CsPbI_3$ NWs on the chip LJ40 is probed. To this end, a pulsed SAW is applied with increasing acoustic power without a fixed phase to the laser excitation and the emitted light is collected and spectrally resolved. Figure 5.2(a) shows four examples of such recordings with increasing power of the SAW with $f_{SAW} = 324\,\text{MHz}$ and an aperture of $400\,\mu\text{m}$. The emission is clearly reduced down to one

third of its initial value while the centre wavelength of the emission peak stays constant. The underlying process is a separation of electrons and holes due to the piezoelectric field [Roc97]. The dynamic nature of this process will be further confirmed and analysed by time-dependent investigations later in this section. Before, the spectral analysis is completed by a small step power variation to resolve the quenching in the NWs as a function of the SAW's electric field.

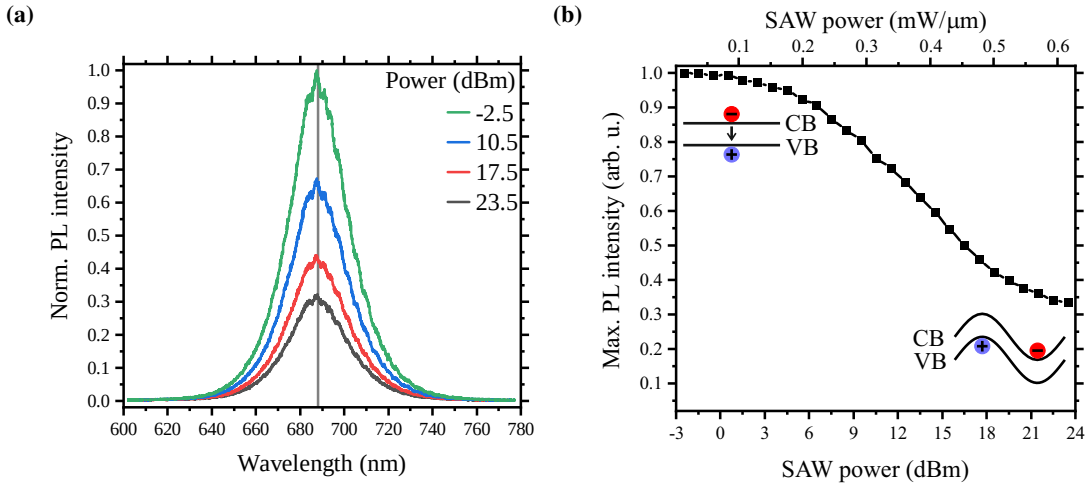

Figure 5.2: (**a**) PL spectra of NW bundle NWB1 modulated by a $f_{SAW} = 324\,\text{MHz}$ SAW of increasing intensity propagating parallel to the NW axis. (**b**) Summary of a complete series of power densities and the corresponding extracted maximum of the PL emission peak. The insets indicate the band modulation by the SAW at low and high acoustic powers.

In figure 5.2(b), the maximum peak intensity of the measurement series presented in (a) is plotted for various acoustic powers. The onset of PL reduction at the lower end and the saturation at the higher end of acoustic powers can in this way be clearly seen. The electrical power is denoted in dBm and is thus in a logarithmic power scale. At low SAW powers the conduction and valance band of the semiconductor are practically not altered by the weak electric field and the recombination of the electron-hole pair is not suppressed or delayed (c. f. left inset of figure 5.2(b)). At the onset of the influence from the SAW, quenching sets in very slowly as many carriers are bound as excitons which need to overcome the threshold of their binding energy to be separated. Furthermore, the drift velocity $v_{drift} = \mu_{n,p} \cdot \mathscr{E}$ is dependent on the amplitude of the electric field $\mathscr{E}$ and is thus very small for low SAW powers, inducing only small travel distances before the switch of directions. At high acoustic powers the spatial band structure modulation induced by the electric field of the SAW results is a large separation of the charge carriers as indicated in the right inset of figure 5.2(b). At this point an additional increase of the SAW power does not reduce the emission any more as the quenching saturates for high acoustic powers. The reason, why the emission does not drop down to zero, arises from the finite length of the nanowires. Being only about a tenth of the wavelength of the SAW, they form bundles of half λ_{SAW} in length. This means, that for every instant in time there exist NWs in the bundle which are at a position with approximately zero electric field along their axis. At this place and time the recombination of electrons and holes in these NWs can happen just as normal. This study is a first indication of the processes that the charge carriers undergo inside the NW which can be seen more clearly in the time-resolved studies in the further course of this section.

To gain deeper insight into the dynamics, time correlated single photon detection is employed. The light emitted from the nanostructure is spectrally filtered with the spectrometer to a spectral width of a few nm around the peak maximum is guided to a SPAD and the arrival of each photon is correlated with the laser trigger signal. This standard method for the analysis of PL decays is also perfectly suitable here to resolve SAW-induced dynamics. The decay times in the $CsPbI_3$ nanowires have an ideal value of up to 17 ns enabling a sub-decay time modulation of the PL with the field of the SAW whose period is much shorter, $T_{SAW} = 3.1\,\text{ns}$.

For phase-resolved studies, phase-locking, which is introduced in subsection 4.1.2, was employed. For time correlated single photon counting the timing of the excitation with a laser pulse is correlated to the frequency of the SAW. This is performed in such a way that the creation of excitons in the NW for one study happens always at the exact same phase of the acoustic wave, ensuring the same conditions for every collected photon. The main aspects during the creation of the charge carriers are the direction and strength of the electric field that guides electrons and holes, each towards a specific direction which changes according to the phase of the wave.

In figure 5.3(a) the time-dependent modulated emission of the NW bundle NWB1 in phase-locked mode with increasing strength of the SAW field is studied. Without a SAW applied, the NWs show a monotonic triple exponential decay. The temporal PL decay of perovskites is quite complex due to a mixture of free-carrier and excitonic recombinations occurring both and strong inhomogeneities in the ensembles leading to subpopulations [Gab19; Boh18; Dir18; Dir17]. To quantify the decay dynamics, the time-resolved emission is fit with a triple exponential decay which results in lifetimes of $\tau_1 = 16.8\,\text{ns}$, $\tau_2 = 4.8\,\text{ns}$ and $\tau_3 = 1.4\,\text{ns}$. The recordings with a strong SAW applied along the axis of the nanowires exhibit a distinct oscillation whose period is half of $T_{SAW} = 3.08\,\text{ns}$. Remarkably, the maximum of this modulation does not fully return to the level of PL emission observed at the same time in the unmodulated decay, which indicates the presence of more than one effect. This will be of importance for the basic assumptions of the phenomenological model described in section 5.2. The observed modulation persists over all measured time scales which is the full duration of the unperturbed reference signal.

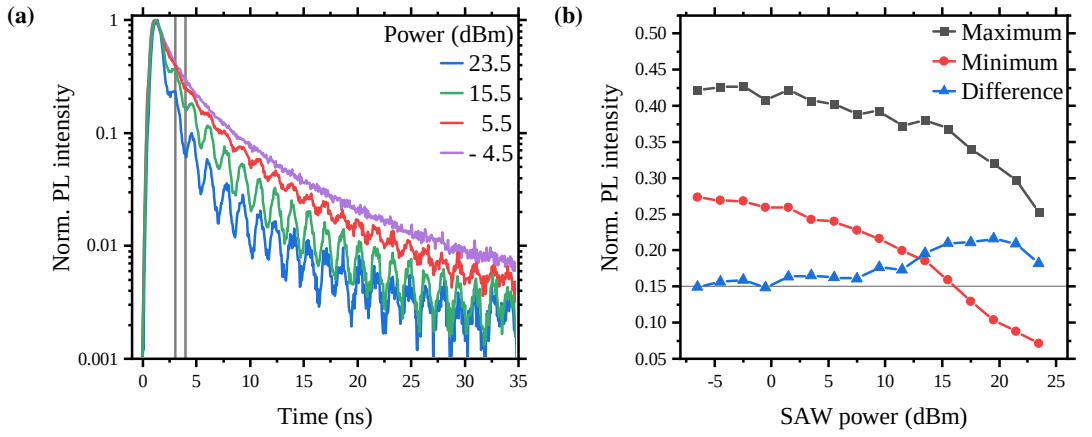

Figure 5.3: (**a**) PL decay of the $CsPbI_3$ nanowire bundle NWB1 on a semi-logarithmic scale show pronounced oscillations with the same frequency as the SAW propagating along the axis of the bundle. The coloured lines represent increasing strengths of SAW fields. The two vertical grey lines indicate the approximate position of the second maximum and minimum. (**b**) The extracted peak height of the second maximum (black) and the second minimum (red) of all applied powers. Their difference is shown in blue. The horizontal line marks the difference in height due to the normal decay of the charge carrier.

The amplitude of the oscillations is a result of the polarisation of electron and hole pairs. The larger their spatial separation, the stronger is the suppression of the recombination due to a reduction of the overlap of the wave functions of both charge carriers. To examine the evolution of this for increasing acoustic power, the first full oscillation from the data after the initial peak is taken and its maximum and minimum are extracted. The results are plotted in figure 5.3(b) in black and red, respectively, together with their difference in blue. At the lowest SAW powers where no modulation is observed, the plotted difference corresponds to the normal exponential PL decay during half a period of the SAW. Consequently, the actual contrast of the modulation as difference between the two extrema is only real above the reference value indicated in the graph by the grey horizontal line. Overall, one can see that the amplitude of the modulation increases slightly towards stronger fields, which indicates a stronger polarization of the excitons. More notably, the absolute values of both extrema decrease strongly. This points towards an additional non-radiative loss mechanism of charge carriers for high electric fields together with the already mentioned observation that the maximum does not reach the emission intensity for the unperturbed decay at increased field strengths. Those two findings can be used to explain the data in a phenomenological model based on the processes of exciton dissociation and exciton polarization (c. f. section 5.2).

The general mechanism underlying the dynamics probed in the experiment is depicted in figure 5.4. The piezoelectric SAW propagates along the NW bundle axis and induces a local shift in the bandstructure following the phase of the field. Its potential is superimposed on the conduction and valence band in a type II band modulation, which means both bands are shifted in the same direction. During one cycle, each phase traverses the NW bundle once. When the maximum of the electric potential is located at the position of the bundle, an unstable point is created for the electrons, but the holes remain at a stable point. After half the period of the SAW, the electric field vector points exactly in the opposite direction and the situation is reversed. Between those two points, the bandstructure is maximally slanted and the carriers are under the influence of a large electric field ($\mathscr{E}$) parallel to the axis of the NWs in the bundle. This large field along the axis impacts on the electron-hole pairs and leads to their polarization. The two charge carriers of opposite sign can be addressed independently to a certain extent and are accelerated in opposite directions leading to two drift currents. The oscillating nature of the electric field gives thus rise to cyclic motion of both, electron and hole, in anti-parallel directions. At the times when the electric field points out of or into the substrate, one of the charge carriers is fixed at its position while the other one is driven away from it in both directions. As the electron and hole exchange places twice during one cycle of the SAW, they are spatially located at the same position two times.

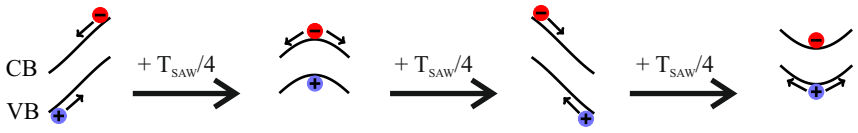

Figure 5.4: Illustration of the dynamics driven by the SAW. During a full acoustic cycle the electric field vector gyrates around the NWs with components in all three spatial directions. Every half period, the charge carriers are located at extrema of the conduction (electrons) or valence band (holes). In between, the electric field vector points parallel to the NW axis inducing a drift in or against the propagation direction of the SAW. This drift induces the dissociation of photo-excited excitons.

During that time the radiative recombination is enhanced while it is maximally suppressed

when the charge carriers are furthest apart. This gives rise to the observed oscillating nature of the time-resolved PL emission presented in figure 5.3(a) with a periodicity of $1/2 \cdot T_{SAW}$, i. e. a doubled frequency $f_{\mathrm{mod}} = 2 \cdot f_{SAW} = 648\,\mathrm{MHz}$.

A further confirmation is performed by an analogous time-resolved study with a 90° phase shift between the driving RF signals of power $P_{SAW} = 23.5\,\mathrm{dBm}$ and frequency $f_{SAW} = 324\,\mathrm{MHz}$. The laser pulse is still synchronized to the phase of the SAW to enable repeated recordings with the same initial situation, but is now changed by 90°. The result is shown in figure 5.5 clearly demonstrating an inversely oscillating PL emission. This behaviour lasts over the full decay and is reproducible throughout all investigations. These findings further confirm the $1/2 \cdot T_{SAW}$-periodic modulation and prove its correlation to the phase of the SAW and therefore to the direction of the electric field.

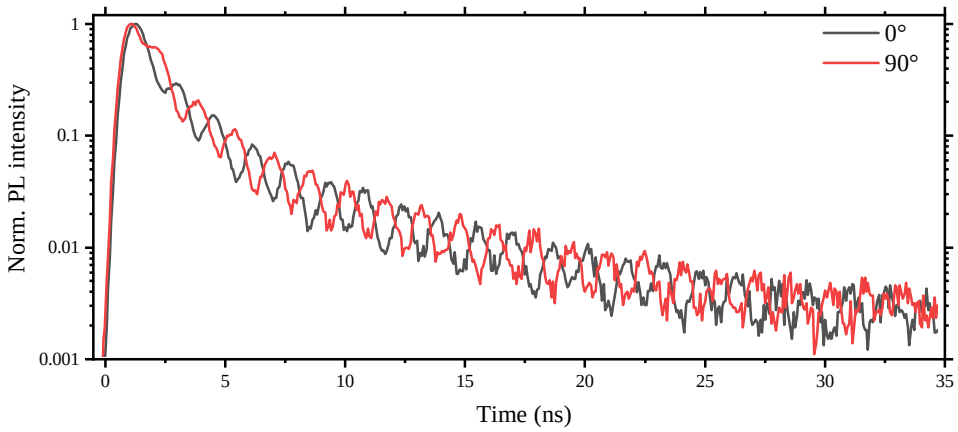

Figure 5.5: Time-resolved PL decay from NWB1 as in figure 5.3(a) for the highest SAW power and a 90° phase shifted laser excitations. It shows a 180° phase shift in the recorded data.

These findings differ strongly from similar experiments performed on GaAs NWs at cryogenic temperatures [Kin16]. Therein the PL is highly quenched through the application of a SAW and the once per cycle restored PL emission never recovers even closely to the unperturbed case. The facets of these nanowires favour non-radiative loss channels through surface recombinations. Furthermore, the modulation occurs with a frequency equal to that of the SAW. The halving of the modulation period in perovskites in comparison to the GaAs NWs studies by Jörg Kinzel *et al.* is only a result of the NW length. Due to the longer transport distance before being blocked in forward motion by the end facet, many charge carriers recombine non-radiatively. Comparisons with very short GaAs NWs reveal that there, too, two maxima in the PL per SAW period are present. The main difference to the examined perovskite material is a significant difference in height of the two maxima which is a huge indicator of the transport mobilities of electrons and holes being largely disparate. In the conventional semiconductor the mobilities are found to be largely dissimilar with $\mu_h \leq 0.1\mu_e$ [Kin16]. As a consequence, the holes in this material remain mostly stationary up to large electric fields while the electrons start following the field rather early. Thus, the spatial overlap of the charge carriers depends mostly on the movement of the electrons and the amount of recombination on the velocity of their transport over the holes. This speed is different for the two recombination times: during the forward movement, the electrons follow the velocity of the SAW while in the backward movement they are only limited by their own drift velocity.

In contrast, the observed oscillations for the $CsPbI_3$ NWs where no discrimination happens between phases of 180° difference prove that both charge carriers are mobile. This leads to the conclusion that the mobilities in the novel material are equal as commonly assumed for bulk crystals of metal halide perovskite semiconductors.

Before the next two sections focus on the analysis and quantitative interpretation of the experimental findings from the previously shown data, a short look is taken on the reproducibility and the life span of the metal halide perovskite NWs. Figure 5.6 compares two time-resolved PL emission studies of the bundle NWB1 lying eight days of additional recordings apart from each other. While in principle all examined wires have a tri-exponential decay with very similar decay constants their behaviour changes under long term laser illumination. This is not largely measurable in intra-day studies, but adds up to significant changes after one week of constant studies. The laser illumination used in the experiment is comparably low with around 45 nW. At a repetition rate of 8.1 MHz this results in a power of 5.6 fJ per pulse. Nonetheless, together with the application of a SAW with various powers this is enough for a partial alteration of the material. The transition manifests itself in a reduced total PL emission and even more in the acceleration of the decay, indicating stronger non-radiative trap states or surface recombinations. The black line of figure 5.6 shows the result on the first day of the study while the

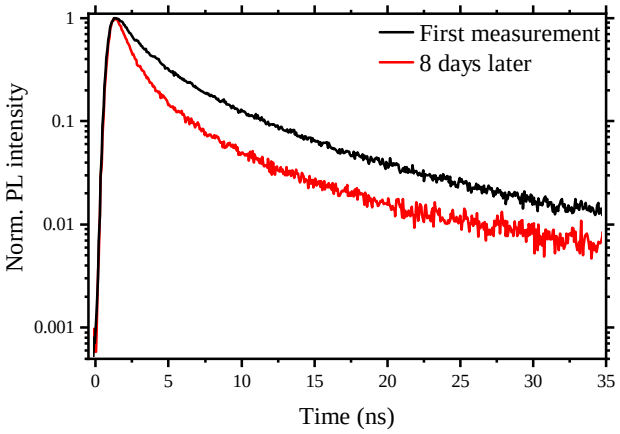

Figure 5.6: PL decay of two different studies on NWB1 lying more then one week apart. The data recorded later shows a significant reduction of the lifetime.

red line was recorded eight days later. The data were both recorded under the influence of a perpendicular surface acoustic wave which will be discussed later on (see section 5.4). The week long treatment of the NW with laser excitation and SAW clearly reduces the lifetime of the photoexcited carriers. The lifetime changes are summarized in table 5.1.

	τ_1	τ_2	τ_3
reference day	18.2 ns	5.2 ns	1.5 ns
8 days later	19.2 ns	4.0 ns	1.0 ns

Table 5.1: Lifetime changes of NWB1 after eight days with repeated studies in between.

Interestingly, the change only occurs at the exact NW that was examined and thus the one where the laser was pointing at. Other NWs that were not studied and thus not excited by the

laser but still under the influence of the SAW as they are lying in the aperture of the wave do not show any change in their behaviour. Hence, it is clear that the laser plays an important role in the altering of the material and that for applications of metal halide perovskites in solar cells this ageing phenomenon has to be taken into account and addressed further [Yua17; Akb18; Lu19; Pra19]. For this work, it is relevant only in so far that different studies in this theses were partly performed on different NW bundles due to the ageing.

5.2 Phenomenological Model

The phenomenological model is based on the assumption of two effects being involved in the charge carrier dynamics induced by the SAW. At first, the electric field can polarize the photoexcited electron-hole pairs creating an oscillating dipole. Secondly, spatio-temporal carrier dynamics can be induced when excitons are dissociated and free carriers emerge. Those two processes will be used to develop a model describing the processes in the nanowire and by fitting the decay formula obtained in this way to the data, new insights can be obtained.

The starting point of the model is the tri-exponential decay (equation 5.1) observed in the unperturbed time-resolved emission. This is the basis for the following adoptions that account for the dynamics produced by the SAW.

$$I(t) = \sum_{i=1}^{3} A_i \cdot e^{-\Gamma_{i,ref} \cdot t} \tag{5.1}$$

describes the temporal evolution of the intensity decay of excitons as a sum of the three independent decays with their decay rates $\Gamma_{i,ref}$ and amplitudes A_i. The second participating process, the dissociation of electron-hole pairs affects the PL emission in a reduction of the recombination rate as spatially separated charge carriers contribute less to the radiative emission unless they are bound again. This is included in the model by the modification of the basic decay rate Γ which is increased compared to the initial Γ_{ref}.

Due to the similar mobilities for electrons and holes in the metal halide perovskites, the SAW leads to dynamic transport of both charge carrier species. This stands in contrast to traditional semiconductors like GaAs, in which only the electrons are mobile and are spatially transported by the SAW while the holes remain stationary [Gar04; Sch12; Kin16]. To account for the two mobile particles involving polarization of the exciton, the resulting variation in the overlap of the wave functions is considered. As both follow a sinusoidal path the change in overlap varies in a $\sin^2(\omega_{SAW} t)$-like oscillation. In the model this means that the decay rates Γ_i become dependent on the time and vary according to the overlap function with the angular frequency of the SAW ω_{SAW}.

$$\Gamma_i(t) = \Gamma_{i,0} + \Delta_i \cdot \sin^2(\omega_{SAW} t) \tag{5.2}$$

The amplitude of the oscillation is denoted here with Δ_i for each decay, respectively. This time-dependent decay rate is then included in the intensity function to result in the full time-modulated expression in equation 5.3.

$$I(t) = \sum_{i=1}^{3} A_i \cdot e^{-\Gamma_{i,0} \cdot t} \cdot e^{-\Delta_i \cdot \sin^2(\omega_{SAW} t) \cdot t} \tag{5.3}$$

This phenomenological model is now applied to the experimental data to verify its validity.

Figure 5.7 shows the experimental data (black dots) from the NW bundle at the maximum SAW power of $P_{SAW} = 23.5\,\mathrm{dBm}$ and the best fit of equation 5.3 (red line) to it for the bundles NWB1 (a) and NWB3 (b). Both follow an oscillation frequency of 324 MHz. The good agreement between experimental data and best fit shows that the model indeed reproduces the carrier dynamics inside the NW well and that the two main processes are exciton dissociation and exciton polarization. This knowledge is important to justify the applicability of the drift- and diffusion-based simulation in section 5.3.

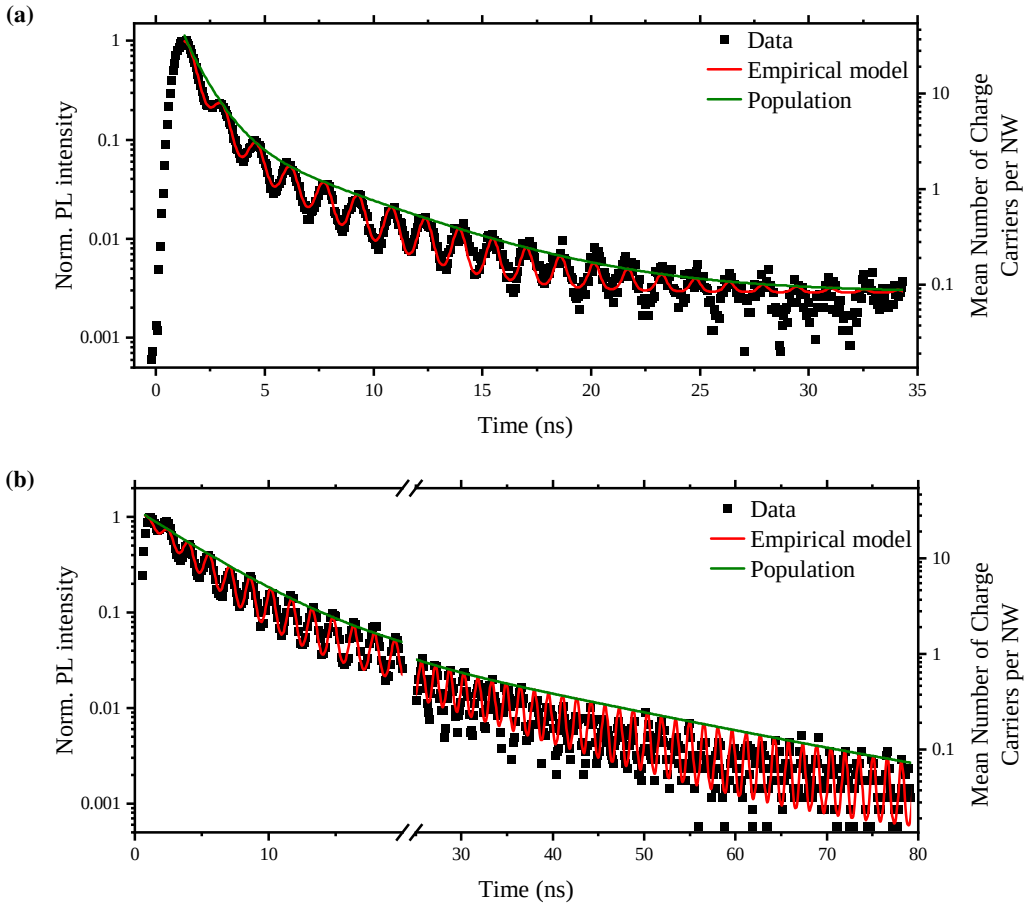

Figure 5.7: (**a**) The fit of equation 5.3 (red line) from the phenomenological model to the experimental data (black dots) of bundle NWB1 shows good agreement. (**b**) For NWB3, which has a longer lifetime and stronger emission and thus a longer observation time of the decay, it can be seen that the modulation perfectly matches in the general course as well as in the reproduction of the small oscillations even on a long time scale.

Figure 5.7(a) shows the time-resolved PL emission of NWB1 (symbols), its modelled fit (red line) and the extracted approximate charge carrier density (green line). The strong agreement of data and fit justifies the assumptions of the model and the extraction of the fitting parameters, which are analysed in figure 5.8. Figure 5.7(b) shows the data and fit of NWB3 which has a stronger emission and a longer lifetime. Compared to NWB1, there is a very good agreement here of the fit with the phenomenological model and the data over a very long time scale encompassing the full duration of the decay and thus a wide range of charge carrier densities, covering more then three orders of magnitude. First, it is remarkable that the oscillations in

the data persist for so long without being suppressed by the charge carriers being trapped in impurities. This is a result of the very low deep trap state density in these nanomaterials which is also proven here to remain during the transfer and the treatment with SAWs. Secondly, even the small modulations at later times being on the order of only a few counts in the SPAD after an integration time of 5 min are perfectly reproduced by the model. The charge carriers in the NW thus behave according to the phenomenological model, sticking to the same parameters for all measured times and, correspondingly, charge carrier densities.

The density of the charge carriers contributing to the radiative decay can be extracted from the model by assuming a full restoration of the decay rate at each maximum which is reached when the sin-function equals zero. Hence, the population decay is given by

$$N_{excitons}(t) = \sum_{i=1}^{3} A_i \cdot e^{-\Gamma_{i,0} \cdot t} \tag{5.4}$$

and is equal to the upper envelope of the modelled PL decay as depicted in figure 5.7 (green line). From this the number of excitons as a function of time can be extracted, using the mean number of excitons per NW determined by the number of absorbed photons and the bulk absorption coefficient of the material which is approximately 1 for the laser wavelength of 532 nm. The number of photons is roughly estimated by the radiation of the laser multiplied with a geometric factor for the bundle and divided by the number of NWs in a circle with the size of the laser spot which is evaluated by scanning electron microscopy.

The fitted model function now allows for the extraction of the fitting parameters which describe the assumed two processes of exciton polarization and dissociation and to draw conclusions on their evolution with SAW power. To that end, the analysis is performed for a series of time-resolved emissions under various acoustic powers on the same NW bundle. Figure 5.8 shows the two parameters of the model, $\Gamma_{i,0}$ in panel (a) and Δ_i in panel (b), that are determined for the three decay rates of each data set for NWB1 as a function of the applied acoustic power. The symbols in different colors represent the extracted parameters for the three decay rates while the the solid lines are fits in the power-dependent regions. The values of the slow, middle and fast decay rate are $\Gamma_{\text{slow, ref}} = 0.10\,\frac{1}{\text{ns}}$, $\Gamma_{\text{middle, ref}} = 0.27\,\frac{1}{\text{ns}}$ and $\Gamma_{\text{fast, ref}} = 0.89\,\frac{1}{\text{ns}}$, respectively. The data points marked by the blue ellipses correspond to the values of the phenomenological model presented in figure 5.7(a). The two parameters of figure 5.8 are indicators for the two processes underlying the dynamics of the charge carriers in the NWs. On the one hand, $\Gamma_{i,0}$ i panel (a) is a measure for the exciton dissociation and reveals that there exists a threshold around $6\,\frac{\mu\text{W}}{\mu\text{m}}$ of the electric field that is needed to separate the electron-hole pair. Using equation 3.35 the potential at the first value above the threshold of $9\,\frac{\mu\text{W}}{\mu\text{m}}$ can be calculated from the corresponding acoustic power to $\Phi_{max} = 0.96\,\text{eV}$. Taking into account the diameter of the exciton, which is $2 \cdot a_{ex} = 24\,\text{nm}$ and the sinusoidal nature of the wave with wavelength λ_{SAW}, the maximum potential difference across the diameter of an exciton can be calculated as

$$\Delta\Phi_{ex} = \Phi_{max} \cdot \left[\sin\left(\frac{2\pi a_{ex}}{\lambda_{SAW}}\right) - \sin\left(-\frac{2\pi a_{ex}}{\lambda_{SAW}}\right) \right] = \Phi_{max} \cdot 0.014 \tag{5.5}$$

With the above calculated Φ_{max} this results in a deposited energy of 13.4 meV into the exciton for the lowest SAW power that results in an increased decay rate. This value is slightly below the binding energy of the exciton of 25 meV and should in theory not yet result in exciton

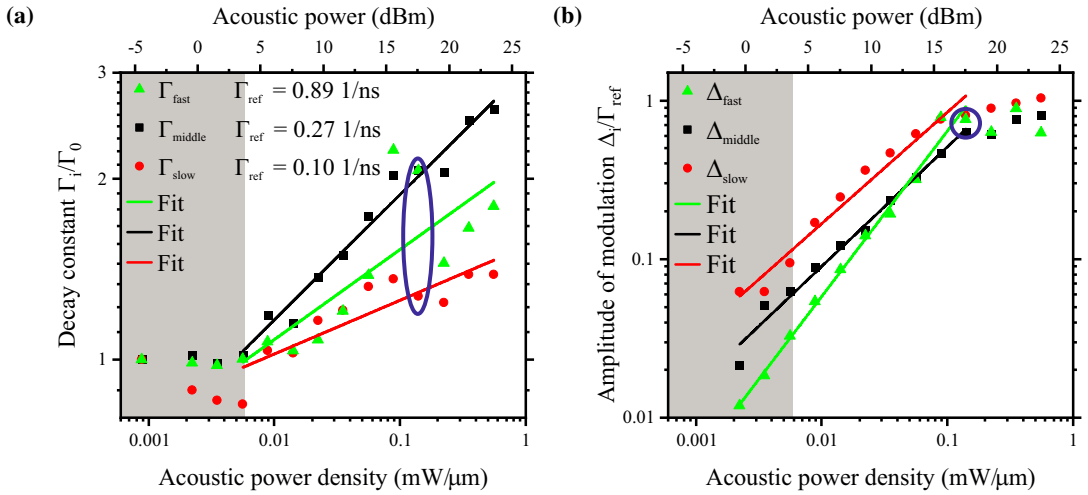

Figure 5.8: Extracted fitting parameters of the phenomenological model for a series of time-resolved recordings with different applied acoustic power on NW bundle NWB1. The values for the three decay rates are treated separately as they represent distinct decay channels. (**a**) The increased decay rate as a function of the applied acoustic power shows a clear threshold on a double-logarithmic scale, indicted by the end of the grey shaded area. (**b**) The modulation amplitude of the oscillations for the same recordings in a double-logarithmic plot. The grey shaded area from (a) is shown here for reference.
The ellipsis and the circle indicate the recording that is used later for the comparison with the simulation.

dissociation. However, as the investigations are not performed at cryogenic temperatures, additional thermal energy is provided by the environment, lowering the threshold for charge carrier separation.

On the other hand, the amplitude of the modulation gives insight into the electron-hole separation of the exciton polarization as both are correlated through the overlap of the wave functions. The first few recordings of the series in figure 5.8(b) are neglected as the amplitude of the oscillation was smaller then or equal to the noise level. The grey box shows the region without exciton dissociation. Remarkably, visible oscillations start before the dissociation of excitons sets in. This is a clear indication that the two processes are independent and that the exciton polarization requires smaller field strengths. The amplitude of the oscillation also increases exponentially with SAW power as can be seen from the linear fit in figure 5.8(b) in a double-logarithmic scale. At high fields above 0.14 $\frac{\text{mW}}{\mu\text{m}}$, it saturates, indicating that a further separation is not possible without dissociating the electron-hole pair.

This simple phenomenological model already describes the data very good over all times. Furthermore, by extracting the fitting parameters, it is possible to make qualitative statements about the contribution of exciton dissociation and exciton polarization which helps understanding the underlying mechanisms. However, the model does not allow to draw quantitative conclusions on the electronic properties of the material. For this purpose, the next section will present a numerical simulation of the full process which allows to determine the mobilities of both charge carriers at once.

5.3 Numerical Simulation

The basis for the numerical calculations of the charge carrier dynamics in the NWs are the drift and diffusion equations determining the spatio-temporal dynamics of electrons and holes

[Gar04]. In the simulation they are solved for electrons, holes and excitons and the calculated PL is compared to the experimental data. The coupled differential equations for spatial and temporal evolution are derived in subsection 3.5.5 for a one dimensional structure like a nanowire. The implementation of the simulation in Matlab was performed by Florian Schülein during his PhD thesis. A detailed description of the full model and further reasoning for applied simplifications can be found in [Sch14b]. Here, only a few comments will be given on the solving of the coupled differential equations.

In the simulation a finite difference method for the time and the 1D spacial axis along the SAW propagation is used in an explicit method. Exemplary, the equation for electrons (n) shall be mentioned here once more together with the one for the exciton which is adapted for the triple exponential decay. The recombination rate R of electrons and holes to form excitons is substituted with its formula $R = c_X \cdot np$ which is a constant $c_X$times the density of electrons n and holes p.

$$\begin{aligned} \frac{\partial n}{\partial t} &= D_n \frac{\partial^2 n}{\partial x^2} + \mu_n \frac{\partial (\mathscr{E}_x \cdot n)}{\partial x} + G - c_X \cdot np + T \\ \frac{\partial X}{\partial t} &= D_X \frac{\partial^2 X}{\partial x^2} + c_X \cdot np - \frac{X}{\tau_1} - \frac{X}{\tau_2} - \frac{X}{\tau_3} - T \end{aligned} \tag{5.6}$$

The generation rate of charge carriers through the photons of a laser is denoted by G and T represents the tunnelling ionization rate. The latter is described by the dissociation of an exciton through the energy the electron gains with the electric field within the diameter of the exciton. The thermal dissociation is not considered in the calculations because the system is assumed to be in an equilibrium and the spontaneous generation and dissociation will compensate for each other.

The diffusion term which is based on the second derivative tends to create unphysical oscillations which could be reduced by an increase in the number of time steps. But as this would drastically raise the computation time, an alternative method is preferred: the discrete Fourier transform. This discrete frequency analysis is used to approximate the density of carriers for the second derivative term. For computer-based calculations this can be implemented very efficiently through the FFT.

The drift term, represented through the first derivative, is simplified by neglecting the spatial dependence of the electric field. Thus, the derivative is only executed on the electron density n (and similarly for the hole density):

$$\mu_n \frac{\partial (\mathscr{E}_x \cdot n)}{\partial x} = \mu_n \mathscr{E}_x \frac{\partial n}{\partial x} + \mu_n \cdot n \frac{\partial \mathscr{E}_x}{\partial x} \tag{5.7}$$

$$= \mu_n \left(\mathscr{E}_x + \underbrace{n \frac{\partial \mathscr{E}_x}{\partial x} \frac{\partial x}{\partial n}}_{\ll \mathscr{E}_x} \right) \frac{\partial n}{\partial x} \approx \mu_n \mathscr{E}_x \frac{\partial n}{\partial x} \tag{5.8}$$

This approach is justified with the very low dependence of the electric field on the carrier density in the regime of weak carrier injection. The main part of the field, the SAW field, is not dependent on n and the derivative of the field induced by the charges can be approximated to be

very low [Sch14b].

The generation of the charge carriers in the simulation is solely based on photoexcitation and no thermal generation is taken into account. It is modelled as a temporal and spatial pulse described with Gaussian functions.

$$G(t,x) = G_0 \cdot e^{-\frac{1}{2}\frac{(t-t_0)^2}{w_t^2}} \cdot e^{-\frac{1}{2}\frac{(x-x_0)^2}{w_x^2}} \tag{5.9}$$

The parameters w_i are given by the full width half maximum in time and space of the laser pulse and can be adapted in the simulation to match the real experimental conditions. For the simulation presented in this section the values are $w_x = 1.5\,\mu\text{m}$ and $w_t = 80\,\text{ps}$. Through t_0 and x_0 the time and position of the excitation can be varied.

To account for the properties of lead halide perovskite nanowires, the simulation program was modified to be able to handle multiple exponential decays and to extract the temporal dependence of the spatially integrated PL. Then, the simulation parameters were adjusted to the experiment and the code was executed several times while varying the free parameters (subsection 5.3.1 and the table in appendix 8.2). These include in particular the mobilities of electrons and holes. Furthermore, the number of photons is investigated in subsection 5.3.2 to confirm the estimate of the absorbed photon flux.

5.3.1 Analysis of the Mobility

As a starting point two assumptions were made. It is known from bulk and thin film metal halide perovskites [Her17; Bre15] that the mobilities of both charge carriers lie in the same range and the previously shown experiments indicate that this is also the case for NWs. Secondly, in previous simulations performed by Jörg Kinzel [Kin16], values of μ_e and μ_h for GaAs nanowires were determined which are assumed to be significantly higher then those for $CsPbI_3$. Bearing this in mind, the initial parameters are set to be equal for electron and hole and two orders of magnitude lower than GaAs NWs. The mobilities in the simulation are varied and for each set of parameters the emitted PL is calculated and compared to the experimental data. In an iterative process the values of the parameters for the simulation are adapted to maximize the accordance with the experiment. In this process, the value of the mobility under the assumption of equal values for electrons and holes and the ratio between the mobilities μ_e and μ_h are varied, both in coarse and fine steps. In the following, a few of the intermediate stages are presented to justify the end result.

Figure 5.9 presents the simulated PL emission for $\mu_e = \mu_h = 3\,\frac{\text{cm}^2}{\text{Vs}}$ (red line) together with the experimentally obtained data on NW bundle NWB3 (black dots) for a SAW with $P_{SAW} = 23.5\,\text{dBm}$ and $f_{SAW} = 324\,\text{MHz}$. Remarkably, the calculated emission matches well the recorded data over the full duration of the decay and reproduces the frequency and amplitude of the oscillations, even though the modulation height changes with reduced carriers in the system. The semi-logarithmic plot also shows the population evolution during the decay as blue line – this time calculated indirectly as the upper envelope of the simulated decay. As shown, the experimental data and the corresponding simulation agree over more than two orders of magnitude in exciton density even reproducing the contrast of the oscillations. As the difference between all the simulations manifest most at long times when the density of charge carriers is low, the comparisons in the following are presented in the time window between 60 ns and 75 ns, indicated in the graph by the grey box.

The transport properties of bulk $CsPbI_3$ have been studied theoretically with various ap-

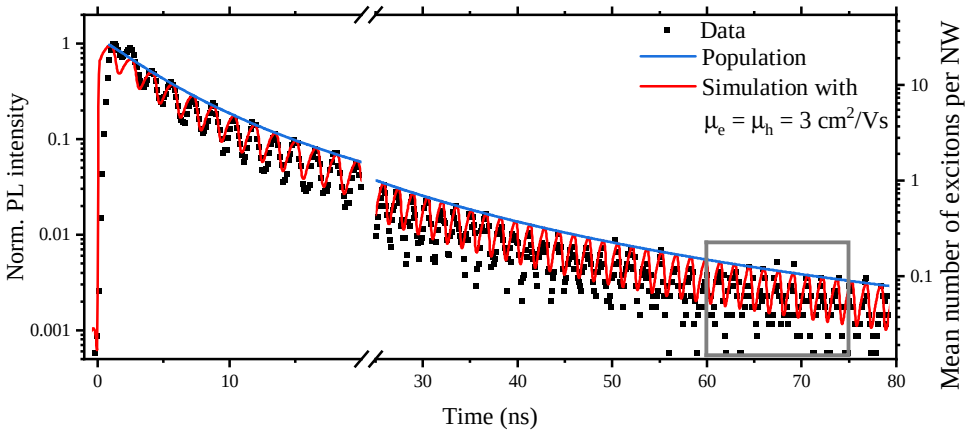

Figure 5.9: Best fitting simulated time evolution of the PL emission for mobilities of $\mu_e = \mu_h = 3\,\frac{\mathrm{cm}^2}{\mathrm{Vs}}$ (red line) compared to the experimentally observed data (black symbols) of NWB3 in a semi-logarithmic scale. The blue line represents the extracted number of electron-hole pairs per NW corresponding to the right axis. The grey box indicates the region used for further detailed studies of varying mobilities.

proaches. However, in literature the mobilities for electrons (holes) vary widely and are stated to be 258 $\frac{\mathrm{cm}^2}{\mathrm{Vs}}$ [Fro17] and 74 $\frac{\mathrm{cm}^2}{\mathrm{Vs}}$ (98 $\frac{\mathrm{cm}^2}{\mathrm{Vs}}$) [Myu18]. In experiments the values for $CsPbI_3$ thin films turned out to be in the range of 30 $\frac{\mathrm{cm}^2}{\mathrm{Vs}}$ [Das17] and 25 $\frac{\mathrm{cm}^2}{\mathrm{Vs}}$ [Hut17]. The NWs are expected to have even smaller mobilities as their surface to volume ratio is much larger which increases surface scatterings.

In figure 5.10 the four panels show different variations in the order of magnitude and the ratio of the mobilities of electrons and holes in the simulation for otherwise fixed parameters. The black symbols always represent the data of NW bundle NWB3 at $f_{SAW} = 324\,\mathrm{MHz}$ and $P_{rf} = 31\,\mathrm{dBm}$ applied RF power, which results in an actual SAW power of $P_{SAW} = 23.5\,\mathrm{dBm}$ by subtracting the insertion loss. Under the assumption that the mobilities are the same for both charge carriers, their magnitude is changed by one order of magnitude up and down (figure 5.10(a)). The figure compares mobilities for electrons and holes of 30 $\frac{\mathrm{cm}^2}{\mathrm{Vs}}$ (dark blue), 3 $\frac{\mathrm{cm}^2}{\mathrm{Vs}}$ (grey), 0.3 $\frac{\mathrm{cm}^2}{\mathrm{Vs}}$ (mid blue) and 0.03 $\frac{\mathrm{cm}^2}{\mathrm{Vs}}$ (turquoise). These values cover a wide range around the parameters expected for nanostructures of metal halide perovskites.

The simulations of the time-resolved PL emission are normalized such that their third maximum is at the same level to ensure comparability and exclude the effects of overshooting at the beginning. Clearly demonstrated by figure 5.10(a) the highest value (dark blue line) in the simulation results in a large deviation from the experiment with a completely different shape. While for short time scales (not shown here) the periodicity follows the experimental data, at the presented time window, it shows a periodicity following the SAW's and not twice f_{SAW}. Furthermore, the amplitude of the oscillations is largely increased compared to the other simulations. One of the two peaks within one SAW period in the beginning of the decay delays more and more with time and in the region between 60 ns and 75 ns overlaps with the other. As a result the PL forms only one emission peak. For these high values of mobility it seems that the propagation direction of the wave comes into play and causes a long time favouring of one direction of motion for each charge carrier over the other. The other three simulations of panel (a) follow the doubled frequency analogous to the data and differ only in the amplitude of the oscillation. A comparison of these simulations with the experimental data pin the mobilities'

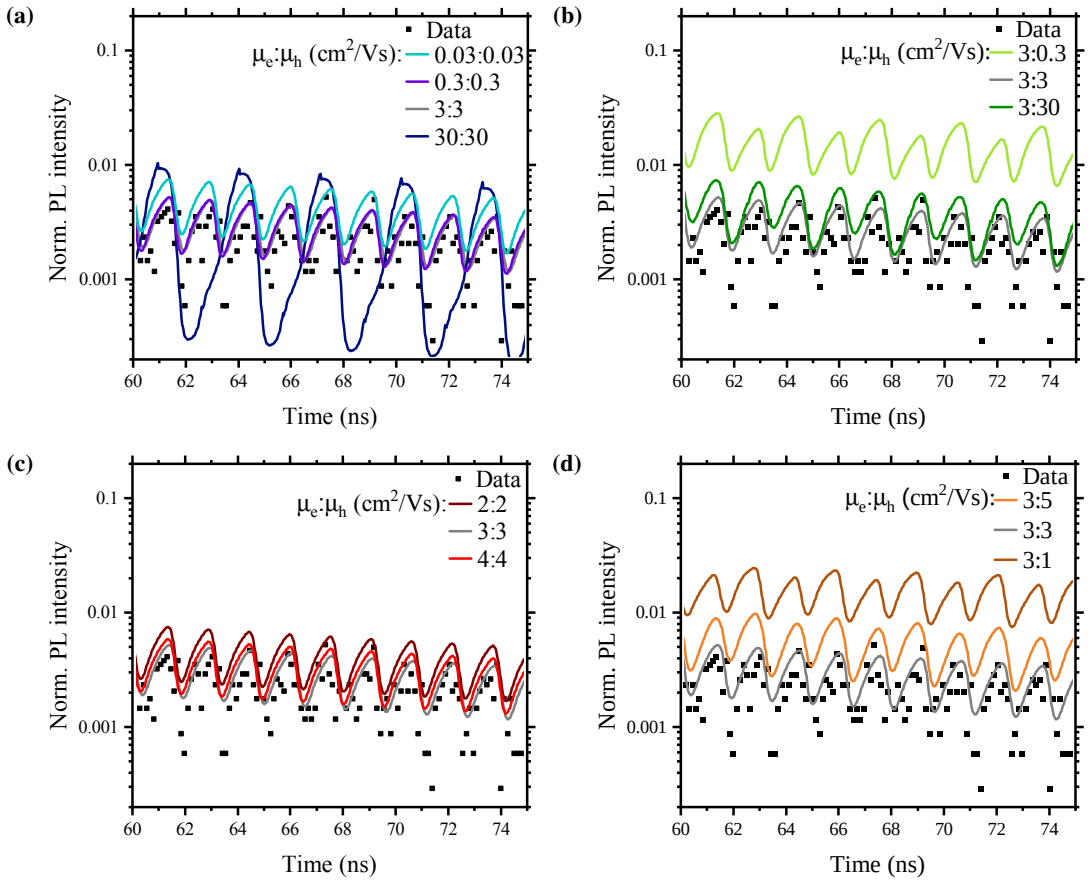

Figure 5.10: (**a**) Extracted time evolution of the PL from the simulation with varying order of magnitude of the mobilities under the assumption of equal values for electrons and holes. (**b**) When keeping the mobility of the electrons constant, a variation of the hole mobility results in drastic changes of the calculated time-dependence. (**c**) and (**d**) show finer variations of the magnitude and ratio, respectively.
In all four graphs, the black dots represent the experimentally determined data from NW bundle NWB3.

order of magnitude to $10^0 \frac{\mathrm{cm}^2}{\mathrm{Vs}}$.

To confirm the assumption of $\mu_e = \mu_h$, their ratio is varied while keeping $\mu_e = 3 \frac{\mathrm{cm}^2}{\mathrm{Vs}}$ fixed. Figure 5.10(b) presents the time-resolved PL emission of three simulations with fixed μ_e and varying μ_h from $0.3 \frac{\mathrm{cm}^2}{\mathrm{Vs}}$ (dark green) to $3 \frac{\mathrm{cm}^2}{\mathrm{Vs}}$ (grey) and $30 \frac{\mathrm{cm}^2}{\mathrm{Vs}}$ (light green). They demonstrate that for all presented hole mobilities the simulations follow the same periodicity as the experiment (symbols), but their global decay rate differs significantly in the chosen time window of the graph. This is calculated as effect of the SAW as the unperturbed decay rates are kept constant. The semi-logarithmic intensity scale enhances the view of the differences because the absolute values this far in the decay lie in the range of only a few counts collected in the 20 min integration time. But still it is clearly shown by the graph that the simulation for similar mobilities match the data best.

After determining coarse values of the parameters with the two comparisons explained so far, the variations are made smaller to further narrow down the range. Figure 5.10(c) illustrate additional simulation results for a fine variation of the value of μ_e of $2 \frac{\mathrm{cm}^2}{\mathrm{Vs}}$, $3 \frac{\mathrm{cm}^2}{\mathrm{Vs}}$ and $4 \frac{\mathrm{cm}^2}{\mathrm{Vs}}$

while keeping the ratio constant at $\mu_e = \mu_h$. Finally, panel (d) presents a further study of fine variations in the ratio between the two mobilities with μ_h ranging from 1 $\frac{\text{cm}^2}{\text{Vs}}$ to 5 $\frac{\text{cm}^2}{\text{Vs}}$ while μ_e is kept constant. In a small range around 3 $\frac{\text{cm}^2}{\text{Vs}}$ the calculated curves nicely coincide with the experimental data. The same is done for the ratio between the two mobilities. The very clear results denote equal values for both parameters as already slight variations lead to significant changes in the shape of the calculated time-resolved emission. This procedure enables an accurate determination of the average mobilities of both mobile carriers separately in the examined NWs.

In summary, a value of $\mu_e = \mu_h = (3 \pm 1)\,\frac{\text{cm}^2}{\text{Vs}}$ can be determined as result of the simulations. In a small range of 1 $\frac{\text{cm}^2}{\text{Vs}}$ around the best fit of 3 $\frac{\text{cm}^2}{\text{Vs}}$ the calculated PL emission stays close to the experimental data and follows the same trend. Remarkably, the values are independent of the charge carrier concentrations that decrease during the decay over more than two orders of magnitude down to the intrinsic material limit. Moreover, the mobilities, determined with the presented method of simulating the charge carrier dynamics, are comparable to the values determined for bulk or thin film crystals [Her17]. These modest values of mobilities in the halide perovskites in comparison to conventional semiconductors like GaAs with $\mu_e = 500\,\frac{\text{cm}^2}{\text{Vs}}$ and $\mu_h = 50\,\frac{\text{cm}^2}{\text{Vs}}$ [Kin16] are in no contradiction to their excellent performances in solar cells. In these halide perovskite materials a long diffusion length of around 1.5 µm [Li18] does not necessarily imply a high charge carrier mobility but instead results from the long carrier lifetime, which can be several tens of nanoseconds and indicates the lack of non-radiative surface recombination centres and trap states, which is a strong advantage in comparison to traditional semiconductors such as GaAs [Dem10].

5.3.2 Photon Number Estimation

For the simulations presented in the previous subsection, the number of excitons created is set to be the number of pump laser photons incident on the NW. With the power and energy of the laser and a geometric correction factor the numbers are estimated. The wavelength of the excitation source of 532 nm corresponds to an energy per photon of $2.33\text{eV} = 3.73 \cdot 10^{-19}\text{J}$. With an average power of 34 nW and a repetition rate of 8.15 MHz this sums up to a number of 11000 photons per pulse. A geometric correction factor accounts for the area overlap between the laser spot and the nanowire bundle (c. f. figure 5.11) and is determined as ratio between the area of a NW and the excitation spot. For the longest wires of 1 µm of length the factor is $1/180$, for the shorter ones with 0.5 µm it is $1/360$. In one bundle there exists approximately 150 NW of different length. As a result there are at most around 60 photons and in average around 45 photons reaching a nanowire and creating an exciton.

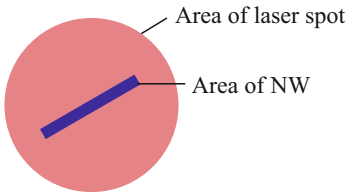

Figure 5.11: Sketch of the approximate size relation of the excitation laser spot and the NW. The overlap in area is used to estimate the number of photons reaching a NW per laser pulse.

Figure 5.12 compares the time-resolved PL emission from simulations with $\mu_e = \mu_h = 3\,\frac{\text{cm}^2}{\text{Vs}}$

and 1, 10, 30 or 100 photons per pulse of the laser irradiation (coloured lines) with the experimental data (symbols) from the same bundle NWB3 that was considered in the previous subsection. In the simulations the initial exciton creation rate is set to 100 %, i. e. all pump laser photons are absorbed and create an electron-hole pair. The normalization of the PL is adapted to the number of incident photons to account for the increased or decreased PL emission through the higher or lower number of excitons. To this end, the normalized PL is multiplied by one tenth of the number of photons.

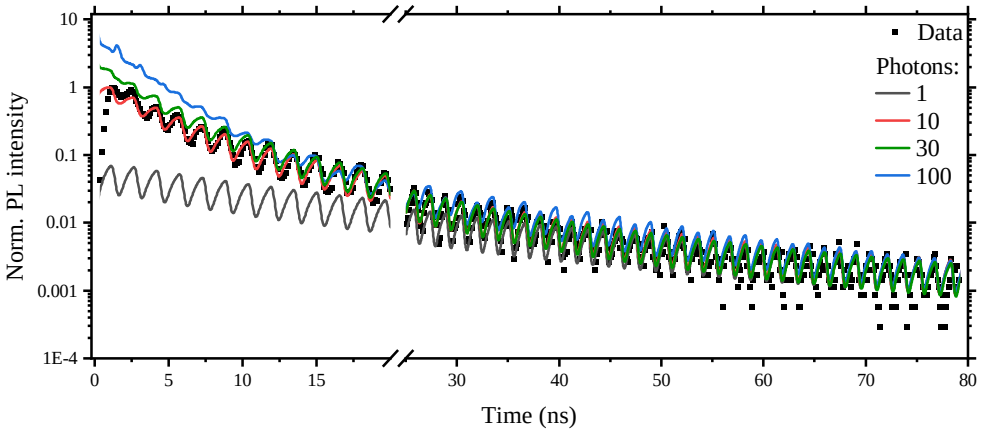

Figure 5.12: Simulated emission with $\mu_e = \mu_h = 3\,\frac{\mathrm{cm}^2}{\mathrm{Vs}}$ for four different numbers of incident pump laser photons on the NW bundle NWB3. The emission functions for 1 (grey line), 10 (red line), 30 (blue line) and 100 (green line) photons are compared to the experimental data (symbols).

A comparison of the temporal evolution with the four different numbers of photons used to excite the nanowire bundle reveals huge changes. As shown in figure 5.12 all emission functions show high agreement after 30 ns, when the charge carrier densities have become similar in all settings. In this region, all simulated curves match the experimental data. In the first few nanoseconds the simulations differ largely in height and also reveal differences in the markedness of the oscillations. If the number of incident photons is very high, some charge carriers screen the electric field and suppress the transport and thus the periodic modulation. It can be clearly seen for the green line in figure 5.12 with 100 excitons created per laser pulse that the amplitude of the oscillations shortly after the excitation is massively reduced. For 30 incident photons per pump laser pulse (blue line), the difference to the data becomes much smaller and only during the first few oscillations a suppression can be seen. The perfect match of the red line is calculated with 10 photons, while after a further reduction to only one photon per pulse, creating one exciton (grey line), the modulation occurs directly at the beginning and persists over the whole time scale, but does not fit to the three decay rates. The first few nanoseconds show the significance of determining the correct number of incident photons. The result of the parameter scan of around 10 incident photons fits roughly to the estimated number of excitons in the system of 60 which assumed a complete absorption of all photons incident on the NW bundle in the experiment and hence is slightly too high. It can be seen from the blue line in figure 5.12 that an assumption of 30 photons is also close to the experiment with screening only occurring in the beginning and a full recovery of the modulation within 10 ns. The consistency between the calculated estimate and the result of the simulation indicates that, indeed, the absorbance of the lead halide perovskites is high and the number of excitons

present in the system at the same time can be pinned to at most a few tens. This proves that the experiments were performed at low charge carrier densities and in a regime of very low field screening, revealing the real single carrier mobilities and no collective effect.

The screening of the field and the resulting suppression of the modulation observed in the simulation is also examined experimentally through a variation of the excitation power. The results of this study are presented in section 5.6.

5.3.3 Additional Experimental Parameters

Despite the obvious relevant parameters such as the mobility and the number of excitons in the system, there are some more variables in the modelling of the structure that have to be considered to mimic the real setting as accurately as possible. The basic material parameters are taken from literature or are received from other experiments performed by the collaborators of the Photonics and Optics Group of the LMU who also grow the samples. But the experimental environment also plays a major role for the behaviour of the charge carriers in the system. This includes the acoustic power applied to the system, the temperature and the length of the NW, i. e. the transportation length for charge carrier.

The simulation offers different ways to include those settings. The temperature and the length of the wire are fixed for one simulation run as they are generally also not changed during one experimental series. In contrast, the power of the SAW P_{SAW} can be included as a sweep through several values similar to the experiments. Figure 5.13 presents five such simulations of the time-resolved PL emission in a power series. All other simulation parameters are kept constant. There are clear differences not so much in the trend of the curves but all the more in the amplitude of the oscillations. While for low acoustic powers only small modulations in the decay rate are visible, the high fields induce pronounced oscillations. Too high power levels result in artefacts of the simulation due to its finite step method. If the transport of a particle in one time step is too far, the simulation will produce false results. This can be prevented by decreasing the step size which in turn will lead to an increase of the computation times. As the simulated range of SAW powers is already nicely fitting to the maximum power in the experiment $P_{SAW} = 23.5\,\mathrm{dBm}$, higher values are not further considered.

In the simulation the acoustic power denotes the actual energy of the surface acoustic wave in the system. In the experiment, the applied power is reduced by the efficiency of the IDTs (c. f. the insertion loss in subsection 3.3.3) and the given values correspond to the power applied to the chip. Furthermore, the simulation does not include power losses of the wave due to heating of the substrate. A direct comparison of the two power values is thus not possible. Nevertheless, it can be used to qualitatively analyse the behaviour which in both cases shows that the amplitude of the modulation correlates with the strength of the electric field (see the inset of figure 5.13 and the study of section 5.1). This fits nicely to the developed phenomenological model from section 5.2 where a higher field results in stronger polarizations of the excitons. The non-existent increase in the decay rate with stronger fields is a result of the non-radiative losses being neglected in the simulation. In the model there exists no surface of the nanowire and no explicit surface recombinations are implemented. Therefore the power variation in this case was used for a comparison of the shape of the oscillations.

Despite its more intrinsic effects, the temperature has significantly less influence on the simulated PL emission then the applied electric field. Since the exciton binding energy of the metal halide perovskites is relatively high compared to classical semiconductors, a significant number of excitons already exists at room temperature. At 290 K the thermal energy equals the

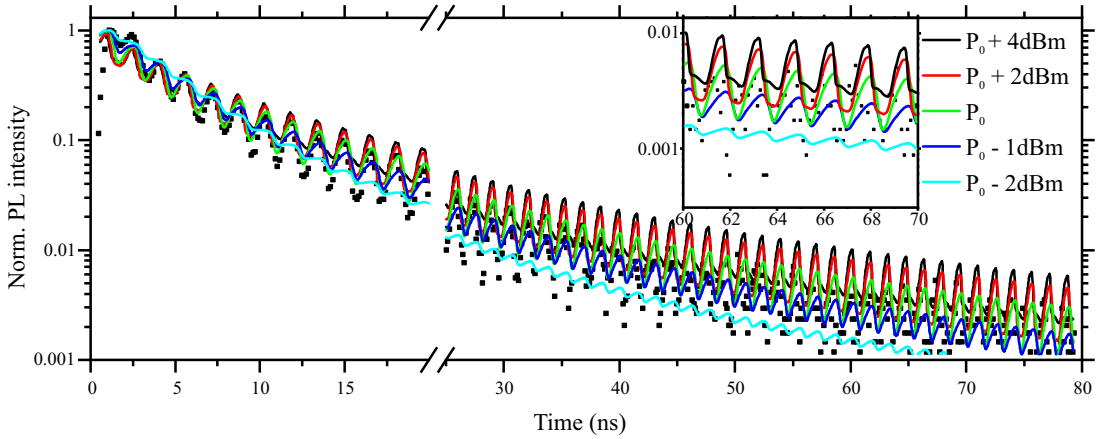

Figure 5.13: A variation of the applied acoustic power in the simulation (coloured lines) reveals a strong dependence. The absolute numbers are not directly comparable to the experiment. The inset represents a zoom-in of the indicated region for a closer inspection. For reference the experimental data of NWB3 (black dots) is shown.

binding energy of 25 meV for $CsPbI_3$, whereas for GaAs one would need to go down to 116 K. Hence, in the perovskites a large number of charge carriers is present in the form of an exciton at room temperature. This is the reason, why no big changes are expected in the dynamics of the particles when cooling the system down to low temperatures. The corresponding simulation presented in figure 5.14 confirms this. Panel (a) presents the simulation for five different temperatures ranging from 300 K (black line) to 85 K (red), 30 K (green), 10 K (yellow) and 5 K (blue) together with the experimental data for 296 K shown as symbols. To visualize the differences between the simulated data, panel (b) shows a zoom-in to a small time window between 60 ns and 75 ns after the excitation. Taking a closer look on these simulations, it becomes apparent that the main difference between the curves is that at low temperatures the amplitude of the two oscillations in a SAW cycle are no longer the same. This small variation implies a differentiation between the directions of movement of the charge carriers. This discrimination between the two phases of the SAW is induced by the movement of the SAW. At one phase the charge carriers follow the propagation of the wave while half a period later their motion runs counter to that of the wave. During the decrease of temperature and thus the reduction of kinetic energy of the particles, this discrimination of the direction of motion becomes visible.

The dependence of the decay rates on the temperature is neglected here and the lifetimes are kept constant to examine the effect of temperature on the exciton more generally. The change in lifetime would superimpose small effects based on the excitonic behaviour. It is seen in the experiments in section 5.5 that indeed the most prominent effect in the dynamics of charge carriers in the perovskite NWs is the variation of the lifetime with temperature.

The measurement of a whole bundle of NWs at the same time raises the question if they act as a larger compound or as a collection of individually behaving single NWs. In the simulation this can be accounted for by adjusting the length of the area under consideration. The bundle accumulates to a total length which is on the order of half the wavelength of the SAW which is 11 µm, while an individual wire is no longer than 1 to 1.5 µm. This is relevant as it defines the portion of the wave that is simultaneously applied to the wire. The length of the bundle is exactly such that one half of a full wave fits in which means that there is always an extremum

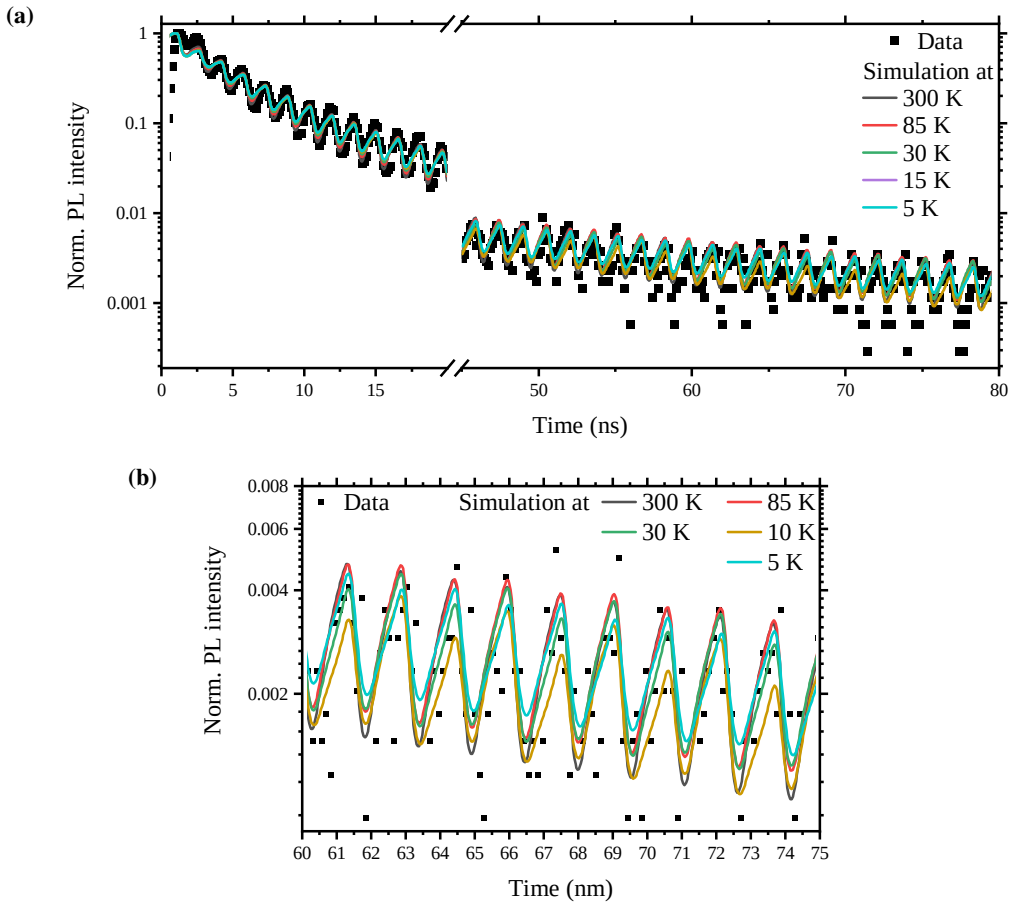

Figure 5.14: (**a**) Simulation of the PL emission arising from the charge carrier dynamics induced by a SAW for different values of the temperature ranging from 300 K down to 5 K (coloured lines). The experimental data of NWB3 at 296 K is shown in black symbols. (**b**) Zoom-in of panel (a) in a small time window from 60 ns to 75 ns after the excitation.

and a zero crossing within the length of the bundle. In contrast, the single wire only experiences a varying electric field pointing in different directions.

As a further consequence the length differences imply that a single wire will be spatially fully excited by the laser whereas the bundle will only have charge carriers created at a certain spot of 1.5 µm width. The mean values extracted from the simulation do not differ much regarding the length of the wire. Thus, it is still not clear whether there is transport of charge carriers between the NWs or the data is a collection of individually emitting NWs. The knowledge of the existence of such an inter-wire transport channel reveals deeper insight into the mechanism that forms the bundles in the solution and during the drying process. Therefore, in the next section, the topic will be addressed experimentally.

5.4 Directionality

For the investigation of the charge carrier dynamics inside the nanowires, it is of huge interest to also probe the inter-wire transport of charge carriers. As in this thesis bundles of NWs were studied instead of single structures, it was possible to study the possibility of transitions between

the individual wires. In the experiments presented so far, the SAW was always travelling along the axis of the bundle and the majority of NWs to enlarge the interaction area and hence, increase the overall effect. Like this, the length of a single NW is large enough for the charge carriers inside to be influenced by the gyrating electric field. But the method does not allow for a differentiation between a collective effect and a collection of individually modulated structures. One way to probe for this question is by exploiting the fundamental geometry of the NWs. Due to their very small cross section of only 10 nm x 10 nm, being smaller than the exciton radius of 12 nm, it is not expected to significantly polarize or even separate the charge carriers in this direction. Thus, the mechanism responsible for the observed modulation in the PL decay is largely restricted. To probe this experimentally, the nicely aligned NW bundles are now set under the influence of a SAW propagating perpendicular to their main axis and hence, applying an electric field that has only a very small interaction length with each single wire. If there is a transition of charge carriers between individual NWs, the modulation persists even in this configuration because the width of the bundle exceeds the exciton radius by two orders of magnitude. But for non-interacting NWs it is expected that any SAW-driven process becomes highly directional with a dependence on the relative orientation of the NW axis and the propagation direction of the SAW. A similar experiment was performed by Jörg Kinzel *et. al* to prove the directionality of SAW-driven charge carrier transport in single GaAs NWs [Kin11].

Figure 5.15 gives an overview over such an investigation of the dynamics of charge carriers in a NW bundle in two perpendicular directions. The substrate is prepared in such a way that there exist two SAW paths that are aligned at a 90° angle towards each other (c. f. figure 3.4(b)). The NW bundles under investigation are placed at the intersection of these two delay lines and the ones lying parallel to either of the paths are chosen. The SAW parallel to the axis of the NW bundle has a frequency of 324 MHz and is applied with its maximum of $P_{SAW} = 23.5\,\mathrm{dBm}$. The perpendicular SAW has a resonance at $f_{SAW} = 438\,\mathrm{MHz}$ and a slightly lower coupled power of $P_{SAW} = 17.5\,\mathrm{dBm}$. When the IDT that creates a wave propagating parallel to the axis of the NW is switched on, the usual modulation of the time-resolved PL emission is observed (figure 5.15(a)). The perpendicular IDT, in contrast, shows no significant change in the recording except for a slight reduction in the lifetime which might come from the massive heat intake the wave deposits on the substrate at these high acoustic powers. In both graphs the period of the applied SAWs of 3.1 ns and 2.3 ns are indicated. In the first panel the oscillations nicely coincide with half of the SAW's period as shown before, while the perpendicular arrangement of panel (b) shows no such features.

For the graph shown in figure 5.15(c) the two SAWs are applied simultaneously on the same NW bundle as before (NWB3). A temporal alignment with a nearby perpendicular bundle ensured the contemporaneity of both waves at the relevant position which is necessary due to the modulated application of the SAW to prevent excessive heating especially in the case of two SAW beams applied concurrently. The result of this experiment is an almost perfect superposition of the effects produced by the individual application of the two SAWs: The manner and height of the oscillations show no dependence on the perpendicular SAW which only imposes a slight increase in the basic decay rate, similar to figure 5.15(b), which fits to the argument of heat creation. The modulation also follows the $2 \cdot T_{SAW,\parallel}$ period and therefore necessarily results from the parallel SAW beam. This is further confirmed by the frequency analysis of figure 5.15(d). The Fast Fourier Transform (FFT) of the data presented in figure 5.15(c), in violet, clearly shows a response at 648 MHz corresponding to twice the frequency of the parallel SAW and no features at the other relevant frequency or its

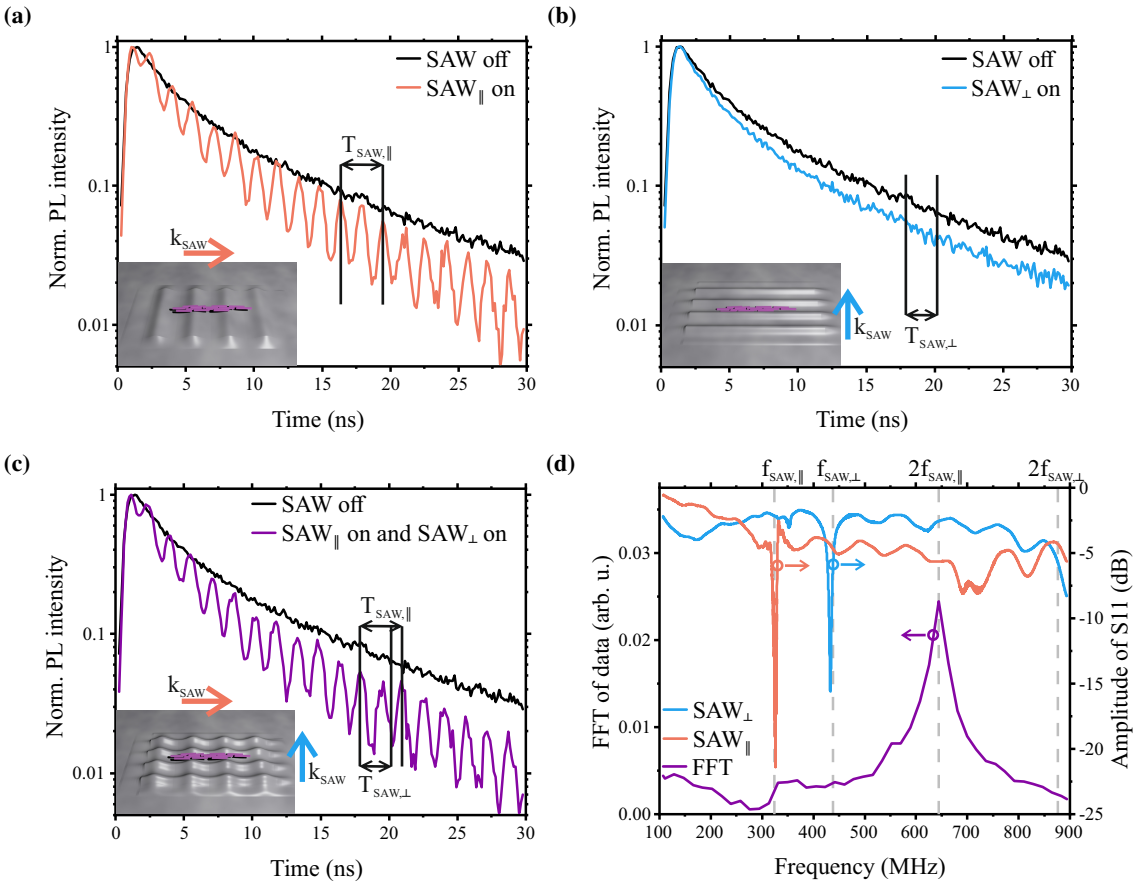

Figure 5.15: Time-dependent PL emission of bundle NWB3 with a SAW applied (**a**) parallel (red) and (**b**) perpendicular (blue) to the axis of the NWs compared to a study without acoustic wave (black). The two SAWs have different frequencies of 324 MHz and 438 MHz, respectively, for a better distinguishability. Their periods are marked in the graphs. The insets and accompanying arrows illustrate the arrangement of wave and nanostructures. In (**c**) both SAWs are applied simultaneously (violet). (**d**) An FFT analysis of the data (violet) from panel (c) complements the analysis together with the reflected electrical signals from both IDTs used to excite the parallel (red) and perpendicular (blue) SAW beams. The frequency analysis of the recorded data clearly shows a response of the modulation to $2 \cdot f_{SAW,\parallel} = 648$ MHz and no signature of the other occurring frequency. The data of this figure was also published in [Jan19].

doubled value. An electric reflection measurement of the IDTs reveals their spectrum by exhibiting a distinct dip at the frequency of maximum energy transmission. The results are the aforementioned values of $f_{SAW,\parallel} = 324$ MHz and $f_{SAW,\perp} = 438$ MHz, respectively. These frequencies and their double are indicated in the graph as a guide for the eye. The analysis proves unambiguously that no evidence of a charge carrier dynamic induced by the perpendicular SAW can be found, not even with the support of a parallel SAW that already brings the charge carrier into motion. As a consequence, the inter-wire transition of electrons or holes from one NW to another can be excluded and the effect determined to be independent in each structure. Thus, the presented studies represent an enhancement of a single NW study through the collections of multiple nanostructures at once

A further control experiment to check the reliability of the finding is to switch the directions and perform the same study on two NW bundles that are aligned perpendicular to each other.

This excludes that the directionality arises from the anisotropy of the piezoelectric material for SAW excitation.

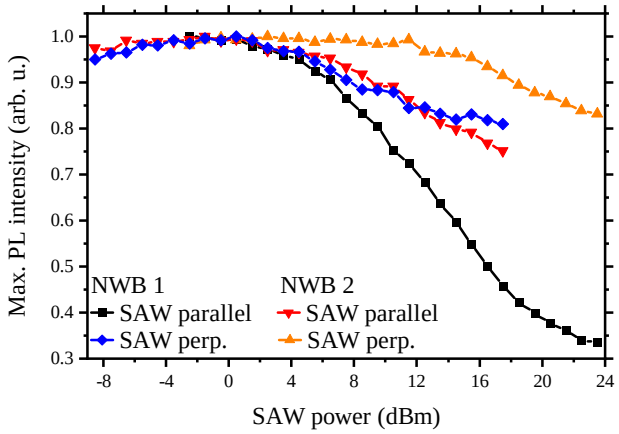

Figure 5.16: PL quenching of the two NW bundles NWB1 and NWB2 perpendicular to each other under the impact of a SAW propagating parallel (black and red) or perpendicular (blue and orange) to their main axis. The power values are the ones applied to the IDTs, the ones for IDT2 (blue and red) are corrected according to the efficiency of the coupling (c. f. figure 5.15(d)).

Figure 5.16 compares the quenching, analogous to figure 5.2(b), of two perpendicular NW bundles due two perpendicular SAWs with increasing acoustic power. The two SAWs, parallel and perpendicular to NWB1, have frequencies of $f_{SAW} = 324\,\mathrm{MHz}$ and $f_{SAW} = 438\,\mathrm{MHz}$, respectively. The characteristic power dependences consist of the slow onset of PL suppression and the steep reduction at intermediate powers before reaching saturation. The black symbols present the data from NWB1 under the influence of a wave propagating parallel to its axis with increasing power. A strong suppression of the emission down to 35 % of its initial value can be found for the strongest SAW. In contrast, when a perpendicular SAW is applied the PL peak intensity is significantly less suppressed and saturates already at around 80 % of the unperturbed emission (blue symbols). The PL data of the second examined NW bundle NWB2 in red and orange exhibit a similar, but less pronounced behaviour. The difference between the PL emission of the bundle under the influence of the parallel and the perpendicular SAW shows that there is a clear directionality observable even for exchanged orientations of the IDTs relative to the NW axis. The lack of saturation in the quenching of the PL emission of this NW bundle is a result of the anisotropic nature of the substrate. The efficiency of the coupling of the electrical power to the mechanical wave in the substrate is strongly dependent on the cut of the material and the propagation direction of the SAW. Here, this effect is already partly compensated by a subtraction of 6 dB from the actually applied power. The value is extracted from the difference in the amplitude of the minima in the electric reflection measurements of both IDTs presented in figure 5.15(d) which evaluates the quality of the IDTs and their couplings. The more accurate power-dependent transmission measurement presented in subsection 3.3.2 can not be applied to the second IDT because of a malfunctioning counterpart on the other end of the delay line. Therefore, the less accurate method of reflection relying only on one IDT has to be used. Nonetheless, the principal insights are clearly visible and allow for the relevant conclusions to be drawn.

5.5 Temperature Dependence

One of the big advantages of the lead halide perovskite structures is their stability and measurability at room temperature, in contrast to many conventional semiconducting materials. Due to a high binding energy of the excitons the low temperatures are not necessary to create the quasi-particles and to be able to study them. The temperature at which the thermal energy is enough to break the excitons is $T_{exciton} = 290\,\mathrm{K}$ – not too far below room temperature. This means under normal conditions already many charge carriers are bound and form excitons.

Nevertheless, it is interesting and worth exploring the behaviour of the NWs under decreasing temperature conditions where the additional complexity from the thermal effects is reduced. This gains deeper insight into the photophysical processes present in the perovskite material. At first, the unperturbed PL emission spectrum and the response to a SAW ($P_{SAW} = 23.5\,\mathrm{dBm}$, $f_{SAW} = 324\,\mathrm{MHz}$) for the bundle NWB4 are analysed in figure 5.17(a) for different temperatures. The peak position (λ_0), the shape (FWHM) and the SAW-induced quenching behaviour presen-

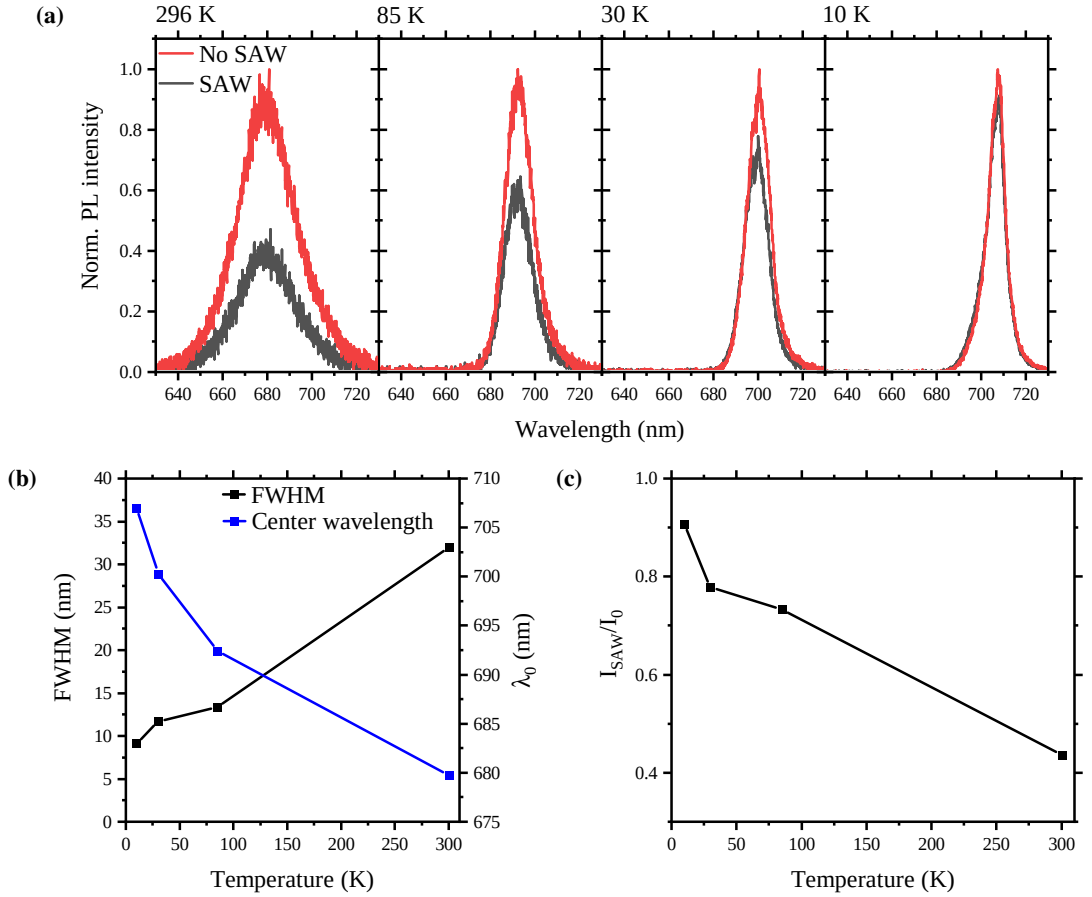

Figure 5.17: (**a**) The normalized temperature-dependent emission spectra of NWB4 are shown for four different temperatures between 296 K and 10 K. The quenching of the PL under the influence of a SAW is shown in comparison to the unperturbed emission spectrum (black and red curves, respectively). (**b**) Extracted temperature-dependence of the FWHM and the center wavelengths of the unperturbed peaks. (**c**) Evolution of the quenching efficiency of the SAW as a function of the temperature. The quenching is given as ratio to the initial peak height I_0.

ted in the panels (b) and (c) change strongly as the temperature is decreased from $T = 296\,\mathrm{K}$ to

85 K, 30 K and 10 K.

In panel (a) the broad PL emission at room temperature narrows down for lower temperatures due to a reduction of the thermal broadening, analogous to other emitting materials and atoms in a gas [Sie86]. To quantify the behaviour, the FWHM for each of the unperturbed emission peaks (red curves) is determined and plotted in figure 5.17(b). The process is based on exciton scattering with phonons and impurities and as a result of composition fluctuations and granular boundaries. The asymmetric broadening of the high energy tail of the spectrum arises from the formation of more energetic excitons with a wider distribution of energy. Interestingly, the wavelength of the emission follows a redshift in the cooling process (c. f. figure 5.17(b)) which is counter-intuitive and in disagreement with the Varshni behaviour for standard semiconductors [Var67]. This phenomenon was until recently a topic of research and was found in various compositions of perovskites [Dir18; Dit15; Yu11; Sai16]. In 2016, it was examined in detail experimentally and theoretically in organic-inorganic halide perovskites. The researchers attributed the phenomenon to a stabilization of the valence band maximum as a consequence of the thermal lattice expansion with increasing temperature [Dar16]. This is possible due to a positive bandgap formation potential of the system with respect to the volume [Fro14]. The expansion reduces the overlap of the participating orbitals and hence, increases the bandgap.

The evaluation of the quenching of the SAW in figure 5.17(c) reveals an easing for lower temperatures as a result of the creation of more and more excitons with a lower probability of complete separation compared to free charge carriers. Hence, their recombination is only temporarily delayed by the SAW but not suppressed. In the time-integrated study this delaying can not be resolved and only completely separated electrons and holes which do not contribute to the radiative decay are seen as effect of the acoustic field.

In the time-resolved studies presented in figure 5.18 the contrary is found. It shows the time-resolved emission of NWB4 for three different temperatures without (light colours) and with (dark colours) a SAW (324 MHz at $P_{SAW} = 23.5\,\mathrm{dBm}$). With decreasing temperature from 296 K (a) to 85 K (b) and 5 K (c), the decay rates and the relative positions of modulated and unmodulated decays change significantly.

When lowering the temperature, at first the response to the SAW's electric field is getting stronger simultaneously with an increase in the lifetime. At a temperature of 85 K the amplitude of the oscillation is three times as high and the unperturbed decay constants change to $\tau_{85K,1} = 29.5\,\mathrm{ns}$, $\tau_{85K,2} = 7.3\,\mathrm{ns}$ and $\tau_{85K,3} = 2.0\,\mathrm{ns}$. This seems to be a consequence of more excitons taking part in the radiative decay and less being separated into electrons and holes or decaying non-radiatively. It was discussed already for figure 5.17 that more excitons are present in the system and the resulting less efficiently quenched PL emission. While this meant, that less electrons and holes can be permanently separated and lower the radiative emission, in time-resolved studies regarding the oscillating response to the SAW the excitons are the important measure. The binding of the electron-hole pair holds them together and enhances the recurrent opposing movement.

Below 85 K the amplitude of the oscillations decreases again as a result of the increased decay rate and the lowered number of charge carriers being present. It reaches a value at 5 K close to the one for room temperature. The same holds for the lifetimes which also approach the original value again. When comparing the lifetimes of the decays with applied SAW to the unperturbed ones it is noticeable that the overall lifetimes change through the SAW. In the case of unperturbed decays, between 85 K and 5 K the lifetimes increase strongly with temperature and are slightly reduced towards room temperature. But there is also a shift of the contributing amounts of the decay rates which shift from 296 K to 85 K towards the slower decays and from

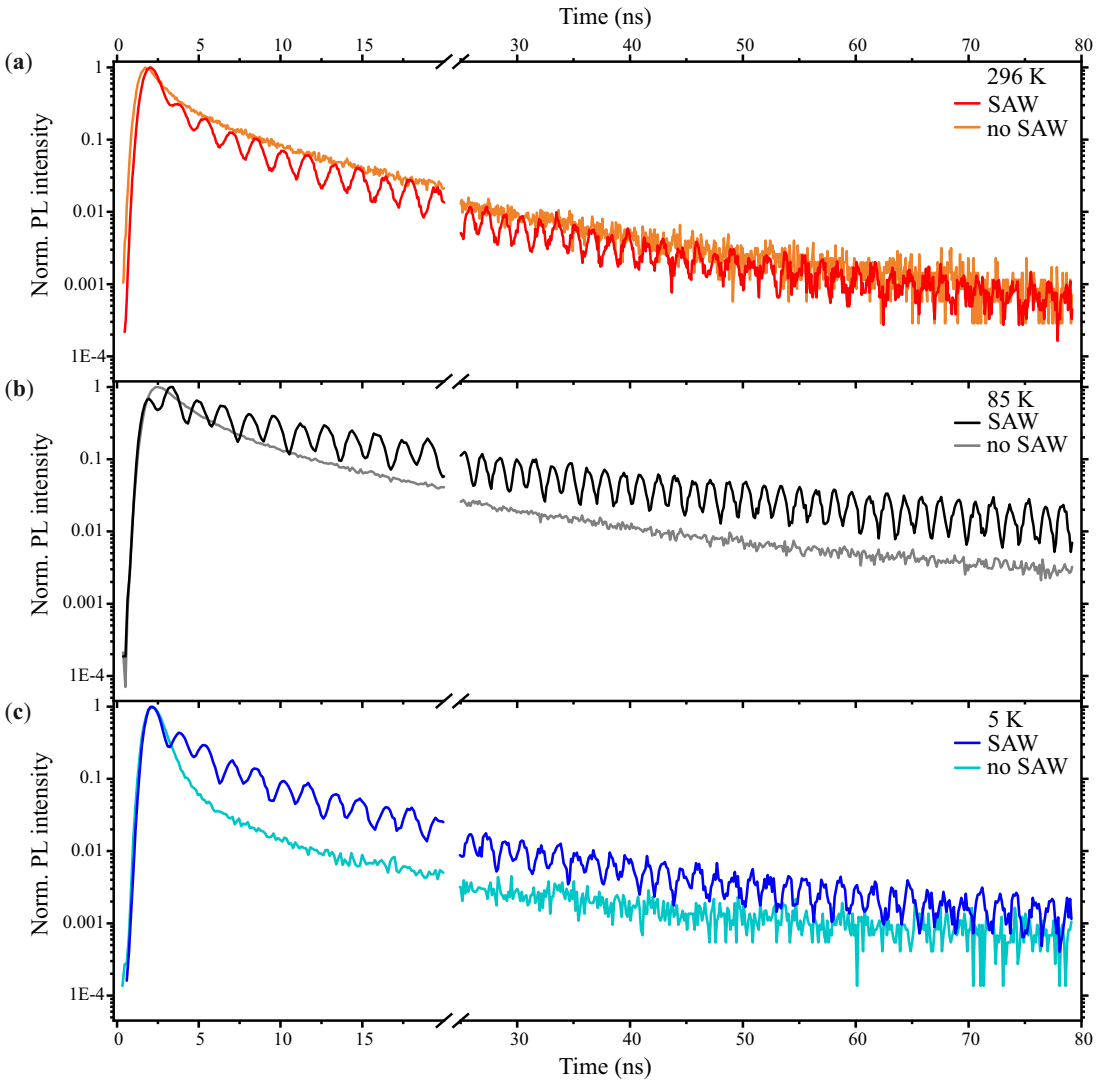

Figure 5.18: Time-resolved PL emissions for 296 K (**a**) , 85 K (**b**) and 5 K (**c**) of NWB4 under the application (dark colours) of a SAW with 324 MHz at $P_{SAW} = 23.5$ dBm compared to the unperturbed decays (lighter colours).

85 K to 5 K back towards the faster ones. The values for all three decays at the three presented temperatures are summarized in table 5.2.

	τ_1	τ_2	τ_3
296 K	16.8 ns	4.8 ns	1.4 ns
85 K	29.5 ns	7.3 ns	2.0 ns
5 K	119.1 ns	11.2 ns	0.9 ns

Table 5.2: Decay constants for the unperturbed tri-exponential decays of the perovskite NWs at three different temperatures.

Adding the SAW results in a slightly different outcome. The basic decay rate of the lowest temperature is now above the one for room temperature indicating that for 296 K the dissociation of charge carriers is a dominant process that significantly reduces the overall lifetime through non-radiative decays. These findings confirm the assumption of the free charge carriers being affected by the SAW via separation and the excitons being mainly first polarized before the dissociation sets in. Finally, it can be noted that the modulation persists over the entire temporal and thermal measurement range. As a consequence it can be denoted that the trap state density inside the NWs must be very low because otherwise at low temperatures and low charge carrier densities, the particles would be trapped and no influence of the SAW would be visible any more. As this is not the case even for very little charge carriers remaining, thus at the very end of the decay, the conclusion of a low trap state density can be drawn.

The long lasting lifetime of the lead halide perovskite at 85 K makes the material an ideal candidate for charge transport devices with a maximum efficiency around the temperature of 85 K. The very low non-radiative decay and trap state density contribute to the long lasting existence of excited charge carriers.

A further analysis of the modulation in a comparison with an unperturbed decay at low temperatures in figure 5.18(b) and (c) reveals for low temperatures that the reference study follows more the lower envelop of the modulated recording in contrast to high temperatures where it resembles the upper envelop function (panel (a)). This allows for a closer look into the changed dynamic of the charge carriers inside the nanostructure. This slowing down of the decay instead of its acceleration is further evidence of the underlying change in the state in which the carriers are present - as free electrons and holes or bound in an exciton. It can be explained by the intuitive picture that takes only the excitons into account. When an excitons is polarized it is less likely to decay in that state. But the electron-hole pair is still excited and thus will decay later when the polarization is reduced. During the maximum overlap of the wavefunctions the decay rate equals the one for a non-perturbed decay, but in between the PL lifetime is enhanced due to the partial and temporal separation of the charge carriers. Without the dissociation and thus without the removal of participants in the decay, one would expect this form of modulation for the whole NW PL emission. The lack of free electrons and holes results in exactly this, as a consequence of the enhanced formation of excitons at lower temperatures due to their by the amount of the binding energy reduced energy.

Applying the model discussed in section 5.2 to the low temperature results in the fitting curves (red lines) shown in figure 5.19(a) and (b) for 85 K and 5 K, respectively, together with the data (black lines) already presented in figure 5.18. The good agreement between the fitting functions and the data also at low temperature indicates that our simple phenomenological model also holds for low temperatures and that no additional mechanism sets in. Interestingly,

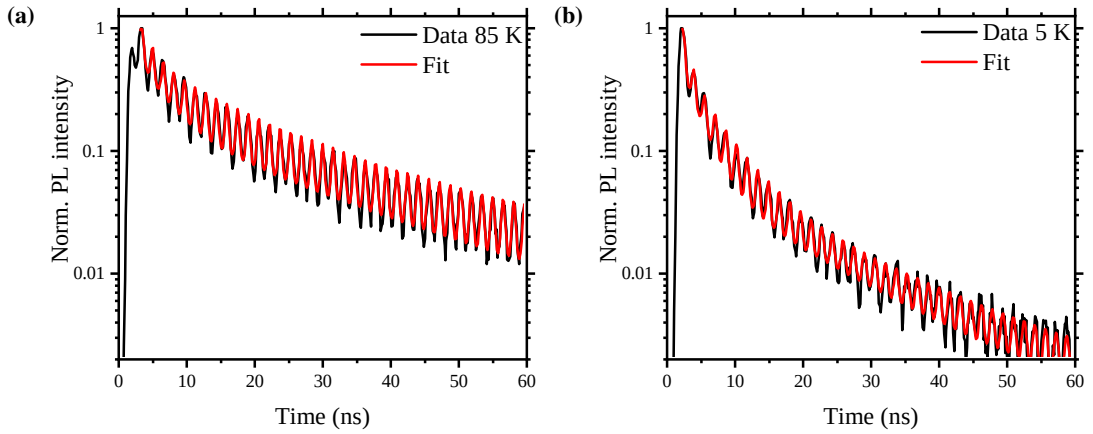

Figure 5.19: Fit of the low temperature data with the phenomenological model introduced in section 5.2 for (**a**) 85 K and (**b**) 5 K.

the fitting parameters for the adapted overall decay rates are above the unperturbed decay, indicating that the decay itself under the influence of a SAW does not slow down for lower temperatures, in contrast, the decay rate changes even partly increase due to the SAW. But the amplitude of the faster decays decreases while the slower decays gain influence, resulting in a slower long term decay of the PL which is also observed in the comparison of the different panels of figure 5.18. For example, for 85 K the contribution of the fastest decay decreases upon applying a SAW from 95 % to 75 %, for 5 K it is even more: from 95 % to 61 %. This is a strong indication that the principal mechanisms stay the same, but when less free electrons and holes are present in the system, these tend to decay through the slower decay channels as this first parameter of the model was previously correlated with the dissociation of an exciton or free charge carriers.

	$\frac{\Gamma_{1,0}}{\Gamma_{1,ref}}$	$\frac{\Gamma_{2,0}}{\Gamma_{2,ref}}$	$\frac{\Gamma_{3,0}}{\Gamma_{3,ref}}$	$\frac{\Delta_1}{\Gamma_{1,ref}}$	$\frac{\Delta_2}{\Gamma_{2,ref}}$	$\frac{\Delta_3}{\Gamma_{3,ref}}$
296 K	1.80	1.39	2.61	0.63	2.04	0.81
85 K	1.50	1.96	5.30	0.63	1.32	4.42
5 K	9.40	4.27	2.53	2.36	1.90	1.74

Table 5.3: Relative fitting parameters for the application of the phenomenological model onto the observed modulations for three different temperatures.

The second parameter is a measure for the polarization of bound pairs and influences the height of the oscillations in the fit. The values of Δ_3, the parameter for the fastest decay, for low temperatures increases massively. As this is the decay with the highest contribution to the overall decay, the result is an increased oscillation amplitude, as seen clearly in figure 5.18(b) for 85 K. For 5 K the change is not that prominent, but still significant. Notably, out of the three presented temperatures, the study at 85 K shows the highest modulation amplitude as well as the slowest decay rate. The reason for the highest polarizeability being at this temperature could be the focus of future detailed studies.

In the experiments of all the different temperatures the modulation of the PL emission persists for the whole time of the decay until the extracted number of photons becomes lower than the

noise level. Thus, the very low trap state density can be confirmed even for low temperatures and corroborates the high crystal quality of the halide perovskite NWs.

5.6 Carrier Density Dependence

For experiments performed under electric fields, it is important to consider not only the externally applied field, but also the internally induced field by the displacement of charge carriers. The separation of electrons and holes leads itself to an electric field pointing towards the opposite direction of the inducing field. Any effects based on the strength thus have to consider the effective electric field which is calculated from the vectorial sum of the two. The induced internal electric field is highly dependent on the number of mobile charge carriers present in the structures and leads to an internal screening of the outer field. To effectively study the dynamics imposed by the external field, it has to be ensured that the density of charge carriers is low enough. The density is controlled via the excitation power of the laser and a trade-off has to be made between the shielding and the amount of emitted signal. In all the presented studies so far, the excitation laser was set to 23 nW $\left(56\,\frac{\mathrm{W}}{\mathrm{cm}^2}\right)$. An analysis of the efficiency of this power level is performed in figure 5.20 for time-integrated spectra in (a) and time-resolved recordings in (b). The laser power is varied between 16 $\frac{\mathrm{W}}{\mathrm{cm}^2}$ and 98 $\frac{\mathrm{W}}{\mathrm{cm}^2}$ corresponding to 6.5 nW and 39 nW at a spot size of 1.6 µm reaching the sample. The applied SAW has a frequency of 324 MHz and a power level of $P_{SAW} = 23.5\,\mathrm{dBm}$.

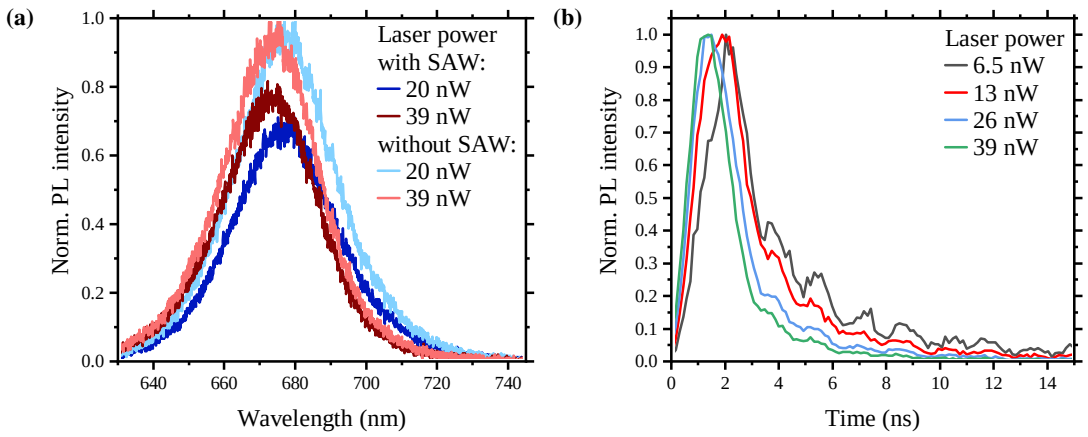

Figure 5.20: A variation of the excitation power leads to different charge carrier densities present in NW bundle NWB4. (**a**) The time-integrated PL emission spectra for 20 nW (blue) and 39 nW (red) excitation with (dark colours) and without (light colour) the application of a SAW. (**b**) Time-resolved study on the emission characteristics for four different power levels of the excitation laser to compare the strength of the modulation.

In the spectrally resolved, time-integrated studies in figure 5.20(a) the reduction of the quenching can be clearly identified. The blue lines represent the NW emission under low laser excitation without (light blue) and with (dark blue) the application of an acoustic wave of high power. The same study is performed with doubled laser power and is shown in the graph with and without the SAW in dark red and light red, respectively. The suppression of the PL for higher laser powers is diminished and accompanied by a blue shift that can be attributed to a local heating of the NW bundle (c. f. section 5.5). A clear shielding effect can therefore be

observed already with a doubling of the laser intensity in the nW regime. According to the calculations performed in subsection 5.3.2 this corresponds to an increase in the number of created electrons and holes from around 50 to 100. Due to the small size of the NWs these small numbers are already sufficient to influence each other and to shield the external electric field.

With increasing power deposited on the sample, the charge carrier lifetime continuously decreases (figure 5.20(b)), which can be explained by a bimolecular recombination mechanism (the electrons and holes exist in non-negligible part as free charge carriers) [Dar16]. The analysis of the time-resolved emission reveals further the effect of too many charge carriers being present which can be saliently observed. With an increasing excitation power the oscillation height of the modulation reduces drastically. While the slightest excitation with 6.5 nW (black curve) facilitates the response to the electric field in a temporarily modulated sinusoidal decaying behaviour, the increasing excitation powers (red, blue and green) suppress this behaviour evermore until it is barely visible for 39 nW. The presence of many free charge carriers in the system favours this reduced reaction to the field. In consequence, the stronger excitation of the NWs mostly involves a drastically enhanced number of free electrons and holes that strongly and permanently counteract the external electric field, reducing its influence on the bound excitons. The chosen excitation level of 23 nW for all studies gives a good compromise between small levels of shielding and enough output emission to have reasonable integration times. To study the dynamics of excitons in these structures it is thus necessary to control the excitation power and keep it at a low level.

5.7 Nanowires of $CsPbBr_3$

During the experiments on the $CsPbI_3$ nanowires the question arose what influence the different properties of the material have on the discovered behaviour. On the one hand the long excitonic lifetime is the key to the long time observations. On the other hand, the relatively high excitonic binding energy compared to III-V semiconductors provides the counter force to the electric field that separates the electrons and holes and thus enables the polarization and dynamic modulation of the excitons. The wide range of metal halide perovskites provides other materials with only small changes in the mentioned properties. In studying these, one can corroborate further the theory developed in the previous sections. In order to have only small variations in the compositions of the materials, materials with a single sort of anions were considered as the mixed halides tend to have structures with varying ratios of the halide.

In this subsection, the time-resolved study on $CsPbBr_3$ is presented, which has slightly faster exciton decay times and a higher exciton binding energy of around 47 meV [Dir18]. The bandgap of the material has also shifted to 520 nm, corresponding to 2.38 eV, so that for the excitation now a laser of 405 nm is used. To ensure comparability with the previous studies the same SAW chip was used. Figure 5.21 presents the dynamic modulation of the PL decay of $CsPbBr_3$ nanowires for a SAW of 324 MHz propagating parallel to the NW bundle. The black line shows a reference recording of the unperturbed PL emission of the structures, while red and blue show the effect of a strong SAW with $P_{SAW} = 23.5\,\mathrm{dBm}$ with two different phases with a distance of 90°, analogous to figure 5.5. The investigations show evidence that the higher binding energy of the excitons leads to a reduced reaction on the electric field of the wave. Nevertheless, the dynamic modulation of the emission is clearly visible and follows the $2f_{SAW}$ periodicity. A phase shift of 90° in the SAW function relative to the laser excitation results in a

reversed modulation of the time-resolved PL further emphasizing the periodicity. The reduction of the PL lifetime plays only a minor role here as it is still longer than the period of the SAW and thus, the observation of charge carrier modulation is still possible.

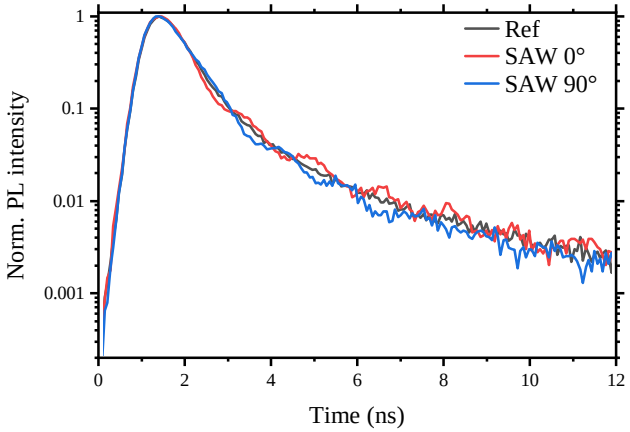

Figure 5.21: Time-resolved studies on a $CsPbBr_3$ NW bundle showing also slight modulations and a periodicity that corresponds to twice the SAW frequency.

One can also see that the overall increase in the decay rate, which was previously associated with the dissociation of the excitons or free charge carriers, is not very prominent for $CsPbBr_3$. This is consistent with the higher binding energy as this results in stronger binding of the exciton and less free charge carriers being present at room temperature. While for $CsPbI_3$ NWs the temperature at which the thermal energy equals the binding energy is 290 K, just below room temperature, the value for $CsPbBr_3$ is 545 K and lies much higher. As a result, only very few free charge carriers are naturally present in the material and the effect of dissociation can thus be neglected here. Due to the very small effect the SAW has in general on these wires at the provided acoustic power, an increase in the lifetime similar to low temperature studies on $CsPbI_3$ can not be observed.

These experiments on $CsPbBr_3$ show the high impact of the exciton binding energy on the polarizability of the quasi-particles. Similar to a reduction of the SAW power, an increase in the binding leads to less pronounced oscillations in the time-resolved PL emission. This further underlines the conclusion drawn from the investigations before that the modulation of the PL arises from the polarization of the excitons within the NWs.

5.8 Conclusion

This chapter demonstrated sub-decay time modulations on the PL emission of $CsPbI_3$ and $CsPbBr_3$ NWs. Time-resolved studies revealed the transport dynamics of electrons and holes under the influence of the electric field of a SAW. For $CsPbI_3$ were be shown to be persistent in large amplitude over the complete time scale of the decay. The periodicity being twice the one of the SAW lead to the assumption of exciton polarization being the underlying process. An analysis with a phenomenological model based on the dissociation and polarization of the excitons and free electrons and holes as mechanisms behind the behaviour revealed good agreement with the data. The model could also be used to estimate the number of charge carriers present in the system. The evolution of the fitting parameters with SAW power gave

insight in the onset and saturation of the two mentioned processes and revealed the same trend for all three decay constants.

A numerical simulation by solving the drift and diffusion equations was shown to be an expedient tool for the determination of the charge carrier mobilities of both charge carriers separately. To this end, numerous simulations were performed with varying values for the mobilities where the ratio between both parameters and their order of magnitude was changed and the best fit was extracted. As a result the mobilities could be pinned (a) to be the same for both charge carriers and (b) to be on the order of $\mu = 3\frac{\mathrm{cm}^2\,\mathrm{s}}{\mathrm{V}}$. A variation of other physical parameters in the simulation, such as the number of excitons created, the temperature of the system or the power of the applied SAW revealed more insights into the dynamics of the charge carriers in the NW system.

A subsequent study of the directionality of the observed phenomenon showed that the SAW can only affect the dynamic of the charge carrier if the interaction length is large enough. In the case of perpendicular application of the SAW no modulation of the time-resolved PL signal could be found, indicating that inter-wire charge transport between individual NWs does not occur and the examined bundles are loosely coupled structures. This implies that the observed data represents an ensemble mean and thus, no statistical analysis of a large number of individual NWs is needed.

A temperature-dependent study showed the unusual red shift of the halide perovskite crystal under cool down and unexpected behaviours of the decay times. The application of the SAW could further corroborate the findings at room temperature and revealed changes in the sensitivity to the wave depending on the temperature which ware confirmed by the results of the phenomenological model when applied to the new data. Finally, through the excitation laser power the charge carrier density at the beginning of the process could be controlled and the onset of the screening effect could be seen. This is reflected by the fact that the modulation decreases with increasing numbers of charge carriers as they compensate for the electric field of the SAW.

In conclusion, this chapter provided a deep insight into the dynamics of charge carriers in halide perovskite NWs at room and low temperature and led to the determination of the mobilities of both species.

Chapter 6

SAW-Based 2D Absorption Tomography

The idea of using a SAW device as a sensors is not new: for a long time they have been used in electronics, mainly for filtering frequency bands in the field of communication. Due to their high flexibility and capability to meet low and high frequencies up to GHz while still being small and at low cost, they are the most common filters used in mobile phones [Mil15]. But their potential is much broader. Due to the small layer of only about a wavelength in depth from the surface the acoustic wave is propagating in, SAWs are very sensitive to structural changes along their path which can be mass loading, stiffness changes or variations in the conductivity [Jia19; Kar19; Pas17; Fuh10; Siv08; Ric91; DAm89; Ric85]. The technique that exploits this property has the unique feature of being able to probe the desired properties of a material completely contact-free. In combination with different sensing materials, the SAW device chip offers a highly flexible, long lasting, easy to use and portable sensor. By the choice of the right material, the SAW device can act as a light detection sensor for various wavelengths ranges. In the conducted research perovskite NWs of different material compositions are used to produce an energy resolving visible light sensor through their tunable absorption edge in the visible range. Through the absorption of light by the material, free charge carriers are created that alter the conductivity within the travelling path of the SAW and lead to measurable changes in the SAW's transmission. This contact-free optical absorption measurement can be useful to probe the optoelectronic behaviour of the deposited material and check for the response to light.

In the previous chapter this characteristic was exploited to probe the dynamics of charge carriers in small nanostructures. This chapter focuses on the influence that the excited electrons and holes inside the NW have on the passing surface acoustic wave. In addition to the sensing performance, the SAW is used to enable spatially resolved 2D tomography through the application of specially designed IDTs which convert frequency information into spatial resolution. In taking advantage of this method, it is possible to build a multifunctional detector which is limited in the number of detection "pixels" only by the resolution of the frequency to location conversion and the size of the field of the sensing materials.

This acousto-optoelectronic interplay is explained in the following (section 6.1), before its practicability and fundamental evaluation are shown on the basis of first investigations on the chip LJ70 in section 6.2. Subsequently, the effective recording of the wavelength-dependent absorption of different materials is presented in section 6.3, which is necessary for the use and evaluation of a SAW device sensor based on 2D absorption tomography (section 6.4).

6.1 Principle of Spatially Resolved Photoconductivity Measurement

The near-surface nature of the SAW makes the wave highly sensitive to any influences that cause changes in the environment and especially on the surface. This property can be exploited in the design of SAW-based sensors which gained a lot of interest in recent years. The interaction between a SAW and a semiconducting material at the surface of the piezoelectric substrate is of reciprocal nature. On the one hand, as seen in the previous chapter, the electric and also potentially the mechanic potential of the acoustic wave can induce dramatic changes in the behaviour and dynamics of the charge carriers created in the material to probe. On the other hand, the excited electrons and holes in the system are also the origin of an electric field when separated and generate an electric current that can be e. g. subject to losses. Thus, it is not a one-sided influence, but generated charge carriers and surface waves are in a reciprocal relationship. The back action of the semiconducting material on the transmission of the surface acoustic wave is examined during this section and later on used to enable the sensing application of the device.

As already mentioned, the SAW is not only used to sense light in this chapter, but also acts as a position sensitive detector. This is achieved by the usage of so called tapered interdigital transducers (TIDTs). The principle is a variation of the thickness and distance of the fingers of the IDT perpendicular to the propagation direction as sketched in figure 6.1(a)). As the frequency $f_{SAW} = v_{sound}/\lambda_{SAW}$ is defined via the sound velocity of the material, which is constant, and the wavelength is defined by the fingers, the result of this arrangement is a change of frequency along the aperture of the structure. A single frequency applied to the transducer will thus excite a SAW only in that part of the IDT where the period of the fingers match the corresponding wavelength. The aperture of this wave is much smaller than the one of the whole transducer and therefore only interacts with a small strip of the area within the delay line. This basic mechanism converts frequency information into location information and vice versa through the detection.

An array of four such transducers is shown in figure 6.1(b), where always two opposing IDTs form a common delay line. Through this arrangement, it is possible to probe the inner area in a two-dimensional manner. The IDT pairs are designed to have frequency ranges from 294 MHz to 344 MHz and from 228 MHz to 284 MHz for the top-down and the left-right oriented delay line, respectively. The actual frequencies are slightly shifted due to uncertainties in the fabrication and the load of the metal electrodes. Thus the experimental values are 294 MHz to 343 MHz and from 223 MHz to 281 MHz, respectively. The wider end of the IDT always belongs to the lower end of the frequency rang as there the wavelength is the largest. Two drops of different materials are then applied to the area in the centre of the arrangement in such a way that they have a proper distance from each other. The narrower these drops are, the less already their weight influences the transmission of the SAW. If too much viscous weight is applied to the sample, the damping of the wave is so strong that no measurement is possible. Therefore it is important to keep the active areas as light and thus as small as possible, but large enough to induce a number of charge carriers that can significantly alter the SAW on its passing-through.

To calculate the effect of a conducting material on top of the piezoelectric substrate for the SAW, two different effects should be considered. The longitudinal electric field accompanying the SAW can couple to the free charge carriers in the material. This leads to a charge transfer

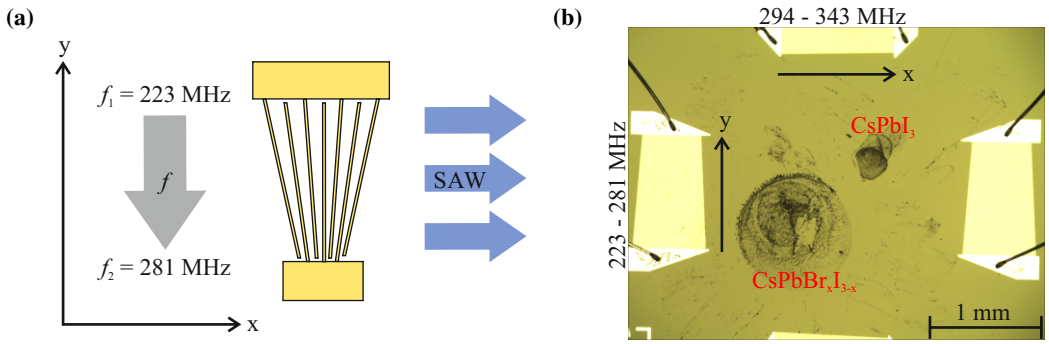

Figure 6.1: (**a**) Schematic of the principle of a TIDT with spatial resolution. (**b**) Configuration of four TIDTs arranged in pairs opposite to each other. In the delay line area in between drops of $CsPbI_3$ and $CsPbBr_xI_{3-x}$ are placed such, that they do not overlap. The two pairs are designed for non-overlapping frequency ranges and define the x- and y-axis by their frequency variation.

and thus, induces currents which experience ohmic losses $\sigma_{\square}\mathscr{E}^2$ [Wix89]. Since this lost power has to originate from somewhere, it is transferred from the SAW and the wave will be attenuated. Secondly, the presence of a semiconducting load on the surface of the piezoelectric substrate results in a piezoelectric stiffening of the material. This in turn alters the sound velocity and can be recorded as a phase shift in the transmitted signal. The equations describing the attenuation Γ and the change in SAW velocity Δv as functions of the conductivity $\sigma_{\square}$ in the case of a homogeneous piezoelectric conductor (c. f. subsection 3.5.4) are derived in [Wix89] and [Bal97] to

$$\Gamma = k\frac{K_{eff}^2}{2}\frac{\sigma_{\square}/\sigma_M}{1+(\sigma_{\square}/\sigma_M)^2} \tag{6.1}$$

$$\frac{\Delta v}{v_0} = \frac{K_{eff}^2}{2}\frac{1}{1+(\sigma_{\square}/\sigma_M)^2} \tag{6.2}$$

with $k = 2\pi/\lambda_{SAW}$ being the wave vector, K_{eff}^2 the effective coupling constant of the electric signal into a wave and $\sigma_M = v_0(\varepsilon_1+\varepsilon_2)$ a normalizing factor for the conductivity which combines the unperturbed velocity of the SAW and the dielectric constants of the piezoelectric substrate and the surrounding material above it. The equations are true if the frequency of the SAW is much smaller than the inverse of the transport relaxation time τ_t of the conducting material $f_{SAW} \ll 1/\tau_t$ [Wix89]. In this regime, $\sigma_{\square}$ can be seen as frequency independent. Furthermore, the relations are restricted to local regimes where the thickness of the layer and the electronic mean free path are much smaller then the wavelength λ_{SAW}. Figure 6.2(a) visualizes the relations of equations 6.1 and 6.2, i. e. the attenuation per unit length and the relative change in the velocity, both as a function of the conductivity $\sigma_{\square}$. For conductivities $\sigma_{\square} \ll \sigma_M$ the attenuation increases proportional to the conductivity, for high values $\sigma_{\square} \gg \sigma_M$ it follows the hyperbolic trend $1/\sigma_{\square}$. This means that for conductivities significantly lower than σ_M, small changes result in high variations of the attenuation. The sound velocity change follows a rather step-like function in the vicinity of $\sigma_{\square} = \sigma_M$. For low and high conductivities, small changes do not result in remarkable variations of the change in velocity. For low $\sigma_{\square}$, Δv is large, but constant, whereas for high values of $\sigma_{\square}$ the travelling of the SAW remains unperturbed. In the limit of $\sigma_{\square} = 0$ the deposited material becomes an insulator and Poisson's equation requires $\partial D/\partial x = 0$. As a result, the wave will not be attenuated, but experiences

a phase shift of π as commonly known from reflections at insulating barriers. On the other hand, if $\sigma_{\square} \to \infty$, the material is a very good conductor with vanishing field in the interior. This material then has no effect on the passing SAW, neither in its attenuation, nor does it result in a change of velocity.

To sum it up, the relevant parameters that will change during an introduction of conductive material on the surface of the piezoelectric substrate within the delay line are the attenuation of the SAW measured as the relative amplitude change with respect to the unperturbed case and the change in sound velocity which becomes measurable by the relative phase shift of the wave.

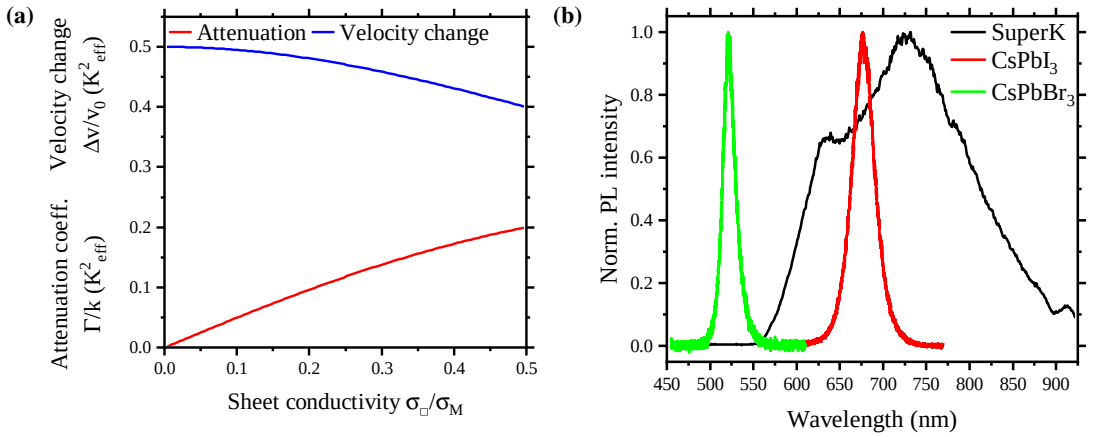

Figure 6.2: (**a**) Theoretically calculated attenuation and relative velocity change in a piezoelectric material due to added conductive thin film layers at the surface. Non-logarithmic zoom-in of figure 3.12. (**b**) PL spectra of $CsPbBr_3$ (in green) and $CsPbI_3$ (in red) compared to the visible emission spectrum of the supercontinuum light source SuperK (black).

In order to account for the different band gaps and to investigate the absorption edges of the examined materials a spectrally broad, high power laser source is used. The pulsed supercontinuum white light source ranges from 500 nm up to 1800 nm. This light source combines the spectral brightness of a laser with the bandwidth of a lamp and can in combination with standard filtering, e. g. a monochromator, be used to selectively excite the sample with the desired wavelength. This enables a wavelength-dependent study of the photoconductivity and thus, of the absorption. As a result, one can extract the absorption edge of a material determined by electrical probing.

The visible wavelength range of the supercontinuum source is presented in figure 6.2(b) to be compared with the emission spectra of two exemplary shown perovskite materials. The lower end of the laser spectrum only slightly overlaps with the emission from $CsPbBr_3$ (green line) which means, that this material is at the edge of the measurable range. The focus of this work lies therefore on materials that emit more into the red, like the mixed halide perovskite $CsPbBr_xI_{3-x}$ with wavelength corresponding to the bandgap of 615 nm and the already presented $CsPbI_3$ (red line) with emission around 660 nm.

The supercontinuum is generated by a photonic crystal fibre based on non-linear optics that do not provide a perfectly flat power output for every wavelength. To avoid manual adjustments of the pump laser power the studies are performed at a fixed setting of the pump laser and are recalibrated by calculations afterwards (c. f. section 6.3).

In practice, the transmission of the SAW is recorded with either a signal generator and an

oscilloscope that processes the full waveform or a VNA that records amplitude and phase of the reflected and transmitted electric signal. In the oscilloscope the wave can be directly seen and it can be distinguished between the primary wave and reflections at structures or the sample edge, like the triple transit signal. This method is therefore preferred for initial tests and proof-of-principle studies on the change in conductivity of $CsPbI_3$ on irradiation. In contrast, for investigations onTIDTs the VNA is of greater usage due to its integrated variation of the frequency of the test signal. This enables a native, easy and time saving spatial detection integrated in the basic measurement. Because the simple transfer of material on the path of the SAW leads to a change in the load and stiffness of the $LiNbO_3$ substrate material, the bare delay line does not serve as a reference. But as the semiconducting material's conductivity strongly increases with energy deposition, it is examined under irradiation from a strong light source and the non-excited case acts as reference. In this way the additional conductivity induced by the light is probed. The bandgaps of the materials under observation lie in the range of 1.8 eV and 2.4 eV, far above the thermal energy provided at room temperature of 26 meV and thus the materials without excitation can be regarded as insulators.

The spatial resolution through the TIDT is natively included in the frequency sweep of the VNA. This enables a fast detection of the conductivity induced changes simultaneously with the determination of their position. The principle can be used in two ways: In a fully illuminated sensing area the detector can distinguish between various materials within the active area via the location sensitivity and enables a determination of the colour of the incoming light. On the other hand, the device can be used as a position detector of highly focused light when the full active area is covered with sensing material. Both methods will be demonstrated in the course of this chapter.

6.2 Photoconductivity Studies

The near-surface nature of the SAW is the foundation of the photoconductivity measurement. The wave's proximity to the surface and the environment is an integral component of the high sensitivity. As seen in the theoretical calculations of the last section the sensitivity to conductive material depends very much on the level of conductivity. Perfectly conductive materials will not affect the transmission of the SAW as flowing currents in these will not result in losses. The perovskites regarded in this thesis are on the other end of the spectrum: they have rather low ratios of $\sigma_{\square}/\sigma_M$. As a result, the relative velocity change is, in theory, approximately 0.5, but as the reference study is performed with non-excited material or air, which are even less conductive, the measurable effect will not be huge. Nevertheless, it is possible to see a change in the velocity induced by laser irradiation as will be shown in the following sections. But the focus of the studies will be on the observation of the wave's amplitude changes. At first, the principal effect is checked with simple oscilloscope-based studies under high power LED illumination and in darkness with a delay line with $f_{SAW} = 324\,\mathrm{MHz}$ at an applied power level of $P_{rf} = -15\,\mathrm{dBm}$. In order to compare the amplitudes of the waves, an FFT is performed on the recorded sinusoidal data and their values at the resonance frequency are plotted in figure 6.3(a).

The SAW chip with perovskites placed in the centre of a delay line is fully illuminated with the high power LED during a certain time interval. The recording of the SAW's transmission is started before and persists after the irradiation to investigate the amplitude change and to reveal any slow or long term effects that were seen in other materials like the persistent

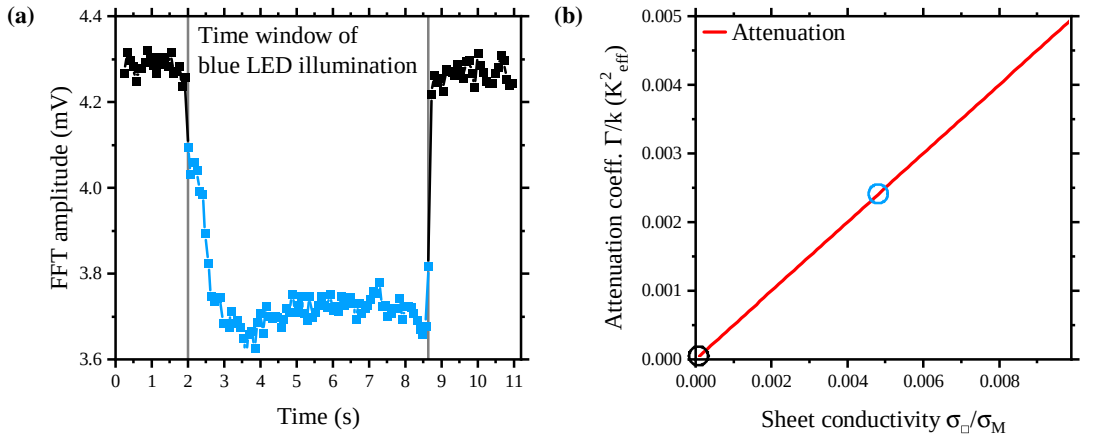

Figure 6.3: (**a**) Extracted FFT amplitudes of transmitted SAWs detected with an oscilloscope without (left and right in black) and with (blue) illumination of a blue, high power LED of the whole chip. (**b**) Attenuation values of the experiment indicated in a zoom-in of the theoretical curve from figure 6.2.

photoconductivity effect [Fuh10]. Subsequently, the amplitude of the wave is examined by Fast Fourier analysis and only the extracted size of the Fourier factor as a measure for the amplitude of the wave is compared. During the unperturbed parts of the series the SAW's amplitude varies only slightly (left of the blue region in the graph). As soon as the light is switched on, a sudden decrease of the wave's intensity can be detected which is attributed to the creation of free charge carriers in the perovskites that are accelerated to form induced currents. This reduced amplitude is maintained throughout the entire illumination time. Turning the LED off again results in an instantaneous recovery to the original height of the signal. Hence, in these materials, there is no long-term effect that prevents the charge carrier from recombinations as soon as the electric field is switched off. The lifetime of the charge carriers as determined in the previous chapter is in the order of nanoseconds and can thus not be tracked by the studies presented here. The persistent photoconductivity observed in similar experiments on other materials does not show up in the metal halide perovskites.

The approximate values of the attenuation and conductivity of the two studies, with and without LED illumination, are indicated in figure 6.3(b) at the theoretical attenuation function from subsection 3.5.4. The relevant region here can be approximated to be linear as the value are not close to the characteristic conductivity σ_M.

The LED with an electrical power of 5 W induces in the largely deposited sensing material a reduction of the amplitude in the FFT of around 0.6 mV at an overall amplitude of the wave of around 4.3 mV. This 10 % reduction is clearly visible and proves that the mechanism works in principle and that the conductivity of the perovskites is enough to be detected by the SAW. In this study a normal IDT of $f_{SAW} = 324\,\text{MHz}$ was used.

The TIDTs are recorded with a VNA to speed up the process and integrate the position detection easily. Figure 6.4(a) presents a study on a SAW chip with input power $P_{rf} = -3\,\text{dBm}$ on two TIDTs delay lines, one with (red line) and one without (black line) deposited material in the path. Through the tapering of the IDTs, there is a frequency band that can be excited and transmitted over the sample. The IDTs of this study have a a range from 223 MHz to 281 MHz. Due to the load of the metal electrodes it experiences a slight shift of about 4 MHz towards lower frequencies. The transmission band lies clearly more than 20 dB above the background and indicates a good coupling of the electric signal to the mechanical wave for all expected

frequencies. Upon depositing material between the two transducers the SAW already undergoes a change through the mere presence of the material (c. f. red curve of figure 6.4(a)). Two drops of the perovskite materials $CsPbI_3$ and $CsPbBr_xI_{3-x}$ were placed at diagonal corners of the active area. Through the position sensitivity of the TIDT their actual position can be reconstructed via the transmission measurement. It can be seen that after the deposition there appears a dip at around 244 MHz and a reduction in the signal at the higher end of the frequency band. Those two reductions in transmitted wave signal are a result of the material deposited in the travelling path of exactly those frequencies. As a consequence, one can deduce that one of the drops was placed at the edge of the field (right one) whereas the other one is closer to the centre of the delay line in this direction (compare the picture of the sample in figure 6.1(b)). The same analysis can be performed for the second, perpendicular IDT pair to get a two dimensional estimate of the positions of the drops. The sensitivity of the system in its position detection is dependent on the resolution of the IDT and the spot size of the laser. For small irradiation sources the spatial width of a single frequency sent through the chip becomes of relevance. Even a non-tapered IDT is not perfectly single frequency, but the emission of the wave has a certain spectral width. It can be controlled by the number of fingers in the structure and is inversely correlated to the temporal sharpness, thus the width of the onset and the running out of the wave packet. The more fingers are taking part in the creation of the SAW, the more precisely the frequency is defined, since the periodicity is more precisely defined over a longer distance. But this also implies a longer duration until the full amplitude of the SAW is reached. For the studies conducted here, the resolution of the IDT is large enough and the detection is rather limited by the spot size of the laser.

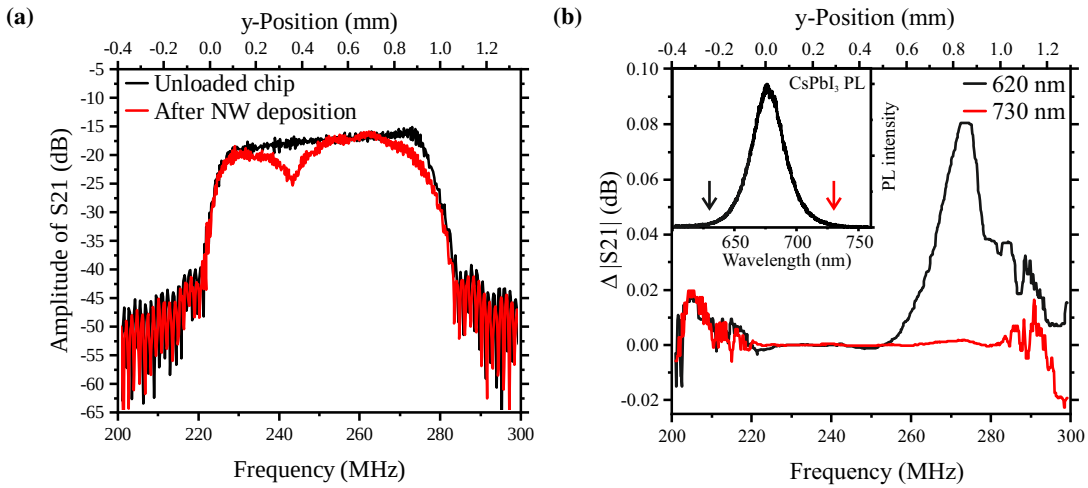

Figure 6.4: (**a**) Transmission signal of a TIDT with a frequency band of 50 MHz on the measured chip without (black) and with (red) perovskite material deposited on the chip. Both studies are performed without laser illumination. (**b**) Analysis of the amplitude change via laser excitation of $CsPbI_3$ material. Two analyses analogue to the ones in (a) are performed with and without irradiation through the laser and the signals are subtracted. The resulting curves are shown for an illumination with 620 nm and 730 nm. The inset indicates the wavelengths of the illumination in relation to the PL emission of the material.

To get to know more about the conductivity of the material, it is illuminated by a laser with tunable energy. This is important to test for the absorption of the material. Wavelengths above the bandgap are absorbed while a photon with an energy below the bandgap is not sufficient to excite an electron to the conduction band and is thus not absorbed. Figure 6.4(b)

compares the SAW amplitude change through the sample under illumination with two different wavelength: 620 nm (black line) and 730 nm (red line). The recordings are performed with a VNA applying an input signal of $P_{rf} = -3$ dBm. The curves are extracted as differences between the transmission of the SAW without and with the irradiation of the laser. This difference directly gives the absolute amplitude change generated by the drops with an interaction length of the spot size of the laser of 0.4 mm. In figure 6.4(b) one can see a nearly flat line at the frequencies of the band for the illumination with the low energy wavelength (red curve). For lower and higher frequencies that do not belong to the band of the IDT the noise of the signals does not cancel out. The very low transmission of these signals due to electromagnetic propagation is sensitive to any slight changes in the setup and thus undergoes variations. The features of the transmission band of the IDT stay the same for all studies except for the effects from the irradiation. The second curve in black reveals a huge difference to the red curve above 255 MHz which is the region previously assigned to a drop of $CsPbI_3$ NWs. Under illumination with the above-bandgap wavelength of 620 nm this material increases its conductivity largely resulting in significant amplitude differences of the SAW by almost 0.1 dB at an intermediate laser power. This corresponds to a change in voltage that is equivalent to 2.3 %. This seems to be a small number, but in comparison to the otherwise perfectly flat curve within the frequency band, this reveals a good sensitivity to the increase in conductivity. In contrast, when illuminated with laser light of 730 nm the calculated difference remains completely flat at a value of 0 dB. The responses to the different wavelengths of the laser proves that the amplitude change actually results from the absorption of the laser light and thus, the creation of free charge carriers. Reference investigations with laser irradiation within the delay line but not at the deposited material further confirm this assumption as they reveal no change in the transmission of the SAW.

For completeness also the phase change of the transmitted SAW was analysed which results from the change in sound velocity across the delay line. In figure 6.5(a) the phase corresponding to the amplitude data of figure 6.4(a) is presented before (black) and after (red) the deposition of sensing material in the travelling path of the SAW. The assumption of the perovskite conductivity being in the low regime, far below σ_M, predicts that the influence on the phase will not be major. But the additional viscous load of placing the nanostructures in the travelling path increases the mechanical stiffness of the substrate material and induces a significant phase change even without illumination (c. f. figure 6.5(a)). The borders of the frequency band are again clearly visible, this time due to its significantly increased noisiness. This noise results from the fact the only the signals within this band are actually converted into a piezoelectric wave that passes the substrate. Frequencies that do not match the wavelengths of the IDT can only be transmitted through electro-magnetic waves travelling through the air around the sample, called crosstalk, and are thus not affected by the small area of changed dielectric constant on the substrate. The behaviour of the device under illumination is examined in figure 6.5(b) where the difference in phase between the sensing material lying in darkness and being illuminated with the high power laser source is presented. The presented phase data corresponds to the SAW amplitude study shown in figure 6.4(b). The illumination of the sensing material does not reveal a big change of the phase, but due to the high matching of all unchanged regions of the frequency sweep the difference is clearly visible despite the small value of only a few hundredth of a degree. The range of frequencies where the difference occurs perfectly match the range where an amplitude change is observed in figure 6.4.

The two presented methods of amplitude and phase change investigations are equally useful in the sensing of conductivity changes. The absolute value of conductivity determines the

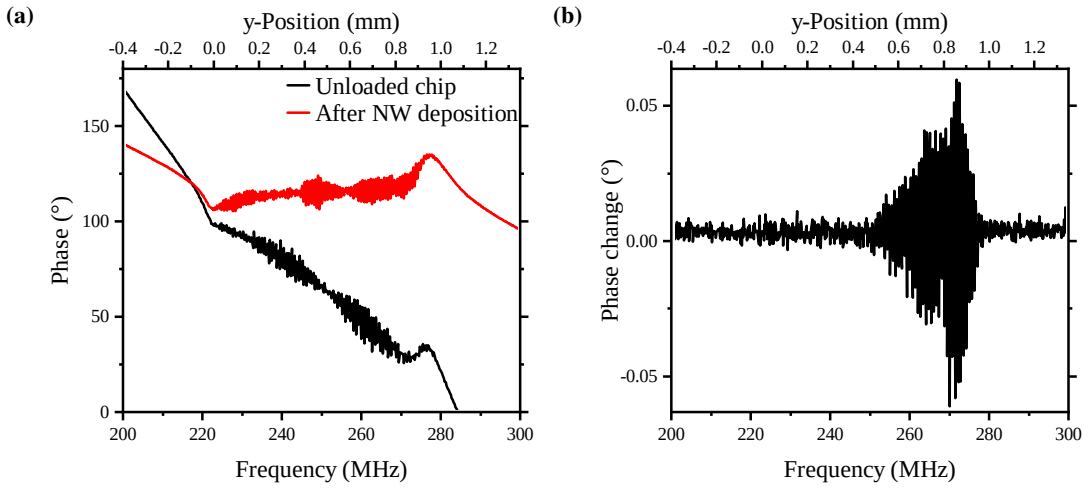

Figure 6.5: (**a**) Phases of the transmitted signal from the SAW that passes through the delay line before (black) and after (red) the deposition of perovskite material in the travelling path. (**b**) Phase difference that arises from the illumination of the sample with a laser of wavelength 620 nm. The presented curve is a subtraction of the phase values during and before illumination.

sensitivity of both methods and which one results in a more sensitive analysis. In the following, the amplitude change is used to characterize different compositions of metal halide perovskite material.

6.3 Spectrally Resolved Absorption via SAW Spectroscopy

The principal measurement methods introduced in the previous section can be used to determine the response of materials to light of certain wavelengths. The absorption of the irradiation highly depends on the transported energy in relation to the bandgap of the perovskite. In addition to conventional optical absorption studies, the SAW chip can be used to probe the photoconductance induced by the absorption of light. The method does not rely on the amount of transmitted light through the substrate, but measures directly the energy transfer to the material in form of the creation of free charge carriers. This implies that the scattering of the excitation light at the surface of the sample can be neglected and the analysis of reflecting material is also possible. Furthermore, the emission from the material under examination does not have to be taken into account as no optical recording is performed which might underestimate the absorption of the wavelength where the PL emission occurs.

As seen in figure 6.2(b) the emission spectrum of the white light source is not equally strong at all wavelengths. In order to simplify the measurement, the power of the pump laser is kept constant for the wavelength scans and an afterwards performed recalibration ensures comparability of the resulting data. To this end, the wavelength-dependent emission of the light source is recorded after it passed the monochromator. Figure 6.6(a) presents the spectrally filtered integrated intensity of the output of the white light source at 65 % power of the pump laser normalized to the integrated value at 610 nm. The output is filtered by the monochromator to an emission with 6 nm FWHM as in all the other studies. It is recorded by a spectrometer and integrated to be used as normalizing factor to recalibrate the effective power level of the laser. The wavelength-dependent sensitivity of the spectrometer in the range between 550 nm and

750 nm varies only about 6 % and is therefore neglected here. The integrated spectra vary by almost two orders of magnitude which emphasizes the need for the calibration. As the output power of the pump laser actually scales linear with the displayed percentage, these factors can now be used to recalculate the laser power percentage.

The charge carrier creation in the semiconducting material is not only dependent on the wavelength of the excitation laser, but also on its intensity. At low to moderate excitation powers the increase in the number of charge carriers created depends linearly on the power, while for high excitation intensity it saturates. Therefore, an additional calibration step is needed to account for this dependency. To this end, a detailed analysis of the power-dependent amplitude change is conducted and included in the interpretations. Figure 6.6(b) shows the power-dependency of the SAW attenuation for six different illumination wavelengths from 570 nm to 750 nm in steps of 40 nm with already corrected effective light source intensities as explained before normalized to the power levels of an emission with 610 nm. They were recorded with the VNA at an input power of $P_{rf} = -3\,\mathrm{dBm}$ on the chip LJ70.

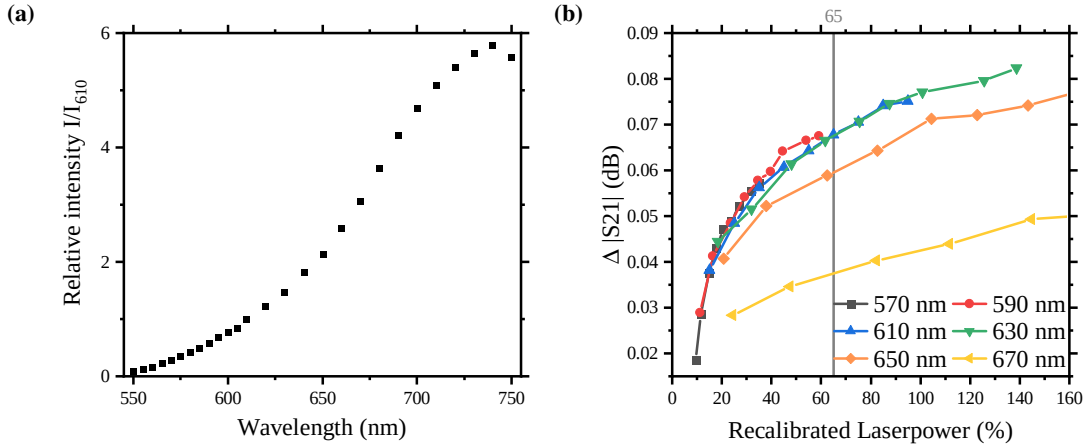

Figure 6.6: (**a**) Integrated intensity of the white light source at each center wavelength filtered by a monochromator acting as a bandpass filter with 6 nm width. (**b**) Illumination power-dependent attenuation of the SAW for different wavelength from 570 nm to 750 nm exciting a large ensemble of $CsPbI_3$ NWs. The power of the light source is already corrected for its wavelength-dependent intensity. The grey vertical line at 65 % marks the power level, at which the following studies are evaluated.

For wavelengths far above 660 nm, corresponding to the bandgap of $CsPbI_3$, the change in amplitude is not dependent on the energy of the light and the power dependence for all four curves from 670 nm down to 630 nm are nicely aligned (black, red, blue and green). When reaching wavelengths close to the bandgap, the transmission of the wave is less attenuated as less irradiation is absorbed and converted into mobile charge carriers. To be able to compare the values of amplitude change of the different wavelengths, it is necessary to recalculate the recorded data to the same power level. The non-linearity of the power-dependence on the transmission of the SAW requires a correction to the 65 %, the power value of all following studies. This is achieved through an interpolation of the experimentally obtained power-dependent curves of each wavelength and the extraction of the respective value at 65 % as indicated in the figure (grey line). This procedure ensures the direct comparability of the experimental data without a fixed power level of the excitation. It is especially relevant for the comparison of absorption values of different materials that have significant differences in the bandgap. But the effects are also substantial when it comes to the wavelengths at the edge of

the laser spectrum at which the emitted power drastically decreases.

Figure 6.7 presents the absorption edges investigated through the attenuation of the SAW transmission in a VNA study with $P_{rf} = -3\,\mathrm{dBm}$. It shows the data of two materials, (a) $CsPbI_3$ and (b) $CsPbBr_xI_{3-x}$, without (black) and with (blue) the correction procedure applied and compares the onset of absorption with the PL emission of the corresponding material (in red and orange). For high wavelengths, the change in amplitude becomes very small which hinders a good determination of the power dependence. The correction factor is therefore not applied above 680 nm and 650 nm for $CsPbI_3$ and $CsPbBr_xI_{3-x}$, respectively, and would anyhow be very small due to the small absolute value which does not induce strong changes. For lower wavelengths, in contrast, the correction has a huge effect as it compensates for the reduction in laser power when reaching the edge of the spectrum. It can be clearly seen in the experimental data of figures 6.7(a) and (b) that the untreated data points at lower wavelengths drop drastically which is unphysical and only due to the decrease in laser power. The correction compensates for the reduced creation of mobile charge carriers and restores the flatness of the curve in the region of strong absorption. The jump at the absorption edge of around 0.05 dB to 0.1 dB is equal to a change of less than 2.5 % in the amplitude of the wave. With this method of SAW-based photoconductivity detection it is therefore possible to record very small numbers of excitation induced mobile charge carriers.

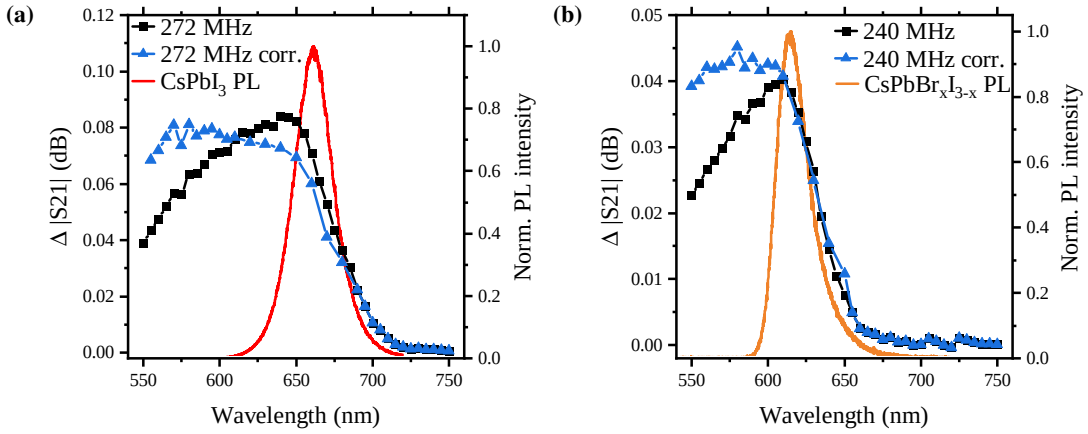

Figure 6.7: Absorption edges of (**a**) $CsPbI_3$ and (**b**) $CsPbBr_xI_{3-x}$ without the consideration of varying laser power outputs for the different wavelength (black) and with the application of the procedure described in the text (blue). Below a threshold of changes in amplitudes, the process it not applied because the correction factor becomes uncertain and very small. The emission spectra of the materials are included in red and orange.

The two graphs show also how nicely the difference in the bandgaps can be resolved. The switch between insulation and conductivity for both materials takes place in a transition region of 60 nm width around 670 nm and 635 nm, respectively. A comparison with the maximum of the PL peak of the emission of these nanowires (red and orange) reveals a good coincidence proving that it is actually a measurement of the bandgap. The shift between the two materials arises from the halide exchange from an equal mixture of bromide and iodide to pure iodide structures. The data shows that even in the mixture the distribution of the halides is homogeneously as the width of the transition zone is comparable to that of the pure iodide NWs. The absolute value of absorption of both samples is not comparable as the density of NWs in the provided solutions were not standardized.

The amplitude change plotted in the previous graphs was determined as the difference in dB-scale between the data and the reference, both in the ratio of transmitted to emitted power of the SAW which is equivalent to the ratio between the non-changed and the attenuated transmission. To compare this with the theoretical curve shown in figure 6.2, the attenuation coefficient Γ has to be calculated. For the following calculations, the maximum attenuation of the data presented in graph 6.7(a) is used.

$$\frac{I}{I_0} = e^{-s\Gamma} = -0.1\,\mathrm{dB} \tag{6.3}$$

$$s\Gamma = 0.023 \tag{6.4}$$

$$\frac{\Gamma}{k}(K_{eff}^2) = \frac{s\Gamma}{s \cdot k \cdot K_{eff}^2} = 0.0024 \tag{6.5}$$

$$\frac{\sigma_\square}{\sigma_M} = 4.7 \cdot 10^{-3} \tag{6.6}$$

The characteristic conductivity is given by $\sigma_M = \varepsilon_0 v(1+\varepsilon_{eff})$ and thus depends on the sound velocity in the material along the propagation direction and the effective dielectric constant of the system. An approximation of ε_{eff} can be found in [Sim96] and equals here $\varepsilon_{eff} = 22.75$. With the sound velocity of $LiNbO_3$ in the X-propagation direction of the 128° cut, this results in a value of $\sigma_M = 8.0 \cdot 10^{-7} 1/\Omega$. Finally, the conductivity of the ensemble of perovskite NWs can be estimated to $\sigma_\square = 2.0 \cdot 10^{-9} 1/\Omega$. This small value seems to be a contradiction to the excellent performance of perovskite solar cells. But in fact, the presented study actually probes to a large extent the inter-wire conductivity as the distances in single wires are small. But as shown before, the tunnelling of charge carriers between single wires is very low, which makes the ensemble an insulator and explains the reason for the extremely small value of extracted ensemble conductivity. This very low value also explains the only slight change in the phase seen in the previous section, but shows all the more how sensitive the SAW transmission is to the conductivity and that such small changes in the velocity can be resolved very well.

6.4 2D Tomography

With the characteristics of the sensing materials being analysed in the previous section, they can now be used to detect light. In a two dimensional arrangement of perpendicular delay lines of different frequencies, two types of studies can be thought of: a position and a colour sensitive application. In a configuration with drops of two or more distinct materials the setup can be used to determine the wavelength of the irradiation source through the position of absorption. The two perovskites investigated in this study, $CsPbI_3$ and $CsPbBr_xI_{3-x}$, are fully covered by the supercontinuum light source and are placed at diagonal ends of the square shaped active area between the four TIDTs. The bandgap of the two materials were determined in advance with PL spectrometry to 660 nm and 615 nm for $CsPbI_3$ and $CsPbBr_xI_{3-x}$, respectively. Hence, the two curves in figure 6.4(b), where light of two correctly chosen wavelengths is shone on one drop, would be already sufficient to tell the materials apart. But in order to make the process more accurate, the spot size of the laser is increased for the following study to cover the full active area of 1 mm $\times$ 1 mm and thus both sensing materials at once. With the two different bandgaps it is possible to determine if an irradiation on the device is in energy above, between or below both materials. The experimental data presented in figure 6.8(a) shows the changes

in amplitude as a function of the frequency (and thus position) under laser light illumination with different wavelength between 590 nm and 750 nm in a VNA study with an input signal of $P_{rf} = -3$ dBm. The frequency dependency reproduces the two material spots on the left and right side of the delay line.

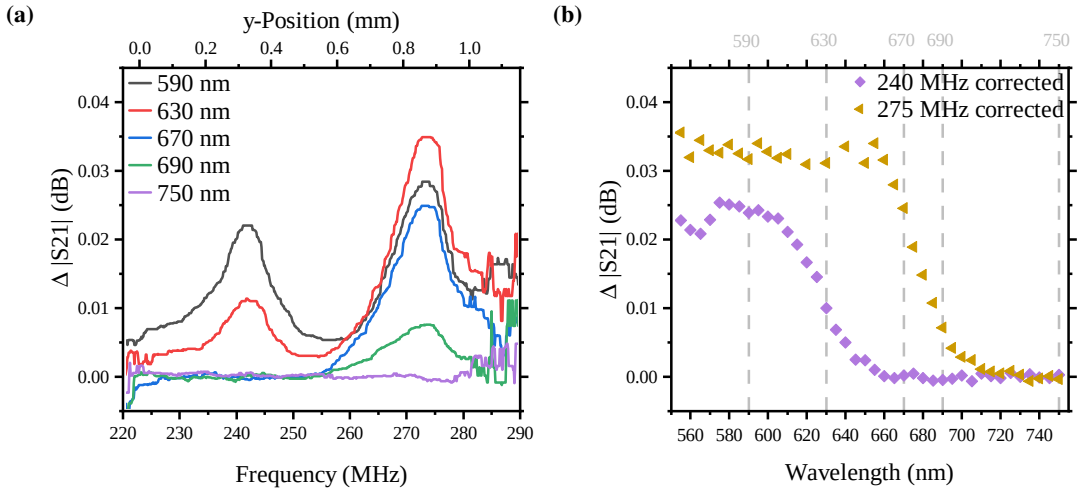

Figure 6.8: (**a**) Amplitude changes of the SAW at different frequencies under the spatially broad illumination of wavelengths from 590 nm to 750 nm (not normalized to power variances) to show the reaction of the two sensing materials $CsPbBr_xI_{3-x}$ (left) and $CsPbI_3$ (right). The values used for excitation in (a) are indicated in (b) by the dashed lines. (**b**) Wavelength-dependent, power-corrected amplitude changes of both sensing materials under the illumination of a spatially broad light source.

The lowest shown wavelengths of 590 nm (black) and 630 nm (red) demonstrate clear amplitude changes of the transmitted SAW for the frequencies that pass the drops of material. The broad illumination of the whole area ensures the creation of mobile electrons and holes everywhere in the deposited materials. The data in panel (a) is not yet recalibrated with the process explained above and therefore shows a strong increase of the amplitude reduction from the black (590 nm) to the red line (630 nm) on the right side, which is where the $CsPbI_3$ is deposited. This growth can be attributed to the higher laser power at this wavelength. The mixed bromide and iodide material on the left side already shows a significant decrease between the two curves as the energy of the irradiation is already above its bandgap of 615 nm. This effect dominates the increase in irradiation power which is therefore not visible for these frequencies. The slow drop of absorption above the bandgap results from additional thermal energy which also broadens the PL peak. The middle frequency region is affected by both materials because they overlap in the projection of this direction as can be seen in the picture of the sample in figure 6.1(b). They do not overlap in the perpendicular direction. For an illumination with 670 nm (blue line) no change of the transmitted SAW can be recorded when passing the $CsPbBr_xI_{3-x}$ as the energy is already below the bandgap. But for $CsPbI_3$ this energy is still above the threshold and thus alters significantly the travelling wave. The irradiation with 630 nm and with 670 nm (red and blue lines) lie both in the interesting region where at least on of the two sensing materials is in the transition from conductive to insulating. The wavelength of 690 nm (green line) marks the end part of the detectable amplitude changes of this sample and the last presented wavelength of 750 nm in violet leaves the passing wave completely unaffected at its full aperture.

A summary of the response of this sensor for various different irradiation energies from 555 nm to 750 nm is presented for two exemplary frequencies in figure 6.8(b). The two

frequencies (240 MHz and 275 MHz) are chosen to be located at the middle of each of the two materials. At these two positions the the amplitude change for each wavelength is extracted and power corrected by the method explained in section 6.3. The dashed lines indicate the chosen example values shown in panel (a) and their position in relation to the absorption edges of the two perovskite materials. They are spread broadly to cover all relevant regions in relation to the absorption edges.With a completely calibrated chip and fixed, known drops of sensing material it is even possible to further localize the wavelength of the illumination by the use of the amount of amplitude change, if the light is in the transition region of one of the materials. In this region the amplitude drop of the transmitted SAW correlates with the energy of the excitation and this correlation, when known, can be used to back calculate to the wavelength.

Additional sensing materials that could be integrated in the very same chip can further expand the detectable wavelength range or can be used to enhance the precision, depending on their bandgap in comparison to the materials already in use. To expand the described analysis to more variance, it is important to introduce the second direction of the two dimensional device to order the sensing materials that can be seen as pixels and reduce their physical overlap. For the purpose of this thesis, only two different perovskites are used to prove the principle of high sensitive light colour detection on the basis of surface acoustic waves and to introduce the 2D tomography.

The presented design can already with the two materials additionally be used as a position sensitive detector. As each of the two delay lines determines the position of excitation in one direction a map of the active area can be produced from the projections on both directions. In the following, the two drops of material from the previous study will be used to determine the position of the laser on the sample. Figure 6.8 already demonstrates that both drops cover each approximately half of the aperture of the IDT which is in accordance with the picture of the sample shown in figure 6.1(b). The $CsPbI_3$ drop reaches almost up to the middle and the $CsPbBr_xI_{3-x}$ material has a wider but less homogeneous density distribution. This is also reflected in the study by a higher amplitude reduction in the region of highest density (slightly to the right from the middle of the drop). The two dimensional analysis is performed by the application of the second IDT pair which is perpendicular to the first one. Due to the non-uniformity of the $LiNbO_3$ substrate, this second direction has a reduced coupling efficiency of the electric signal into the mechanical wave. The study in figure 6.9 compares the amplitude changes through $CsPbBr_xI_{3-x}$ nanowires of both SAW directions, with the delay line in (a) y- and (b) x-direction with an input signal of $P_{rf} = -3\,\mathrm{dBm}$. With colour coding five different excitation energies of the laser are presented. It can be seen that the y-direction results in a worse SNR and also a decreased sensitivity to the created charge carriers as a result of the reduced coupling efficiency. In panel (a) the data is therefore slightly flattened to increase the readability. Nevertheless, the effect can be clearly extracted from both data sets. Even in the less sensitive direction, the varying power of the laser depending on the wavelength can be observed. The curve of amplitude change for 550 nm (black) is located below the curves for 590 nm (blue) and 610 nm (green) as a result of the reduced number of photons available for the free charge carrier creation. That this is not affected by the direction of SAW propagation can be seen in a comparison of panel (a) and (b): The heights of the curves keep their relative position towards each other, independent of the coupling efficiency. The amplitude change at 590 nm (blue) and 610 nm (green), for example, are in both directions approximately the same, as well as 550 nm (black) and 630 nm (violet). This proves once more that the described power correction process is useful and consistent.

Despite the low SNR in the y-direction, the absorption coefficient with the transition from

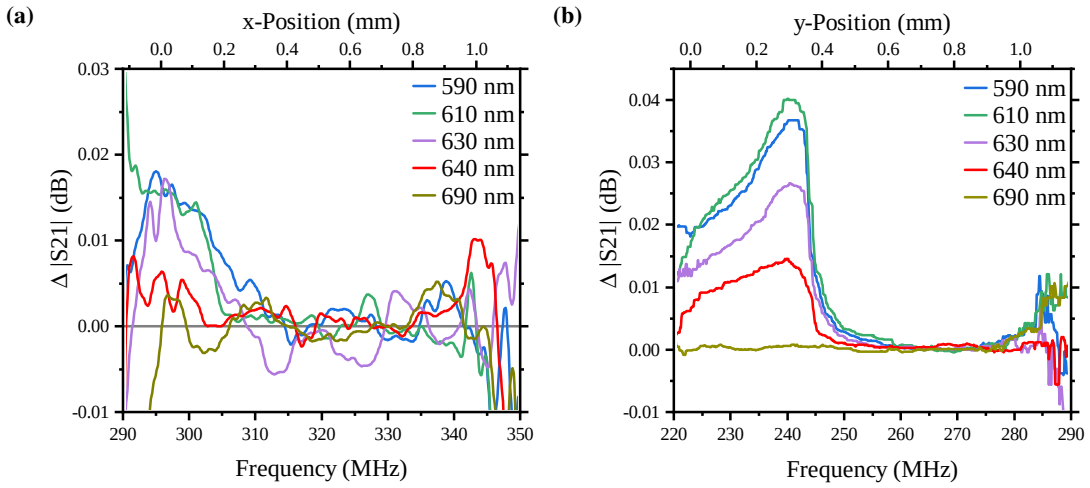

Figure 6.9: Change in transmission amplitude of different irradiations on $CsPbBr_xI_{3-x}$ nanowires in the (**a**) y- and (**b**) x-direction of SAW propagation on the chip. The coupling quality differs largely between the two directions which lowers the SNR and slightly reduces the attenuation. For better readability, the data in panel (a) was slightly flattened.

conductive to insulating, can be clearly observed and matches the data extracted from the SAW propagating in the x-direction. Excluding the increased noise in the y-direction, it can also be seen that the relative height of the amplitude change for each wavelength can be scaled with a constant factor to match the values of the longitudinal direction. This consistency is of huge importance for the reliability and repeatability of the studies and for the comparability between different directions and even chips.

The two dimensional arrangement provides the basis for determining the position of the laser excitation. In the presented setting, only two diagonal spots are covered by sensing material (c. f. the overview over the chip in figure 6.1(b)). In between and in the two other corners of the square shaped active area, there is no material and thus no amplitude change present. In the next experiment, the laser spot is moved from the middle of the $CsPbBr_xI_{3-x}$ drop to the middle of $CsPbI_3$ in several steps. At the intermediate positions the wavelength-dependent absorption is also recorded and used to reconstruct the location of the laser. The locations and approximate size of the laser spot are indicated in figure 6.10(a) and are numbered beginning in the middle of the $CsPbBr_xI_{3-x}$ covered area, continuing more and more towards the middle of the active area, which lies in between the two materials and ending at the middle of the $CsPbI_3$ covered area. Figure 6.10(b) and (c) compare the frequency-dependent amplitude change of the SAW for a $P_{rf} = -3\,\mathrm{dBm}$ signal measured through the VNA for the y-oriented and the x-oriented delay line, respectively and an illumination with 610 nm at the six positions. In principle, both directions show again exactly the same results. The major difference is the sensitivity and the SNR. Positions 1 and 2 in black and red, respectively, are completely on the $CsPbBr_xI_{3-x}$ and show no indications of an amplitude reduction of the SAW at the region of the other material. Both delay lines reveal that the maximum density of the $CsPbBr_xI_{3-x}$ is located at the edge of the drop at position 2. Towards the middle positions, marked in blue (P 3) and green (P 4), the influences of both drops become visible in different amounts as both are in reach of the stray light of the laser, but none is directly illuminated. Hence, both effects are rather small, but clearly visible. The last two studies are performed on the edge (P 5 in violet) and in the middle (P 6 in yellow) of $CsPbI_3$. Finally, position 5 and 6 (violet and yellow) are on the deposited

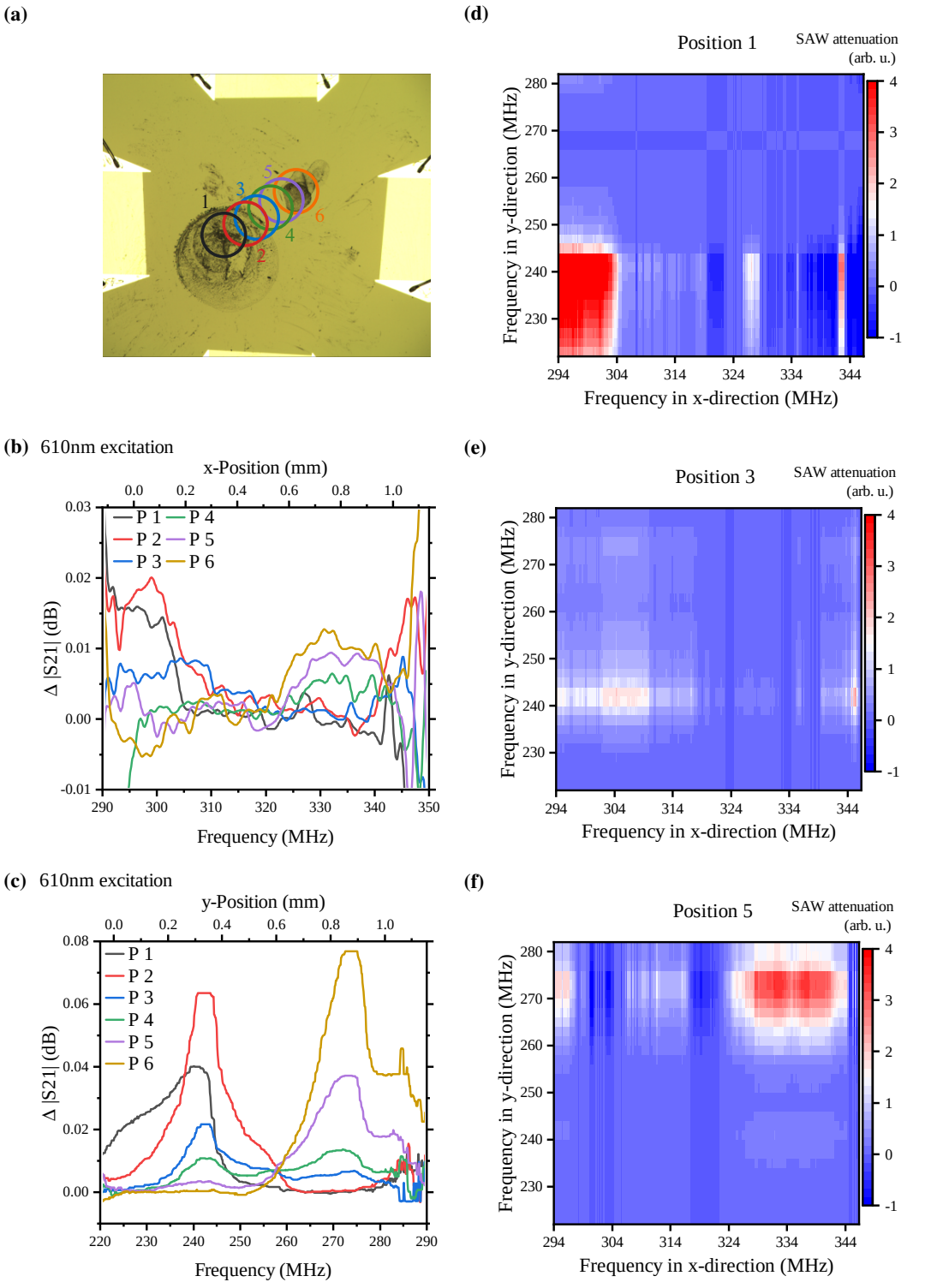

Figure 6.10: (**a**) Indication of the illumination positions referred to in (b) to (f). (**b**) Determination of the amplitude changes in the y-direction (slightly flattened) through the deposited materials recorded at different positions at 610 nm illumination. (**c**) Same as (b) with the delay line in the x-direction.
(**d**) - (**f**) Heat maps of the multiplied datasets of (b) and (c) at positions P 1, P 3 and P 5, respectively.

$CsPbI_3$ and show huge amplitude reductions for higher frequency, but none at the positions where $CsPbBr_xI_{3-x}$ is placed. As a result, such investigations can determine the position of illumination and can even give an estimate of the size of the laser spot through the width of the attenuated frequency range.

The change from one material to the other is even sharper for the y-directional delay line (figure 6.10(b)). The blue curve still shows only reduction in amplitude for $CsPbBr_xI_{3-x}$, while the green curve only shows a reaction at the frequencies where $CsPbI_3$ is deposited.

The position determination becomes even clearer when the data is plotted in a heat map as presented in figure 6.10(d), (e) and (f). The x- and y-axis are the frequencies of the two delay lines and the colour indicates the amount of amplitude reduction as a product of both studies. The graphs show data for an excitation with 610 nm on position 1, 3 and 5 all in the same scale. Position 1 reveals a clear indication of the material in the lower left corner, $CsPbBr_xI_{3-x}$, reacting on the excitation, while $CsPbI_x$ in the upper right corner shows no SAW attenuation. In position 2 the attenuation of the SAW is drastically reduced and there is only a small maximum at the position of $CsPbBr_xI_{3-x}$, due to scattered light from the excitation point position 3 that lies in between the two sensitive regions. Finally, position 5 clearly reveals that $CsPbI_3$ in the upper right corner is reacting massively on the light, while $CsPbI_3$ which is located on the lower left corner is not excited by the laser spot. The two ghost spots arising at the upper left and lower right corners of panel (e) and in the upper left corner of panel (d) are a result of the calculation from the data. During the measurement only the projections of the whole active area onto the x- and y- directions are recorded and no actual full two dimensional mapping is performed. This integration results in a loss of spatial data for each IDT in the perpendicular direction. When the heat map is calculated via multiplication of the data acquired for both delay lines this can not be fully compensated and results in the slightly over rated spots. Nevertheless, this method works perfectly fine for excitation spots no larger than the size of the drops.

6.5 Conclusion

This chapter showed that TIDTs can be used as spatially resolved detectors for SAW attenuation and can be exploited to sense the local creation of charge carriers in sensing material in the active area. Due to the special design a discrimination of the position of change in the SAW can be determined and thus an arrangement of two perpendicular TIDTs can be used to create a full 2D array of active detection area. The creation of conductivity in the sensing materials through the absorption of light with an energy above the bandgap results in mobile charge carriers being influenced by the electric field of the SAW. The induced current undergoes losses which can be measured through the reduced amplitude of transmission and a phase change of the wave through the substrate. Even though, the device was not optimized to sensitivity, the very small conductivity of the deposited drop of individual and non interacting perovskite material could be easily detected and determined to be $\sigma_{\square} = 2.0 \cdot 10^{-9} 1/\Omega$.

Furthermore, the device can be used to determine the absorption edge of the material fully electrically and thus without the need to consider reflectivity or the urge for a transparent substrate. On the one hand, due to the two dimensional arrangement, it is possible to produce a sensor device with multiple materials that provide variable sensitivity to light of different energy. On the other hand, this design also enables the precise detection of the position of irradiation within the active area and can be used to track the path of a laser. The SAW is thus a versatile tool to probe photo-conductivity in a high-sensitive, contact-free setup.

Chapter 7

SAW Resonator-Based Detection

The already very sensitive detection of mobile charge carriers in materials placed in the path of a SAW can be further enhanced by the use of a resonator. The arrangement of reflecting structures is highly sensitive to the smallest changes in the effective path length. In exploiting this property, the change in velocity as an effect of the illumination of the sensing material can be effectively recorded. The principle of SAW resonators is well known for other usages, e. g. in cell phones where the resonators on piezoelectric substrates act as filters for the incoming electromagnetic signals. Their usage is favoured because they combine low insertion loss with good rejection. Moreover, filters with broad bandwidths can be achieved while still being much smaller in size than traditional cavity or ceramic filters [Mil15]. The SAW technology allows for a waver scale fabrication at low cost and an integration of several different bands in one fabrication step. All these properties make the SAW filter an interesting device, not only for communication industry, but also for other filtering or sensing applications.

The basic principles of a resonator are explained in section 3.1. In short, a SAW resonator consists of two finger structures opposing each other which are left floating with no external connection. These act as reflectors for the acoustic wave and create the typical resonator features. In between, a normal IDT with a small number of fingers is placed to excite a wave which travels in both directions to meet the reflectors and interferes with its counterpart. The frequency broadness of the inserted wave is much higher than the free spectral range of the resonator, enabling more than one resonance frequency to exist. The lines can all be used independently for the conductivity analysis and reveal equally satisfying results. In the range where the frequencies of the SAW are much smaller then the inverse of the transport relaxation time of the charge carriers, thus the time they need to react to external fields, the conductivity can be regarded as frequency independent [Wix89]. In the following, the principle of the SAW-based resonator with its structures will be introduced briefly in section 7.1 with an explanation of the reaction on changing sound velocities. Section 7.2 demonstrates this in showing the effect non-excited, viscous semiconducting load has on the transmission properties of the SAW in the resonator on chip LJ82. Finally, the sensitive phase and amplitude change of the wave in the resonator due to the creation of mobile charge carriers in the deposited perovskite are presented in section 7.3.

7.1 Principle

The arrangement of two floating finger structures opposing each other is a well known principle to create SAW resonators. The design used in this thesis was created by Emeline Nysten and kindly made available for this study. The detailed arrangement is presented in figure 7.1(a) showing four reflectors creating two resonators that both have an IDT within the path to excite

the SAW. This arrangement is called a one port resonator. The two extra IDTs on the chip with the same parameters form a delay line and are used for characterization. The sensing material $CsPbI_3$ is placed within a resonator to influence its effective length. The drop of material consists of many randomly oriented NWs. The two different sizes of drops that are analysed in this work to examine the influence of load on the behaviour of the resonator are shown in figure 7.1(b) in a microscope picture of the sample chip.

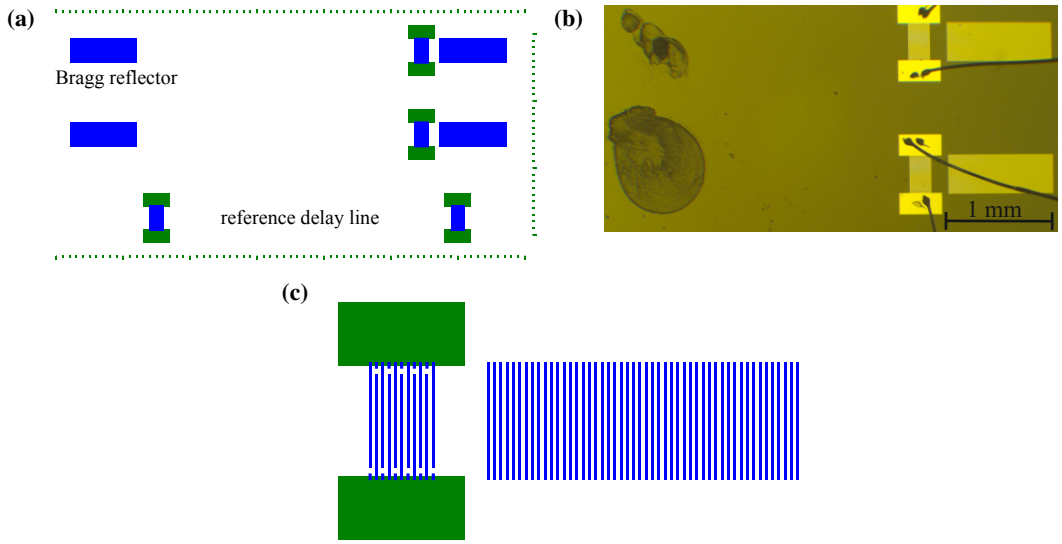

Figure 7.1: (**a**) Sketch of a resonator chip design. It consists of a delay line (bottom) and two single port resonators (middle and top). At the edges of the chip, small markers are located. (**b**) Microscope picture of the resonator chip with a small drop of $CsPbI_3$ in the upper resonator path and a larger drop in the lower path. The IDTs have bonds as electric connections to apply the alternating voltage. To the right, two reflectors are shown. (**c**) Larger sketch of an IDT close to a Bragg reflector with enlarged electrodes for better visibility.

A zoom-in of an IDT and a resonator in figure 7.1(c) shows that the period of the resonators is adapted to the IDT to fulfil the reflection condition for the wave. The distance of the reflectors in panel (a) is 340 times λ, the wavelength the IDT is designed for. With a designed frequency of f_1 =300 MHz this means that the free spectral range of the resonator is in the order of 0.38 MHz, which is reproduced by the following data. The single, but broad dip of the IDT is now superimposed by the matching resonances of the resonator. In this case, ten resonances fit in the bandwidth of the reflectors. The number can be controlled by the number of fingers in the reflector and the reflectivity of each. Here, it consists of 75 finger pairs and the bandwidth is experimentally determined to be 4.2 MHz for this resonator. Assuming a typical reflectivity of each strip of $|r| = 0.01$ [Dat86], the bandwidth can be calculated to

$$\Delta f_b = \frac{2|r|}{\pi} \cdot \sqrt{1 + \left(\frac{\pi}{N|r|}\right)^2} \cdot f_1 = 4.4\,\text{MHz} \tag{7.1}$$

for the 150 strips reflectors [Dat86]. From equation 3.25, the L_p for the given arrangement can

be calculated and used for the determination of the effective length L_{eff} of the resonator.

$$L_p \approx \frac{1}{4|r|} \cdot \lambda = 25\lambda \tag{7.2}$$

$$L_{\text{eff}} = 340\lambda + 2 \cdot L_p \approx 390\lambda \tag{7.3}$$

Thus, the mode index of the resonances is approximately $n = 2 \cdot 390 = 780$.

Figure 7.2(a) illustrates the electric reflection measurement of a VNA with input signal $P_{rf} = -3\,\text{dBm}$ on an IDT in the delay line (red) and in the resonator (black). In the delay line, the energy transfer into the substrate is almost 10 dB corresponding to a standard, not specially optimized IDT. An identical IDT located in the resonator, shows sharp resonance frequencies with a massively increased energy transfer. The strongest resonance reaches even down to $-34\,\text{dB}$.

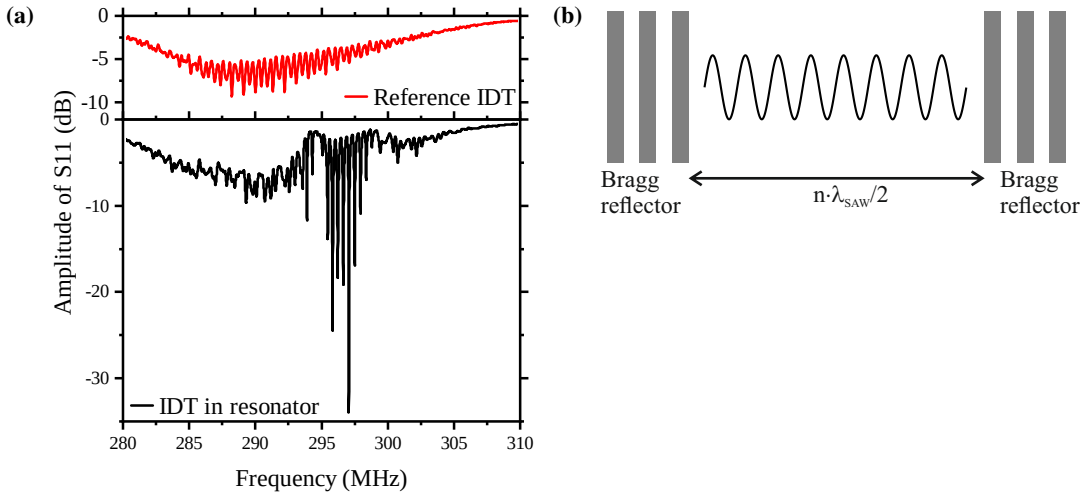

Figure 7.2: (**a**) Reflected electrical power of the inserting IDT with surrounding resonator (black) and in a delay line (red) of chip LJ82. (**b**) Sketch of a wave in a resonator build up of two Bragg reflectors.

The sharp resonances created by the resonator are very sensitive to the effective distance between the two reflectors. They result from the interference of reflected waves travelling back and forth in the resonator. Such an arrangement is illustrated in figure 7.2(b) which also indicates, that constructive interference only occurs when the distance between the reflectors is an integer multiple of $\lambda_{SAW}/2$. A slight variation of the velocity changes the effective length of the resonator and thus shifts the resonance frequencies as it changes the phase of one wave. These shifts enable in principle a much more sensitive detection of the change in velocity in comparison to the study of the transmission of a SAW through a delay line. The change in the resonance is much less subject to any noise and the extraction of the difference is therefore much easier than a direct comparison of the phases of a transmitted wave. Additionally, the amplitude change of the electric reflection can also be measured.

The difference in the principle between the resonator and the delay line is illustrated in figure 7.3. Panel (a) shows the delay line where the SAW passes only once the distance between the sending and the receiving IDT and thus also only once the conductive layer. In the resonator of panel (b), in contrast, the wave is reflected at the reflectors and thus passes the conductive layer of width b more then once. Without the layer, the resonance condition is fulfilled if the wave in the left part of the resonator with width L_{left} interferes constructively with the one in

the right part with width L_{right}. This can be expressed through the phase difference of the path on the left and on the right, φ_l and φ_r, respectively.

$$\Delta\varphi = \varphi_l - \varphi_r = n \cdot 2\pi \tag{7.4}$$

where the φ_l consists of two contributions, $\varphi_{l,0}$ from the distance to the reflector and φ_{load} from the conductive layer. $\varphi_{l,0}$ and φ_r can be calculated by

$$\varphi_l = \varphi_{l,0} + \varphi_{\text{load}} = \frac{2(L_1 + L_p)}{\lambda} \cdot 2\pi + 2 \cdot \frac{b}{\lambda} \cdot \frac{\Delta v/v}{1 - \Delta v/v} \cdot 2\pi \tag{7.5}$$

$$\varphi_r = \frac{2(L_2 + L_p)}{\lambda} \cdot 2\pi. \tag{7.6}$$

The widths are also indicated in figure 7.3. With these equations the new resonance condition is

$$\Delta\varphi = \varphi_{l,0} + \varphi_{\text{load}} - \varphi_r = \frac{2\pi}{\lambda}\left(2L_1 - 2L_2 + 2b\frac{\Delta v/v}{1 - \Delta v/v}\right) = n \cdot 2\pi. \tag{7.7}$$

This shows that the change in velocity in the small part of the load has an influence on the resonance wavelength. In the next subsection these resonance shifts due to the deposition of load can be observed. An additional resonance shift due to charge carrier creation could not be observed in this sample due to the frequency resolution of the VNA.

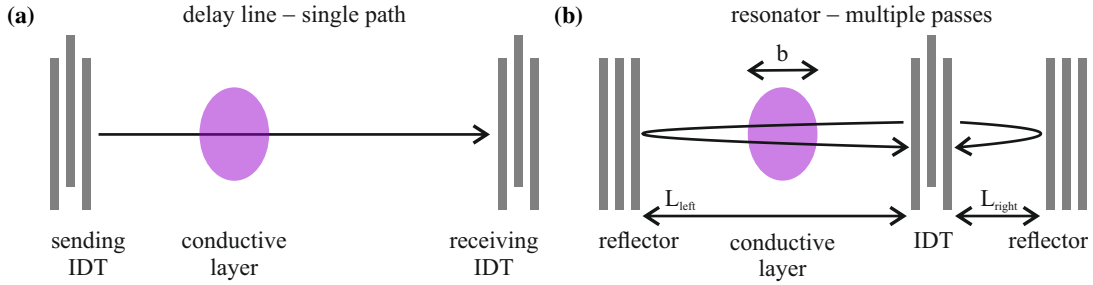

Figure 7.3: (**a**) In a delay line, the detected SAW passes only once the distance between the IDTs and therefore also the conductive layer. (**b**) In a resonator arrangement, the SAW is reflected at the ends and traverses the chip more than once, interacting with itself to form the resonances. The conductive layer is thus also passed more then once.

7.2 High Sensitivity of Resonator Under Load

The reaction of semiconducting load on a travelling SAW plays an important role in the quality of a potential sensor. That the material influences the transmission even without being illuminated was already discussed in section 6.2. This effect is also present in the resonator and due to its higher sensitivity even enhanced. On the one hand, this can be seen as a reduction of the potential sensitivity to the mobile charge carrier creation by laser irradiation. But on the other hand, this means also that the chip can act as a sensor for viscous load on a very fine scale. The small drop of lead halide perovskite material from the microscope picture in figure 7.1(b) induces a huge reduction of the coupled power into the substrate as well as a large frequency shift.

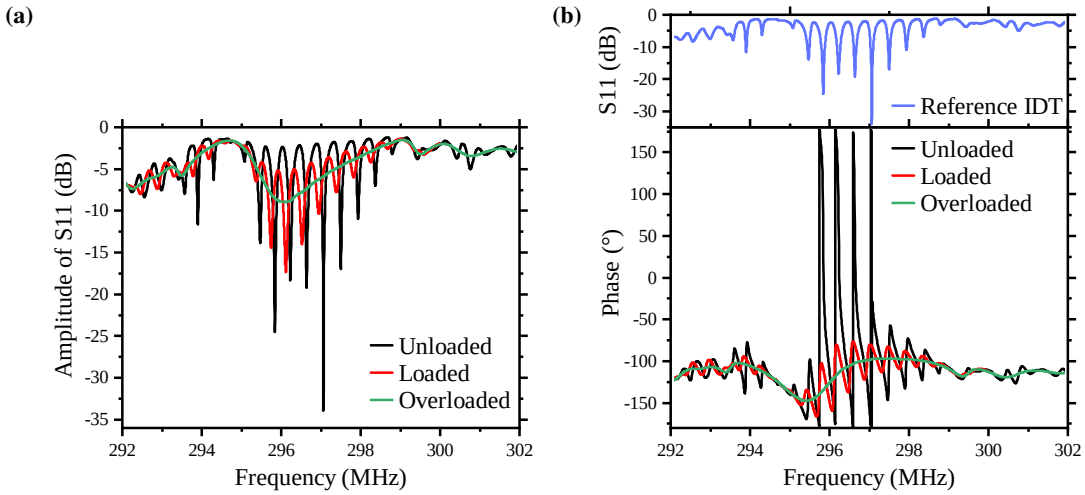

Figure 7.4: (**a**) Reflection measurement of the electric power coupled into the substrate from an IDT between two SAW reflectors. The unloaded resonator (black) is compared to the loaded (red) and overloaded (green) resonator. (**b**) The phase of the coupled signal is also influenced by the deposition of load within the resonator path. The amplitude of the S_{11} recording on the unloaded resonator of (a) is included in blue.

Figure 7.4(a) presents three studies with the VNA of the frequency-dependent amplitude of the electric reflection of a SAW with input power $P_{rf} = -3\,\mathrm{dBm}$ without any material (black), with a small drop (red) and with a large drop (green) of deposited material. It reveals a strong frequency shift produced by the transfer of the additional material. While the unloaded resonator has resonance dips that reach down to $-34\,\mathrm{dB}$, the introduction of a small load alters the acoustic path such that the resonances are massively weakened. The change in resonance frequency is approximately constant for all existing dips and amounts to $\Delta f 110\,\mathrm{kHz}$. Despite the reduced depth, the resonances are still clearly visible and take up more power than the IDT in the delay line outside the resonator. The changes in the resonances can be best displayed by the Q-factor which measures the quality of a cavity. Through all frequencies it drops massively under load. Table 7.1 summarizes the values for the eight main resonances of the resonator and lists their quality factor before and after the deposition of the small drop of perovskite material. Remarkably, not all resonators lose quality to the same extent and there is a reordering of the best resonances.

	f_{n+7}	f_{n+6}	f_{n+5}	f_{n+4}	f_{n+3}	f_{n+2}	f_{n+1}	f_n
f_{unloaded} (MHz)	298.37	297.94	297.50	297.06	296.64	296.23	295.84	295.46
Q_{unloaded}	4050	3790	4580	7310	4140	3230	4370	3520
Δf (MHz)	0.09	0.1	0.11	0.12	0.11	0.11	0.12	0.11
Q_{loaded}	1530	1650	1508	1820	2160	2550	2360	1670

Table 7.1: Evolution of the Q-factors and the resonance frequency of all relevant modes in the resonator from the unloaded chip to the deposition of a small load. The resonances are numbered starting at the lowest frequency with $n \approx 780$.

The huge sensitivity to the load is revealed when a larger drop of material is placed within the resonator. The green line of figure 7.4(a) shows that too much material can lead to a full disappearance of the single resonances and leave only a broad, smeared out dip in the reflection

spectrum. The load has then two effects. First, its inhomogeneous material density broadens the FWHM of the resonances as the exact resonance varies along the aperture of the IDT. And secondly, the attenuation due to the deposited perovskites becomes so huge already without external excitation that there is no significant part of the wave left to interfere with. Altogether, this results in the presented loss of the resonance frequencies and the properties of the resonator. As a consequence, the load should be kept small, but if so, the SAW resonator is a very sensitive tool to determine the amount of material placed within it.

Regarding the phase of the coupled signal, one sees similar effects of the additional material. In figure 7.4(b) the phases of the electric reflection measurement for a resonator without (black), with a small (red) and with a large (green) drop of material are presented. Additionally, the black curve of panel (a) is repeated here in blue as an indication of where the resonance frequencies are located. In the phase of the unloaded resonator (black), the positions of steepest change correspond to the resonances, while the exact resonance frequency matches with the point of slope change of the phase. The strongest resonances experience the largest changes, while less good modes only slightly vary their phases. The phase is highly dependent on the impedance which changes massively in the region of resonance.

With the resonance condition fulfilled, the change in velocity through the deposited load, clearly shifts the resonance frequencies and with them the phase of the inserted electrical signal of the IDT between the two reflectors. The red line in graph 7.4(b) presents the phase when a load is placed in the path. Similar to the amplitude of reflection in figure 7.4(a), the phase undergoes a shift and a massive reduction of the phase range. The main reason for this is the superposition of different waves, which were influenced by the material to different degrees by the inhomogeneous density along the aperture. The recorded phase change is an average over the whole wave front and thus suppresses the sharp transitions. The deposition of a heavy load on the sample also has an effect on the phase of the inserted electric signal. Analogue to the amplitude of the resonances, also the phase variation vanishes (shown by the green line). Due to no resonances building up, the phase follows the global trend with no oscillations marking any good coupling to the substrate.

This section has shown, that a proper dosage of the sensing material is important and too much of it can lead to a suppression of the resonances. But on the other side, this sensitivity already to the load can be exploited to use the device not only as light sensor, which will be shown in the next section, but also as a detector of the load.

7.3 Photoinduced Conductivity

The accurate positional detection of light by a SAW-based sensor has already been shown in the previous chapter using TIDTs. The resonator design introduced in this chapter follows a similar aim, but increases the sensitivity to the velocity change and for simplicity reasons gives up the position sensitivity. It was already shown that the load has a huge influence not only on the amount of power transported by the SAW but also on the resonance frequency of the arrangement. In this section, the effect of additional light induced mobile charge carriers on the properties of the resonator will be examined. The main advantage of the resonator design is the largely enhanced reaction to the change in velocity compared to the delay line-based method. While in the latter case, the induction of a small phase shift is barely visible in the detected signal after passing the sensing material once, the resonator profits from the repeated passing of the sensing material and its change of the effective length of the resonator. With

the excitation of the wave being between the two reflectors, the phase change of the reflected electric signal can also be observed. In the following, two methods of recording the change in conductivity will be compared: the reduction in the transmission of the wave and the phase change of the wave. Figure 7.5 studies the electric reflection measurement recorded by a VNA with $P_{rf} = -3\,\mathrm{dBm}$ under the illumination of light with wavelength $\lambda = 600\,\mathrm{nm}$ focused on the sensing material. The small drop of $CsPbI_3$ material already examined in section 7.2 is also used for the study on conductance creation through the illumination of the sample. In Figure 7.5(a) and (b) the amplitude and phase of the electric reflection measurement of the SAW in the resonator are shown. The non-illuminated (black) and the illuminated (red) case are compared for a frequency range around the $n+2$nd resonance. The timeline of the studies is depicted in panel (e). When the light source is turned off, a waiting time of approximately half a minute ensures that all effects from previous illuminations are negligibly small. Then a whole measurement of one frequency sweep is performed before the illumination is turned on. A second waiting time ensures, that, here, again all is in equilibrium before the next recording is started. Finally, another waiting time is implemented between the light source being switched off and the last measurement being performed.

In these studies the differences are much less then the ones of the load. Nevertheless, the effects are clearly visible and studied in detail for all resonances. Figure 7.5 (a) and (b) compare the changes that occur as a direct result of the light (black line) with the effects that persist after the switching off of the irradiation (red line). They are calculated as the difference between the reference and the recording either during or after the illumination. Panel (c) and (d) show the difference of both studies, without and with laser illumination, for the whole relevant frequency range. The non-irradiated chip with the load already placed in the resonator was used as a reference to extract the changes resulting from the illumination with the laser. The change in amplitude that occurs over time (red line) and not due to the irradiation, i. e. after the light is switched off, is mostly only in the positive direction and exactly at the same frequencies where the strongest difference through the illumination occurs. Hence, it is a small effect of persistent charge carriers in, for example, trap states.

The amplitude change is also correlated to the strength of the resonances in the reference (shown in blue). A comparison with their amplitude reveals that the strongest resonances also exhibit the strongest changes. It also shows that the resonance frequency matches the approximate middle of the trailing edge of the change through illumination. That means that the strongest variation in the amplitude happens on the right edge of the peak, illustrating the very slight resonance shift towards higher frequencies. At the non-resonant frequencies the changes in amplitude are only very small.

Similar findings can be observed for the phase change presented in figure 7.5(b) where again the differences between the reference phase and the recordings during as well as after the illumination are presented. The reference plot of the amplitude in reflection measurement of the resonator before the illumination shows that the highest phase changes occur exactly at the resonance frequencies. This indicates a large variation of the impedance caused by the creation of charge carriers that change the electric properties of the whole setup. It only emerges at the resonances because only electric signals that were converted into surface waves can sense the change and are influence by it. As already seen before in the reaction to load, the strongest resonances exhibit the largest phase changes and hence, are most sensitive to slight conductivity variations.

The absolute values are very small, but differ clearly from the zero line in both cases, the amplitude and the phase. Thus, this arrangement is also capable of detecting conductivity

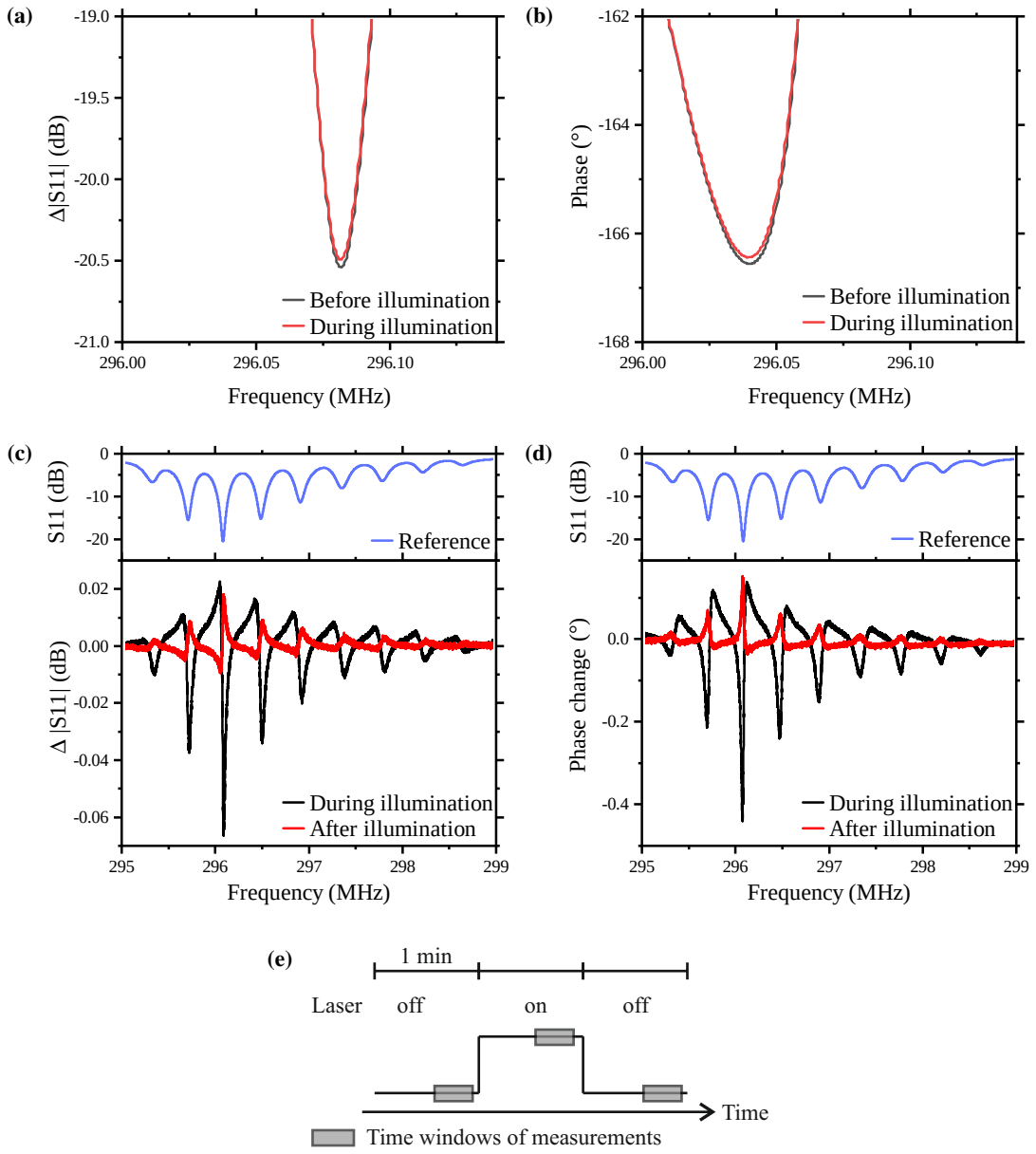

Figure 7.5: Changes in the electric reflection signal from the IDT within the resonator due to the illumination of the sensing material $CsPbI_3$ with light of 600 nm. (**a**) Amplitude of the reflection signal for the resonance $n+2$ before (black) and during (red) illumination. The difference between the two signals is regarded in panel (c). (**b**) Comparison of the phase for the same frequency range as in (a) from the reflection signal before (black) and during (red) illumination. (**c**) Reduction of the wave's amplitude during (black) and after (red) illumination with the laser, both as difference to the signal before illumination. (**d**) Phase change during (black) and after (red) illumination. (**e**) Schematic of the temporal arrangement of the recordings.
In (c) and (d) the amplitude of the S_{11} measurement of the resonator before illumination is included in blue.

changes in deposited material despite the already huge influence the drop has on the frequencies of the resonator. Moreover, the recorded phase changes are one order of magnitude higher as for the delay line presented in figure 6.5(b), despite the attenuation being weaker. This shows once more that the resonator design is especially good in detecting velocity changes.

To further confirm that the small changes in amplitude and phase of the coupled electric signal actually result from the creation of charge carriers in the deposited material and not due to an interaction of the laser with the substrate, another study is performed in the same manner as before with the excitation laser focused not on the perovskite drop but next to it at a sufficiently large distance still within the acoustic path. In this way, the intake from the laser onto the substrate stays the same and its direct influence on the acoustic wave in the resonator can be examined.

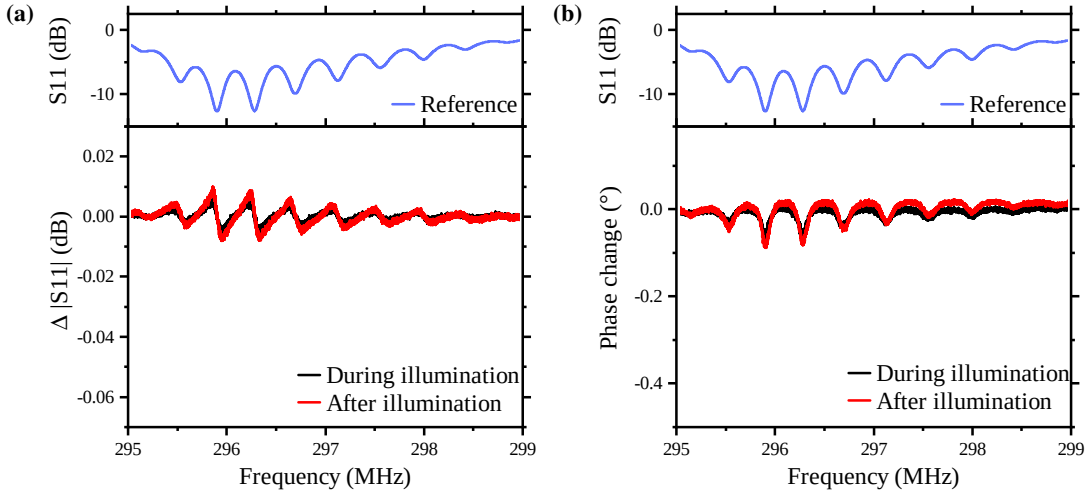

Figure 7.6: Changes in the electric reflection measurement of the IDT within the resonator due to the illumination with 600 nm of a spot in the acoustic path, but not on the sensing material. As a reference the S_{11} measurement of the resonator before illumination is again included in blue. The scales in these graphs match figure 7.5. (**a**) Change in the transmission amplitude at the time of irradiation (black) and after the light is switched off again (red), both subtracted from the measurement directly before the laser was turned on. (**b**) Phase change during (black) and after (red) the illumination subtracted from the phase recording directly before the illumination.

The studies of amplitude and phase change of an input signal with $P_{rf} = -3\,\mathrm{dBm}$ during (black) and after (red) an illumination with 600 nm light on a reference spot are presented in figure 7.6(a) and (b), respectively. The scale of the left axis in both graphs is chosen to match figure 7.5 in order to simplify a comparison of the orders of magnitude of the two studies. It is immediately clear that the effect of the laser directly on the substrate has significantly smaller dimensions on the change in transmission of the wave than the conductivity in the perovskite material. This order of magnitude in both graphs clearly demonstrates the observed changes in the wave are truly a result of mobile charge carrier creation in the perovskite. Additionally, the huge differences that appear in figure 7.5 between the data during and after the illumination do not reproduce in the reference series.

The slight changes in amplitude and phase that appear also in the reference study can be a result of heat creation or of a scattering process of the light at the top and bottom surfaces of the substrate. Due to the limited space between the two reflectors, the position of the laser is at maximum a few millimetres away from the perovskite material. As a result, even with

no direct illumination of the sensing material, it becomes partly excited and the created free charge carriers induce a small conductivity, which influences the transmission of the SAW. It is also conceivable the heat intake from the laser has a small influence on the SAW as the sound velocity in the material is dependent on the temperature. Due to the high absorption of the perovsiktes, there is less heat intake on the substrate in the study of conductance creation through illumination which could explain why the shape of the signal in this reference study is not reproduced in the background of figure 7.5.

Similar to the previous chapter, also the resonator design can be employed to perform excitation energy-resolved studies. Just like before, the absorption edge of the material can be nicely reproduced and coincides for all available resonance frequencies. Exemplary, the data set for the three frequencies f_{n+1}, f_{n+2} and f_{n+3} are presented in figure 7.7. The recordings are performed with the VNA and an input power of $P_{rf} = -3\,\mathrm{dBm}$ for the SAW. Panel (a) shows the extracted absolute peak amplitude of f_{n+2} as a function of the excitation wavelength. Analogously to section 6.3, a white light laser source is combined with a monochromator to selectively excite the perovskite nanowires with a distinct wavelength. The spectral width of the excitation amounts to approximately 10 nm and illuminates the full drop of material. For each recording, the amplitude at the resonance dip is extracted before and during the irradiation.

The results are plotted in figure 7.7(a) where the peak amplitude of the mode $n+2$ is plotted as a function of the excitation wavelength before (black) and during (red) the illumination. The excitation is provided by the white light source which is filtered by the monochromator to a bandwidth of around 6 nm. The data clearly shows that the amplitude is reduced for lower wavelengths under illumination. At laser energies far below the bandgap of the material, corresponding to 660 nm, no difference between the two recordings can be found. The global trend of the amplitude in the recordings is a long term effect and is not directly correlated to the wavelength of the laser but rather a shift over time. To check this, the resonances before and after the illumination were compared and found to be similar for all data sets (c. f. figure 7.5(c).

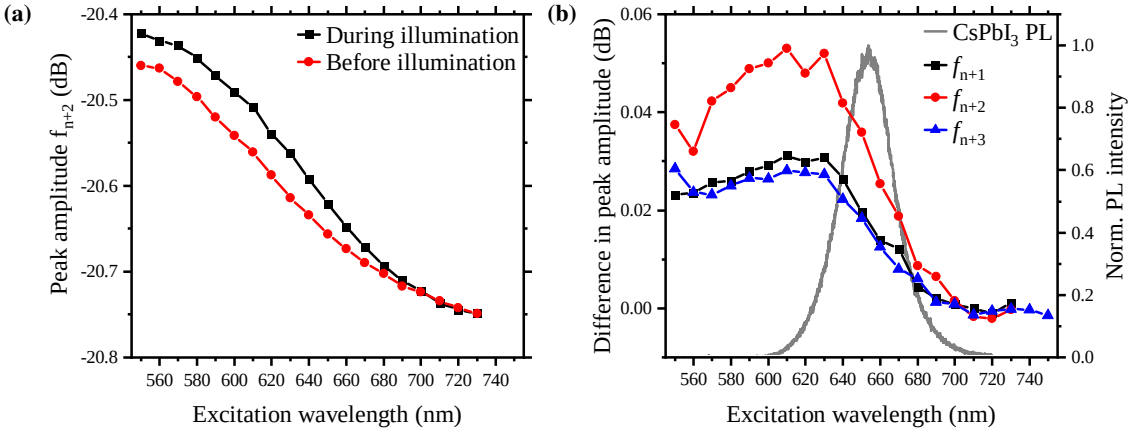

Figure 7.7: (**a**) Extracted peak amplitude of resonance f_{n+2} of a reflection measurement of the IDT in the resonator before (red) and during (black) illumination with a laser of variable wavelength. (**b**) Extracted difference in peak amplitude for each wavelength for the data of panel (a) and the two other resonances f_{n+1} and f_{n+3}. The PL emission from $CsPbI_3$ is included in grey.

For a clearer presentation and to compare the results of several resonances, the difference of the two studies is calculated and plotted in panel (b). The red curve represents the data

from panel (a) while the black and blue ones are taken from f_{n+1} and f_{n+3}. All show the same trend of a smeared out step-like function showing no difference between illumination and no illumination for high wavelengths and revealing significantly large deviations for low wavelengths. As a reference, the PL data of $CsPbI_3$ is plotted in grey. Its center wavelength coincides nicely with the position of the decrease in amplitude change. All three curves show the same onset and saturation point of the change with no dependence on the mode number n. The only difference is the effectiveness, i. e. the absolute amplitude change, which correlates with the strength of the resonance mode. Thus, similarly to section 6.3 the data reproduces nicely the absorption edge of $CsPbI_3$ and shows that the resonator design is equally well suitable for photoconductivity-based absorption studies on low conductive material.

7.4 Conclusion

The surface acoustic wave resonator is a very sensitive tool for the detection of small changes in the surroundings of its cavity. This chapter showed the creation of a small bandwidth resonator with few resonances in the band which are reacting on the deposition of sensing material on the surface area inside the cavity. Already the existence of mass load in the path of the SAW evokes great changes in the electric characteristic of the resonator. The resonance frequencies shift to lower values while their peak amplitude and the phase change are drastically reduced. These huge influence of the deposited material could be used as a mass sensor in future applications. Here, it is remarkable that despite these massive reduction of sensitivity, it is still possible to detect photo-induced conductivity in the perovskite material. The changes in amplitude and phase of the reflection measurement nicely coincide with the positions of the resonance frequencies and an additional reference study with an illumination far away from the deposited material could further corroborate that the observed effects are indeed arising locally from the creation of charge carriers in the material.

Finally, a study under the variation of the excitation energy confirmed the energy dependence of the absorption of the perovskite material. As expected and already seen in the previous chapter, the resonance frequencies only experience changes when the excitation light creates free electrons and holes in the material under examination, which is correlated with the bandgap of the material. Hence, also the resonator setup is capable of reproducing the absorption edge of a material and match nicely to the PL emission.

The resonator design is a very sensitive tool to viscous mass loading and is even capable of detecting conductivity changes in the loaded material. With some more optimization its sensitivity could be significantly increased, for example already by the reduction of the distance between the reflectors or the mass of the sensing material and it could be used as a high sensitive conductivity and viscous load detector.

Chapter 8

Conclusion and Outlook

The SAW as a tool for the investigation and manipulation of nanostructures has become an established method in our group and worldwide [Kin16; Wei14a; Wei14b; Fuh10; Lio17; Her18; Vil17; Fan18]. The huge advantage of being contact-free is especially relevant when it comes to very small objects. Moreover, the remote application of mechanical and electric wave enables two possible mechanisms. This thesis focused on the electric field and its influence on optically excited charge carriers in metal halide perovskites. It was possible to determine the average mobility of electron and hole for a whole ensemble of single, non-interacting nanowires. This was performed through acousto-optoelectric spectroscopy where the band structure, in which the optically excited charge carriers live, is modulated by the electric field of the SAW. This in turn induces a movement of the electrons and holes to energetically favourable positions which results in a spatial separation. This reduced overlap in the wavefunctions was investigated by the quenching of the photoluminescence which decreases with increasing acoustic power. In additional time-resolved studies the temporal emission in slowly changing electric fields was analysed and revealed very interesting and previously unknown behaviour. It was described in a pure phenomenological model that mathematically describes the effect of exciton polarization and exciton dissociation via reduced and sinusoidally modulated decay rates. A fit of the model's function onto the experimental data revealed great agreement, confirming that the two main phenomena during the experiment are indeed, dissociation and polarization of the excitons. A subsequent simulation with the basic drift and diffusion equations led to the determination of the mobilities of electrons and holes. The result was that both charge carriers, in accordance with expectancies from bulk material, have equal mobility and that it can be pinned to a value of around 3 $\frac{\mathrm{cm}^2}{\mathrm{Vs}}$. Low temperature studies showed enhanced reaction on the electric field in the form of polarization as the number of free charge carriers is reduced. Finally, in the presence of many charge carriers the effect of the electric field becomes screened, such that studies at higher excitation laser powers have a reduced response to the electric field. In summary, this thesis gave profound insight into the dynamics of charge carriers in the very small system of nanowires of metal halide perovskite material.

The second major part of the thesis concentrated on the opposite effect: the influence of the surface waves by the charge carriers in the nanostructure. To use the SAW in sensor applications is already well established and ranges from temperature over pressure and humidity to bio-sensors [Bo16]. In our implementation, the change in conductivity induced the measurable effects on the wave. A TIDT design was realized to enable spatially resolved detection. Through the perovskite material deposited in the path of the SAW, sensing material could be integrated. With above bandgap laser light exciting the structures, an attenuation and velocity change of the SAW could be recorded. These function as a measure for the created photoconductivity and can reproduce nicely the absorption edge of the material without the need of a transparent substrate. An arrangement with two perpendicular delay lines with tapered IDTs enabled a full

two dimensional position detection which was combined with the deposition of two different materials at the same chip to allow for a discrimination of different excitation wavelengths.

Finally, the concept of sensing was conveyed to the more sensitive arrangement of SAW resonators. It could be shown that these can even work as high sensitive viscous mass loading sensors as the exact position of resonance frequency is strongly dependent on the phase shift due to externally induced velocity changes in the resonator. These influence the wave in a resonator much stronger. Furthermore, despite the resonator's advantage lying in the detection of velocity changes, its recording of attenuation is also good and can be used, similar to the delay line, to measure the absorption edge of a material.

In conclusion, it could be shown that the SAW is a versatile tool to probe and manipulate nanosystems, but also to sense changes in its surroundings. Its flexibility is of great advantage in numerous applications and can be exploited for fundamental materials research as well as in the construction of sensitive detectors.

The following two sections will introduce two more experiments that could be conducted with the SAW to investigate material parameters that are otherwise difficult to access.

8.1 Detection of Minibands with a SAW

Despite the examination of perovskite nanowires, it is also possible to use the methods of this thesis for other kinds of nanostructures, such as thin films. As a result of the small size in all directions of, for example, thin, square shaped films with an area of approximately $10\,\text{nm} \times 10\,\text{nm}$, so called platelets, or their three dimensional counterpart, the cubes, it is very hard to precisely detect single structures with a standard optical microscope. Moreover, their cross section is too small for the usual frequencies of the SAW to provide a sufficiently large interaction length. This phenomenon was shown for NWs in section 5.4 when comparing the influence of a parallel and a perpendicular SAW on the wire: trying to modulate the charge carrier perpendicular to the axis of the NW is not possible due to their similar small cross section. But for nanocubes there exists an interesting phenomenon which would be ideal to be examined with acousto-optical spectroscopy. When prepared with the correct kind of ligands, the nanocubes can form super-crystals (c. f. the SEM picture in figure 8.1) [Ton18]. These consist of individual nanocubes which are bound very closely together. As a result the barrier between the structures becomes very low and transport of charge carriers between the cubes is possible. The formation of these so called minibands [Sal13] is a very hot topic in current research and could be nicely determined by SAW-induced transport studies. The bands enable a transport over larger distances than just the length of one cube and can thus be ideally probed by acousto-electric transport. The only challenge that has still to be overcome is the clearing of the nanostructures from excessive ligands and other material that forms a jelly-like substance around the actual super-crystals. This viscous supporting material absorbs the energy from the SAW through the mechanical vibration and transports it away from the direct surface and thus attenuates the wave. When this technical challenge is solved, the SAW is a perfect tool to probe the minibands in the compound system.

8.2 Combining Perovskite Nanowires with VdW-Materials

The very interesting class of 2D materials that rose after the invention of the scotch tape fabrication method for graphene has in many aspects very similar properties to the nanoscale

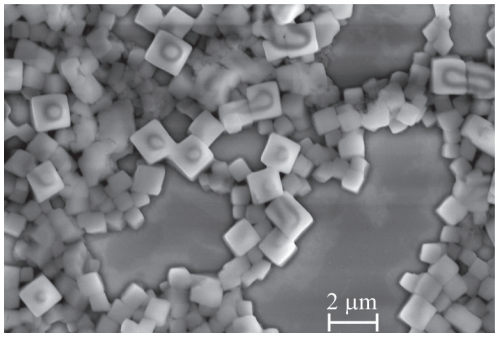

Figure 8.1: SEM picture of super-crystals that emerge through the reallocation of smaller nanocubes. They build up bonds such that their bands come energetically closer together and so called minibands form.

perovskites. Hence, it comes naturally to mind to examine their electronic behaviour with the methods of acousto-optical spectroscopy. This is already in the scope of our group and crystal direction dependencies as well as heterostructures are being investigated. The possibility of creating heterostructures from different 2D materials rose the idea of creating an even more heterogeneous structure by placing perovskite nanowires on top of monolayers of the van-der-Waals material MoS_2. This composite should behave differently than both materials on their own when excited as the presence of charge carriers in the respective other material influences the electronics reciprocally.

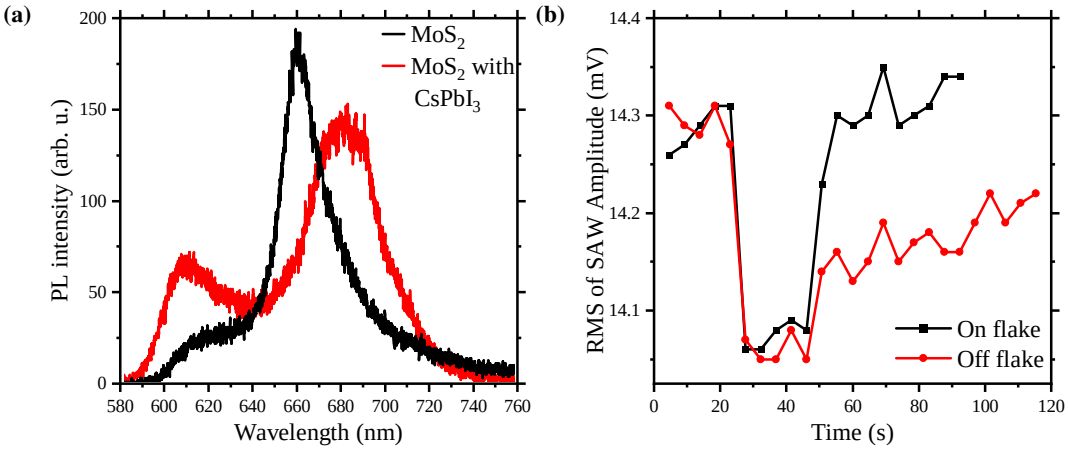

Figure 8.2: (**a**) PL emission from a MoS_2 flake on $LiNbO_3$ without (black) and with additional perovskite NWs deposited on top (red). (**b**) SAW attenuation before, during and after laser illumination of the perovskite NWs on top of the MOS_2 flake (black) and directly on the substrate (red).

This can remarkably clearly be seen in figure 8.2(a) in a demonstration of the change in PL emission of the few-layer MoS_2 through the deposition of additional perovskite material on top. The black line shows the emission peak from a MoS_2 flake transferred onto the $LiNbO_3$ substrate. It is centred at around 660 nm or 1.88 eV. By depositing perovskite NWs on top of the flake, this emission profile can be massively affected. Instead of showing one single peak, there exist now two distinct emission energies, one above and one below the former value (red line in figure 8.2). This already points towards a strong influence of the perovskite NWs on the 2D material.

An examination with the SAW also gives hints towards this being an interesting field of study.

Figure 8.2(b) presents studies of the SAW attenuation by the heterostructure of perovskite NWs and MoS_2 before, during and after illumination in comparison to the attenuation by only the perovskite NWs. These studies with $f_{SAW} = 99\,\mathrm{MHz}$ at an applied power of $P_{rf} = -3\,\mathrm{dBm}$ reveal that the electronic recovery after an illumination with a high power, above bandgap laser strongly depends on the environment. There is a clear difference in the recovery behaviour when the laser is switched of. In one case, the attenuation persists over several more minutes, in the other the SAW amplitude recovers instantly. These differences further proof the existence of a reciprocal influence between the 2D material flake and the perovskite NWs and require deeper research about their origin and nature. This very interesting field of heterostructures of novel materials can be promising for future applications and their examination with the surface acoustic wave could be one way to easily access the evolution of their electronic properties.

Appendix

Parameters for the Numerical Simulation of Charge Carrier Dynamics

Sound velocity	$3488\,\mathrm{m/s}$
Aperture	$400\,\mu\mathrm{m}$
Admittance	$0.21\,\mathrm{mSv}$
Permittivity of $LiNbO_3$	$27.5 \cdot \varepsilon_0$
Temperature	$300\,\mathrm{K}$
Exciton binding energy	$25\,\mathrm{meV}$
Exciton radius	$12\,\mathrm{nm}$
Exciton generation rate	$100\,\mathrm{cm^2/s}$
Direct recombination rate	$1\,\mathrm{cm^2/s}$
Spot width	$1.5\,\mu\mathrm{m}$
Pulse Width	$80\,\mathrm{ps}$
Repetition time of laser	$40 \cdot T_{SAW}$

Preparation of the SAW Chip

Cleaning	
Sonicate in Aceton	10 min
Cleanse	Aceton & Isopropanol
Dry	Nitrogen
Baking out	2 min @ 180 °C on hotplate
Spin Coating	
first layer	PMMA 495K
second layer	PMMA 950K
Spinning	5 s @ 500 rpm & 30 s @ 5000 rpm
Baking	2 min @180 °C on hotplate
Conductive layer	Electra92
Spinning	5 s @ 500 rpm & 60 s @ 2000 rpm
Baking	2 min @90 °C on hotplate
Lithography	
Voltage	10 kV
Area dose	100 $\mu As/cm^2$
Dose	0.6 to 0.9
Remove conductive layer	60 s in H_2O
Develop	MIBK : Isopropanol in 1:3 solution, 30 s
Stop	Isopropanol, 15 s
Metallization	
Plasma cleaning	600 W, 13 s
Metal	5 nm titan (adhesion agent), rate ≈ 0.5 Å/s 50 nm aluminium (IDTs), rate ≤ 1 Å/s 50 nm gold (marker), rate ≈ 0.7 Å/s
Lift-off	Remover PG or mr-REM 500 or MicroPur D350 for several hours, sonication when required
Cleaning	Aceton, Isopropanol and drying with nitrogen

CB conduction band 7
DOS density of states 12
FFT Fast Fourier Transform 59
FWHM full width half maximum 23
IDT interdigital transducer 15
IL insertion loss 30
μ-PL μ-photoluminescence 45
NW nanowire 6
PL photoluminescence 5
QW quantum well 49
SAW surface acoustic wave 3
SNR signal to noise ratio 56
SPAD single photon avalanche diode 46
TIDT tapered interdigital transducer 25
VB valence band 7
VNA vector network analyser 31

Bibliography

[Aam16a] M. Aamir, M. Sher, M. A. Malik, N. Revaprasadu and J. Akhtar. 'A facile approach for selective and sensitive detection of aqueous contamination in DMF by using perovskite material'. *Materials Letters* 183 (2016), pp. 135–138. DOI: 10.1016/j.matlet.2016.07.066.

[Aam16b] M. Aamir, M. Sher, M. A. Malik, J. Akhtar and N. Revaprasadu. 'A chemodosimetric approach for the selective detection of Pb^{2+} ions using a cesium based perovskite'. *New Journal of Chemistry* 40.11 (2016), pp. 9719–9724. DOI: 10.1039/C6NJ01783E.

[Abd18] G. Abdelmageed, H. R. Sully, S. Bonabi Naghadeh, A. El-Hag Ali, S. A. Carter et al. 'Improved Stability of Organometal Halide Perovskite Films and Solar Cells toward Humidity via Surface Passivation with Oleic Acid'. *ACS Applied Energy Materials* 1.2 (2018), pp. 387–392. DOI: 10.1021/acsaem.7b00069.

[Adl71] R. Adler. 'Simple theory of acoustic amplification'. *IEEE Transactions on Sonics and Ultrasonics* 18.3 (1971), pp. 115–118. DOI: 10.1109/T-SU.1971.29605.

[Aha16] I. Aharonovich, D. Englund and M. Toth. 'Solid-state single-photon emitters'. *Nature Photonics* 10.10 (2016), pp. 631–641. DOI: 10.1038/nphoton.2016.186.

[Ahm17] W. Ahmad, J. Khan, G. Niu and J. Tang. 'Inorganic $CsPbI_3$ Perovskite-Based Solar Cells: A Choice for a Tandem Device'. *Solar RRL* 1.7 (2017), p. 1700048. DOI: 10.1002/solr.201700048.

[Ahm19] M. Ahmadi, E. S. Muckley, I. N. Ivanov, M. Lorenz, X. Li et al. 'Environmental Gating and Galvanic Effects in Single Crystals of Organic-Inorganic Halide Perovskites'. *ACS applied materials & interfaces* 11.16 (2019), pp. 14722–14733. DOI: 10.1021/acsami.8b21112.

[Akb18] B. Akbali, G. Topcu, T. Guner, M. Ozcan, M. M. Demir et al. '$CsPbBr_3$ perovskites: Theoretical and experimental investigation on water-assisted transition from nanowire formation to degradation'. *Physical Review Materials* 2.3 (2018), p. 034601. DOI: 10.1103/PhysRevMaterials.2.034601.

[Akk16] Q. A. Akkerman, M. Gandini, F. Di Stasio, P. Rastogi, F. Palazon et al. 'Strongly emissive perovskite nanocrystal inks for high-voltage solar cells'. *Nature Energy* 2.2 (2016), p. 141. DOI: 10.1038/nenergy.2016.194.

[Als01] F. Alsina, P. V. Santos, R. Hey, A. García-Cristóbal and A. Cantarero. 'Dynamic carrier distribution in quantum wells modulated by surface acoustic waves'. *Physical review. B, Condensed matter* 64.4 (2001), p. 3389. DOI: 10.1103/PhysRevB.64.041304.

[Als02] F. Alsina, P. V. Santos, H.-P. Schönherr, W. Seidel, K. H. Ploog et al. 'Surface-acoustic-wave-induced carrier transport in quantum wires'. *Physical review. B, Condensed matter* 66.16 (2002), p. 939. DOI: 10.1103/PhysRevB.66.165330.

[Ash85] E. A. Ash, E. G. S. Paige and L. B. Felsen. *Rayleigh-Wave Theory and Application*. Vol. 2. Springer Berlin Heidelberg, 1985. DOI: 10.1007/978-3-642-82621-4.

[Bal19] L. Balaghi, G. Bussone, R. Grifone, R. Hübner, J. Grenzer et al. 'Widely tunable GaAs bandgap via strain engineering in core/shell nanowires with large lattice mismatch'. *Nature communications* 10.1 (2019), p. 2793. DOI: 10.1038/s41467-019-10654-7.

[Bal97] D. S. Ballantine. *Acoustic wave sensors. Theory, design, and physico-chemical applications*. Applications of modern acoustics. Acad. Press, 1997.

[Bao15] C. Bao, J. Yang, W. Zhu, X. Zhou, H. Gao et al. 'A resistance change effect in perovskite $CH_3NH_3PbI_3$ films induced by ammonia'. *Chemical communications* 51.84 (2015), pp. 15426–15429. DOI: 10.1039/C5CC06060E.

[Bao18] C. Bao, J. Yang, S. Bai, W. Xu, Z. Yan et al. 'High Performance and Stable All-Inorganic Metal Halide Perovskite-Based Photodetectors for Optical Communication Applications'. *Advanced materials* 30.38 (2018), p. 1803422. DOI: 10.1002/adma.201803422.

[Bas95] M. Bass, ed. *Handbook of optics*. 2. ed. McGraw-Hill, 1995.

[Ber18] A. Bercegol, F. J. Ramos, A. Rebai, T. Guillemot, D. Ory et al. 'Slow Diffusion and Long Lifetime in Metal Halide Perovskites for Photovoltaics'. *The Journal of Physical Chemistry C* 122.43 (2018), pp. 24570–24577. DOI: 10.1021/acs.jpcc.8b08252.

[Bha19] U. K. Bhaskar, S. A. Bhave and D. Weinstein. 'Silicon acoustoelectronics with thin film lithium niobate'. *Journal of Physics D: Applied Physics* 52.5 (2019), p. 05LT01. DOI: 10.1088/1361-6463/aaee59.

[Bie72] P. Bierbaum. 'Interaction of ultrasonic surface waves with conduction electrons in thin metal films'. *Applied Physics Letters* 21.12 (1972), pp. 595–598. DOI: 10.1063/1.1654269.

[Bo16] L. Bo, C. Xiao, C. Hualin, M. Mohammad, T. Xiangguang et al. 'Surface acoustic wave devices for sensor applications'. *New Journal of Physics* 37.2 (2016), p. 021001. DOI: 10.1088/1674-4926/37/2/021001.

[Boh18] B. J. Bohn, Y. Tong, M. Gramlich, M. L. Lai, M. Döblinger et al. 'Boosting Tunable Blue Luminescence of Halide Perovskite Nanoplatelets through Postsynthetic Surface Trap Repair'. *Nano letters* 18.8 (2018), pp. 5231–5238. DOI: 10.1021/acs.nanolett.8b02190.

[Bor08] I. Borriello, G. Cantele and D. Ninno. 'Ab initio investigation of hybrid organic-inorganic perovskites based on tin halides'. *Physical Review B* 77.23 (2008), p. 29. DOI: 10.1103/PhysRevB.77.235214.

[Boy19] C. C. Boyd, R. Cheacharoen, T. Leijtens and M. D. McGehee. 'Understanding Degradation Mechanisms and Improving Stability of Perovskite Photovoltaics'. *Chemical reviews* 119.5 (2019), pp. 3418–3451. DOI: 10.1021/acs.chemrev.8b00336.

[Bre15] T. M. Brenner, D. A. Egger, A. M. Rappe, L. Kronik, G. Hodes et al. 'Are Mobilities in Hybrid Organic-Inorganic Halide Perovskites Actually High?' *The journal of physical chemistry letters* 6.23 (2015), pp. 4754–4757. DOI: 10.1021/acs.jpclett.5b02390.

[Bre17] R. Brenes, D. Guo, A. Osherov, N. K. Noel, C. Eames et al. 'Metal Halide Perovskite Polycrystalline Films Exhibiting Properties of Single Crystals'. *Joule* 1.1 (2017), pp. 155–167. DOI: 10.1016/j.joule.2017.08.006.

[Bre19] M. C. Brennan, M. Kuno and S. Rouvimov. 'Crystal Structure of Individual $CsPbBr_3$ Perovskite Nanocubes'. *Inorganic chemistry* 58.2 (2019), pp. 1555–1560. DOI: 10.1021/acs.inorgchem.8b03078.

[Bus17] K. A. Bush, A. F. Palmstrom, Z. J. Yu, M. Boccard, R. Cheacharoen et al. '23.6%-efficient monolithic perovskite/silicon tandem solar cells with improved stability'. *Nature Energy* 2.4 (2017), p. 1035. DOI: 10.1038/nenergy.2017.9.

[But93] P. Butcher, N. H. March and M. P. Tosi. *Physics of Low-Dimensional Semiconductor Structures*. Springer US, 1993. DOI: 10.1007/978-1-4899-2415-5.

[Cam68] J. J. Campbell and W. R. Jones. 'A method for estimating optimal crystal cuts and propagation directions for excitation of piezoelectric surface waves'. *IEEE Transactions on Sonics and Ultrasonics* 15.4 (1968), pp. 209–217. DOI: 10.1109/T-SU.1968.29477.

[Cam89] C. Campbell. *Surface acoustic wave devices and their signal processing applications*. Acad. Press, 1989.

[Cec04] M. Cecchini, G. de Simoni, V. Piazza, F. Beltram, H. E. Beere et al. 'Surface acoustic wave-driven planar light-emitting device'. *Applied Physics Letters* 85.15 (2004), pp. 3020–3022. DOI: 10.1063/1.1803936.

[Cha18] S. Chang, Z. Bai and H. Zhong. 'In Situ Fabricated Perovskite Nanocrystals: A Revolution in Optical Materials'. *Advanced Optical Materials* 6.18 (2018), p. 1800380. DOI: 10.1002/adom.201800380.

[Che13] Y. Chen, X. Ding, S.-C. Steven Lin, S. Yang, P.-H. Huang et al. 'Tunable nanowire patterning using standing surface acoustic waves'. *ACS nano* 7.4 (2013), pp. 3306–3314. DOI: 10.1021/nn4000034.

[Che17a] M. Chen, Y. Zou, L. Wu, Q. Pan, Di Yang et al. 'Solvothermal Synthesis of High-Quality All-Inorganic Cesium Lead Halide Perovskite Nanocrystals: From Nanocube to Ultrathin Nanowire'. *Advanced Functional Materials* 27.23 (2017), p. 1701121. DOI: 10.1002/adfm.201701121.

[Che17b] X. Chen, H. Hu, Z. Xia, W. Gao, W. Gou et al. '$CsPbBr_3$ perovskite nanocrystals as highly selective and sensitive spectrochemical probes for gaseous HCl detection'. *Journal of Materials Chemistry C* 5.2 (2017), pp. 309–313. DOI: 10.1039/C6TC04136A.

[Cho18] H. Cho, Y.-H. Kim, C. Wolf, H.-D. Lee and T.-W. Lee. 'Improving the Stability of Metal Halide Perovskite Materials and Light-Emitting Diodes'. *Advanced materials* 30.42 (2018), p. 1704587. DOI: 10.1002/adma.201704587.

[Dab97] B. O. Dabbousi, J. Rodriguez-Viejo, F. V. Mikulec, J. R. Heine, H. Mattoussi et al. '(CdSe)ZnS Core-Shell Quantum Dots: Synthesis and Characterization of a Size Series of Highly Luminescent Nanocrystallites'. *The Journal of Physical Chemistry B* 101.46 (1997), pp. 9463–9475. DOI: 10.1021/jp971091y.

[Dai16] J. Dai, H. Zheng, C. Zhu, J. Lu and C. Xu. 'Comparative investigation on temperature-dependent photoluminescence of $CH_3NH_3PbBr_3$ and $CH(NH_2)_2PbBr_3$ microstructures'. *Journal of Materials Chemistry C* 4.20 (2016), pp. 4408–4413. DOI: 10.1039/c6tc00563b.

[DAm89] A. D'Amico and E. Verona. 'Saw sensors'. *Sensors and Actuators* 17.1-2 (1989), pp. 55–66. DOI: 10.1016/0250-6874(89)80064-2.

[Dar16] M. I. Dar, G. Jacopin, S. Meloni, A. Mattoni, N. Arora et al. 'Origin of unusual bandgap shift and dual emission in organic-inorganic lead halide perovskites'. *Science Advances* 2.10 (2016), p. 1601156. DOI: 10.1126/sciadv.1601156.

[Das17] S. Dastidar, S. Li, S. Y. Smolin, J. B. Baxter and A. T. Fafarman. 'Slow Electron–Hole Recombination in Lead Iodide Perovskites Does Not Require a Molecular Dipole'. *ACS Energy Letters* 2.10 (2017), pp. 2239–2244. DOI: 10.1021/acsenergylett.7b00606.

[Dat86] S. Datta. *Surface Acoustic Wave Devices*. Prentice-Hall, 1986.

[Dem10] O. Demichel, M. Heiss, J. Bleuse, H. Mariette and A. Fontcuberta i Morral. 'Impact of surfaces on the optical properties of GaAs nanowires'. *Applied Physics Letters* 97.20 (2010), p. 201907. DOI: 10.1063/1.3519980.

[Des14] F. Deschler, M. Price, S. Pathak, L. E. Klintberg, D.-D. Jarausch et al. 'High Photoluminescence Efficiency and Optically Pumped Lasing in Solution-Processed Mixed Halide Perovskite Semiconductors'. *The journal of physical chemistry letters* 5.8 (2014), pp. 1421–1426. DOI: 10.1021/jz5005285..

[Dir17] B. T. Diroll, G. Nedelcu, M. V. Kovalenko and R. D. Schaller. 'High-Temperature Photoluminescence of $CsPbX_3$ (X = Cl, Br, I) Nanocrystals'. *Advanced Functional Materials* 27.21 (2017), p. 1606750. DOI: 10.1002/adfm.201606750.

[Dir18] B. T. Diroll, H. Zhou and R. D. Schaller. 'Low-Temperature Absorption, Photoluminescence, and Lifetime of $CsPbX_3$ (X = Cl, Br, I) Nanocrystals'. *Advanced Functional Materials* 28.30 (2018), p. 1800945. DOI: 10.1002/adfm.201800945.

[Dit15] T. Dittrich, C. Awino, P. Prajongtat, B. Rech and M. C. Lux-Steiner. 'Temperature Dependence of the Band Gap of $CH_3NH_3PbI_3$ Stabilized with PMMA: A Modulated Surface Photovoltage Study'. *The Journal of Physical Chemistry C* 119.42 (2015), pp. 23968–23972. DOI: 10.1021/acs.jpcc.5b07132.

[Don15] R. Dong, Y. Fang, J. Chae, J. Dai, Z. Xiao et al. 'High-gain and low-driving-voltage photodetectors based on organolead triiodide perovskites'. *Advanced materials (Deerfield Beach, Fla.)* 27.11 (2015), pp. 1912–1918. DOI: 10.1002/adma.201405116.

[Dou14] L. Dou, Y. M. Yang, J. You, Z. Hong, W.-H. Chang et al. 'Solution-processed hybrid perovskite photodetectors with high detectivity'. *Nature communications* 5 (2014), p. 5404. DOI: 10.1038/ncomms6404.

[Eat16] S. W. Eaton, A. Fu, A. B. Wong, C.-Z. Ning and P. Yang. 'Semiconductor nanowire lasers'. *Nature Reviews Materials* 1.6 (2016), p. 318. DOI: 10.1038/natrevmats.2016.28.

[Ell57] R. J. Elliott. 'Intensity of Optical Absorption by Excitons'. *Physical Review* 108.6 (1957), pp. 1384–1389. DOI: 10.1103/PhysRev.108.1384.

[Fan18] R. Fandan, J. Pedrós, J. Schiefele, A. Boscá, J. Martínez et al. 'Acoustically-driven surface and hyperbolic plasmon-phonon polaritons in graphene/h-BN heterostructures on piezoelectric substrates'. *New Journal of Physics* 51.20 (2018), p. 204004. DOI: 10.1088/1361-6463/aab8bd.

[Fis18] E. M. Fisher. 'Principles and Early Historical Development of Silicon Avalanche and Geiger-Mode Photodiodes'. *Photon Counting - Fundamentals and Applications*. InTech, 2018. DOI: 10.5772/intechopen.72148.

[Fre31] J. Frenkel. 'On the Transformation of light into Heat in Solids. I'. *Physical Review* 37.1 (1931), pp. 17–44. DOI: 10.1103/PhysRev.37.17.

[Fro14] J. M. Frost, K. T. Butler, F. Brivio, C. H. Hendon, M. van Schilfgaarde et al. 'Atomistic origins of high-performance in hybrid halide perovskite solar cells'. *Nano letters* 14.5 (2014), pp. 2584–2590. DOI: 10.1021/nl500390f.

[Fro17] J. M. Frost. 'Calculating polaron mobility in halide perovskites'. *Physical Review B* 96.19 (2017), p. 195202. DOI: 10.1103/PhysRevB.96.195202.

[Fu16] Y. Fu, H. Zhu, A. W. Schrader, D. Liang, Q. Ding et al. 'Nanowire Lasers of Formamidinium Lead Halide Perovskites and Their Stabilized Alloys with Improved Stability'. *Nano letters* 16.2 (2016), pp. 1000–1008. DOI: 10.1021/acs.nanolett.5b04053.

[Fuh10] D. A. Fuhrmann, H. J. Krenner, A. Wixforth, A. Curran, K. A. Prior et al. 'Noninvasive probing of persistent conductivity in high quality ZnCdSe/ZnSe quantum wells using surface acoustic waves'. *Journal of Applied Physics* 107.9 (2010), p. 093717. DOI: 10.1063/1.3373415.

[Gab19] F. Gabelloni, F. Biccari, N. Falsini, N. Calisi, S. Caporali et al. 'Long-living nonlinear behavior in $CsPbBr_3$ carrier recombination dynamics'. *Nanophotonics* 8.9 (2019), pp. 1447–1455. DOI: 10.1515/nanoph-2019-0013.

[Gao19] Z. Gao, X. Zhang, J. Yu and X. Yu. 'Bio-inspired materials as interfacial layers for high performance perovskite photodetectors'. *Optical Materials Express* 9.10 (2019), p. 3968. DOI: 10.1364/OME.9.003968.

[Gar04] A. García-Cristóbal, A. Cantarero, F. Alsina and P. V. Santos. 'Spatiotemporal carrier dynamics in quantum wells under surface acoustic waves'. *Physical Review B* 69.20 (2004), p. 4099. DOI: 10.1103/PhysRevB.69.205301.

[Gel07] J. R. Gell, M. B. Ward, A. J. Shields, P. Atkinson, S. P. Bremner et al. 'Temporal characteristics of surface-acoustic-wave-driven luminescence from a lateral p-n junction'. *Applied Physics Letters* 91.1 (2007), p. 013506. DOI: 10.1063/1.2753759.

[Gla75] A. M. Glazer. 'Simple ways of determining perovskite structures'. *Acta Crystallographica Section A* 31.6 (1975), pp. 756–762. DOI: 10.1107/S0567739475001635.

[Gol26] V. M. Goldschmidt. 'Die Gesetze der Krystallochemie'. *Die Naturwissenschaften* 14.21 (1926), pp. 477–485. DOI: 10.1007/BF01507527.

[Gov00] A. Govorov, A. Kalameitsev, M. Rotter, A. Wixforth, J. Kotthaus et al. 'Nonlinear acousto-electric transport in a two-dimensional electron system'. *Physical Review B* 62.4 (2000), pp. 2659–2668.

[Gra15] G. Grancini, V. D'Innocenzo, E. R. Dohner, N. Martino, A. R. Srimath Kandada et al. '$CH_3NH_3PbI_3$ perovskite single crystals: surface photophysics and their interaction with the environment'. *Chem. Sci.* 6.12 (2015), pp. 7305–7310. DOI: 10.1039/c5sc02542g.

[Gru06] M. Grundmann. *The Physics of Semiconductors. An Introduction Including Devices and Nanophysics*. Springer-Verlag Berlin Heidelberg, 2006. DOI: 10.1007/3-540-34661-9.

[Han18] Q. Han, Y.-T. Hsieh, L. Meng, J.-L. Wu, P. Sun et al. 'High-performance perovskite/$Cu(In,Ga)Se_2$ monolithic tandem solar cells'. *Science* 361.6405 (2018), pp. 904–908. DOI: 10.1126/science.aat5055.

[Her11] A. Hernández-Mínguez, M. Möller, S. Breuer, C. Pfüller, C. Somaschini et al. 'Acoustically driven photon antibunching in nanowires'. *Nano letters* 12.1 (2011), pp. 252–258. DOI: 10.1021/nl203461m.

[Her17] L. M. Herz. 'Charge-Carrier Mobilities in Metal Halide Perovskites: Fundamental Mechanisms and Limits'. *ACS Energy Letters* 2.7 (2017), pp. 1539–1548. DOI: 10.1021/acsenergylett.7b00276.

[Her18] A. Hernández-Mínguez, Y.-T. Liou and P. V. Santos. 'Interaction of surface acoustic waves with electronic excitations in graphene'. *Journal of Physics D: Applied Physics* 51.38 (2018), p. 383001. DOI: 10.1088/1361-6463/aad593.

[Hir71] S. Hirotsu. 'Experimental Studies of Structural Phase Transitions in $CsPbCl_3$'. *Journal of the Physical Society of Japan* 31.2 (1971), pp. 552–560. DOI: 10.1143/JPSJ.31.552.

[How98] C. J. Howard and H. T. Stokes. 'Group-Theoretical Analysis of Octahedral Tilting in Perovskites'. *Acta Crystallographica Section B Structural Science* 54.6 (1998), pp. 782–789. DOI: 10.1107/S0108768198004200.

[Hsu97] R. Hsu, E. N. Maslen, D. Du Boulay and N. Ishizawa. 'Synchrotron X-ray Studies of $LiNbO_3$ and $LiTaO_3$'. *Acta Crystallographica Section B Structural Science* 53.3 (1997), pp. 420–428. DOI: 10.1107/S010876819600777X.

[Hua13] L.-y. Huang and W. R. L. Lambrecht. 'Electronic band structure, phonons, and exciton binding energies of halide perovskites $CsSnCl_3$, $CsSnBr_3$, and $CsSnI_3$'. *Physical Review B* 88.16 (2013), p. 122. DOI: 10.1103/PhysRevB.88.165203.

[Hua15] H. Huang, F. Zhao, L. Liu, F. Zhang, X.-g. Wu et al. 'Emulsion Synthesis of Size-Tunable $CH_3NH_3PbBr_3$ Quantum Dots: An Alternative Route toward Efficient Light-Emitting Diodes'. *ACS applied materials & interfaces* 7.51 (2015), pp. 28128–28133. DOI: 10.1021/acsami.5b10373.

[Hua16] W. Huang, J. S. Manser, S. Sadhu, P. V. Kamat and S. Ptasinska. 'Direct Observation of Reversible Transformation of $CH_3NH_3PbI_3$ and NH_4PbI_3 Induced by Polar Gaseous Molecules'. *The journal of physical chemistry letters* 7.24 (2016), pp. 5068–5073. DOI: 10.1021/acs.jpclett.6b02499.

[Hua17] H. Huang, Q. Xue, B. Chen, Y. Xiong, J. Schneider et al. 'Top-Down Fabrication of Stable Methylammonium Lead Halide Perovskite Nanocrystals by Employing a Mixture of Ligands as Coordinating Solvents'. *Angewandte Chemie (International ed. in English)* 56.32 (2017), pp. 9571–9576. DOI: 10.1002/anie.201705595.

[Hut17] E. M. Hutter, R. J. Sutton, S. Chandrashekar, M. Abdi-Jalebi, S. D. Stranks et al. 'Vapour-Deposited Cesium Lead Iodide Perovskites: Microsecond Charge Carrier Lifetimes and Enhanced Photovoltaic Performance'. *ACS Energy Letters* 2.8 (2017), pp. 1901–1908. DOI: 10.1021/acsenergylett.7b00591.

[Isl69] M. N. Islam and J. Woods. 'Acoustoelectric interaction and the drift mobility of holes in CdS'. *Solid State Communications* 7.20 (1969). PII: 0038109869900210, pp. 1457–1461. DOI: 10.1016/0038-1098(69)90021-0.

[Jac81] J. L. Jackel and C. E. Rice. 'Topotactic $LiNbO_3$ to cubic perovskite structural transformation in $LiNbO_3$ and $LiTaO_3$'. *Ferroelectrics* 38.1 (1981), pp. 801–804. DOI: 10.1080/00150198108209543.

[Jan19] L. Janker, Y. Tong, L. Polavarapu, J. Feldmann, A. S. Urban et al. 'Real-Time Electron and Hole Transport Dynamics in Halide Perovskite Nanowires'. *Nano letters* (2019), pp. 8701–8707. DOI: 10.1021/acs.nanolett.9b03396.

[Jia19] T. Jiang, Z. Ju, H. Liu, F. Yang, H. Tian et al. 'High sensitive surface-acoustic-wave optical sensor based on two-dimensional perovskite'. *2019 International Conference on IC Design and Technology (ICICDT)*. 2019 International Conference on IC Design and Technology (ICICDT). IEEE, 2019, pp. 1–4. DOI: 10.1109/ICICDT.2019.8790835.

[Joh05] M. Johnsson and P. Lemmens. 'Crystallography and Chemistry of Perovskites'. *arXiv:cond-mat/0506606* (2005).

[Kar19] G. Y. Karapetyan, V. E. Kaydashev, D. A. Zhilin, M. E. Kutepov, T. A. Minasyan et al. 'A surface acoustic wave impedance-loaded high sensitivity sensor with wide dynamic range for ultraviolet light detection'. *Sensors and Actuators A: Physical* 296 (2019), pp. 70–78. DOI: 10.1016/j.sna.2019.07.010.

[Kim16] Y.-H. Kim, H. Cho and T.-W. Lee. 'Metal halide perovskite light emitters'. *Proceedings of the National Academy of Sciences of the United States of America* 113.42 (2016), pp. 11694–11702. DOI: 10.1073/pnas.1607471113.

[Kin11] J. B. Kinzel, D. Rudolph, M. Bichler, G. Abstreiter, J. J. Finley et al. 'Directional and dynamic modulation of the optical emission of an individual GaAs nanowire using surface acoustic waves'. *Nano letters* 11.4 (2011), pp. 1512–1517. DOI: 10.1021/nl1042775.

[Kin14] J. B. Kinzel. 'Akusto-elektrisch getriebene Modulation der Ladungsträgerdynamik in GaAs-Nanodrähten'. Doctoral Thesis. Universität Augsburg, 2014.

[Kin16] J. B. Kinzel, F. J. R. Schülein, M. Weiß, L. Janker, D. D. Bühler et al. 'The Native Material Limit of Electron and Hole Mobilities in Semiconductor Nanowires'. *ACS nano* 10.5 (2016), pp. 4942–4953. DOI: 10.1021/acsnano.5b07639.

[Koj09] A. Kojima, K. Teshima, Y. Shirai and T. Miyasaka. 'Organometal halide perovskites as visible-light sensitizers for photovoltaic cells'. *Journal of the American Chemical Society* 131.17 (2009), pp. 6050–6051. DOI: 10.1021/ja809598r.

[Kov90] G. Kovacs, M. Anhorn, H. E. Engan, G. Visintini and C. Ruppel. 'Improved material constants for $LiNbO_3$ and $LiTaO_3$'. *IEEE Symposium on Ultrasonics* (1990), pp. 435–438. DOI: 10.1109/ULTSYM.1990.171403.

[Laz17] S. Lazić, A. Hernández-Mínguez and P. V. Santos. 'Control of single photon emitters in semiconductor nanowires by surface acoustic waves'. *New Journal of Physics* 32.8 (2017), p. 084002. DOI: 10.1088/1361-6641/aa7295.

[Laz18] S. Lazić, E. Chernysheva, A. Hernández-Mínguez, P. V. Santos and H. P. van der Meulen. 'Acoustically regulated optical emission dynamics from quantum dot-like emission centers in GaN/InGaN nanowire heterostructures'. *Journal of Physics D: Applied Physics* 51.10 (2018), p. 104001. DOI: 10.1088/1361-6463/aaa8d5.

[Leh79] R. F. Leheny, J. Shah, R. L. Fork, C. V. Shank and A. Migus. 'Dynamics of hot carrier cooling in photo-excited GaAs'. *Solid State Communications* 31.11 (1979), pp. 809–813. DOI: 10.1016/0038-1098(79)90393-4.

[Lei15] T. Leijtens, G. E. Eperon, N. K. Noel, S. N. Habisreutinger, A. Petrozza et al. 'Stability of Metal Halide Perovskite Solar Cells'. *Advanced Energy Materials* 5.20 (2015), p. 1500963. DOI: 10.1002/aenm.201500963.

[Li08] C. Li, X. Lu, W. Ding, L. Feng, Y. Gao et al. 'Formability of ABX_3 (X = F, Cl, Br, I) halide perovskites'. *Acta crystallographica. Section B, Structural science* 64.Pt 6 (2008), pp. 702–707. DOI: 10.1107/S0108768108032734.

[Li18] B. Li, Y. Zhang, L. Fu, T. Yu, S. Zhou et al. 'Surface passivation engineering strategy to fully-inorganic cubic $CsPbI_3$ perovskites for high-performance solar cells'. *Nature communications* 9.1 (2018), p. 1076. DOI: 10.1038/s41467-018-03169-0.

[Li19] Y. Li, X. Zhang, H. Huang, S. V. Kershaw and A. L. Rogach. 'Advances in metal halide perovskite nanocrystals: Synthetic strategies, growth mechanisms, and optoelectronic applications'. *Materials Today* (2019), pp. 204–221. DOI: 10.1016/j.mattod.2019.06.007.

[Lin12] C. Lin, Y. Zhang, J. Liu, X. Li, Y. Li et al. 'Pressure-induced structural change in orthorhombic perovskite $GdMnO_3$'. *Journal of physics. Condensed matter : an Institute of Physics journal* 24.11 (2012), p. 115402. DOI: 10.1088/0953-8984/24/11/115402.

[Lio17] Y.-T. Liou, A. Hernández-Mínguez, J. Herfort, J. M. J. Lopes, A. Tahraoui et al. 'Acousto-electric transport in MgO/ZnO-covered graphene on SiC'. *New Journal of Physics* 50.46 (2017), p. 464008. DOI: 10.1088/1361-6463/aa8e8a.

[Liu18] Y. Liu, X. Tang, T. Zhu, M. Deng, I. P. Ikechukwu et al. 'All-inorganic $CsPbBr_3$ perovskite quantum dots as a photoluminescent probe for ultrasensitive Cu^{2+} detection'. *Journal of Materials Chemistry C* 6.17 (2018), pp. 4793–4799. DOI: 10.1039/C8TC00249E.

[Lu19] Y.-B. Lu, W.-Y. Cong, C. Guan, H. Sun, Y. Xin et al. 'Light enhanced moisture degradation of perovskite solar cell material $CH_3NH_3PbI_3$'. *Journal of Materials Chemistry A* 7.48 (2019), pp. 27469–27474. DOI: 10.1039/C9TA10443G.

[Luo17] B. Luo, S. B. Naghadeh and J. Z. Zhang. 'Lead Halide Perovskite Nanocrystals: Stability, Surface Passivation, and Structural Control'. *ChemNanoMat* 3.7 (2017), pp. 456–465. DOI: 10.1002/cnma.201700056.

[Mal13] O. Malinkiewicz, A. Yella, Y. H. Lee, G. M. Espallargas, M. Graetzel et al. 'Perovskite solar cells employing organic charge-transport layers'. *Nature Photonics* 8.2 (2013), pp. 128–132. DOI: 10.1038/nphoton.2013.341.

[Man16a] J. S. Manser, J. A. Christians and P. V. Kamat. 'Intriguing Optoelectronic Properties of Metal Halide Perovskites'. *Chemical reviews* 116.21 (2016), pp. 12956–13008. DOI: 10.1021/acs.chemrev.6b00136.

[Man16b] N. A. Manshor, Q. Wali, K. K. Wong, S. K. Muzakir, A. Fakharuddin et al. 'Humidity versus photo-stability of metal halide perovskite films in a polymer matrix'. *Physical chemistry chemical physics* 18.31 (2016), pp. 21629–21639. DOI: 10.1039/C6CP03600G.

[Mas16] R. Mastria and A. Rizzo. 'Mastering heterostructured colloidal nanocrystal properties for light-emitting diodes and solar cells'. *Journal of Materials Chemistry C* 4.27 (2016), pp. 6430–6446. DOI: 10.1039/c6tc01334a.

[Mat04] K. Matsuishi, T. Ishihara, S. Onari, Y. H. Chang and C. H. Park. 'Optical properties and structural phase transitions of lead-halide based inorganic–organic 3D and 2D perovskite semiconductors under high pressure'. *physica status solidi (b)* 241.14 (2004), pp. 3328–3333. DOI: 10.1002/pssb.200405229.

[Mat77] H. Matthews, ed. *Surface wave filters. Design, construction, and use*. A Wiley-Interscience publication. Wiley, 1977.

[Mer85] M. Merian and A. K. Bhattacharjee. 'Momentum matrix elements in III–V semiconductor alloys'. *Solid State Communications* 55.12 (1985), pp. 1071–1073. DOI: 10.1016/0038-1098(85)90135-8.

[Mer98] E. Merzbacher. *Quantum mechanics*. 3. ed. Wiley, 1998.

[Mi19] Y. Mi, Y. Zhong, Q. Zhang and X. Liu. 'Continuous–Wave Pumped Perovskite Lasers'. *Advanced Optical Materials* 7.17 (2019), p. 1900544. DOI: 10.1002/adom.201900544.

[Mil15] L. Miller. *RF Filter Technologies*. John Wiley & Sons, Inc., 2015.

[Mit01] D. B. Mitzi, C. D. Dimitrakopoulos and L. L. Kosbar. 'Structurally Tailored Organic–Inorganic Perovskites: Optical Properties and Solution-Processed Channel Materials for Thin-Film Transistors'. *Chemistry of Materials* 13.10 (2001), pp. 3728–3740. DOI: 10.1021/cm010105g.

[Mor05] L. Moretti, M. Iodice, F. G. Della Corte and I. Rendina. 'Temperature dependence of the thermo-optic coefficient of lithium niobate, from 300 to 515 K in the visible and infrared regions'. *Journal of Applied Physics* 98.3 (2005), p. 036101. DOI: 10.1063/1.1988987.

[Mor07] D. P. Morgan. *Surface acoustic wave filters. With applications to electronic communications and signal processing*. 2. ed. Studies in Electrical and Electronic Engineering. Elsevier, 2007.

[Mül09] U. Müller. *Anorganische Strukturchemie*. 6. Aufl. Studienbücher Chemie. Vieweg + Teubner, 2009.

[Myu18] C. W. Myung, J. Yun, G. Lee and K. S. Kim. 'A New Perspective on the Role of A-Site Cations in Perovskite Solar Cells'. *Advanced Energy Materials* 8.14 (2018), p. 1702898. DOI: 10.1002/aenm.201702898.

[Nat19] National Renewable Energy Laboratory. *Best Research-Cell Efficiencies*. 2019. URL: www.nrel.gov/pv/device-performance.html (visited on 26/10/2019).

[Nov04] K. S. Novoselov, A. K. Geim, S. V. Morozov, D. Jiang, Y. Zhang et al. 'Electric field effect in atomically thin carbon films'. *Science* 306.5696 (2004), pp. 666–669. DOI: 10.1126/science.1102896.

[Oxf19] Oxford PV. *The perovskite-silicon tandem*. 2019. URL: www.oxfordpv.com/perovskite-silicon-tandem (visited on 19/11/2019).

[Pal16] F. Palazon, F. Di Stasio, S. Lauciello, R. Krahne, M. Prato et al. 'Evolution of $CsPbBr_3$ nanocrystals upon post-synthesis annealing under an inert atmosphere'. *Journal of Materials Chemistry C* 4.39 (2016), pp. 9179–9182. DOI: 10.1039/c6tc03342c.

[Pas17] B. Paschke, A. Wixforth, D. Denysenko and D. Volkmer. 'Fast Surface Acoustic Wave-Based Sensors to Investigate the Kinetics of Gas Uptake in Ultra-Microporous Frameworks'. *ACS Sensors* 2.6 (2017), pp. 740–747. DOI: 10.1021/acssensors.7b00014.

[Pico] PicoQuant GmbH. 'Photon counting and timing' (2019).

[Pig07] F. Pignatiello, M. de Rosa, P. Ferraro, S. Grilli, P. de Natale et al. 'Measurement of the thermal expansion coefficients of ferroelectric crystals by a moiré interferometer'. *Optics Communications* 277.1 (2007), pp. 14–18. DOI: 10.1016/j.optcom.2007.04.045.

[Pra04] P. N. Prasad. *Nanophotonics*. Wiley-Interscience, 2004. DOI: 10.1002/0471670251.

[Pra19] V. Prakasam, D. Tordera, H. J. Bolink and G. Gelinck. 'Degradation Mechanisms in Organic Lead Halide Perovskite Light–Emitting Diodes'. *Advanced Optical Materials* 7.22 (2019), p. 1900902. DOI: 10.1002/adom.201900902.

[Pro15] L. Protesescu, S. Yakunin, M. I. Bodnarchuk, F. Krieg, R. Caputo et al. 'Nanocrystals of Cesium Lead Halide Perovskites ($CsPbX_3$, X = Cl, Br, and I): Novel Optoelectronic Materials Showing Bright Emission with Wide Color Gamut'. *Nano letters* 15.6 (2015), pp. 3692–3696. DOI: 10.1021/nl5048779.

[Pus95] T. Pustelny. 'Acoustic method of investigating the surface potential in semiconductors. Study of the GaP:Te (110) real surface'. *Ultrasonics* 33.4 (1995), pp. 289–294. DOI: 10.1016/0041-624X(94)00040-V.

[Ray85] Rayleigh. 'On Waves Propagated along the Plane Surface of an Elastic Solid'. *Proceedings of the London Mathematical Society* s1-17.1 (1885), pp. 4–11. DOI: 10.1112/plms/s1-17.1.4.

[Reg13] M. E. Regler, H. J. Krenner, A. A. Green, M. C. Hersam, A. Wixforth et al. 'Controlling exciton decay dynamics in semiconducting single-walled carbon nanotubes by surface acoustic waves'. *Chemical Physics* 413 (2013), pp. 39–44. DOI: 10.1016/j.chemphys.2012.10.014.

[Ren17] K. Ren, Le Huang, S. Yue, S. Lu, K. Liu et al. 'Turning a disadvantage into an advantage: synthesizing high-quality organometallic halide perovskite nanosheet arrays for humidity sensors'. *Journal of Materials Chemistry C* 5.10 (2017), pp. 2504–2508. DOI: 10.1039/C6TC05165K.

[Ric85] A. J. Ricco, S. J. Martin and T. E. Zipperian. 'Surface acoustic wave gas sensor based on film conductivity changes'. *Sensors and Actuators* 8.4 (1985), pp. 319–333. DOI: 10.1016/0250-6874(85)80031-7.

[Ric91] A. J. Ricco and S. J. Martin. 'Thin metal film characterization and chemical sensors: monitoring electronic conductivity, mass loading and mechanical properties with surface acoustic wave devices'. *Thin Solid Films* 206.1-2 (1991), pp. 94–101. DOI: 10.1016/0040-6090(91)90399-I.

[Rid88] B. K. Ridley. 'Space charge waves and the piezo-electric interaction in 2D semiconducting structures'. *Journal of the Physical Society of Japan* 3.6 (1988), pp. 542–545. DOI: 10.1088/0268-1242/3/6/005.

[Roc97] C. Rocke, S. Zimmermann, A. Wixforth, J. P. Kotthaus, G. Böhm et al. 'Acoustically Driven Storage of Light in a Quantum Well'. *Physical Review Letters* 78.21 (1997), pp. 4099–4102. DOI: 10.1103/PhysRevLett.78.4099.

[Ros39] G. Rose. 'Beschreibung einiger neuen Mineralien des Urals'. *Annalen der Physik und Chemie* 124.12 (1839), pp. 551–573. DOI: 10.1002/andp.18391241205.

[Rot97] M. Rotter, C. Rocke, Böhm S., Lorke A. and A. Wixforth. 'Single-chip fused hybrids for acousto-electric and acousto-optic applications'. *Applied Physics Letters* 70.16 (1997), pp. 2097–2099. DOI: 10.1063/1.118960.

[Roy00] D. Royer and E. Dieulesaint. *Elastic waves in solids*. Advanced texts in physics. Springer, 2000.

[Rup93] C. W. Ruppel, R. Dill, A. Fischerauer, G. Fischerauer, A. Gawlik et al. 'SAW devices for consumer communication applications'. *IEEE transactions on ultrasonics, ferroelectrics, and frequency control* 40.5 (1993), pp. 438–452. DOI: 10.1109/58.238094.

[Sab16] M. Saba, F. Quochi, A. Mura and G. Bongiovanni. 'Excited State Properties of Hybrid Perovskites'. *Accounts of chemical research* 49.1 (2016), pp. 166–173. DOI: 10.1021/acs.accounts.5b00445.

[Sai16] W. A. Saidi, S. Poncé and B. Monserrat. 'Temperature Dependence of the Energy Levels of Methylammonium Lead Iodide Perovskite from First-Principles'. *The journal of physical chemistry letters* 7.24 (2016), pp. 5247–5252. DOI: 10.1021/acs.jpclett.6b02560.

[Sal13] B. E. A. Saleh and M. C. Teich. *Fundamentals of Photonics*. 2. ed. John Wiley & Sons, 2013.

[Sap16] B. Saparov and D. B. Mitzi. 'Organic-Inorganic Perovskites: Structural Versatility for Functional Materials Design'. *Chemical reviews* 116.7 (2016), pp. 4558–4596. DOI: 10.1021/acs.chemrev.5b00715.

[Sch12] F. J. R. Schülein, J. Pustiowski, K. Müller, M. Bichler, G. Koblmüller et al. 'Surface acoustic wave controlled charge dynamics in a thin InGaAs quantum well'. *JETP Letters* 95.11 (2012), pp. 575–580. DOI: 10.1134/S0021364012110082.

[Sch13] F. J. R. Schülein, K. Müller, M. Bichler, G. Koblmüller, J. J. Finley et al. 'Acoustically regulated carrier injection into a single optically active quantum dot'. *Physical Review B* 88.8 (2013), p. 085307. DOI: 10.1103/PhysRevB.88.085307.

[Sch14a] L. C. Schmidt, A. Pertegás, S. González-Carrero, O. Malinkiewicz, S. Agouram et al. 'Nontemplate synthesis of $CH_3NH_3PbBr_3$ perovskite nanoparticles'. *Journal of the American Chemical Society* 136.3 (2014), pp. 850–853. DOI: 10.1021/ja4109209.

[Sch14b] F. J. R. Schülein. 'Dynamische Kontrolle optisch aktiver Halbleiter-Quantenpunkte mittels akustischer Oberflächenwellen'. Doctoral Thesis. Universität Augsburg, 2014.

[Sch15] F. J. R. Schülein, E. Zallo, P. Atkinson, O. G. Schmidt, R. Trotta et al. 'Fourier synthesis of radiofrequency nanomechanical pulses with different shapes'. *Nature nanotechnology* 10.6 (2015), pp. 512–516. DOI: 10.1038/nnano.2015.72.

[Sch93] Schlarb and Betzler. 'Refractive indices of lithium niobate as a function of temperature, wavelength, and composition: A generalized fit'. *Physical review. B, Condensed matter* 48.21 (1993), pp. 15613–15620. DOI: 10.1103/PhysRevB.48.15613.

[See04] K. Seeger. *Semiconductor physics. An introduction*. 9. ed. Advanced texts in physics. Springer, 2004.

[Sel84] S. Selberherr. *Analysis and Simulation of Semiconductor Devices*. Springer Vienna, 1984. DOI: 10.1007/978-3-7091-8752-4.

[Sha14] R.-w. Shao, K. Zheng, B. Wei, Y.-f. Zhang, Y.-j. Li et al. 'Bandgap engineering and manipulating electronic and optical properties of ZnO nanowires by uniaxial strain'. *Nanoscale* 6.9 (2014), pp. 4936–4941. DOI: 10.1039/c4nr00059e.

[She17] Q. Shen, T. S. Ripolles, J. Even, Y. Ogomi, K. Nishinaka et al. 'Slow hot carrier cooling in cesium lead iodide perovskites'. *Applied Physics Letters* 111.15 (2017), p. 153903. DOI: 10.1063/1.4991993.

[She18] T. Sherahilo. *Oxford PV perovskite solar cell achieves 28% efficiency*. 2018. URL: www.oxfordpv.com/news/oxford-pv-perovskite-solar-cell-achieves-28-efficiency (visited on 14/11/2019).

[Shi15] D. Shi, V. Adinolfi, R. Comin, M. Yuan, E. Alarousu et al. 'Solar cells. Low trap-state density and long carrier diffusion in organolead trihalide perovskite single crystals'. *Science* 347.6221 (2015), pp. 519–522. DOI: 10.1126/science.aaa2725.

[Sic15] J. A. Sichert, Y. Tong, N. Mutz, M. Vollmer, S. Fischer et al. 'Quantum Size Effect in Organometal Halide Perovskite Nanoplatelets'. *Nano letters* 15.10 (2015), pp. 6521–6527. DOI: 10.1021/acs.nanolett.5b02985.

[Sie86] A. E. Siegman. *Lasers*. University Science Books, 1986.

[Sim96] Simon. 'Coupling of surface acoustic waves to a two-dimensional electron gas'. *Physical review. B, Condensed matter* 54.19 (1996), pp. 13878–13884. DOI: 10.1103/PhysRevB.54.13878.

[Sin03] J. Singh. *Electronic and optoelectronic properties of semiconductor structures*. Cambridge Univ. Press, 2003.

[Siv08] S. Sivaramakrishnan, R. Rajamani, C. S. Smith, K. A. McGee, K. R. Mann et al. 'Carbon nanotube-coated surface acoustic wave sensor for carbon dioxide sensing'. *Sensors and Actuators B: Chemical* 132.1 (2008), pp. 296–304. DOI: 10.1016/j.snb.2008.01.041.

[Smi10] A. M. Smith and S. Nie. 'Semiconductor nanocrystals: structure, properties, and band gap engineering'. *Accounts of chemical research* 43.2 (2010), pp. 190–200. DOI: 10.1021/ar9001069.

[Smi75] W. R. Smith and W. F. Pedler. 'Fundamental- and Harmonic-Frequency Circuit-Model Analysis of Interdigital Transducers with Arbitrary Metallization Ratios and Polarity Sequences'. *IEEE Transactions on Microwave Theory and Techniques* 23.11 (1975), pp. 853–864. DOI: 10.1109/TMTT.1975.1128703.

[Son19] M. M. Sonner, A. Sitek, L. Janker, D. Rudolph, D. Ruhstorfer et al. 'Breakdown of Corner States and Carrier Localization by Monolayer Fluctuations in Radial Nanowire Quantum Wells'. *Nano letters* 19.5 (2019), pp. 3336–3343. DOI: 10.1021/acs.nanolett.9b01028.

[Son20] M. M. Sonner, L. Janker, D. Rudolph, A. Sitek, A. Manolescu et al. 'Electron cycloids driven by the transverse spin of a surface acoustic wave' (2020). *In preparation*.

[Sto13] C. C. Stoumpos, C. D. Malliakas, J. A. Peters, Z. Liu, M. Sebastian et al. 'Crystal Growth of the Perovskite Semiconductor $CsPbBr_3$: A New Material for High-Energy Radiation Detection'. *Crystal Growth & Design* 13.7 (2013), pp. 2722–2727. DOI: 10.1021/cg400645t.

[Str13] S. D. Stranks, G. E. Eperon, G. Grancini, C. Menelaou, M. J. P. Alcocer et al. 'Electron-hole diffusion lengths exceeding 1 micrometer in an organometal trihalide perovskite absorber'. *Science* 342.6156 (2013), pp. 341–344. DOI: 10.1126/science.1243982.

[Sut14] B. R. Sutherland, S. Hoogland, M. M. Adachi, C. T. O. Wong and E. H. Sargent. 'Conformal organohalide perovskites enable lasing on spherical resonators'. *ACS nano* 8.10 (2014), pp. 10947–10952. DOI: 10.1021/nn504856g.

[Sut16] B. R. Sutherland and E. H. Sargent. 'Perovskite photonic sources'. *Nature Photonics* 10.5 (2016), pp. 295–302. DOI: 10.1038/nphoton.2016.62.

[Swa15] A. Swarnkar, R. Chulliyil, V. K. Ravi, M. Irfanullah, A. Chowdhury et al. 'Colloidal $CsPbBr_3$ Perovskite Nanocrystals: Luminescence beyond Traditional Quantum Dots'. *Angewandte Chemie (International ed. in English)* 54.51 (2015), pp. 15424–15428. DOI: 10.1002/anie.201508276.

[Sze07] S. M. Sze and K. K. Ng. *Physics of semiconductor devices*. 3. ed. Wiley-Interscience, 2007. DOI: 10.1002/0470068329.

[Tan14] Z.-K. Tan, R. S. Moghaddam, M. L. Lai, P. Docampo, R. Higler et al. 'Bright light-emitting diodes based on organometal halide perovskite'. *Nature nanotechnology* 9.9 (2014), pp. 687–692. DOI: 10.1038/nnano.2014.149.

[Thu05] F. Thuselt. *Physik der Halbleiterbauelemente. Einführendes Lehrbuch für Ingenieure und Physiker*. Springer-Lehrbuch. Springer, 2005.

[Til16] J. Tilchin, D. N. Dirin, G. I. Maikov, A. Sashchiuk, M. V. Kovalenko et al. 'Hydrogen-like Wannier–Mott Excitons in Single Crystal of Methylammonium Lead Bromide Perovskite'. *ACS nano* 10.6 (2016), pp. 6363–6371. DOI: 10.1021/acsnano.6b02734.

[Tom17] S. Tombe, G. Adam, H. Heilbrunner, D. H. Apaydin, C. Ulbricht et al. 'Optical and electronic properties of mixed halide (X = I, Cl, Br) methylammonium lead perovskite solar cells'. *Journal of Materials Chemistry C* 5.7 (2017), pp. 1714–1723. DOI: 10.1039/c6tc04830g.

[Ton16] Y. Tong, E. Bladt, M. F. Aygüler, A. Manzi, K. Z. Milowska et al. 'Highly Luminescent Cesium Lead Halide Perovskite Nanocrystals with Tunable Composition and Thickness by Ultrasonication'. *Angewandte Chemie (International ed. in English)* 55.44 (2016), pp. 13887–13892. DOI: 10.1002/anie.201605909.

[Ton17] Y. Tong, B. J. Bohn, E. Bladt, K. Wang, P. Müller-Buschbaum et al. 'From Precursor Powders to $CsPbX_3$ Perovskite Nanowires: One-Pot Synthesis, Growth Mechanism, and Oriented Self-Assembly'. *Angewandte Chemie (International ed. in English)* 56.44 (2017), pp. 13887–13892. DOI: 10.1002/anie.201707224.

[Ton18] Y. Tong, E.-P. Yao, A. Manzi, E. Bladt, K. Wang et al. 'Spontaneous Self-Assembly of Perovskite Nanocrystals into Electronically Coupled Supercrystals: Toward Filling the Green Gap'. *Advanced materials* (2018), p. 1801117. DOI: 10.1002/adma.201801117.

[Tsa19] W.-L. Tsai, C.-Y. Chen, Y.-T. Wen, L. Yang, Y.-L. Cheng et al. 'Band Tunable Microcavity Perovskite Artificial Human Photoreceptors'. *Advanced materials* 31.24 (2019), p. 1900231. DOI: 10.1002/adma.201900231.

[Uch15] K. Uchino. 'Glory of piezoelectric perovskites'. *Science and technology of advanced materials* 16.4 (2015), p. 046001. DOI: 10.1088/1468-6996/16/4/046001.

[Urb13] M. Urbańczyk and T. Pustelny. 'The Application of Surface Acoustic Waves in Surface Semiconductor Investigations and Gas Sensors'. *Modeling and Measurement Methods for Acoustic Waves and for Acoustic Microdevices*. InTech, 2013. DOI: 10.5772/53717.

[Var67] Y. P. Varshni. 'Temperature dependence of the energy gap in semiconductors'. *Physica* 34.1 (1967), pp. 149–154. DOI: 10.1016/0031-8914(67)90062-6.

[Vil17] B. Villa, A. J. Bennett, D. J. P. Ellis, J. P. Lee, J. Skiba-Szymanska et al. 'Surface acoustic wave modulation of a coherently driven quantum dot in a pillar microcavity'. *Applied Physics Letters* 111.1 (2017), p. 011103. DOI: 10.1063/1.4990966.

[Vog93] T. Vogt and W. W. Schmahl. 'The High-Temperature Phase Transition in Perovskite'. *Europhysics Letters (EPL)* 24.4 (1993), pp. 281–285. DOI: 10.1209/0295-5075/24/4/008.

[Völ11] S. Völk, F. Knall, F. J. R. Schülein, T. A. Truong, H. Kim et al. 'Direct observation of dynamic surface acoustic wave controlled carrier injection into single quantum posts using phase-resolved optical spectroscopy'. *Applied Physics Letters* 98.2 (2011), p. 023109. DOI: 10.1063/1.3541881.

[Wan37] G. H. Wannier. 'The Structure of Electronic Excitation Levels in Insulating Crystals'. *Physical Review* 52.3 (1937), pp. 191–197. DOI: 10.1103/PhysRev.52.191.

[Wei14a] M. Weiß, J. B. Kinzel, F. J. R. Schülein, M. Heigl, D. Rudolph et al. 'Dynamic acoustic control of individual optically active quantum dot-like emission centers in heterostructure nanowires'. *Nano letters* 14.5 (2014), pp. 2256–2264. DOI: 10.1021/nl4040434.

[Wei14b] M. Weiß, F. J. R. Schülein, J. B. Kinzel, M. Heigl, D. Rudolph et al. 'Radio frequency occupancy state control of a single nanowire quantum dot'. *Journal of Physics D: Applied Physics* 47.39 (2014), p. 394011. DOI: 10.1088/0022-3727/47/39/394011.

[Wel93] H. L. Wells. 'Über die Cäsium- und Kalium-Bleihalogenide'. *Zeitschrift für anorganische Chemie* 3.1 (1893), pp. 195–210. DOI: 10.1002/zaac.18930030124.

[Whi16] P. S. Whitfield, N. Herron, W. E. Guise, K. Page, Y. Q. Cheng et al. 'Structures, Phase Transitions and Tricritical Behavior of the Hybrid Perovskite Methyl Ammonium Lead Iodide'. *Scientific reports* 6 (2016), p. 35685. DOI: 10.1038/srep35685.

[Whi65] R. M. White and F. W. Voltmer. 'Direct piezoelectric coupling to surface elastic waves'. *Applied Physics Letters* 7.12 (1965), pp. 314–316. DOI: 10.1063/1.1754276.

[Wix89] A. Wixforth, J. Scriba, M. Wassermeier, J. Kotthaus, G. Weimann et al. 'Surface acoustic waves on GaAs/$Al_xGa_{1-x}As$ heterostructures'. *Physical Review B* 40.11 (1989), p. 7874. DOI: 10.1103/PhysRevB.40.7874.

[Wol14] S. de Wolf, J. Holovsky, S.-J. Moon, P. Löper, B. Niesen et al. 'Organometallic Halide Perovskites: Sharp Optical Absorption Edge and Its Relation to Photovoltaic Performance'. *The journal of physical chemistry letters* 5.6 (2014), pp. 1035–1039. DOI: 10.1021/jz500279b.

[Xia14] H.-R. Xia, J. Li, W.-T. Sun and L.-M. Peng. 'Organohalide lead perovskite based photodetectors with much enhanced performance'. *Chemical communications* 50.89 (2014), pp. 13695–13697. DOI: 10.1039/C4CC05960C.

[Xia19] W. Xiang and W. Tress. 'Review on Recent Progress of All-Inorganic Metal Halide Perovskites and Solar Cells'. *Advanced materials* 31.44 (2019), p. 1902851. DOI: 10.1002/adma.201902851.

[Xin14] G. Xing, N. Mathews, S. S. Lim, N. Yantara, X. Liu et al. 'Low-temperature solution-processed wavelength-tunable perovskites for lasing'. *Nature materials* 13.5 (2014), pp. 476–480. DOI: 10.1038/nmat3911.

[Xin15] J. Xing, X. F. Liu, Q. Zhang, S. T. Ha, Y. W. Yuan et al. 'Vapor Phase Synthesis of Organometal Halide Perovskite Nanowires for Tunable Room-Temperature Nanolasers'. *Nano letters* 15.7 (2015), pp. 4571–4577. DOI: 10.1021/acs.nanolett.5b01166.

[Xu16] W. Xu, F. Li, Z. Cai, Y. Wang, F. Luo et al. 'An ultrasensitive and reversible fluorescence sensor of humidity using perovskite $CH_3NH_3PbBr_3$'. *Journal of Materials Chemistry C* 4.41 (2016), pp. 9651–9655. DOI: 10.1039/C6TC01075J.

[Xu19] L. Xu, J. Li, T. Fang, Y. Zhao, S. Yuan et al. 'Synthesis of stable and phase-adjustable $CsPbBr_3@Cs_4PbBr_6$ nanocrystals via novel anion–cation reactions'. *Nanoscale Advances* 1.3 (2019), pp. 980–988. DOI: 10.1039/C8NA00291F.

[Yak15] S. Yakunin, L. Protesescu, F. Krieg, M. I. Bodnarchuk, G. Nedelcu et al. 'Low-threshold amplified spontaneous emission and lasing from colloidal nanocrystals of caesium lead halide perovskites'. *Nature communications* 6 (2015), p. 8056. DOI: 10.1038/ncomms9056.

[Yu10] P. Y. Yu and M. Cardona. *Fundamentals of Semiconductors. Physics and Materials Properties*. 4. ed. Graduate Texts in Physics. Springer-Verlag Berlin Heidelberg, 2010. DOI: 10.1007/978-3-642-00710-1.

[Yu11] C. Yu, Z. Chen, J. J. Wang, W. Pfenninger, N. Vockic et al. 'Temperature dependence of the band gap of perovskite semiconductor compound $CsSnI_3$'. *Journal of Applied Physics* 110.6 (2011), p. 063526. DOI: 10.1063/1.3638699.

[Yua17] G. Yuan, C. Ritchie, M. Ritter, S. Murphy, D. E. Gómez et al. 'The Degradation and Blinking of Single $CsPbI_3$ Perovskite Quantum Dots'. *The Journal of Physical Chemistry C* 122.25 (2017), pp. 13407–13415. DOI: 10.1021/acs.jpcc.7b11168.

[Zha14] Y. Zhao and K. Zhu. 'Optical bleaching of perovskite $(CH_3NH_3)PbI_3$ through room-temperature phase transformation induced by ammonia'. *Chemical communications* 50.13 (2014), pp. 1605–1607. DOI: 10.1039/C3CC48522F.

[Zha15] F. Zhang, H. Zhong, C. Chen, X.-g. Wu, X. Hu et al. 'Brightly Luminescent and Color-Tunable Colloidal $CH_3NH_3PbX_3$ (X = Br, I, Cl) Quantum Dots: Potential Alternatives for Display Technology'. *ACS nano* 9.4 (2015), pp. 4533–4542. DOI: 10.1021/acsnano.5b01154.

[Zha16] Y. Zhang, J. Liu, Z. Wang, Y. Xue, Q. Ou et al. 'Synthesis, properties, and optical applications of low-dimensional perovskites'. *Chemical communications* 52.94 (2016), pp. 13637–13655. DOI: 10.1039/c6cc06425f.

[Zha18a] X. Zhang, S. Chen, X. Wang and A. Pan. 'Controlled Synthesis and Photonics Applications of Metal Halide Perovskite Nanowires'. *Small Methods* 3.1 (2018), p. 1800294. DOI: 10.1002/smtd.201800294.

[Zha18b] Z. Zhao, F. Gu, H. Rao, S. Ye, Z. Liu et al. 'Metal Halide Perovskite Materials for Solar Cells with Long-Term Stability'. *Advanced Energy Materials* 9.3 (2018), p. 1802671. DOI: 10.1002/aenm.201802671.

[Zhu15] H. Zhu, Y. Fu, F. Meng, X. Wu, Z. Gong et al. 'Lead halide perovskite nanowire lasers with low lasing thresholds and high quality factors'. *Nature materials* 14.6 (2015), pp. 636–642. DOI: 10.1038/nmat4271.

[Zhu18] Z. Zhu, Q. Sun, Z. Zhang, J. Dai, G. Xing et al. 'Metal halide perovskites: stability and sensing-ability'. *Journal of Materials Chemistry C* 6.38 (2018), pp. 10121–10137. DOI: 10.1039/c8tc03164a.

Acknowledgements

At this point, I would like to express my gratitude for all the support I have received over the years in the course of this thesis. Many people have contributed to this work and the successful finalization.

First of all, I would like to thank Hubert Krenner for inviting me to his group and supporting me throughout the years. He made it possible for me to have the wonderful opportunity to attend several international conferences and encouraged me to hold presentations. The many new ideas he had were sometimes challenging, but always exciting and fruitful.

I also want to thank Achim Wixforth. The open atmosphere at the chair is based on his good attitude towards teamwork. His interest in all the projects and his large knowledge base made him a great help in discussions.

Many results of my thesis are the outcome of fruitful collaborations. Therefore, I want to thank both groups with whom I have worked in the last few years. Jonathan Finley who believed in me already during my Master's thesis at his chair. He was a great motivator even during my PhD when I met him at conferences. His group, in particular Gregor Koblmüller and Bernhard Loitsch, prepared the nanowires of GaAs for the first project of my thesis and helped analyse the results. For my second collaboration, I want to thank Jochen Feldmann, Alexander Urban, Lakshminarayana Polavarapu and Yu Tong for the quick and easy provision of perovskite samples and the extensive discussions which led to new ideas and investigations. In particular, I am grateful to Alexander Urban, who was willing to become by second referee and always gave constructive feedback to my work.

Life during the PhD would have been exhausting without the distraction of my office mates and the other members of the Hoobgroup – Sebastian Hammer, Moritz Mangold, Emeline Nysten, Tobias Petzak, Maximilian Sonner and Matthias Weiß. I enjoyed a lot the after-work beer sessions and the excursions we did together.
In particular, I want to thank Sebastian Hammer for making my train travel time less boring during my time of commuting, the very fun Python coding weekend and his open ear when I needed someone to listen.

The persons who really run all the instruments in the laboratories are most of the time more in the background. I want to thank Andreas Hörner, Sidonie Lieber, Adrian Mainka, Andreas Spörhase and Olga Ustinov for keeping the equipment alive and for always being present for urgent help.

Alexander Hupfer, the EDV technician of the chair is more then just that. He helps out in the workshop, he provides beverages and music and he is always available for a chat to help with practical tips at work or discuss life and the world.

Funda Cevik cares about all the bureaucratic and organizational issues and is a great help in filling out strange forms.

I also want to express my gratitude to all the other members of Experimentalphysik 1 for the great support, the legendary parties, the fun chair seminars and all the other activities.
I want to give a special thank to Anna Jötten and Emeline Nysten for caring about me.

* * *

Beside all the people at the workplace, there are some more whose support for me started way earlier than my PhD, but who have been caring for me since we know each other.

To one of my best friends, Jost Migenda, I have to express the deepest gratitude. Despite the large spatial distance that separates us, they are always close and cheered me up in my worst days. We have known each other for so long now and I hope that this friendship will last forever. Thank you for the practical and emotional support during all those years.

Two more friends have helped me with their emotional support and an open ear during the calm and the stressful times of the last years. Alexander Backs and Michael Fritscher have each one in their own way given me the feeling of not being alone and that I can always count on them.

Finally, I have no words to describe how thankful I am to my beloved family, my parents Elke and Reinhard Janker and my sister Julia Janker, for the lifelong support in any possible way, for their unconditional, endless love, for their constructive criticism and for always believing in me. Home is where your heart is – and for me that is where you are. The same holds for my boyfriend Ulrich Greiner who supported me in so many ways.

And in addition, I would like to thank all those people that I do not know in person, but who enrich my work and life so much by their podcasts, blogs and TEX and Python packages.

* * *

This work was financially supported by the Nanosystems Initiative Munich (NIM) and the Deutsche Forschungsgemeinschaft (DFG). The NIM cluster provided the great opportunity to connect to and exchange ideas with other young scientists and to attend workshops.